Downloaded from orbit.dtu.dk on: May 05, 2023

DTU Library

Ordering Phenomena and Non-equilibrium Properties of Lattice Gas Models

Fiig, Thomas

Publication date:
1994

Document Version
Publisher's PDF, also known as Version of record

Link back to DTU Orbit

Citation (APA):
Fiig, T. (1994). *Ordering Phenomena and Non-equilibrium Properties of Lattice Gas Models*. Technical University of Denmark.

General rights
Copyright and moral rights for the publications made accessible in the public portal are retained by the authors and/or other copyright owners and it is a condition of accessing publications that users recognise and abide by the legal requirements associated with these rights.

- Users may download and print one copy of any publication from the public portal for the purpose of private study or research.
- You may not further distribute the material or use it for any profit-making activity or commercial gain
- You may freely distribute the URL identifying the publication in the public portal

If you believe that this document breaches copyright please contact us providing details, and we will remove access to the work immediately and investigate your claim.

DK9400062

RISØ

Risø-R-734(EN)

Ordering Phenomena and Non-equilibrium Properties of Lattice Gas Models

Thomas Fiig

Risø National Laboratory, Roskilde, Denmark
March 1994

Ordering Phenomena and Non-equilibrium Properties of Lattice Gas Models

Risø-R-734(EN)

Thomas Fiig

Risø National Laboratory, Roskilde, Denmark
March 1994

Abstract This report falls within the general field of ordering processes and non-equilibrium properties of lattice gas models. It is divided into three main parts. First, the theory of diffuse scattering of lattice gas models originating from a random distribution of clusters is considered. We obtain relations between the diffuse part of the structure factor $S_{\rm diff}(q)$, the correlation function $C(r)$, and the size distribution of clusters $P(n)$. For a number of distributions we calculate $S_{\rm diff}(q)$ exactly in one dimension, and discuss the possibility for having a Lorentzian and a Lorentzian square lineshape. We discuss the two- and three-dimensional oxygen ordering processes in the high T_c superconductor $YBa_2Cu_3O_{6+x}$ based on a simple anisotropic lattice gas model, known as the ASYNNNI model. We calculate the structural phase diagram by Monte Carlo simulation of both the ASYNNNI model and an extension of the model to three dimensions. The results are compared with experimental data. The structure factor of the oxygen ordering properties has been calculated in both two and three dimensions by Monte Carlo simulation. We report on results obtained from large scale computations on the Connection Machine, which are in excellent agreement with recent neutron diffraction data. As a subject of particular interest, we consider the effect of the diffusive motion of metal-ion dopants on the oxygen ordering properties of $YBa_2Cu_3O_{6+x}$. Second, the stationary properties of metastability in long-range interaction models are studied by application of a constrained transfer matrix (CTM) formalism. The model considered, which exhibits several metastable states, is an extension of the Blume Capel model to include weak long-range interactions. We show, that the decay rate of the metastable states is closely related to the imaginary part of the equilibrium free-energy density obtained from the CTM formalism. Third, we discuss a class of lattice gas model for dissipative transport in the framework of a Langevin description, which is capable of producing power law spectra for the density fluctuations. We compare with numerical results obtained from simulations of a lattice gas model consisting of repulsive particles obeying deterministic dynamics, driven by a white noise boundary condition.

This report is submitted in partial fulfillment of the requirements for a Ph.D. degree at the Technical University of Denmark. Supervisors on this project were Dr. P.-A. Lindgård at Risø National Laboratory, Prof. O. G. Mouritsen at the Technical University of Denmark, and Dr. N. H. Andersen at Risø National Laboratory.

This thesis is based on research work reported in the five journal papers listed below, and included in appendix A.

- Theory and Computer Simulation of Diffuse Scattering from Lattice Gas Models, submitted to *Phys. Rev. B.*
- Oxygen Ordering Phenomena in $YBa_2Cu_3O_{6+x}$ Studied by Monte Carlo Simulation, *Physica C*, 217:34, 1993.
- Monte Carlo Simulation of a Two-Species Diffusive Lattice Gas in Optimized C* on the Connection Machine, submitted to *Comp. Mat. Sci.*
- Numerical Transfer-matrix Study of a Model with Competing Metastable States, submitted to *Phys. Rev. E.*
- Diffusive Description of Lattice Gas Models, *J. Stat. Phys.*, 71:653, 1993.

ISBN 87-550-1959-5
ISSN 0106-2840

Grafisk Service · Risø · 1994

Contents

1 General Introduction

The present thesis falls in the general field of equilibrium ordering phenomena and non-equilibrium properties of physical systems, which have been the focus of intense research. It has been known for a long time that ordering phenomena arises as a result of a cooperative phenomenon and is therefore intimately related to the microscopic interactions between the constituents of the material. Generally, systems become more ordered as the temperature is lowered, because the interparticle interactions creating the order, can overcome the thermal motion. The theoretical basis for a description of these phenomena, is by means of statistical mechanics, which has proven to be a highly successful tool in characterizing the *equilibrium* behavior of thermodynamic systems. The behavior of thermodynamic systems sufficiently close to the equilibrium state, can also be treated within the context of statistical mechanics. By perturbing the system by a weak external field, the system responds in a way, which depends entirely on the spectrum of the equilibrium fluctuations. However, no such general formalism exist for describing the non-equilibrium behavior of systems far from equilibrium. As we shall see, some of the most striking phenomena exist in system, that are far from equilibrium.

Computer simulation studies have found widespread applications in particular within the field of statistical physics, see Refs. [1, 2, 3]. The reason for this is that computer simulation yields exact information on ideal model systems. Despite the fact that analytical results are often desirable from a theoretical point of view, such results can only be obtained in very few and specialized cases. From the experimental point of view the information obtained is often hampered by an influence of unwanted effects from impurities and other imperfections of the system. Obviously, computer simulation has a great advantages here, since the calculations do not suffer from these problems. A particular application of computer simulations which we shall consider is the calculation of the diffuse part of the structure factor $S_{\text{diff}}(\mathbf{q})$. This is of particular importance because the information obtained from diffraction experiments is given in reciprocal space. Since in computer simulation we have access to both real space and reciprocal space, the computer simulations come in as an important tool in the interpretation of the experimental data.

The computer simulation of systems undergoing structural transformations, usually proceed by the use of a simplified statistical mechanical model in which the particles and their degrees of freedom are placed on a regular lattice. The interactions between the particles is given by an effective Hamiltonian, which is often tailored on the basis of a lattice gas model, which captures the essential structural properties of the system. The formulation of the problem as a lattice gas implies some major reduction of the computational effort. On a serial computer the CPU time for one Monte Carlo step per site increases as N^d, where N is the linear extension of the system and d is the dimension. But more seriously the intrinsic relaxation time required to reach equilibrium also increases with the system size. Therefore, in order to obtain reliable statistical information on particle ensembles which are sufficiently large to give an accurate description, we need to make use of optimized programs on supercomputers. We will report on such studies making use of some of the fastest vector and parallel computers available today.

In Chap. 3 we investigate by Monte Carlo simulation the two- and three-dimensional oxygen ordering processes in the ceramic copper-oxide superconductor $YBa_2Cu_3O_{6+x}$, based on the anisotropic two-dimensional lattice gas model, known as the ASYNNNI model. In addition we discuss the effects of the diffusive motion of metal-ion dopants on the two-dimensional oxygen ordering process, based on simulation studies on a massively parallel computer, the Connection Machine.

These ordering processes in $YBa_2Cu_3O_{6+x}$ are of particular interest, because there is experimental evidence, that not only the oxygen contents x but also the nature of the oxygen ordering is important for the superconducting transition temperature. Experimentally there have been many attempts to change the superconducting properties of $YBa_2Cu_3O_{6+x}$ by chemical substitution. In principle it should be possible to increase the superconducting transition temperature T_c by additional hole doping, but in all cases T_c has been found to decrease. Doping with M = Co, Fe, and Al is in particular interesting for the studies of the oxygen structural ordering and its influence on T_c, because they substitute predominantly for Cu in the CuO_x basal planes of the structure, and consequently they cause oxygen disordering.

In the Monte Carlo simulation studies of equilibrium statistical physics, the emphasis is to achieve a realistic statistical distribution of particle configurations at a given temperature. From such single configurations one can get a physical insight in the problem, however they are not very useful in a statistical sense and therefore one needs to condense the information. Traditionally this is done by calculating order parameters, susceptibilities, correlation functions *etc*. However, when it comes to comparison with experimental data obtained by diffraction techniques, such as neutron scattering and X-ray scattering, the above methods have serious shortcomings. This is because the experimental information is obtained in reciprocal space in terms of the structure factor $S(\mathbf{q})$.

Even though the theories for analysing $S(\mathbf{q})$ were developed a long time ago, there still exist unsolved questions about how to characterize the corresponding real space behavior. We have tried to answer some of these questions, by analyzing the diffuse scattering, that arises from a random distribution of clusters in an undistorted one-dimensional crystal, see Chap. 2. Our viewpoint is somewhat different from the traditional way of describing a system in terms of the pair correlation function. We focus on the cluster size distribution function $\mathcal{D}(n)$, which measures the probability of finding a cluster of size n. Since in these simple models for the cluster distributions we have access to both real space and reciprocal space we have gained some insight into which real-space properties that determine the behavior of the structure factor.

In computer simulation of $S_{\mathrm{dif}}(\mathbf{q})$ using serial computers a direct Fourier transformation of the real space information is generally very inefficient, since only the total projection of the real space information along the $\mathbf{q}$-direction is needed. This means that for a d-dimensional system with N^d lattice sites only N numbers need to be Fourier transformed. However on the Connection Machine (CM), it is equally fast to Fourier transform the entire real-space configuration. In Chap. 3 we will discuss the results of a three-dimensional simulation of $S_{\mathrm{dif}}(\mathbf{q})$ on a $256\times256\times16$ lattice for the oxygen ordering properties in $YBa_2Cu_3O_{6+x}$ using the CM. The results from this study have contributed in a decisive way to interpret experimental neutron diffraction data.

So far we have considered statistical mechanical systems in equilibrium. As we drive the system away from its thermodynamic regime, the system may change dramatically. Some of the most striking phenomena of this kind associated with phase transitions are hysteresis and metastability. Experimentally, metastable states have been found in a variety of systems, *e.g.* parts of the hysteresis loop associated with the magnetization reversal in a ferromagnet, or phase separation in alloys, supercooled vapor *etc*. Metastable states can be characterized as long-lived non-equilibrium states, that exist in a kind of quasi-equilibrium. Under small changes of the intensive variables of the system, the metastable state responds by small reversible changes. However, under large changes the system changes irreversibly (escapes) out of the metastable state.

The description of metastable states at a fundamental level, is both an interest-

ing and unsolved problem in statistical mechanics. The very long lifetime observed for metastable states in many systems, suggests that equilibrium statistical mechanics might be extended to include these states. One way this can be done, is by the introduction of a restricted statistical ensemble, which excludes or severely reduces the statistical weights of those microstates, that correspond to the true equilibrium state. This approach was followed by Langer [4] in a study of the analytical properties of free energy at the condensation point. Langer considered the imaginary part of the *equilibrium* free energy $\mathrm{Im}f$, which is the analytical continuation of that for the equilibrium state. Langer suggested that $\mathrm{Im}f$ may be associated with the decay rate of the metastable state.

In computer simulations, the equilibrium free energy f is most easily obtained from the largest eigenvalue λ_0 of the equilibrium transfer matrix by $f = k_B T \ln(\lambda_0)$. It was then *conjectured* by Newman and Schulman [5], that the remaining eigenvalues of the transfer matrix might provide useful information about the *non-equilibrium* behavior of the system. By analogy they defined a set of generalized free energies by $f_n = k_B T \ln(\lambda_n)$, $n>0$. However, since these eigenvalues are in general not positive, the generalized free energies are complex. The method by Newman and Schulman clearly showed some promise in the characterization of metastable states, although quantitative agreement with model systems could not be claimed.

Along the same line of thoughts, a constrained transfer-matrix (CTM) formalism was recently developed. Unlike the method of Newman and Schulman, the CTM formalism focuses on non-equilibrium probability densities, which are generated through the construction of non-equilibrium transfer matrices, which in turn are obtained from the eigenvalues and eigenvectors of the equilibrium transfer matrix. In this fashion, the CTM formalism provides us with a set of non-equilibrium free-energy densities.

In a recent study of an Ising model with weak, long-range interactions, Gorman *et al.* [6] found strong quantitative agreement between the imaginary part of the non-equilibrium free-energy density from the CTM formalism and the decay rate density of the metastable state as measured from the activation barrier. However, for systems with several metastable states, Gaveau and Schulman [7] have argued that the analytical continuation of the free energy is not a valid measure of the decay rate density. Motivated by this, we consider in Chap. 4 the application of the CTM formalism to a Blume-Capel model, in order to establish to what extent the imaginary part of the free energy from the CTM formalism can be interpreted as a decay rate in more complicated systems, containing several metastable states.

We have studied an extension of the Blume-Capel model to include weak, long-range interactions. The reasons are that for a certain field-range a region with two competing metastable states exists, and that the model is simple enough to allow extensive symmetry reduction of the transfer matrix so that large systems can be considered.

We will now turn to the description of dynamical systems, that are driven into a non-equilibrium steady state. Dynamical systems are fundamentally different from systems being in an equilibrium or quasi-equilibrium state. As we shall see dynamical systems open up a whole new world of phenomena. Despite, or because of the complexity and non-linearity of the dynamical system, they can self-organize in ordered non-equilibrium structures which act as attractors for the dynamics.

In certain chemical reactions, which are driven by a constant flow of chemicals, the self-organized structures may be steady states in which the relative concentrations of the constituents vary in space, creating non-linear traveling waves in the concentrations of some constituents. Other phenomena include examples from biological evolution, economics *etc.*

From a theoretical point of view, the description of dynamical systems with few

degrees of freedom has given rise to a whole new field in physics. This field, by now known as chaos, has been hailed as one of the most important breakthroughs in physics. In contrast the description of dynamical systems with a huge number of degrees of freedom has proven to be exceedingly difficult, and our knowledge is almost exclusively restricted to computer simulations.

A few years ago Bak, Thang, and Wiesenfeld (BTW) [8] suggested that the frequent occurrence of 1 f-noise and fractal structures are the generic temporal and spatial characteristic of dynamical driven systems with many spatial degrees of freedom. They used a lattice gas model or cellular automaton, as they are commonly called, to illustrate the idea, which has now become the paradigm of self-organized criticality.

Motivated by the self-organized-critical model studied by Bak, Thang, and Wiesenfeld, we consider in Chap. 5 a deterministic lattice gas model. The deterministic lattice gas model consists of repulsive particles following deterministic dynamics driven by particles, which are injecting stochastically at the boundary. Even this simple model exhibits a remarkable complex spatial and temporal behavior, as the boundary drive exceeds a critical value, which gives rise to a $1/f$ power spectrum for the density fluctuations. This is interesting because such a power spectrum does not contain any characteristic frequency. Moreover, the autocorrelation function of the time signal is a constant, which implies that the correlations among the particles are preserved in time. By studying this and other related models, we have gained insight into how the nature of the microscopic dynamics influence the collective behavior of the system and thereby also the power spectrum of the density fluctuations.

This thesis is based on research work reported in the journal papers: I, II, III, IV and V, which are included in appendix A. The thesis is organized as follows. In Chap. 2 we discuss the theory of diffuse scattering of lattice-gas models, originating from spatial inhomogeneities in the material composition as clusters in an undistorted periodic lattice. In Chap. 3 we consider the oxygen ordering processes both in the pure and in the metal-ion doped $YBa_2Cu_3O_{6+x}$. Specifically we calculate the three-dimensional structure factor. In Chap. 4 we apply the constrained transfer-matrix formalism to study metastability in an extension of the Blume-Capel model to include weak, long-range interactions. Chapter 5 contains a discussion of boundary driven deterministic lattice gas model. In addition we analyze a specific class of driven systems in the framework of a Langevin description.

2 Theory of Diffuse Scattering of Lattice Gas Models

In this chapter we discuss the theory of diffuse scattering of lattice-gas models, originating from spatial inhomogeneities in the material composition as clusters in an undistorted periodic lattice, based on the results of paper I. In Sec. 2.1 we define the structure factor for an arbitrary crystal system, and review basic properties of structure factor calculations on lattice-gas models. In Sec. 2.2, we obtain a decomposition of the structure factor $S(\mathbf{q})$ into two contributions $S(\mathbf{q}) = S_{\text{Bragg}}(\mathbf{q}) + S_{\text{diff}}(\mathbf{q})$, where the first part represents the Bragg scattering from the average particle configuration and the second part represents the diffuse scattering, which carries information about the correlation lengths. Section 2.2 contains our main results. In the approximation, where the clusters are assumed to be non-interacting, so that overlapping clusters are allowed, we obtain for a one-dimensional lattice gas a relation between $S_{\text{diff}}(\mathbf{q})$, the correlation function $C(r)$, and the cluster size distribution $P(n)$, which can be generalized to higher dimensions. These relations are then used to calculate the cluster size distributions, that give rise to a Lorentzian, and a Lorentzian square lineshape for $S_{\text{diff}}(\mathbf{q})$. We then generalize these relations to the case where the interference effects between different clusters are included, and calculate exactly for a number of one-dimensional cluster distributions the line shapes of $S_{\text{diff}}(\mathbf{q})$.

2.1 Introduction

The diffuse scattering of X-rays and neutrons provides a powerful tool to investigate disorder and defects in structure at a microscopic level in condensed matter physics. The full treatment of the theoretical background for the diffuse diffraction pattern lies beyond the scope of this thesis, and we will only consider the situation where the diffuse scattering is due to spatial inhomogeneities in the material composition as clusters with a given distribution in a periodic lattice. For a discussion of the diffuse scattering arising from elastic deformations, defects, impurities and other imperfections of the lattice, the reader is referred to Ref. [9]. Unlike other experimental methods, such as optical, electronic, and tunneling microscopy techniques, the information obtained from a diffraction experiment is given in reciprocal space. This is often preferable to a description of the order parameters and correlation functions. However, when it comes to obtaining a physical intuition of the system, real space information is generally much more useful. In order to fill in this gap computer simulations of model systems have been of increasing importance. The simulation usually proceeds by the use of a simplified statistical mechanical model, *e.g. a lattice-gas model*, in which the particles are placed on a regular lattice, where the interactions are given by an effective Hamiltonian [2, 3]. In Chap. 3 we calculate the diffuse part of the structure factor of the ceramic high-temperature superconductor $YBa_2Cu_3O_{6+x}$ by the use of Monte Carlo simulations of an anisotropic lattice-gas model, the ASYNNNI model and compare the results with recent neutron diffraction data. In order to discuss the simulation results of the diffuse part of the structure factor, we wish to start with a quantitative discussion of the interpretation of diffuse scatting on the basis of exactly solvable models in one dimension. Before doing so, we need to briefly review some of the fundamental concepts and basic results in structure factor calculations of lattice-gas models.

The unit cell of a crystal is spanned by the primitive vectors $\mathbf{a}_1$, $\mathbf{a}_2$, and $\mathbf{a}_3$, along the crystallographic axis. If we have p atomic sites in the unit cell, the atomic

sites are given by $\mathbf{r} + \mathbf{d}_j$, $j = 1 \ldots p$, where $\mathbf{r} = n_1\mathbf{a}_1 + n_2\mathbf{a}_2 + n_3\mathbf{a}_3$, with n_1, n_2 and n_3 being integers and $\mathbf{d}_j$ are the position vectors in the unit cell. The crystal system is treated as a lattice-gas, where the occupation numbers $\sigma(\mathbf{r}+\mathbf{d}_j) = \{1, 0\}$ depending on whether the site is occupied or not. Primitive vectors in reciprocal space can then be defined as $\mathbf{b}_1 = 2\pi(\mathbf{a}_2 \times \mathbf{a}_3)/(\mathbf{a}_1 \cdot \mathbf{a}_2 \times \mathbf{a}_3)$, and analogous for $\mathbf{b}_2$ and $\mathbf{b}_3$ by cyclic permutation of the indices. In general, the structure factor is defined as the Fourier transform of the density-density correlation function $C_{j,j'}(\mathbf{r},\mathbf{r}') = \langle \sigma(\mathbf{r}+\mathbf{d}_j)\sigma(\mathbf{r}'+\mathbf{d}_{j'})\rangle$, where $\langle\cdots\rangle$ denote ensemble average. It is shown in paper I, that by assuming translational invariance of the correlation function i.e. $C(\mathbf{r},\mathbf{r}') = C(\mathbf{r}-\mathbf{r}')$ the structure factor can be written as:

$$S(\mathbf{q}) = \frac{1}{N}\left\langle \left| \sum_{\mathbf{r}} \sum_{j=1}^{p} e^{i\mathbf{q}\cdot\mathbf{r}+\mathbf{d}_j} \sigma(\mathbf{r}+\mathbf{d}_j) b_j \right|^2 \right\rangle . \qquad (1)$$

where b_j is the coherent scattering amplitude for neutron diffraction, and N is the number of unit cells. Equation (1) is equally valid for X-ray diffraction provided that b_j is replaced by the atomic form factor $f_j(\mathbf{q})$. Consider first the case, where the crystal structure itself can be described as a Bravais lattice. Then the number of atoms in the unit cell is $p = 1$ and $\mathbf{d}_1 = 0$. Hence $S(\mathbf{q})$ is a periodic function with periodicity given by the primitive reciprocal lattice vectors. The structure factor $S(\mathbf{q})$ can then be uniquely specified with only the $\mathbf{q}$-vectors in the first Brillouin zone, assuming that no other symmetry element exists. For a general crystal system with a basis, the structure factor $S(\mathbf{q})$ will possess translational symmetry if and only if the basis vectors occupy rational fractional positions.

2.2 Disorder Diffuse Scattering

Diffuse scattering is due to disorder phenomena, which result from deviations from perfect translational invariant scattering objects. Fluctuations in scattering amplitudes and phase shifts reduce the intensities of the Bragg reflections, and are responsible for the diffuse scattering at the non-Bragg positions in reciprocal space. Thermal motion of the atoms in the crystal around their equilibrium positions gives rise to a reduction in the intensities of the Bragg reflections, and to inelastic and quasi-elastic diffuse scattering at the non Bragg positions in the rest of reciprocal space, if true elastic scattering conditions are not assured. However, the contributions from thermal motion are absent in the lattice gas approximation considered here, because the atoms are assumed to occupy fixed positions. We will restrict ourselves to the situation where the deviation from translational invariance only arises from spatial inhomogeneities in the material composition. We then proceed by separating the structure factor into two parts: $S(\mathbf{q}) = S_{\mathrm{Bragg}}(\mathbf{q}) + S_{\mathrm{diff}}(\mathbf{q})$, where the first part represents the coherent contribution from the average atomic configuration, and the second part is the diffuse part, which carries information about the *fluctuations* of the atomic configurations from the average, and hence the correlation lengths. Formally this is done by separating the occupation numbers into two terms $\sigma(\mathbf{r}+\mathbf{d}_j) = c_j + \Delta\sigma(\mathbf{r}+\mathbf{d}_j)$, where the first term is the average occupation at the atomic site j, and $\Delta\sigma(\mathbf{r}+\mathbf{d}_j)$ is the deviation from average occupation. As shown in Ref. [10] the separation yields

$$S_{\mathrm{Bragg}}(\mathbf{q}) = \frac{1}{N}\left| \sum_{\mathbf{r}} \sum_{j=1}^{p} e^{i\mathbf{q}\cdot(\mathbf{r}+\mathbf{d}_j)} c_j b_j \right|^2 ,$$

$$S_{\mathrm{diff}}(\mathbf{q}) = \frac{1}{N}\left\langle \left| \sum_{\mathbf{r}} \sum_{j=1}^{p} e^{i\mathbf{q}\cdot(\mathbf{r}+\mathbf{d}_j)} \Delta\sigma(\mathbf{r}+\mathbf{d}_j) b_j \right|^2 \right\rangle . \qquad (2)$$

We now turn to one-dimensional models for which the diffuse part of the structure factor can be solved exactly. We consider an infinite one dimensional lattice Q with lattice spacing a. We can treat the system as a chain with N sites for $N \to \infty$. We have $N_p = N$ identical particles, with scattering amplitude b. Hence the concentration of particles is $x = \lim_{N\to\infty}(N_p/N)$. The distribution of the particles on the lattice gives rise to formation of clusters, separated by vacancies. Traditionally, such a system would have been described in terms of the density-density correlation function $C(r)$, which naturally arises in linear response theory, and are related to the diffuse part of the structure factor $S_{\rm diff}(q)$ by the Wiener-Khinchin theorem (see *e.g.* Ref. [11]). However the approach which we shall follow consists of characterizing the system by the cluster size distribution $P(n)$. In the approximation, where the clusters are assumed to be non-interacting, so that overlapping clusters are allowed, we will show that the description of the system is complete in terms of any of the functions $P(n)$, $S_{\rm diff}(q)$, and $C(r)$, since each one can be found from the knowledge of one of the others. For the relation between the structure factor and the correlation function, the reader is referred to paper I. At a fundamental level, the description of the system in terms of the cluster distribution $P(n)$ rather that the correlation function $C(r)$ seems physically to be the most appealing, even though guide lines exist for choosing $C(r)$ such as mean-field theories, *e.g.* Ornstein-Zernike and the cluster variation method. This point becomes especially clear in the case where interactions between clusters are taken into account. In this case the relation between $P(n)$ and $S_{\rm diff}(q)$ becomes non-linear, so that the cluster distribution $P(n)$ cannot in general be obtained from the structure factor. However the correlation function $C(r)$ can always be obtained from the knowledge of $S_{\rm diff}(q)$. Physically a description of the system from $P(n)$ can be much simpler. Consider for example a random distribution of particles, which leads to a Poisson distribution of the cluster sizes. This follows from the fact that the Poisson distribution, with an average cluster size of fa, can be obtained from the Binomial distribution in the limit $p \to 0$, and $N \to \infty$, such that $f \equiv Np \ll N$, where p is the probability that a particle occupy a given lattice site, and N is the number of lattice sites. A description in terms of the correlation function would be very complicated. The problem with using the correlation function at a fundamental level for describing the system, is that $S_{\rm diff}(q)$ will depend on the details of $C(r)$ especially for large r, which are troublesome in computer simulations. On the other hand, the cluster size distribution $P(n)$ is readily determined from computer simulations up to a maximal cluster size $n_{\max}$ depending on the system size used in the simulations. By truncating the cluster size distribution, so that $P(n) = 0$, for $n > n_{\max}$, the relative error in $S_{\rm diff}(q)$ for large $n_{\max}$ becomes $(1-x)^{-1}\sum_{n=n_{\max}}^{\infty} P(n)$, which shows that $S_{\rm diff}(q)$ is insensitive to the details of the cluster distribution for large n.

Mathematically a single cluster $f_{R,n}(r)$ can be represented as a box $A_{R,n}(r)$ of unit height and length na centered at R containing n delta functions with spacing a:

$$f_{R,n}(r) = \sum_{j=0}^{n-1} \delta\left\{r - R + \left(\frac{n-1}{2} - j\right)a\right\} = A_{R,n}(r)D(r),$$

$$D(r) = \sum_{j=-\infty}^{\infty} \delta\{r - ja\}. \qquad (3)$$

In the following discussion we will only be interested in diffuse scattering, so that q does not coincide with the Bragg positions $q \neq Q_m = 2\pi m/a$, where m is an integer. The Fourier transform of $f_{R,n}(r)$, is given by a folding of the Fourier transform of the box function $A_{R,n}(r)$ and that of the perfect structure $D(r)$ [12]. Thus $f_{R,n}(q) = A_{R,n}(q) \otimes D(q)$. The Fourier transform of $f_{R,n}(r)$ can also be

evaluated directly [12] and yields

$$f_{R,n}(q) = \frac{\sin(qan/2)}{\sin(qa/2)} e^{iqR} . \tag{4}$$

Consider a distribution of randomly placed clusters $f_{R,n}(r)$ with a size distribution $\mathcal{D}(n)$. The distribution is normalized, so that the concentration of particles is $x = \lim_{N\to\infty}(N_p/N)$ which gives the constraint: $\sum_{n=1}^{\infty} n\mathcal{D}(n) = x$. In the approximation where we neglect interference phenomena between clusters (overlapping clusters are accepted), we can apply Campbell's theorem, which calculates the power spectrum of a function consisting of a random repetition of elementary signals (see appendix L in Ref. [12]). The structure factor normalized to one lattice site can then be written as

$$S_{\mathrm{dif}}(q) = b^2 \sum_{n=0}^{\infty} \mathcal{D}(n) |f_{R,n}(q)|^2 , \tag{5}$$

which is just a weighted average of the structure factors arising from a single cluster containing n delta functions. Equation (5) is valid without any restriction of dimensionality. In one dimension the applicability of Eq. (5) is restricted to the limit $x \to 0$, since overlapping clusters are not physically acceptable. In higher dimensions, for $\mathbf{q}$ in the direction where all mass points in planes perpendicular to $\mathbf{q}$ can be projected onto the delta functions of a linear chain, overlap naturally arises and the modification is simply that instead of using $f_{R,n}(q)$ as evaluated from Eq. (4) we have to consider the folding $f_{R,n}(q) = A_{R,n}(q) \odot D(q)$, with $A_{R,n}(q)$ replaced by the Fourier transform of the projected shape function. Naturally it is interesting to be able to invert Eq. (5), so that given $S_{\mathrm{dif}}(q)$ we are able to determine the cluster size distribution function $\mathcal{D}(n)$. If we assume that the projected shape function is that of a box function, Eq. (4), this can be done analytically. For details of the derivation the reader is referred to paper I. We obtain

$$\mathcal{D}(n) = \frac{-2}{\pi b^2} \int_0^{2\pi} dt\, S_{\mathrm{dif}}(t) \sin^2\left(\frac{t}{2}\right) \cos(nt) , \quad (n \geq 1) . \tag{6}$$

Data from diffraction experiments are often fitted to a Lorentzian $L^1(q) \propto (q^2 + \kappa^2)^{-1}$, or a Lorentzian square $L^2(q) \propto (q^2 + \kappa^2)^{-2}$. It is interesting to determine the cluster size distributions, that give rise to these lineshapes. It is important to note that since $S_{\mathrm{dif}}(q)$ in Eq. (6) is periodic, *i.e.* $S_{\mathrm{dif}}(q + Q_m) = S_{\mathrm{dif}}(q)$, we must chose the lineshapes, so that they satisfy this constraint. As discussed in paper I, the proper choice for $S_{\mathrm{dif}}(q)$ may be written:

$$\begin{aligned} S_{\mathrm{dif}}(q) &= xb^2 \frac{C_p}{(1 + \alpha^2 - 2\alpha\cos(qa))^p} , \\ \alpha &= e^{\kappa a} , \end{aligned} \tag{7}$$

with $p = 1$ for a Lorentzian, and $p = 2$ for a Lorentzian square, and normalization constants C_p. Obviously Eq. (7) has the correct periodicity, and by expanding Eq. (7) to second order in κ and q we obtain the expected limiting behavior $L^p(q)$, $p = 1, 2$. From Eq. (6) we obtain

$$\mathcal{D}(n) = \frac{-2xC_p}{\pi} \int_0^{2\pi} dt \frac{\sin^2(t/2)\cos(nt)}{(1 + \alpha^2 - 2\alpha\cos(t))^p} . \tag{8}$$

This integral can be calculated analytically, see Ref. [13] p. 369. The normalized cluster distributions may then be written for $n \geq 1$:

$$\mathcal{D}(n) = \begin{cases} \frac{x(\alpha-1)^2}{\alpha} \alpha^{-n} & p = 1 \\ \frac{x(\alpha+1)(\alpha-1)^3}{\alpha(1+\alpha^2)} \left[n(\alpha^2 - 1) - 2\alpha\right] \alpha^{-n} & p = 2 . \end{cases} \tag{9}$$

Thus from Eq. (9) we see that a Lorentzian lineshape ($p = 1$) gives rise to a cluster size distribution, that decays exponentially. The condition for a non-negative cluster distribution yields $x \leq 1/(2-e^{\kappa a})$, which means that for a given x, there exists a maximum value for κ. This can easily be understood as follows: In the limit where the particles occupy all sites on the lattice $x \rightarrow 1$, it follows from the inequality that $\kappa \rightarrow 0$, corresponding to a delta function as expected. The cluster distribution for a Lorentzian square ($p = 2$) unlike the exponential distribution is suppressed at small n and has a maximum at $n_{\max} = (-1 + \alpha^2 + 2\alpha \ln\alpha)/[(-1 + \alpha^2)\ln\alpha]$. For $n \gg n_{\max}$ the distribution decays exponentially. The condition for a non-negative cluster distribution gives $\kappa a \geq \ln(1 + \sqrt{2})$. The physical consequence of the lower bound in κ is that only a narrow distribution around small cluster sizes is compatible with an exact Lorentzian square. At lower temperatures the cluster sizes become larger and the correlation length diverges ($\kappa \rightarrow 0$), in which case the criterion for a non-negative distribution is violated, and the Lorentzian square lineshape is not supported. In other words if an experiment results in a Lorentzian square this implies that only short range order are present (at least in one-dimension).

We now turn to a discussion of the structure factor calculation, in one-dimensional models, where the interference effect between different clusters are taken into account. The problem is stated as follows: determine $S_{\text{dif}}(q)$ for a distribution of unequally sized clusters $f_{R,n}(r)$ separated by vacancies, not allowing overlaps. A simple solution considered in Ref. [14] is to include a vacancy to the right of the cluster in the definition. A problem with this approach arises, since it cannot account for the observed interconnected, sponge-like domain structures which occur in simulations as well as in experiments in many systems of phase separation. This feature can only be included, if correlations between the distribution of the ordered and the vacant regions are taken into account. Experimentally a characteristic limiting behavior for $S_{\text{dif}}(q) \propto q^{-4}$ for large q, called Porod's law [15, 16] (for meso-scopic domains and narrow linewidths, so $q \ll 2\pi/a$) arises as a result of sharp domain walls; and $S_{\text{dif}}(q) \propto q^4$ for small q, called Pego's law [17] (for locally conserved order parameters) arises due to the above mentioned correlations. This problem has not been solved in general, even in the one-dimensional case. However, in Ref. [18] it was shown, that by filling the boxes $A_{R,n}(r)$ symmetrically around R and leaving the remaining part as vacancies at $x = 1/2$, one obtains sufficient of the required correlations to obtain the expected limiting behavior of $S_{\text{dif}}(q)$. However, both methods of including the vacancies yield qualitatively identical results for intermediate q-values. For mathematical simplicity we will follow the approach of including vacancies to the right of a cluster. This means that the cluster size distribution, in addition to the normalization $\sum_{n=1}^{\infty} n\mathcal{D}(n) = x$, has to satisfy the constraint $\sum_{n=0}^{\infty} \mathcal{D}(n) = 1 - x$. The structure factor for the diffuse scattering can be determined exactly [19, 14] and takes the form

$$S_{\text{dif}}(q) = b^2(1-x)\frac{1-u^2}{1+u^2-2u\cos(\phi)}, \quad ue^{i\phi} = \frac{1}{1-x}\sum_{n=0}^{\infty}\mathcal{D}(n)e^{iq(n+1)a}, \quad (10)$$

where ϕ and u are real and defined as phase and modulus of the complex number from the summation over the cluster size distribution in Eq. (10). The normalization condition gives the following constraint: $0 \leq u \leq 1$. In paper I, we calculated exactly $S_{\text{dif}}(q)$ for three different cluster size distributions: $\mathcal{D}_{\text{delta}}(n) = \mathcal{V}\delta_{n,0} + \mathcal{N}\delta_{n,\ell}$, corresponding to a random distribution of clusters of equal length ℓa; $\mathcal{D}_{\text{exp}}(n) = \mathcal{V}\delta_{n,0} + \mathcal{N}e^{-\kappa n a}$, corresponding to an exponential distribution of cluster sizes with width $1/\kappa$; and $\mathcal{D}_{\text{Poisson}}(n) = \mathcal{V}\delta_{n,0} + \mathcal{N}\ell^n/n!$, corresponding to the situation where each particle randomly occupies the lattice sites, with an average cluster size of ℓa. The average cluster length $\langle n \rangle$, and its variance $\sigma^2 = \langle n^2 \rangle - \langle n \rangle^2$ of the distributions are easily determined. For large ℓ and small κ we obtain: $\langle n \rangle_{\text{delta}} = \ell$, $\sigma^2_{\text{delta}} = 0$ for the delta function distribution; $\langle n \rangle_{\text{exp}} = (\kappa a)^{-1}$,

$\sigma^2_{exp} = (\kappa a)^{-2}$ for the exponential distribution; and $\langle n \rangle_{Poisson} = \ell$, $\sigma^2_{Poisson} = \ell$ for the Poisson distribution. We see that by choosing $\kappa a = 1/\ell$ all distributions have the same average cluster length. However the location of where the distributions have maximal weight as well as the variance is quite different. Since the expressions for $S_{dif}(q)$ are rather complicated they are not repeated here. The lineshapes originating from the different distributions are denoted as follows: $S^{delta}_{dif}(q)$, $S^{exp}_{dif}(q)$, and $S^{Poisson}_{dif}(q)$. The lineshapes are displayed in Fig. 1 on a linear scale versus the q-vector in the first Brillouin zone $q \in [-\pi/a; \pi/a]$. It should be noted, that since the cluster size distributions are normalized, for a particular value of the particle concentration x, the integrated intensities of the different structure factors are also the same. The lineshapes presented are calculated with $\ell = 5$, and $\kappa a = 1/\ell$, and a particle concentrations of $x = 0.1$, $x = 0.3$, and $x = 0.5$ respectively. In addition, we have added a Lorentzian lineshape for comparison. In panel (a) $x = 0.1$, we see that $S^{exp}_{dif}(q)$ appears to have a Lorentzian lineshape, with a much smaller full-width-half-maximum (FWHM) than both $S^{Poisson}_{dif}(q)$ and $S^{delta}_{dif}(q)$. This is remarkable, because $\mathcal{D}_{exp}(n)$ has a larger weight on the small cluster sizes, for the parameters chosen, which should give a broader lineshape. It is interesting to note, that the effect of taking the interference between different clusters into account, does not prohibit the intensity for $S^{delta}_{dif}(q)$ to vanish at certain q-vectors. However for $S^{Poisson}_{dif}(q)$, which includes a variation of the cluster sizes around ℓa, the oscillatory behavior in $S^{delta}_{dif}(q)$ is averaged out. In panel (b) and (c) the lineshapes are shown for larger particle concentrations, where it is seen that $S^{delta}_{dif}(q)$ and $S^{Poisson}_{dif}(q)$ develops a satellite peak at a wave vector q_{sat}. However in the case of the Poisson distribution, the particle concentration is much higher for a satellite to appear. This behavior is not found for the exponentially distributed clusters, which always has a maximum at q=0. The position of q_{sat} is related to the inverse length $1/\ell a$ of the clusters and the particle concentration x, because the cluster length and the packing density results in a characteristic separation between the clusters and therefore gives rise to a pseudo periodicity. This behavior has been discussed by Guinier [19], who called it the formation of a 'para-lattice'. The relation between q_{sat} and $1/\ell a$ is not trivial and depends on the value of x. This is demonstrated in Fig. 2, where the position of q_{sat} is plotted versus x, in the range $0 \leq x \leq \ell/(1+\ell)$. The upper bound on x comes from the requirement of a non-negative distribution function. In panel (a) the position of q_{sat} is shown for the delta function distribution for $\ell = 5, 10$ and, 20. It is seen that q_{sat}=0 for $x \leq x_{delta}$. For $x > x_{delta}$, q_{sat} becomes non-zero. Thus for $x \leq x_{delta}$ there is no characteristic length scale in the problem except the cluster size ℓa. For $x > x_{delta}$ a new length scale enters: the characteristic separation between clusters given by $1/q_{sat}$. The satellite position q_{sat} increases monotonically with x, since naturally the distance between clusters becomes smaller at higher particle concentration. It is seen, that apart from the ℓ dependence of x_{delta} the functional form of q_{sat} scales with ℓ. This has important consequences for the experimental situation, since it allows for a determination of the average cluster size from the particle concentration. In panel (b) the corresponding results are shown for the Poisson distribution. Apart from the fact that $x_{Poisson}$ show much less ℓ dependence, the results are qualitatively the same as those for the delta function distribution.

2.3 Discussion

The basic theory for structure factor calculation of lattice-gas models has been reviewed. In the approximation of non-interacting clusters we have obtained linear relations between the diffuse part of the structure factor $S_{dif}(\mathbf{q})$, the correlation function $C(r)$, and the cluster size distribution $\mathcal{D}(n)$. This means that the description of the system is complete in terms of any of the functions $\mathcal{D}(n)$, $S_{dif}(q)$, and

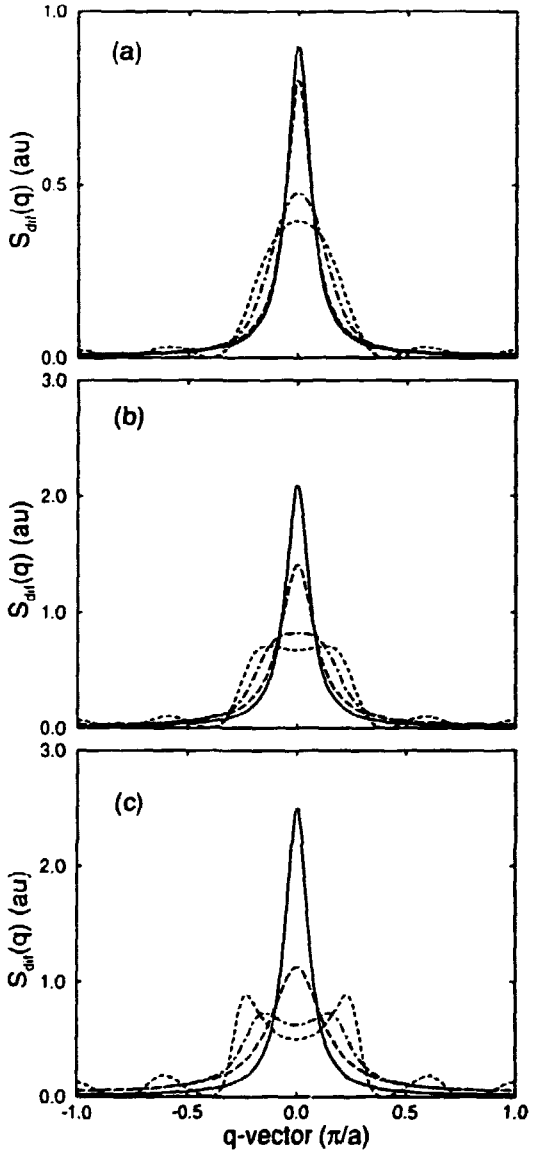

Figure 1. Lineshapes of the structure factor from one-dimensional distributions of non-overlapping clusters. The cluster distributions are indicated as follows: exponential distribution (long-dashed line); delta function distribution (dashed line); Poisson distribution (dashed-dotted line). For comparison we have included a Lorentzian lineshape (solid line). The parameters used are: $\ell = 5$ and $\kappa a = \ell^{-1}$. The panels (a), (b) and (c) show the behavior for a particle concentration of $x = 0.1$, $x = 0.3$, and $x = 0.5$ respectively.

$C(r)$, since each one can be found from the knowledge of one of the others. On this basis we have discussed the possibility of having lineshapes of a Lorentzian and a Lorentzian square. In the one-dimensional case, the results are restricted to the limit of low particle concentration, in order to assure that the clusters are non-overlapping. For larger particle concentration, the interactions between the clusters become important. The interactions give rise to interference phenomena, which introduces non-linearity in the problem. Only in the one-dimensional case, we have been able to treat this exactly, and we have obtained a non-linear expres-

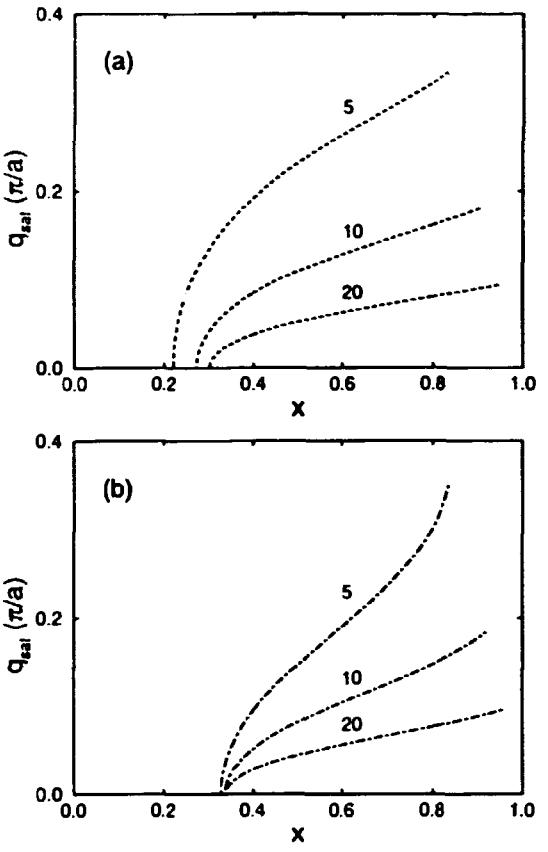

Figure 2. The location of the first maximum q_{sat} of the structure factor $S(q)$ within the Brillouin zone. The satellite positions q_{sat} are displayed as function of particle concentration x, for different values of the average cluster size $\ell = 5, 10$ and, 20. In panels (a) and (b) are shown the results obtained from the delta function distribution (dashed line), and the Poisson distribution (dashed-dotted line) respectively.

sion for $S_{dif}(q)$ in terms of the cluster size distribution $\mathcal{D}(n)$. Consequently $\mathcal{D}(n)$ in contrast to $C(r)$ cannot in general be obtained from the knowledge of $S_{dif}(q)$. For particle concentrations exceeding a critical value, x_{sat}, that depends on the details in the distribution function, satellite peaks develop in $S_{dif}(q)$ for the delta function distributed and the Poisson distributed cluster sizes. These distribution functions have a maximum density for finite cluster length, and as a consequence of the 'excluded volume' effect they give rise to the formation of a para-lattice. The basic reason for the formation of a para-lattice is the tendency for the finite size clusters to pack in the lattice with a characteristic separation which is determined by the average cluster length and the particle density.

The formalism presented so far is valid for a lattice-gas model, where the particles occupy fixed positions, which implies that the structure factor $S_{dif}(\mathbf{q})$ is a periodic function, with periodicity given by the Bragg positions. Alternatively a continuum formulation could have been applied, by letting the lattice spacing a go to zero. All sums would then have been transformed into the corresponding integrals. It should be noted that in such a formulation $S_{dif}(\mathbf{q})$ loses its periodicity, since all Bragg positions except $Q_0 = 0$ moves to infinity. Naturally equations involving integrals would be much simpler to handle mathematically. However, the virtue of the discrete formulation besides being the exact solution, is that we can avoid unphysical divergence of the integrals. Let us elucidate this point further by

considering an important example involving power law distributed cluster sizes. Such distributions would arise if the spatial cluster distribution was a fractal, since the characteristic feature of a fractal is its self similarity, which means that the structure looks statistically the same independent of the length scale used. The lack of a characteristic length scale immediately implies that the cluster sizes are power law distributed $\mathcal{D}(t) \propto t^{-\alpha}$. It is therefore interesting to determine $S_{\rm dif}(q)$ for such a distribution. For the discrete formulation considered in Sec. 2.2 it can be proven that $S_{\rm dif}(q)$ cannot be obtained in closed form, even in the limit where interaction between clusters is neglected. However, in the continuum formulation assuming non-interacting clusters, we obtain $S_{\rm dif}(q) \propto \frac{h^2}{q^2}\int_0^\infty dt\, \mathcal{D}(t)\sin^2(qt/2)$. The solution of this integral yields[1] $S_{\rm dif}(q) \propto q^{-\beta}$ with $\beta = 3-\alpha$ for $\alpha > 1$, and $\beta = 2$ for $\alpha \leq 1$. This result shows that also $S_{\rm dif}(q)$ displays power law scaling, which is to be expected due to the absence of a characteristic length scale in the problem. In fact it was shown in Ref. [22] from an argument of the behavior of the pair correlation function, that the exponent β can be identified with the fractal dimension $d_f < d$ of the spatial cluster distribution. Power law scaling of $S_{\rm dif}(q)$ has been observed experimentally in many systems, and the reader is referred to Ref. [22] for a review.

[1] The integral for $S_{\rm dif}(q)$ was considered in a context of noise spectra originating from the flow of sand down a slope in a cellular automaton in Refs. [20, 21]

3 Oxygen Ordering Processes in $YBa_2Cu_3O_{6+x}$

In this chapter we consider the two- and three-dimensional oxygen ordering processes in the ceramic copper-oxide superconductor $YBa_2Cu_3O_{6+x}$, bases on the results of the papers I, II. In addition we discuss the effects of metal-ion doping on the two-dimensional oxygen ordering properties based on results of paper III. In Sec. 3.1, we discuss the applicability of the anisotropic two-dimensional lattice gas model, known as the ASYNNNI model, to describe the structural and thermodynamic properties of $YBa_2Cu_3O_{6+x}$. In Sec. 3.2 we briefly review the crystal structure of $YBa_2Cu_3O_{6+x}$, and discuss the experimentally observed oxygen phases, which consist of a tetragonal disordered phase and two orthorhombic ordered phases ortho-I, and ortho-II. The structural transformation between the tetragonal phase and the orthorhombic phase is associated with the formation of long-range elastic forces, which are of three-dimensional nature. In a phenomenological way, we account for the three-dimensional oxygen ordering, by extending the ASYNNNI model into three dimensions, by adding a weak coupling term between the CuO_x basal planes. In Sec. 3.3 we present our Monte Carlo simulation methods for studying the ASYNNNI model, including the histogram methods of Ferrenberg and Swendsen. In Sec. 3.4 we report on the calculation of the structural phase diagram both in two and three dimensions, and compare the results with experimental data. Section 3.5 contains the structure factor calculations of the oxygen ordering properties. In addition to a mean-field calculation, we describe how the Monte Carlo calculations are implemented on a Connection Machine (CM2). The numerical results are compared with recent experimental data. Section 3.6 contains the results obtained from a Monte Carlo simulation with particular emphasis on the effects of metal-ion doping on the oxygen-ordering properties of $YBa_2Cu_3O_{6+x}$. The results are discussed in relation to experimental observations in Fe-doped systems.

3.1 Introduction

The discovery in 1986-87 [23, 24] of ceramic copper-oxide superconducters with superconducting transition temperatures T_c as high as 125K has led to an unprecedented burst of scientific activity in the condensed matter community. Despite this interest, the physics behind the pairing mechanism leading to these unusual high transition temperatures remains elusive. In conventional so-called BCS superconductors the pairing mechanism is based on the interaction between the electrons and the lattice. Elucidating the relationship between structure and superconductivity in the present case has been a natural focus of both theoretical and experimental attention.

The most obvious candidate for structural studies is the perovskite $YBa_2Cu_3O_{6+x}$, since in addition to being an almost ideal model system for two-dimensional structural ordering phenomena, there is experimental evidence, that not only the oxygen content x [25], but also the nature of the oxygen ordering [26, 27, 28] are important for the superconducting transition temperature T_c. The variable amount of oxygen ($0 < x < 1$) is located in the widely separated (≈ 11.7Å) CuO_x basal planes of the structure and it acts as a charge reservoir creating the necessary holes in the superconducting CuO_2 planes. For low x-values the material is an anti-ferromagnetic insulator/semiconductor with tetragonal symmetry, while for high oxygen contents it becomes orthorhombic, metallic and superconducting. At intermediate oxygen concentrations both the structural and the superconduct-

ing properties exhibit a rich variety of features. For well equilibrated samples a plateau-like dependence of the superconducting transition temperature is observed with $T_c = 93$K for $x > 0.8$, $T_c = 58$K for $0.45 < x < 0.65$ and $T_c = 0$K for $x < 0.3$. It is generally accepted that the oxygen ordering in the basal plane is the driving force for the majority of the observed structural transformations and local ordering phenomena.

For this reason it is natural that two-dimensional lattice gas models [29, 30, 31, 32, 33, 34, 35, 36, 37, 38, 39], and notably the anisotropic nearest and next nearest neighbor interaction model, the ASYNNNI model has attracted considerable interest. This simple model has been found to give a surprisingly good description of a majority of experimental data on the structural phases of the material. In addition, using the inherent features of this model, Poulsen *et al.* [40] were able to propose a simple mechanism for the relationship between the oxygen ordered structure and superconductivity, in close agreement with experimental findings. However it was shown in paper II, using thermodynamic relations between the chemical potential and the measured oxygen-gas pressure, that the ASYNNNI model only qualitatively accounts for the experimental thermodynamic data.

The success of the two-dimensional ASYNNNI model in accounting for the structural properties is not surprising, since the degree of anisotropy is known to be very large: the oxygen mobility within the plane is 10^8 times higher that the mobility between the planes. However the structural transformation between the tetragonal phase and the orthorhombic phase is associated with a formation of oxygen-copper chains in the CuO_x basal planes, which gives rise to a long-range strain field, which are of three-dimensional nature. It was argued in paper II, that in spite of the fact that the stress energy is relaxed by the formation of twin domains, a *long*-range strain field is reminiscent, creating an orthorhombic distortion. Lately it has become urgent to investigate the three-dimensional nature of the oxygen ordering process, since recent neutron and X-ray diffraction results [41, 42] have shown the formation of three-dimensional *long* short-range orthorhombic order in a twinned crystal. One way of achieving this is by adding an effective attractive inter-plane coupling V_4 to the well known ASYNNNI model. The effect of introducing even a weak interaction parameter $V_4 \neq 0$, indicates that the phase transition separating the disordered tetragonal phase from the orthorhombic ordered phase is shifted upwards in temperature, which causes the effective interaction parameters to be renormalized. This is of particular importance when comparing with interaction parameters obtained from first principles. As another subject of interest, we have calculated the diffuse part of the structure factor $S_{\mathrm{dif}}(\mathbf{q})$ from the statistics of the oxygen-ordering properties, and found that it is in good agreement with the experimental findings.

Experimentally there have been many attempts to change the superconducting properties of $YBa_2Cu_3O_{6+x}$ by chemical substitution. In principle it should be possible to increase the superconducting transition temperature T_c by additional hole doping, but in all cases T_c has been found to decrease. Doping with M = Co, Fe, and Al is in particular interesting for the studies of the oxygen structural ordering and its influence on T_c, because the metal ions substitute predominantly for Cu in the CuO_x basal planes for the structure. The valence and the oxygen coordination number of these M-species tend to be larger than that of Cu, and consequently they cause oxygen disordering in the $Cu_{1-y}M_yO_x$ basal plane of $YBa_2Cu_{3-y}M_yO_{6+x}$. In order to determine the effects of the diffusive metal-ion dopants on the oxygen ordering properties, we have performed a Monte Carlo simulation. The results are briefly discussed in relation to experiments on $YBa_2Cu_{3-y}Fe_yO_{6+x}$.

3.2 Modeling of Oxygen Order

Experimentally the oxygen stoichiometry x of $YBa_2Cu_3O_{6+x}$ can only be varied between x=0 and x=1. Under high pressure the compound is unstable towards formation of the superconducting material $YBa_2Cu_4O_8$ [43]. The compound exhibits two structural phases at high temperature. For small x values the compound is tetragonal with space group P4/mmm, while for higher x-values it becomes orthorhombic with space group Pmmm, due to oxygen chain formation in the CuO_x basal plane. This orthorhombic phase is also known as the ortho-I phase and has a stoichiometric composition of $x = 1$. At lower temperature the compound develops an oxygen structure known as the ortho-II phase, which has the stoichiometric composition $x = 1/2$. The crystallographic structure of $YBa_2Cu_3O_{6+x}$ is based on a unit cell, which consists of a stack of three perovskite cubes. The unit cell has almost ideal $1\times1\times3$ dimensions. The primitive unit vectors of the unit cell are $|\mathbf{a}| = 3.9$ Å, $|\mathbf{b}| = 3.9$ Å, and $|\mathbf{c}| = 11.7$ Å, and they are mutually orthogonal. The essential features of the crystal structure are described in Fig. 3, where the unit cell is indicated by solid lines. The interaction parameters V_1, V_2, V_3, and V_4 are discussed below. The notation $A(x, y, z)$ denotes that atom A is located at the coordinates (x, y, z) with respect to the basis of the unit cell, and A refers to the site nomenclature from Jorgensen *et al.* [44]. The unit cell is generated by Y(1/2, 1/2, 1/2), Ba(1/2, 1/2, 0.19), Cu1(0, 0, 0), Cu2(0, 0, 0.36), O1(0, 1/2, 0), O2(1/2, 0, 0.38), O3(0, 1/2, 0.38), O4(0, 0, 0.15), O5(1/2, 0, 0) and by applying the mirror plane symmetry at the level of the yttrium atom. All oxygen atoms assume perovskite positions located halfway between the copper atoms along the cube edges. There are no oxygens at the level of the Y atom, but the oxygen sites O2 and O3 at the level of Cu2 are fully occupied. From recent single crystal neutron diffraction measurements [45] it is established that only the oxygen sites O1 and O5 have a variable occupation. Writing the total number of oxygen atoms in the unit cell as $c_{ox} = 6 + x$, it follows that the oxygen stoichiometry x is given by $x = \langle\sigma(O1)\rangle + \langle\sigma(O5)\rangle$, where $\langle\cdots\rangle$ denotes the average over all equivalent sites in the crystal. Therefore, in the modeling of the oxygen order for $YBa_2Cu_3O_{6+x}$ only the oxygen sites located at O1 and O5 are taken into account. To model the oxygen order in $YBa_2Cu_3O_{6+x}$, the oxygen sites located at O1 and O5 are treated within a lattice gas approximation, by introducing a site occupancy variable $\sigma(\mathbf{r})$. This means that $\sigma(\mathbf{r})$ is restricted to take on two possible values $\sigma(\mathbf{r}) = \{1, 0\}$ depending on whether an oxygen atom is present or absent at site $\mathbf{r}$. The modeling of the ordering of oxygen atoms in the CuO_x basal planes of $YBa_2Cu_3O_{6+x}$, is done by Monte Carlo simulation of an extension of the two-dimensional ASYNNNI model, originally proposed by de Fontaine *et al.* [46], into three dimensions. In Fig. 3 the basal planes can be seen to consist of a square lattice of copper atoms, with oxygen sites located halfway between the copper atoms along the square edges. The pair interaction parameters V_1, V_2, V_3, and V_4 are defined as follows: V_1 is the nearest neighbor repulsion between to oxygen atoms. V_2 is the next nearest neighbor attractive interaction between pairs of oxygen atoms, which are bridged by a copper atom (NNNCu), while V_3 a repulsive interaction between oxygen atoms which are not bridged by a copper atom (NNNV). In the three-dimensional extension of the ASYNNNI model we introduce an attractive interaction V_4 between pairs of oxygen atoms located on adjacent basal planes vertically above and below each other (NNPl). In the computer simulations it is convenient to introduce a new basis $\mathbf{e}_1$, $\mathbf{e}_2$, and $\mathbf{e}_3$ for the O1 and O5 sites, which is rotated 45° around the crystallographic c-axis. The new basis which given by $\mathbf{e}_1 = (\mathbf{a} + \mathbf{b})/2$, $\mathbf{e}_2 = (\mathbf{b} - \mathbf{a})/2$, and $\mathbf{e}_3 = \mathbf{c}$, is an orthogonal lattice. In this basis the oxygen sites at the O1 and O5 can be written $\mathbf{r} = n_1\mathbf{e}_1 + n_2\mathbf{e}_2 + n_3\mathbf{e}_3$, where n_1, n_2, and n_3 are integers. This

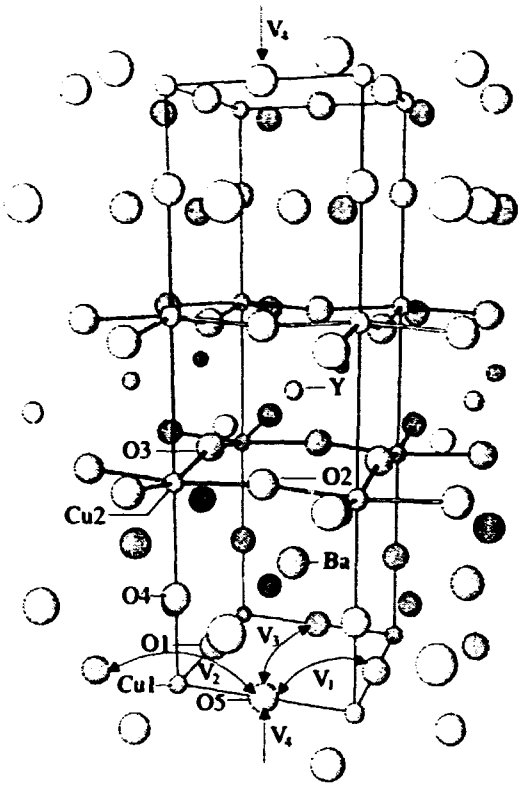

Figure 3. The crystallographic structure of $YBa_2Cu_3O_{6+x}$. The unit cell has almost ideal $1\times1\times3$ dimensions, and is indicated by solid lines. All oxygen sites assume perovskite positions located halfway between the copper atoms along the square edges. The variable oxygen stoichiometry occur at the O1 and O5 sites in the basal planes, which are separated by $|\mathbf{c}| = 11.7$ Å along the c-axis. The oxygen pair interaction parameters V_1, V_2, V_3, and V_4 are defined as follows: V_1 is the nearest neighbor repulsion; V_2 is the next nearest neighbor attraction between pairs bridged by Cu; V_3 is the next nearest neighbor repulsion between pairs not bridged by Cu; V_4 is the nearest neighbor attraction between pairs on adjacent basal planes.

leads to a three-dimensional grand canonical Hamiltonian:

$$\mathcal{H} = -V_1 \sum_{(\mathbf{r}\mathbf{r}')}^{\mathrm{NN}} \sigma(\mathbf{r})\sigma(\mathbf{r}') - V_2 \sum_{(\mathbf{r}\mathbf{r}')}^{\mathrm{NNNCu}} \sigma(\mathbf{r})\sigma(\mathbf{r}') - V_3 \sum_{(\mathbf{r}\mathbf{r}')}^{\mathrm{NNNV}} \sigma(\mathbf{r})\sigma(\mathbf{r}')$$
$$-V_4 \sum_{(\mathbf{r}\mathbf{r}')}^{\mathrm{NNPl}} \sigma(\mathbf{r})\sigma(\mathbf{r}') - \mu \sum_{\mathbf{r}} \sigma(\mathbf{r}) \,. \qquad (11)$$

The sum runs over all oxygen pairs $\langle \mathbf{r}, \mathbf{r}' \rangle$, which are nearest neighbor (NN and NNPl) or next nearest neighbors (NNNV and NNNCu) respectively. The chemical potential μ acts as an external field, and can be related to the equilibrium oxygen partial pressure in the sample. For details the reader is referred to paper II. We have simulated the oxygen order in both two and three dimensions in order to study the effect of the inter-plane coupling V_4 on the oxygen ordering process. In the two-dimensional simulation studies we set $V_4 = 0$, which effectively decouples the CuO_x basal planes. In this case the relative magnitude between the interaction parameters has been established by a comparison between experimental data and

simulation studies [36, 37, 47] and paper II, to be

$$(V_1, V_2, V_3) = (-V_0, 0.36V_0, -0.12V_0)\,, \tag{12}$$

with $V_0/k_B = 5430$K. In the three-dimensional study we have chosen to use the same intra-plane interaction parameters. For the inter-plane interaction parameter we have used $V_4 = 0.02V_0$ suggested by de Fontaine *et al.* in Ref. [48]. As a consequence of the coupling between the basal planes, it is necessary to redefine the energy scale, (see paper I), so that $V_0/k_B = 4490$K.

In the MC simulations, the stoichiometric factor x is calculated from the average number of oxygen atoms on the lattice by

$$x = \frac{2}{N_{\rm tot}}\langle\sum_{\mathbf{r}}\sigma(\mathbf{r})\rangle\,. \tag{13}$$

where $N_{\rm tot}$ is the number of available oxygen sites.

A full analysis of the ground state oxygen configurations arising from the two-dimensional ASYNNNI model (Eq. (11) with $V_4 = 0$) was given in Ref. [31]. For the interaction parameters chosen the ground states, in the CuO_x basal plane are shown in Fig. 4. The ortho-I phase, which at perfect order corresponds to x=1,

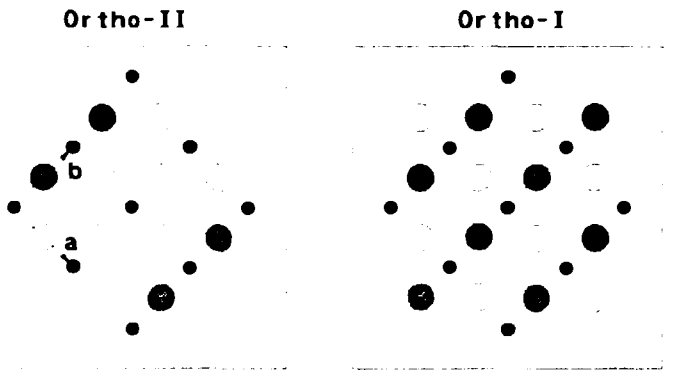

Figure 4. Schematic presentation of the two ideal orthorhombic phases, the ortho-II phase ($x = 1/2$) and the ortho-I phase ($x = 1$). The dots denote copper atoms, while circles denote oxygen sites. In the ortho-II phase, the domain shown is of the b-type with oxygen chains in the b-direction. There are two possible b-type ortho-II domains and two a-type ortho-II domains. In the ortho-I phase, the grey sublattice represents a b-domain, while the white sublattice represents an a-domain.

is a two fold degenerate oxygen structure. The ortho-II phase, which at perfect order corresponds to x=1/2 is a four fold degenerate oxygen structure. The ideal tetragonal phase consists of an empty oxygen lattice (x=0). For stoichiometries deviating from the ideal ones (x = 0, 1/2, 1), the ASYNNNI model exhibits an infinite number of ground states. For stoichiometries with $0<x<1/2$ they are degenerate with the ortho-II and the tetragonal ground states at the order-disorder transition, while for stoichiometries with $1/2<x<1$, they are degenerate with the ortho-II and ortho-I ground states at the order-disorder transition.

3.3 Monte Carlo Simulation Methods

For a comprehensive review of the Monte Carlo techniques in statistical mechanics the reader is referred to Ref. [2, 49, 50]. The aim of a Monte Carlo simulation of a statistical mechanical model with Hamilton $\mathcal{H}$ is to provide a sequence of configurations of the system, which are distributed with the appropriate Boltzmann

probability. After having established equilibrium in the system, the subsequent sequence of measurements of physical quantities corresponds to a time-averaging process by which the system evolves according to stochastic dynamics. In the Metropolis algorithm the successive configurations are not chosen independently of each other, but rather constructed as a Markov chain, in which the transition probability is given by

$$W(\omega \to \omega') = \begin{cases} \exp\left[-\left(\mathcal{H}(\omega') - \mathcal{H}(\omega)\right)/k_B T\right] & \text{if } \mathcal{H}(\omega') \geq \mathcal{H}(\omega) \\ 1 & \text{otherwise.} \end{cases} \qquad (14)$$

We used the Metropolis algorithm with both Kawasaki and Glauber dynamics, corresponding to conserved and non-conserved number of oxygen atoms, respectively. The Monte Carlo simulation with Glauber dynamics is performed in the usual manner, where at each step in the Markov process individual oxygen atoms were attempted to be inserted and removed at random according to the transition probability, Eq. (14). Since the number of oxygen atoms are not conserved in this fashion, the corresponding ensemble average is taken from the grand canonical ensemble. It should be noted, that in a Monte Carlo simulation process the emphasis is to achieve a realistic statistical distribution of the configurations at a given temperature. However, the updating procedure needs not be physically realistic, except for fulfillment of certain constraints. Such constraints could be to preserve the number of oxygen atoms at every new Monte Carlo step (MCS). A simple way of doing this is to use Kawasaki dynamics, which only allows interchange of particles and vacancies.

In the real physical system the oxygen atoms have to jump from place to place. It might be a good approximation to consider only jumps to vacant nearest neighbor and next nearest neighbor sites. This can easily be simulated using the Kawasaki dynamics which allows only such interchanges; let us call this update (A). After many MCS it is expected that the phase space will be properly visited. However, a much faster method (B) is obtained by allowing oxygen atoms to 'jump' over arbitrary distances. This should not be considered as modeling the real oxygen diffusion, but rather an efficient sampling procedure of other relevant independent configurations. The point is that as far as equilibrium properties are concerned, there should be no difference between (A) and (B), but clearly the equilibrium condition is much easier obtained by (B). The ensemble properties obtained by both these methods correspond to the canonical ensemble. An exception to this behavior may be introduced at the surface where a direct exchange of adsorbed oxygen atoms and the oxygen gas phase is possible. In this case the Glauber dynamics is realistic with a grand canonical Hamiltonian including a chemical potential for the oxygen exchange.

In all the simulations we have enforced periodic boundary conditions (PBC). The simulations for the two-dimensional oxygen ordering process, where we set $V_4 = 0$ were performed on a HP9000/735 workstation. The system sizes chosen were $N_x \times N_y \times N_z$, with $N_x = N_y = 32, 60, 100$, and 200, and $N_z = 1, 8$. The decoupled N_z planes were used in the averaging to gain better statistics. The performance was measured as the number of Monte Carlo steps per site (MCSS) updated each second, by which we obtain $5.4 \cdot 10^4$ MCSS/sec. For the three-dimensional simulations, where $V_4 \neq 0$ we used a system size of $N_x \times N_y \times N_z$, with $N_x = N_y = 64, 100$, and 256, and $N_z = 8, 16$. For the largest system sizes, the simulations were performed on a massively parallel computer, the Connection Machine using 16384 processors, where we obtained a peak performance of $8.7 \cdot 10^6$ MCSS/sec. For the results presented, the total number of Monte Carlo steps per site used in the calculations varied between $2 \cdot 10^4$ and $5 \cdot 10^5$.

The main drawback of the standard Monte Carlo simulation is its large demand for computer resources. The demand grows proportionally to the system size, but

more seriously the time for reaching equilibrium also grows with the system size. Even for moderately small system sizes several hours of CPU time are usually needed for each data point. Therefore, the development of more efficient Monte Carlo schemes has attracted a lot of interest. Recently Ferrenberg and Swendsen [51, 52, 53] proposed a reweighting technique for studying phase transitions. The idea is to calculate the energy histogram $H_T(E)$ at different temperatures T. Typically in standard MC implementations only the first few moments of the histogram are stored. The histograms are combined self-consistently to obtain the probability distribution $P(E,T)$ in the following way. The energy histograms $H_m(E)$ at a particular temperature T_m with $(m = 1, \ldots, R)$ are most easily accumulated by initially calculating the total energy E_{tot} of the start configuration. Subsequently for each Metropolis proposal E_{tot} is updated by the energy difference ΔE (which is calculated anyway) between successive oxygen configurations. Then the total energy and the histograms are updated according to

$$E_{tot} \Rightarrow E_{tot} + \Delta E. \tag{15}$$

$$H_m(E_{tot}) \Rightarrow H_m(E_{tot}) + 1. \tag{16}$$

We will assume that all the histograms contain the same number of Monte Carlo updates n. Then the sum of all the histograms normalized by the number of updates can be written

$$H(E) = \frac{1}{n} \sum_{m=1}^{R} H_m(E). \tag{17}$$

The multiple histograms equations, as formulated in the original work by Ferrenberg and Swendsen are very troublesome in numerical calculations. This is due to the fact that the solutions of the equations cannot be represented within the range of floating point numbers on the computer. The numerical problem resembles that of stiff differential equations, where the solutions comprise both exponential growth and decay. However, some of the numerical problems can be by-passed by rewriting the equations in a slightly different manner. The multiple histogram equations then take the following form

$$P(E,T) = \frac{H(E)}{\sum_{m=1}^{R} \exp\left[E\left(\frac{1}{kT} - \frac{1}{kT_m}\right) - f_m\right]}, \tag{18}$$

where the free energy term f_m has to be calculated self-consistently. The normalization condition gives rise to the following equations for determining f_m.

$$\sum_{E} \frac{H(E)}{\sum_{m=1}^{R} \exp\left[E\left(\frac{1}{kT_n} - \frac{1}{kT_m}\right) - f_m + f_n\right]} = 1, \quad n = 1, \ldots, R. \tag{19}$$

From Eq. (19) we see that only the difference $(f_m - f_n)$ enters in the equation. As a result only $R - 1$ equations are independent. Equation (19) was solved iteratively by the Newton-Raphson algorithm [54]. The convergence of the algorithms depends crucially on how close the initial guess is to the solution. Therefore, the equations were solved iteratively by first solving for $n = 2$, and then we use the solutions as the starting point for solving the equations with $n = 3$, and so on. In Fig. 5 (a) and (b) the energy histograms $H_m(E)$ and the heat capacity $C_V(T)$ for a particle concentration of $x = 0.4$ are shown. The system size is 32×32, with $V_4 = 0$ and the energy histograms $H_m(E)$ were accumulated at temperatures $T_m = (0.09 + 0.002 \cdot m) V_0/k_B$, $(m = 0, \ldots, 10)$. In each of the histograms $3 \cdot 10^5$ MCSS were used. In (a) the energy histograms $H_m(E)$ are shown. The data has been lumped in small energy boxes in order to obtain a smooth distribution. The location of T_c is determined below to be between T_7 and T_8. The energy histograms for a temperature below T_c that is for $m \leq 7$, are

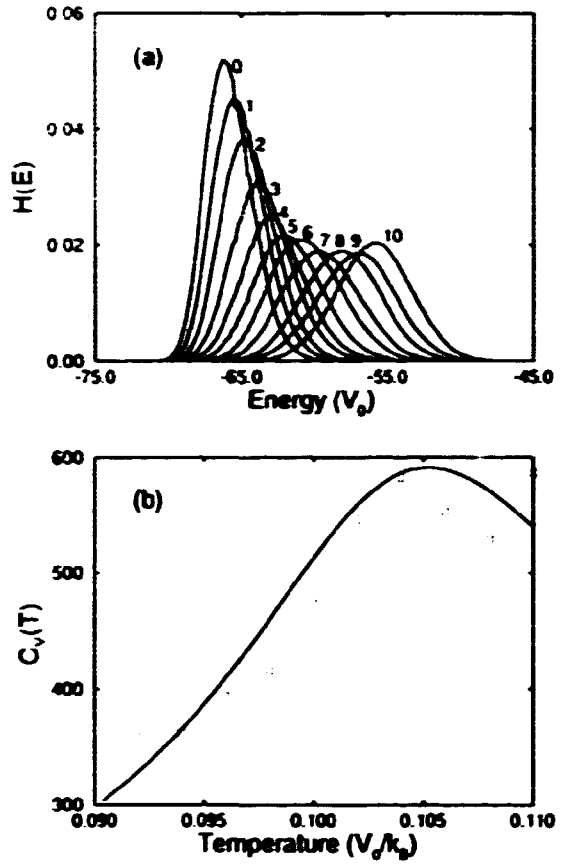

Figure 5. In (a) is shown the energy histograms $H_m(E)$, taken at temperatures $T_m = (0.09 + 0.002 \cdot m)\,V_0/k_B$. ($m = 0, \ldots, 10$), by Monte Carlo simulation with Kawasaki dynamics model (B). In each of the histograms $3 \cdot 10^5$ MCSS were used. The system size is 32×32, with $V_4 = 0$, and an oxygen stoichiometric factor of $x = 0.4$. In (b) is shown the heat capacity $C_V(T)$. The open circles are the data points obtained from Monte Carlo simulation and the solid line represents the results using the Ferrenberg-Swendsen interpolation formula.

characterized by an asymmetry around the mean, with a tail extending toward higher energies (possitive skewness). This is caused by minority fluctuations of the tetragonal phase into the ordered phase. Analogous, energy histograms for a temperature above T_c ($m \geq 8$) are characterized by a negative skewness, due to minority fluctuations of the ordered phase into the tetragonal phase. For a single histogram ($R = 1$), $H(E)$ is proportional to the probability $P(T, E)$ of finding the system in an energy E at temperature T. It was argued in Ref. [2] that away from first- and second-order phase transitions $P(T, E)$ is approximately Gaussian $P(T, E) \propto \exp\left[-(E - \langle E \rangle_T)^2/(2C_V(T)k_BT^2)\right]$. This shows, that the distribution at low temperature becomes narrow and sharply peaked around its mean value, in contrast to the behavior at high temperatures where the distribution is very broad. In Fig. 5 (b) the conventional Monte Carlo data points are shown for $C_V(T)$ obtained by utilizing only the first and the second moments of the histograms, while the solid curve represents the Ferrenberg-Swendsen interpolation formula Eq. (18). We see, that the data point are scattered around the interpolating curve for $C_V(T)$. The reason for this is that unlike the average energy $\langle E \rangle_T$, which only involve the first moment of the distribution, the higher moments, or

statistics involving higher powers of the input data, are almost always less robust than lower moments. Therefore, the data points for $C_V(T)$ appear much more scattered around the interpolation curve, than the corresponding results for $\langle E \rangle_T$ as discussed in paper II. From the interpolation curve, the peak position of $C_V(T)$ may be determined very accurately to be, $T_c = 0.1052 V_0/k_B$. We shall see, that this agrees very well with T_c estimated from the behavior of other quantities.

3.4 Phase Diagram

In this section we report on the calculation of the phase diagram using Monte Carlo simulation (MC). Several other methods have previously been applied to the ASYNNNI model, the most important are the cluster variation method (CVM), which is a mean field type of calculation, and the transfer matrix method (TM). Because of the different accuracy of the methods there exists several sets of values for the interaction parameters describing the oxygen ordering phenomena in $YBa_2Cu_3O_{6+x}$. The transfer matrix and Monte Carlo method are generally accepted to give the most reliable results.

We have calculated the phase diagram by Monte Carlo simulation of the Hamiltonian Eq. (11) with the interaction parameters given in Eq. (12), both in two-dimensions, where $V_4 = 0V_0$, and in three-dimensions with $V_4 = 0.02V_0$, using Glauber as well as Kawasaki updating dynamics. The resulting $x - T$ phase diagram is shown in Fig. 6. Here x is the stoichiometric factor given by Eq. (13). The

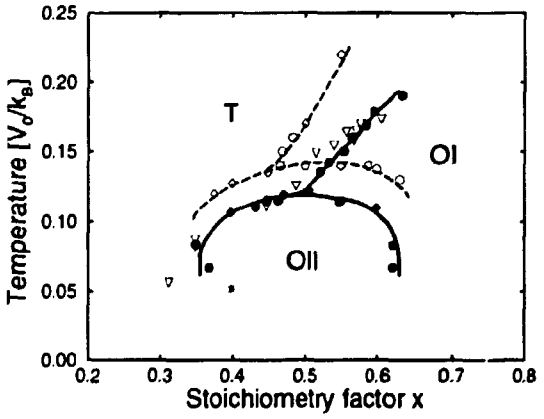

Figure 6. Comparison of the phase diagrams in the $x - T$ plane obtained by the two- and the three-dimensional ASYNNNI model by Monte Carlo simulation. Circles and diamonds represent data obtained by Glauber dynamics and Kawasaki dynamics, model (B) respectively. The triangles are the experimental data points from Ref. [55], and the (*) indicate the position where the neutron diffraction data by Zeiske et al. [41] were obtained. The solid curve are the phase boundaries obtained from the two-dimensional calculation on a 60×60 system, with interaction parameters $V_1 = -V_0$, $V_2 = 0.36V_0$, $V_3 = -0.12V_0$, and $V_4 = 0$. The dashed curve represent the phase boundaries obtained from a three-dimensional calculation on a 64×64×8 system with V_1, V_2, and V_3 as before, and $V_4 = 0.02V_0$. The three oxygen phases shown are the disordered tetragonal phase (T), and the two orthorhombic phases ortho-I (OI) and ortho-II (OII) respectively.

location of the phase boundary was determined by calculating the position of the peak in the fluctuations of the relevant order parameter. In the case of Glauber dynamics x is only indirectly determined from the $x - \mu$ relation. The solid circles and diamonds in Fig. 6 are the actual two-dimensional data points obtained

with Glauber dynamics and Kawasaki dynamics, respectively. Open circles and diamonds, have the same meaning for the data points obtained from the three-dimensional calculation. The Monte Carlo data presented have been calculated with a 60×60 system, in two dimensions and with a 64×64×8 system in three dimensions[2]. To check the finite size dependence of the results in two-dimensions, larger system sizes 100×100 and 200×200 were applied at $x = 0.4$ and $x = 0.5$ for a complete temperature scan across the phase boundary. The differences in T_c were small and within the computational uncertainty. We did not pursue this for the three-dimensional case.

The phase diagram contains the high temperature oxygen disordered tetragonal phase (T) and the two low temperature oxygen ordered orthorhombic phases, the ortho-I phase (OI) and ortho-II phase (OII) as indicated in the figure. The solid and the dashed lines represent the phase boundaries for the two- and three-dimensional calculation respectively. The lines shown in the phase diagram are all consistent with being of second order as expected from finite size scaling analysis of the order parameter discussed by Aukrust *et al.* [56]. The triangles are the experimental points from Andersen *et al.* [55], which have been plotted by using an absolute temperature scale factor of $V_0/k_B = 5430$K. This value has been obtained by fitting at the calculated value of T_c at $x = 0.4$ in two-dimensions, $T_c = 0.105V_0/k_B$, to the experimental value $T_c = 570$ K. For this reason the experimental data points coincide with the two-dimensional data (solid curve).

As can be seen in Fig. 6, the three-dimensional phase diagram has the same topology as the two-dimensional case; the only difference is that the phase boundaries are shifted upwards with about 20%. This difference could not have been anticipated from a mean-field analysis, where the increase in T_c is expected to be a few percent, as will be discussed below in Sec. 3.5.

The phase diagram for the ASYNNNI model presented in Fig. 6 does not account for the possibility of first-order phase transitions and phase coexistence at low temperatures. This is a severe problem, since it follows from the third law of thermodynamics, *i.e. the Nernst principle*, that for stoichiometries deviating from the ideal ones ($x = 0, 1/2, 1$), the low temperature phase must eventually decompose into a mixture of perfectly ordered phases. To elucidate this problem, an extension of the ASYNNNI model to include longer-range interactions within the CuO_x basal plane was considered in Ref. [57, 58]. The extension was introduced as an addition term in the Hamiltonian Eq. (11), as a weak attractive interaction between next-nearest-neighbor oxygen chains. The effect of these interactions is to lower the energies of the tetragonal and ortho-II states with respect to the states with $x<1/2$. In the same fashion the energies of the ortho-II and ortho-I states is lowered with respect to the states with $1/2<x<1$. For this reason a lifting of the low-temperature degeneracies result, which causes the transition lines ortho-I/ortho-II and tetragonal/ortho-II to change from second order to first order at low temperatures. In addition the phase diagram contains regions of phase coexistence between ortho-I and ortho-II, and between tetragonal and ortho-II.

3.5 Structure Factor Calculations

Recently, Zeiske *et al.* [41] measured the oxygen ordering in $YBa_2Cu_3O_{6+x}$ ($x = 0.4$) by neutron diffraction. The measurements were performed at room temperature, and in Fig. 6 the corresponding position in the phase diagram, indicated by an (*), makes it evident that they were expected to be taken well within the ortho-II phase. By measuring the structure factor they observed diffuse superstructure

[2]The reason why a 64×64×8 system has to be chosen is that the number of lattice sites are restricted to be powers of two in order to run on the Connection Machine.

reflections (h,k,l) at $(1/2,0,0)$. This superstructure reflection corresponds to a doubling of the unit cell along the crystallographic a axis (see Fig. 4), but the finite width and the fact that there was no evidence for a Bragg peak show that only short range ordered ortho-II domains are formed. By fitting the profile of the superstructure reflections to a Gaussian, they determined the widths Δh, Δk and Δl, where (h,k,l) are the reduced reciprocal lattice units[3]. They obtained $\Delta h = 0.099$, $\Delta k = 0.049$ and $\Delta l = 0.52$ and deduced the correlation lengths $\xi_a = 10a$, $\xi_b = 24b$, and $\xi_c = 2c$ showing a strong anisotropy of the correlation lengths ξ_a and ξ_b in the basal plane. The small value of the inter-plane correlation length ξ_c shows that the oxygen order is predominantly two dimensional. In order to investigate to what extend the ASYNNNI model can account for the structural properties of $YBa_2Cu_3O_{6+x}$, we have calculated both the two- and three-dimensional structure factor from the simulations of the ASYNNNI model and compared the results with the above experimental values.

Before turning to the results of the Monte Carlo simulation of the structure factor, it is instructive to consider the results of a mean-field calculation of the structure factor from the ASYNNNI model. We will follow the approach discussed in Ref. [59, 60]. In order to develop the theory, it is convenient to rewrite the ASYNNNI model Hamiltonian Eq. (11) by introducing R sublattices. The oxygen site occupation variables are then described by $\{\sigma^\alpha(\mathbf{r}_\alpha)\}$, where $\alpha = 1,\ldots,R$ runs over the different sublattices, and $\mathbf{r}_\alpha$, denote the position vector for the oxygen sites on the α sublattice. We obtain

$$\mathcal{H} = -\frac{1}{2}\sum_{\alpha=1}^{R}\sum_{\beta=1}^{R}\sum_{\mathbf{r}_\alpha}\sum_{\mathbf{r}_\beta}\mathbf{J}^{\alpha\beta}(\mathbf{r}_\alpha - \mathbf{r}_\beta)\sigma^\alpha(\mathbf{r}_\alpha)\sigma^\beta(\mathbf{r}_\beta)\,, \tag{20}$$

with an $R\times R$ pair interaction matrix $\mathbf{J}$, with matrix elements $\mathbf{J}^{\alpha\beta}(\mathbf{r}_\alpha - \mathbf{r}_\beta)$, which contains the pair interaction between oxygen sites $\mathbf{r}_\alpha$ (on sublattice α) and $\mathbf{r}_\beta$ (on sublattice β). We make a change of variables from $\{\sigma^\alpha(\mathbf{r}_\alpha)\}$, to $\{\sigma^\alpha_{\mathbf{q}}\}$ by a discrete Fourier transformation, given by $\sigma^\alpha(\mathbf{r}_\alpha) = (N_{\rm tot}/R)^{-1}\sum_{\mathbf{q}} e^{i\mathbf{q}\cdot\mathbf{r}_\alpha}\sigma^\alpha_{\mathbf{q}}$, where $N_{\rm tot}/R$ is the number of oxygen sites on sublattice α. In the same fashion the inverse Fourier transformation is given by $\sigma^\alpha_{\mathbf{q}} = \sum_{\mathbf{r}_\alpha} e^{-i\mathbf{q}\cdot\mathbf{r}_\alpha}\sigma^\alpha(\mathbf{r}_\alpha)$. The Hamiltonian then takes the form

$$\begin{aligned}\mathcal{H} &= -\frac{R}{2N_{\rm tot}}\sum_{\mathbf{q}}\sum_{\alpha}^{R}\sum_{\beta}^{R}\mathbf{J}^{\alpha\beta}(\mathbf{q})\sigma^\alpha_{\mathbf{q}}\sigma^\beta_{-\mathbf{q}}\\ \mathbf{J}^{\alpha\beta}(\mathbf{q}) &= \sum_{\boldsymbol{\rho}_{\alpha\beta}}\mathbf{J}^{\alpha\beta}(\boldsymbol{\rho}_{\alpha\beta})e^{i\mathbf{q}\cdot\boldsymbol{\rho}_{\alpha\beta}}\,,\end{aligned} \tag{21}$$

where $\boldsymbol{\rho}_{\alpha\beta} = \mathbf{r}_\alpha - \mathbf{r}_\beta$. The diffuse part of the structure factor $S_{\rm dif}(\mathbf{q})$ as discussed in Chap. 2 is defined as the square modulus of the Fourier transform of the particle fluctuations. In the case of only one lattice, R=1, this can be written as

$$S_{\rm dif}(\mathbf{q})/b_{\rm ox}^2 \equiv N_{\rm tot}^{-1}\langle\Delta\sigma_{\mathbf{q}}\Delta\sigma_{-\mathbf{q}}\rangle = k_B T\chi(\mathbf{q})\,, \tag{22}$$

where $b_{\rm ox}$ is the scattering length for an oxygen atom and $\Delta\sigma_{\mathbf{q}} = \sigma_{\mathbf{q}} - \langle\sigma_{\mathbf{q}}\rangle$. The second equality in Eq. (22) follows from the fluctuation dissipation theorem [61] and relates the particle fluctuations to the corresponding response function $\chi(\mathbf{q})$. The susceptibility function obeys a self-consistency relation (Dyson equation) $\chi(\mathbf{q}) = \chi^0(T)[1 + J(\mathbf{q})\chi(\mathbf{q})]$, relating the interacting and the non-interacting susceptibility $\chi^0(T)$, where $J(\mathbf{q})$ (to first order) is the Fourier transformed pair interaction function. The generalization to the situation with R>1 sublattices is straightforward. The susceptibility function becomes an $R\times R$ matrix $\boldsymbol{\chi}$, with

[3]The widths along q_x, q_y, and q_z are conventionally expressed in reduced reciprocal lattice units $h = q_x a/2\pi$, $k = q_y b/2\pi$, $l = q_z c/2\pi$ and are denoted $\Delta h(T)$, $\Delta k(T)$, and $\Delta l(T)$.

matrix elements $\chi^{\alpha,\beta}(\mathbf{q}) = [(N_{\rm tot}/R)k_BT]^{-1}\langle\Delta\sigma^{\alpha}_{\mathbf{q}}\Delta\sigma^{\beta}_{-\mathbf{q}}\rangle$ for the fluctuation between sublattice α and β (see Reichl [61] Chap. 15). In the same fashion the non-interacting susceptibility function becomes an $R\times R$ matrix $\boldsymbol{\chi}^0$, with matrix elements $(\boldsymbol{\chi}^0)^{\alpha,\beta} = [(N_{\rm tot}/R)k_BT]^{-1}\langle\Delta\sigma^{\alpha}_{\mathbf{q}}\Delta\sigma^{\beta}_{-\mathbf{q}}\rangle_0$, where $\langle\cdots\rangle_0$ denotes average taken over the non-interacting system ($\mathbf{J}(\mathbf{q}) = 0$). Direct evaluation yields $(\boldsymbol{\chi}^0)^{\alpha,\beta} = \delta_{\alpha,\beta}(x(1-x)/k_BT)$, which is a diagonal $R\times R$ matrix, because the different sublattices are non-interacting[4]. The self-consistency relation remains valid, and it is interpreted as a matrix relation between the $R\times R$ matrices $\boldsymbol{\chi}^0$, $\boldsymbol{\chi}(\mathbf{q})$ and $\mathbf{J}(\mathbf{q})$. The solution for $\boldsymbol{\chi}(\mathbf{q})$ yields

$$\boldsymbol{\chi}(\mathbf{q}) = \left[(\boldsymbol{\chi}^0)^{-1} - \mathbf{J}(\mathbf{q})\right]^{-1} . \tag{23}$$

Everything said so far about the mean-field theory is valid for any lattice gas model. We now consider the ASYNNNI model, and for simplicity we will assume that the repulsive interaction parameter V_1, is so strong that the simultaneous occupation of nearest neighbor oxygen atoms are prohibited. For this reason, only the first four sublattices 1, 2, 3, and 4 in Fig. 3 in paper II are used. The Fourier transform of the pair interaction function $\mathbf{J}(\mathbf{q})$ yields

$$\mathbf{J}(\mathbf{q}) = 2\begin{pmatrix} V_4\cos(q_zc) & V_2\cos(q_yb) & V_3\cos(q_xa) & 0 \\ V_2\cos(q_yb) & V_4\cos(q_zc) & 0 & V_3\cos(q_xa) \\ V_3\cos(q_xa) & 0 & V_4\cos(q_zc) & V_2\cos(q_yb) \\ 0 & V_3\cos(q_xa) & V_2\cos(q_yb) & V_4\cos(q_zc) \end{pmatrix} , \tag{24}$$

where $\mathbf{q} = (q_x, q_y, q_z)$ can be confined to lie within the first Brillouin zone given by $\mathbf{q} \in \{(q_x,q_y,q_z)| -\pi/a \le q_x < \pi/a, -\pi/b \le q_y < \pi/b, -\pi/c \le q_z < \pi/c\}$. The diagonalization yields four eigenvalues $\lambda_{\pm,\pm}(\mathbf{q}) = \pm V_3\cos(q_xa) \pm V_2\cos(q_yb) + V_4\cos(q_zc)$. The physical relevant interaction parameters $V_2 > 0 > V_3 > V_1$, and $V_4 > 0$ stabilize the ortho-I and the ortho-II phase. In the discussion that follows we will restrict ourselves to the ortho-II phase. Therefore the relevant $\mathbf{q}$-vector is the one that gives a maximum in $\mathbf{J}(\mathbf{q})$ for $\mathbf{Q} = (\pi/a, 0, 0)$ (in reduced units $(1/2, 0, 0)$) and the symmetry related positions. The structure factor $S_{\rm dif}(\mathbf{q})$ is calculated as the sum of fluctuations of the individual sublattices, so that $S_{\rm dif}(\mathbf{q}) = k_BT{\rm Tr}[\boldsymbol{\chi}(\mathbf{q})]$, where Tr denotes the trace. This is most easily done by diagonalization of $\boldsymbol{\chi}(\mathbf{q})$. By expanding $\lambda_{+,+}(\mathbf{q})$ around $\mathbf{q} = \mathbf{Q}$ we obtain

$$S_{\rm dif}(\mathbf{q}) = \frac{b_{ox}^2 k_BT}{\frac{k_BT}{x(1-x)} - \lambda_{+,+}(\mathbf{Q}) + |V_3|a^2(q_x-\pi/a)^2 + |V_2|b^2q_y^2 + |V_4|c^2q_z^2} , \tag{25}$$

where $\lambda_{+,+}(\mathbf{Q}) = |V_2| + |V_3| + |V_4|$. It seems appropriate to comment on the result of Eq. (25). The mean-field critical temperature $T_c^{\rm MF}(x)$ is given by $k_BT_c^{\rm MF}(x) = x(1-x)\lambda_{+,+}(\mathbf{Q}) = x(1-x)(|V_2| + |V_3| + |V_4|)$. By inserting the numerical values for the interaction parameters, we see that the mean-field estimate for $T_c^{\rm MF}(x)$ is a parabola with maximum for $x = 1/2$ with $T_c^{\rm MF}(1/2) = 0.120V_0/k_{\rm B}$ in two-dimensions. For $x = 0.4$ we obtain $T_c^{\rm MF}(0.4) = 0.115V_0/k_{\rm B}$, which is in remarkable agreement with the Monte Carlo result $T_c^{\rm MF}(0.4) = 0.1052V_0/k_{\rm B}$. It should be noted that this remarkable agreement may be fortuitous, because in the mean-field calculation, the simultaneous occupation on nearest neighbor sites was prohibited, while this was not the case in the Monte Carlo simulation. Further, from $\lambda_{+,+}(\mathbf{Q})$ the inclusion of a weak inter-plane coupling V_4 only change T_c by $|V_4|/(|V_2| + |V_3|) \approx 4\%$, contrary to the results obtained by Monte Carlo simulation, where

[4] This can be seen as follows: $\langle\Delta\sigma^{\alpha}_{\mathbf{q}}\Delta\sigma^{\beta}_{-\mathbf{q}}\rangle_0 = \delta_{\alpha,\beta}\left(\langle\sigma^{\alpha}_{\mathbf{q}}\sigma^{\beta}_{-\mathbf{q}}\rangle_0 - \langle\sigma^{\alpha}_{\mathbf{q}}\rangle_0\langle\sigma^{\alpha}_{-\mathbf{q}}\rangle_0\right)$. Inserting $\sigma^{\alpha}_{\mathbf{q}} = \sum_{\mathbf{r}_\alpha} e^{-i\mathbf{q}\,\mathbf{r}_\alpha}\sigma^{\alpha}(\mathbf{r}_\alpha)$ yields $\langle\Delta\sigma^{\alpha}_{\mathbf{q}}\Delta\sigma^{\beta}_{-\mathbf{q}}\rangle_0 = \delta_{\alpha,\beta}\delta_{q,0}\sum_{\mathbf{r}_\alpha}\left[\langle\sigma^{\alpha}(\mathbf{r}_\alpha)^2\rangle_0 - \langle\sigma^{\alpha}(\mathbf{r}_\alpha)\rangle_0^2\right]$. The concentration of oxygen atoms is $\langle\sigma^{\alpha}(\mathbf{r}_\alpha)\rangle_0 = x$. Since $\sigma^{\alpha}(\mathbf{r}_\alpha) = \sigma^{\alpha}(\mathbf{r}_\alpha)^2$, we have $\langle\sigma^{\alpha}(\mathbf{r}_\alpha)^2\rangle_0 = x$, and finally we obtain: $\langle\Delta\sigma^{\alpha}_{\mathbf{q}}\Delta\sigma^{\beta}_{-\mathbf{q}}\rangle_0 = \delta_{\alpha,\beta}\delta_{q,0}(N_{\rm tot}/R)[x(1-x)]$.

T_c increases with 20%, see Sec. 3.4. This is because the transition temperature in mean-field theory only depends on the coordination number of the particles and the strength of the pair-interaction parameters, and not on the dimensionality of the system, which plays an important role for the critical fluctuations as described by our simulation results.

As seen in Eq. (25) the line shape of $S_{\rm dif}(\mathbf{q})$ near a Bragg point $\mathbf{Q}$, is expected to be a Lorentzian, with different full-width-half-maxima (FWHM), reflecting the anisotropy of $\mathbf{J}(\mathbf{q})$ in the different q-directions. From Eq. (25) we see that the anisotropy is given by the square root of the ratio of the interaction parameters $\Delta k(T)/\Delta h(T)=\sqrt{|V_3|/|V_2|}$. Analogously we obtain $\Delta l(T)/\Delta h(T) = \sqrt{|V_3|/|V_4|}$. This fact is important, since it allows for a determination of the interaction parameters, from a measurement of the relative widths of the structure factor. Also it follows that the widths $\Delta h(T)$, $\Delta k(T)$, and $\Delta l(T)$ should scale with the reduced temperature as a power law $|T - T_c|^{\nu}$, with $\nu = 1/2$. It is also important to note, that the mean-field theory, indicates that the anisotropies $\Delta k/\Delta h$ and $\Delta l/\Delta h$ in addition to being independent of dimensionality also might be independent of temperature and oxygen stoichiometry x.

We now turn to a discussion of the computational aspects of calculating the structure factor based on Monte Carlo simulation of the ASYNNNI model. The calculation of the diffuse part of the structure factor was discussed in detail in Chap. 2. Using the basis vectors for the oxygen atoms at the O1 and O5 sites, given by $\mathbf{d}_1 = \mathbf{a}/2$ and $\mathbf{d}_2 = \mathbf{b}/2$, the diffuse part of $S(\mathbf{q})$ for the oxygen atoms can be written

$$S_{\rm dif}(\mathbf{q}) = \frac{1}{N_{\rm tot}} \left\langle \left| \sum_{\mathbf{r}} \sum_{j=1}^{2} e^{i\mathbf{q}\cdot(\mathbf{r}+\mathbf{d}_j)} \Delta\sigma(\mathbf{r}+\mathbf{d}_j) b_{\rm ox} \right|^2 \right\rangle . \tag{26}$$

In the computer simulations, we will consider a finite crystal system with $N_{\rm tot} = N_x \times N_y \times N_z$ lattice sites, and with periodic boundary conditions. In order to remove the shape dependence of the geometry used in the structure factor calculation, the finite system is extended by periodic boundary conditions to a system of $P(P\to\infty)$ replica of our original finite system on a super lattice with lattice spacing $N_x\mathbf{a}$, $N_y\mathbf{b}$, and $N_z\mathbf{c}$. As discussed in detail in paper I, the structure factor $S_{\rm dif}(\mathbf{q})$ for such a system is only non-zero for the discrete set of $\mathbf{q}$-vectors given by

$$\mathbf{q} = \frac{h}{N_x}\mathbf{a}^* + \frac{k}{N_y}\mathbf{b}^* + \frac{l}{N_z}\mathbf{c}^*, \tag{27}$$

where $\mathbf{a}^*$, $\mathbf{b}^*$, and $\mathbf{c}^*$ are the primitive basis vectors in reciprocal space, and h, k, and l are integers (not to be confused with the reduced reciprocal lattice units above). It is important to note that the resolution in $\mathbf{q}$-space is given *a priori* by the system size of the finite crystal system, and that the resolution can only be enhanced by increasing the system size.

The symmetries of a crystal play an important role in structure factor calculations. The orthorhombic $YBa_2Cu_3O_{6+x}$ compound is topologically almost identical to the tetragonal form. The a and b axis generally differ by less than 2%, giving a pseudo-tetragonal unit cell. In the computer simulations we will ignore this small difference and always consider the compound to be tetragonal using the symmetries of space group P4/mmm. The point group symmetries corresponding to P4/mmm, see Ref. [62] consist of three perpendicular rotors 2_x, 2_y, and 2_z, in addition to a four fold rotor 4_{xy}. As discussed in paper I, $S_{\rm dif}(\mathbf{q})$ will in general have the corresponding symmetries in reciprocal space. However the structure factor will *not* have the periodicity of the first Brillouin zone. For the P4/mmm space group, the basis vectors $\mathbf{d}_1$ and $\mathbf{d}_2$ occupy high symmetry positions, leading to the following translational symmetry. For $\mathbf{u}^* = \mathbf{a}^*, \mathbf{b}^*$: $S_{\rm dif}(\mathbf{q} + 2\mathbf{u}^*) = S_{\rm dif}(\mathbf{q})$, and

$S_{\rm dif}(\mathbf{q}+\mathbf{c}^*) = S_{\rm dif}(\mathbf{q})$. The translational periodicity gives rise to an additional symmetry element, which is a mirror plane perpendicular to the endpoint of the primitive reciprocal lattice vectors. This can be understood as follows: For $\mathbf{u}^* = \mathbf{a}^*, \mathbf{b}^*$ we have $S_{\rm dif}(\mathbf{q}+\mathbf{u}^*) = S_{\rm dif}(-\mathbf{q}-\mathbf{u}^*) = S_{\rm dif}(-\mathbf{q}-\mathbf{u}^*+2\mathbf{u}^*) = S_{\rm dif}(-\mathbf{q}+\mathbf{u}^*)$, where the inversion symmetry and the translational symmetry have been used. The symmetry elements define a minimal zone, or *irreducible zone*, in reciprocal space, which generates the entire structure factor by repetitive use of symmetries. Thus in the computer calculation of the structure factor only the $\mathbf{q}$-vectors in this zone need to be calculated.

As discussed above, the formation of domains of orthorhombic symmetry in the ortho-II phase shows up as a peak in $S_{\rm dif}(\mathbf{q})$ for $\mathbf{q} = \mathbf{Q}$. Therefore, the important information about the structural ordering phenomena is obtained by calculating $S_{\rm dif}(\mathbf{q})$ for a scan along the main axis in reciprocal space through $\mathbf{q} = \mathbf{Q}$. In Fig. 7 is shown the MC data for a two-dimensional calculation, by setting $V_4 = 0$.

The columns (a) and (b) show the profiles of the $(1/2, 0, 0)$ superstructure reflections for scans along the a-axis (h-scan) and b-axis (k-scan) at the temperatures $T = 0.1250V_0/k_B$ ($T \gg T_c$), $T = 0.1175V_0/k_B$ ($T \gtrsim T_c$), $T = 0.1025V_0/k_B$ ($T \approx T_c$), and $T = 0.080V_0/k_B$ ($T \ll T_c$). Column (c) in Fig. 7 shows snap-shots of the corresponding real space oxygen configurations. The system size used in the calculations is 200×200 and the oxygen concentration is kept fixed at a value $x = 0.4$ corresponding to that of Zeiske *et al.* [41]. The points indicate the actual MC data points. In order to gain sufficient statistics in the calculation, the structure factor has been averaged over 100 configurations. In addition the symmetry properties of the lattice were utilized as discussed above. The solid line through the data points represents the best fit to a two dimensional Lorentzian line shape for the diffuse part of the structure factor (including a fitted Lorentzian at the $(1, 0, 0)$ position and a background term). From the fit the amplitude A and the widths Δh and Δk along the main axis are determined. The amplitude is very small in comparison to a Bragg peak in the ordered phase, and will not be discussed here. For the details see paper II. In this context it should be mentioned that at $T = 0.1175V_0/k_B$ the line shapes and widths of the diffuse scattering, $\Delta h = 0.100 \pm 0.004$ and $\Delta k = 0.050 \pm 0.001$ agree very well with the experimental values, even though the experiment was performed at room temperature. We will comment on this below.

A more extensive series of data showing the width of the diffuse scattering at $\mathbf{q} = \mathbf{Q}$ and $x = 0.4$ as a function of temperature is presented in Fig. 8. The widths Δh (h-scan) and Δk (k-scan) have been calculated for several different system sizes in two-dimensions using both Kawasaki dynamics model (A) and (B) for the updating. For the Kawasaki dynamics model (A) the time to reach equilibrium is approximately 10 times longer than the corresponding model (B). However, the equilibrium results for the different updating methods agree both in value and in the trend of the finite size effects. In addition we show the analogous results for a three-dimensional calculation. The critical temperature T_c obtained from the three-dimensional calculation has increased with approximately 20%, even for the weak inter-plane coupling used, as compared with the corresponding two-dimensional result. Although the two-dimensional ASYNNNI model is of the Ising type (for which the exponents are $\nu = 1$ and $\beta = 1/8$), the universality class of the tetragonal to orthorhombic ortho-II phase transition has been suggested by Bartelt *et al.* [63] to be that of the XY-model with cubic anisotropy, with an exponent $\nu \approx 0.8$ which depends on the oxygen concentration. The solid line in Fig. 8 (a) and (b), represents a best fit to the 200×200 data using $\nu = 0.8$, and using the value for $T_c = 0.1052V_0/k_B$ obtained from the peak position of C_V from the Ferrenberg-Swendsen interpolation formula. The two-dimensional data

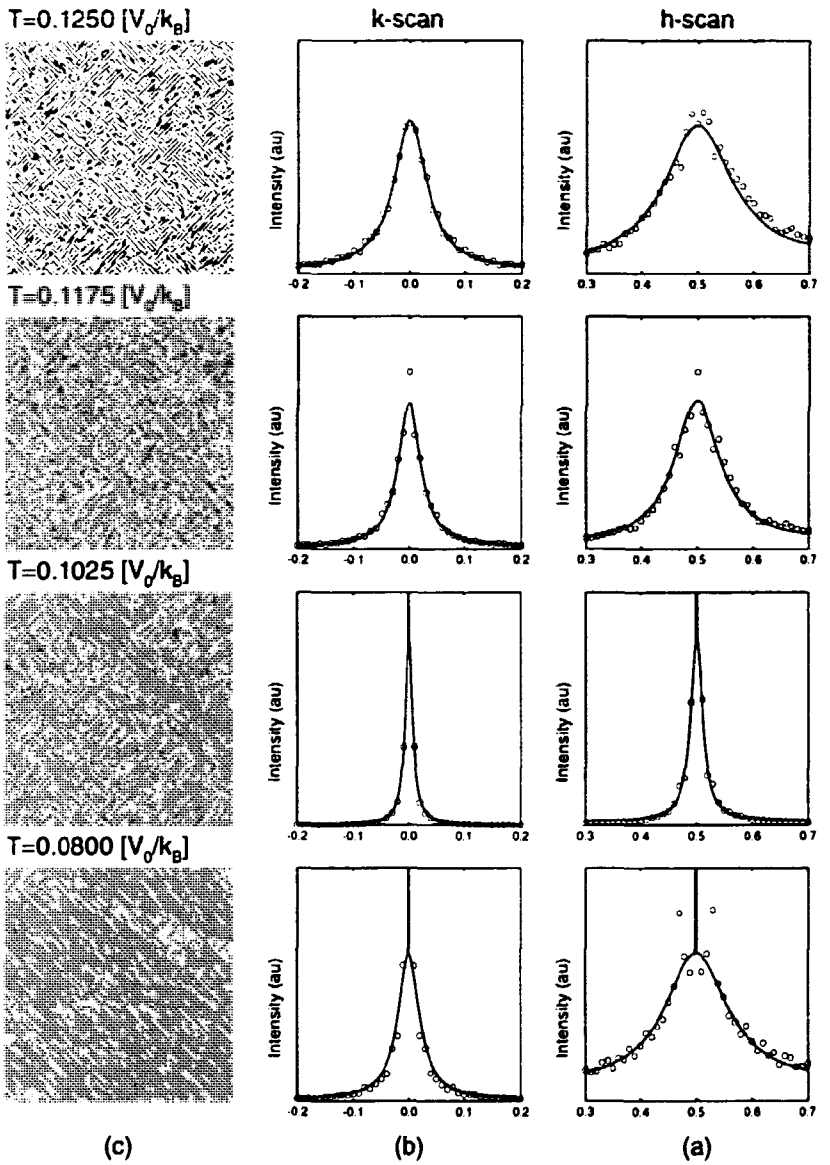

Figure 7. In (a) and (b) are shown a gallery of a two-dimensional calculation of the profiles of the $(1/2,0,0)$ *super structure reflections along the a-axis (h-scan) and along the b-axis (k-scan) for different temperatures. In (c) is shown the corresponding real space snapshots of the oxygen configurations. The system size used in the MC calculation is* 200×200 *and the updating is performed by Kawasaki model (B), with a fixed oxygen concentration* x=0.4 *corresponding to that of the experimental sample, cf. Fig. 6.*

are consistent with this value of ν, but might also be consistent with $\nu = 1$, *i.e.* a straight line. However, the temperature variation of the order parameter is not consistent with the Ising exponent; an approximate value of $\beta \gtrsim 0.2$ is found. In the three-dimensional case, our numerical data are consistent, with the critical exponents $\nu = 0.64$, and $\beta \approx 0.31$ from the three-dimensional Ising model.

The dashed curve in Fig. 8 (a) and (b), represents a best fit to the $100\times100\times8$ data using $\nu = 0.64$. The critical temperature obtained from the fit was $T_c = 0.1275V_0/k_B$.

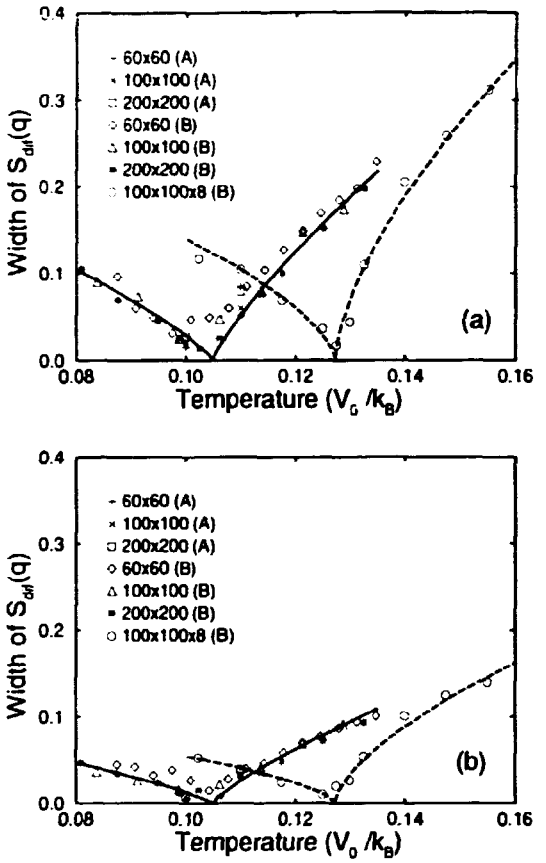

Figure 8. Comparison between the two-dimensional and the three-dimensional calculation of the peak width of the diffuse structure factor $S_{\rm dif}(\mathbf{q})$ *at* $(1/2, 0, 0)$ *as function of temperature for the h-scan and the k-scan, respectively. Symbols are the actual data points, indicating the results from different system sizes and from the Monte Carlo Kawasaki updating method (A) and (B). The solid curves through the two-dimensional data points, are the best fit to the scaling relation* $|T - T_c|^\nu$, *with* $\nu = 0.8$. *Analogously, the dashed curves through the three-dimensional data points, are the best fit using* $\nu = 0.64$.

As can be seen from Fig. 8 (a) and (b) the anisotropy $\Delta k(T)/\Delta h(T)$ is approximately temperature independent. In addition the anisotropy is also independent of dimensionality, in agreement with the mean-field result.

The structure factors presented so far, have been calculated on a serial workstation. Due to limitations in CPU power, the calculations are limited to q-scans along the main crystallographic axis. The reason for this is, that since only the total projection of the oxygen configuration along the chosen q-direction is needed, only a sequence of $N_{\rm tot}^{1/d}$ values are actually Fourier transformed, for a d-dimensional system with $N_{\rm tot}$ lattice sites. The calculation of the structure factor in the entire q-space is far too demanding even for moderate system sizes, because the projection techniques cannot be used. Therefore we have developed a parallel updating algorithm for the three-dimensional extension of the ASYNNNI model, which naturally maps on to the underlying architecture of the highly parallel computer, the Connection Machine (CM2). The Connection Machine is a SIMD computer with 65536 bit-processors, and a hyper-cubic data router. In our simulations we have used 16384 processors. The program was implemented in Connection Machine

Fortran (CMF) with calls to the Connection Machine Scientific Software Library (CMSSL).

To update the lattice we have used the Metropolis algorithm employing the standard method of dividing the lattice into non-interacting sublattices. We have used four sublattices within each a-b plane. However, due to the inter-plane coupling, two alternating sets are used along the c-axis, giving a total of eight sublattices. Since only one of the chosen sublattices is updated at a time, each one has been spread across all the available processors of the CM2.

Using the data layout described above, each oxygen site interacts with ten neighbouring oxygen sites located on eight different sublattices. This complicates the gathering of neighbours somewhat. The complication is, however, almost purely in programming effort, and does only marginally affect the performance of the local stencil. The performance gained by being able to keep all processors active at all times, far outweighs the loss from using a more complicated stencil. To maximize the bandwith of the inter processor communication needed to implement the stencil we have used communication primitives from CMSSL.

The data organization used for Monte Carlo updating is, however, not the optimal one for calculating the structure factor. Before each determination of the structure factor the different sublattices are therefore reassembled into the full lattice. After the data reordering, the structure factor is found using a standard fast Fourier transform.

For the results of the structure factors presented we have used 10^4 Monte Carlo steps per site (MCSS) for equilibration, followed by $5 \cdot 10^4$ MCSS with averaging taken every 10 MCSS. In all simulations we have used periodic boundary conditions.

The results for the structure factor are shown in Fig. 9 for $x = 0.4$ and in Fig. 10 for $x = 0.5$. The structure factors have been calculated for an $256 \times 256 \times 16$ system at $T = 0.15V_0/k_B$, which is above the critical temperature: $T_c(x = 0.4) = 0.13V_0/k_B$ and $T_c(x = 0.4) = 0.14V_0/k_B$. Vertically, the logarithm of the intensity of the structure factor $S_{\mathrm{dif}}(\mathbf{q})$ is shown in arbitrary units. In Figs. 9, and 10 top panels, are shown the result for the $l = 0$ plane in q-space, which extends over four Brillouin zones. The q_x axis along $(h, h, 0)$ and the q_y axis $(k, -k, 0)$ in the plot are rotated 45° around the crystallographic c-axis, and the numbers on the axis refer to the values of h and k respectively. The five peaks shown are, using notation (h, k, l): $(1/2, 0, 0)$, $(1, 0, 0)$, $(3/2, 0, 0)$, $(1, -1/2, 0)$, and $(1, 1/2, 0)$. The delta function contributions at $(0, 0, 0)$ and $(2, 0, 0)$ have been removed for clarity. In Figs. 9, and 10 bottom panels, are shown the corresponding $k = 0$ plane in q-space extending over two Brillouin zones. The axis in the plot are $(h, 0, 0)$ and $(0, 0, l)$. The three peaks shown are: $(1/2, 0, 0)$, $(1, 0, 0)$, and $(3/2, 0, 0)$. The line scan at $l = 0$, for $0 \leq h \leq 2$ in the bottom panel can be identified with the diagonal line through the peaks: $(1/2, 0, 0)$, $(1, 0, 0)$, and $(3/2, 0, 0)$ in the top panel. Again the delta function contributions at $(0, 0, 0)$ and $(2, 0, 0)$ have been removed for clarity.

By fitting the $(1/2, 0, 0)$ peak to a three-dimensional Lorentzian line shape for the diffuse part of the structure factor (including a fitted Lorentzian at the $(1, 0, 0)$ position and a background term), we have determined the widths Δh, Δk, and Δl along the main crystallographic axis. For the structure factor presented in Fig. 9 at $x = 0.4$ we obtain $\Delta h = 0.2738$, $\Delta k = 0.1285$, and $\Delta l = 0.5300$, which gives the following values for the anisotropy $\Delta k/\Delta h = 0.47$, and $\Delta l/\Delta h = 1.94$. In the same fashion we obtain for the structure factor presented in Fig. 10 at $x = 0.5$, $\Delta h = 0.1274$, $\Delta k = 0.0645$, and $\Delta l = 0.2970$, which gives the following values for the anisotropy $\Delta k/\Delta h = 0.51$, and $\Delta l/\Delta h = 2.33$. These values can be compared with the corresponding results from the mean-field theory, where we obtain $\Delta k/\Delta h = \sqrt{|V_3|/|V_2|} = 0.58$, and $\Delta l/\Delta h = \sqrt{|V_3|/|V_4|} = 2.45$. This shows

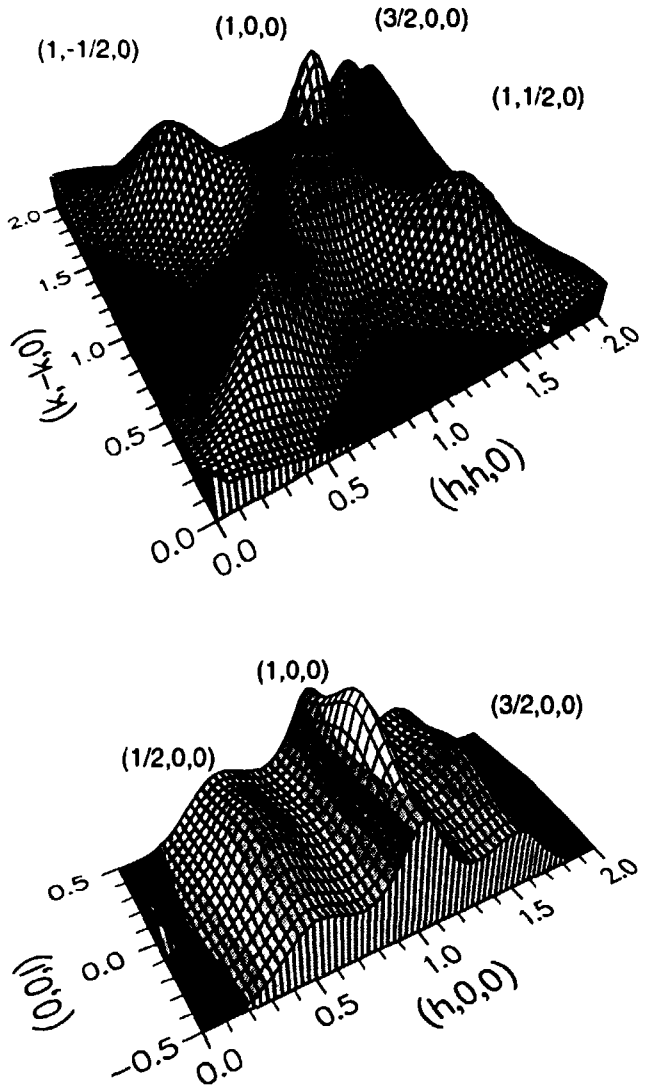

Figure 9. Structure factor for an 256×256×16 system at $T = 0.15V_0/k_B$ above T_c, with $x = 0.4$. Vertically, the logarithm of the intensity of the structure factor $S_{\rm tf}(\mathbf{q})$ is shown in arbitrary units. See detailed description in text.

that the mean-field estimates are fairly good, however to obtain accurate values Monte Carlo simulations are necessary.

The individual widths Δh, Δk, and Δl for the oxygen stoichiometry $x = 0.5$ are smaller than those for $x = 0.4$ by a factor of roughly two. This difference can be attributed to the curvature of the tetragonal/ortho-II phase boundary, see Fig. 6, which implies that the phase boundary for the $x = 0.4$ case is much further away than for the $x = 0.5$ case.

The results for the anisotropy at $x = 0.4$ for the two-dimensional case, where we obtained $\Delta k/\Delta h = 0.50$ can be compared with the corresponding result for the three-dimensional calculation, with $\Delta k/\Delta h = 0.47$. We see, that although the inclusion of an weak inter-plane interaction term has a dramatic effect on the transition temperature T_c, it only marginally affects the anisotropy. Even though the individual widths cannot be compared as discussed above, we can use our

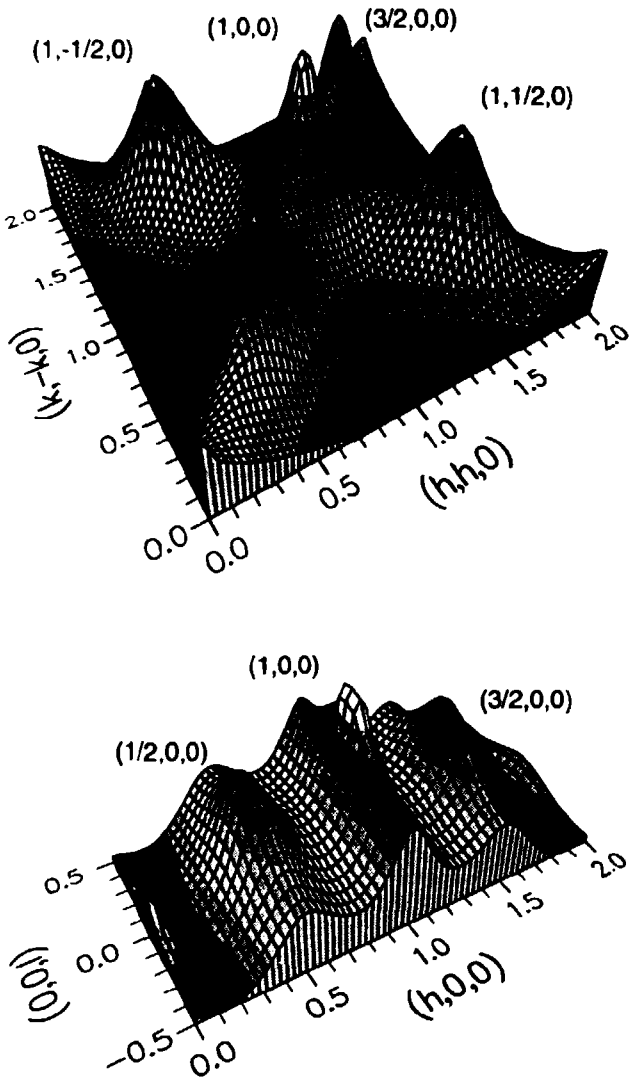

Figure 10. Structure factor for an 256×256×16 system at $T = 0.15V_0/k_B$ above T_c, with $x = 0.5$. Vertically, the logarithm of the intensity of the structure factor $S_{\rm diff}(\mathbf{q})$ is shown in arbitrary units. See detailed description in text.

results to determine the oxygen concentration dependence on the anisotropies. For the anisotropy within the basal plane, there appears to be no concentration dependence, as can be realized from the almost identical values $\Delta k/\Delta h = 0.47$ for $x = 0.4$ and $\Delta k/\Delta h = 0.51$ for $x = 0.5$. For the inter-plane anisotropy, the difference between the results $\Delta l/\Delta h = 1.93$ at $x = 0.4$ and $\Delta l/\Delta h = 2.33$ at $x = 0.5$ seems to be too large to be explained by the statistical uncertainty and is probably due to the fact that the two structure factors were calculated at different distances to the phase boundary.

From the neutron diffraction measurements by Zeiske *et al.* [41] for $YBa_2Cu_3O_{6+x}$ ($x = 0.4$), as discussed previously, we obtain the following values for the anisotropies: $\Delta k/\Delta h = 0.50$ and $\Delta l/\Delta h = 5.25$. By comparing with the corresponding results from the three-dimensional calculation: $\Delta k/\Delta h = 0.47$ and $\Delta l/\Delta h = 1.93$ we see that while the intra-plane anisotropy are in excellent agree-

ment with experiment, the inter-plane anisotropy is too small. The result imply that for particular values of the correlation lengths ξ_a and ξ_b, the correlation length ξ_c along the c-axis in our Monte Carlo simulation is too large as compared to the experimental data. Therefore, the attractive inter-plane interaction parameter V_4 should be reduced. From our mean-field theory the interaction parameter V_4 can be estimated to be $|V_4| = |V_3|/(\Delta l/\Delta h)^2 = 0.0044V_0$ by inserting the values for the experimental widths. This value is smaller by a factor of five compared to $V_4 = 0.02V_0$ as suggested by de Fontaine *et al.* in Ref. [48].

It should be mentioned that the experimental data are measured at room temperature, while the numerical data were obtained above the ortho-II ordering temperature. The rationale for this comparison is the observation that only short-range ordering was observed experimentally, which indicates that short-range ordered domain structures are frozen in at the tetragonal to orthorhombic phase transition (see paper II).

3.6 Metal-ion Doping Effects in $YBa_2Cu_{3-y}M_yO_{6+x}$

Many experiments have shown that the metal ions M = Co, Fe, and Al may substitute for Cu in the basal $Cu_{1-y}M_yO_x$ plane of $YBa_2Cu_{1-y}M_yO_{6+x}$. Because these dopants have a higher oxidation and oxygen coordination number than Cu they cause a reduction of the oxygen ordering, and as a consequence the superconducting transition temperature decreases, see Refs. [64, 65]. For samples prepared under standard oxidizing conditions orthorhombic structure and superconductivity with $T_c \approx 90$ K are maintained up to doping levels of $y \approx 0.1$; for higher doping levels the material becomes tetragonal and T_c decreases to zero for $y \approx 0.4$. However, significant variations in the structural and superconducting properties are found as a result of different preparation processes.

In particular experiments performed on the Fe-doped system by Katsuyama *et al.* [66] have indicated that samples prepared in a reduced atmosphere at high temperatures (800°C) and subsequently oxidized at intermediate temperatures (450°C) maintain orthorhombic structure up to much higher doping levels, than samples prepared under high oxygen pressure. The experimental results may be understood by assuming that the Fe-atoms are mobile at high temperatures, and are randomly distributed in the oxygen rich phase, but tends to cluster when only few oxygen atoms are present. When samples with Fe clustering are oxidized at lower temperatures, where the Fe-atoms are immobile, this may result in orthorhombic oxygen ordered phases that are considerably more spatially coherent, than those ordered states that are formed under high oxygen pressure and high temperature, where the dopant ions are mobile. This is certainly consistent with the observation, that samples with orthorhombic structure and suggested Fe-clustering have significantly higher superconducting transition temperature than those with a more random distribution of Fe-atoms [66].

In order to elucidate the effect on the material properties of the interplay between oxygen ordering and the diffusive motion of the metal ion dopants in $YBa_2Cu_{3-y}M_yO_{6+x}$ with M=Co, Fe, Al, we have developed a Monte Carlo simulation program.

In the absence of a detailed model for the covalent oxygen-metal interactions one has to look for a way of describing phenomenologically the fact that Co, Fe, and Al have higher oxidation and coordination numbers than Cu. We have chosen the simplest possible formulation [64], which can be made within a pairwise interaction scheme and which accounts for the tendency towards increased oxygen coordination around the M-sites. We assume the M-species to be distributed on the Cu sites, and adopt the model Hamiltonian given by Eq. (11) and the interaction parameters for the undoped material except for the inter-plane coupling V_4, which

we take as zero, and the nearest-neighbor interaction parameter for oxygen atoms around the M-atoms, V_1^M, which we assume to be less repulsive than V_1. The Hamiltonian of the modified ASYNXNI model is then given by

$$H = H_{\mathrm{ASYNXNI}} - (V_1^M - V_1) \sum_{(\mathbf{r}\mathbf{r}')}^{\mathrm{NXM}} \sigma(\mathbf{r})\sigma(\mathbf{r}') , \tag{28}$$

where the sum runs over all oxygen pairs $(\mathbf{r}, \mathbf{r}')$, which are nearest neighbor around a metal dopant atom (NXM).

The Monte Carlo simulation of Eq. (28) is performed in the standard fashion as discussed in Sec. 3.3, where the equilibrium is obtained using Glauber dynamics or Kawasaki exchange dynamics (model (A)) for the oxygen atoms. The equilibration of the metal-ions are performed with nearest-neighbor Kawasaki exchange dynamics, with the same attempt frequency as for the oxygen atoms. The Monte Carlo computer-simulation program, was developed in optimized C* and implemented on a 8192-processor CM200 Connection Machine. For details the reader is referred to paper III.

The results of the simulation show the occurrence of a phase separation process, at low oxygen content and high values for the coupling parameter V_1^M, which can be seen from the snapshots in Fig. 11. In Fig. 11 (a)-(f) are shown a series of snapshots taken at high temperature $T = 0.15V_0/k_B$ and with a constant dopant concentration of $y = 0.15$. The snapshots are taken after an equilibration time of $4 \cdot 10^4$ MCSS, except for panel (e) where the equilibration time is 10 times longer. In panels (a) and (b) are shown the results for $x = 0.1$, with a coupling parameter of $V_1^M = 0.2V_0$ and $V_1^M = 0.4V_0$ respectively. The corresponding results for the fully oxidized system $x = 1$ are shown in panels (c) and (d).

It is seen that a metal-ion domain formation sets in at low oxygen contents $x = 0.1$ and for large values of the coupling parameter, $V_1^M = 0.4V_0$, panel (b), and that these domains at late times, (*cf.* Fig. 11 (e)) form a separate phase. At high oxygen content, (panels (c) and (d)) the metal-ions form short linear O-M-O-M chains, which are distributed in a random fashion in the $Cu_{1-y}M_yO_x$ basal plane. The phase separated phase consists of a dense (1×1) oxygen structure in which all metal-ion sites are occupied by the dopant ions, which can be seen in panel (f), which shows an enlargement of panel (e). Not all of the dopant ions take part in the phase separated domain, because at the low oxygen contents (shown in Fig. 11 (e)) there is simply not enough oxygen to get all the M-ions together. Therefore, a substantial part of the M-ions remains dispersed as a gas in the oxygen-poor phase.

Details of the lateral organization of the doped system in terms of domains of M-ions, are given in paper III, where we have calculated the cluster size and its linear extension as function of the coupling parameter V_1^M. We have shown that for low oxygen content, and $V_1^M \approx 0.27V_0$, there is a clear onset of the formation of metal-ion clustering. This can be viewed from the fact that for $V_1^M < 0.27V_0$, the domains are linear consisting of single O-M-O-M chains, while for $V_1^M > 0.27V_0$ the metal-ion domains become more compact. However for large oxygen content, no such metal-ion clustering was observed even for large values of V_1^M. The reader is referred to paper III for more details.

3.7 Discussion

With special emphasis on the three-dimensional oxygen ordering of $YBa_2Cu_3O_{6+x}$ we have extended the two-dimensional ASYNXNI model to three dimensions. We have calculated the phase diagram in two dimensions by Monte Carlo simulation with interaction parameters $(V_1, V_2, V_3) = V_0(-1, 0.36, -0.12)$ and in

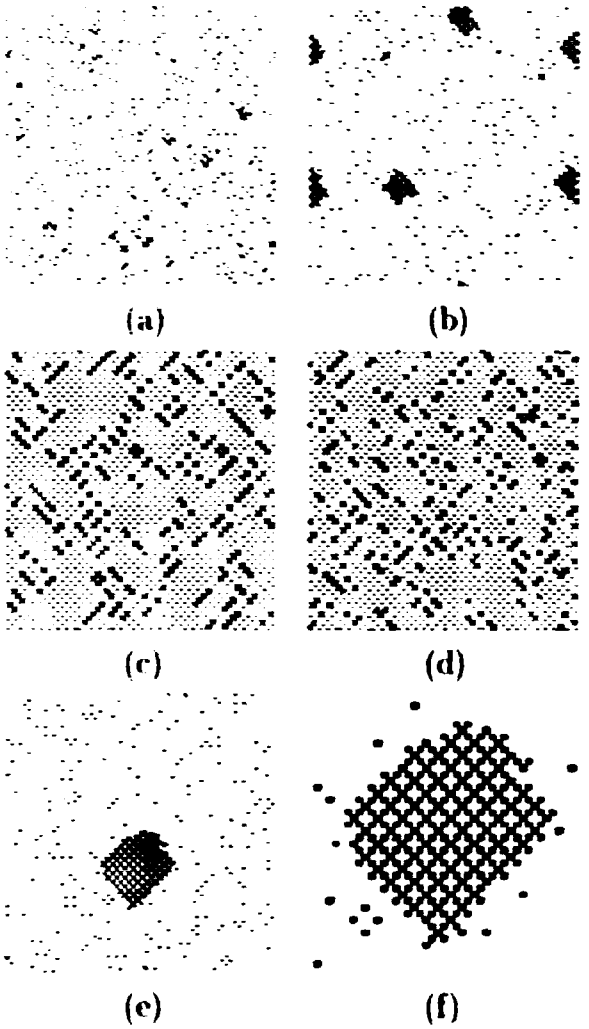

Figure 11. Selected snapshots of oxygen and dopant ion configurations. Grey dots denote oxygen atoms, black dots denote the dopant metal ions, and white denote vacant oxygen sites. The configurations correspond to typical equilibrium states for a lattice with 128×128 *oxygen sites at a temperature* $T = 0.15V_0/k_B$ *and a dopant concentration of* $y = 0.15$. *The configurations correspond to an equilibrium time of* $4 \cdot 10^4$ *MCSS. (a)* $x = 0.1$ *and* $V_1^M = 0.2V_0$. *(b)* $x = 0.1$ *and* $V_1^M = 0.4V_0$. *(c)* $x = 1$ *and* $V_1^M = 0.2V_0$. *(d)* $x = 1$ *and* $V_1^M = 0.4V_0$. *Panel (e) is the same as (b) but after a much longer equilibration time corresponding to* $4 \cdot 10^5$ *MCSS. In (f) is shown an enlargement of a section of the snapshot in (e).*

three dimensions by adding a weak interplane coupling $V_4 = 0.02V_0$, using Glauber as well as Kawasaki dynamics. The Ferrenberg-Swendsen method has also been used and improved slightly in order to make it more numerically stable. The transition temperature obtained in this way from the specific heat can be determined very accurately: it agrees with that obtained by analysis of the other quantities. The resulting phase diagram accounts for many of the structural properties of $YBa_2Cu_3O_{6+x}$ such as the presence of the tetragonal disordered, and the two

major orthorhombic ordered structural phases, ortho-I and ortho-II. The three-dimensional phase diagram has the same topology as the two-dimensional case, the only difference being that the phase boundaries are shifted upwards in temperature with about 20%, which implies that the energy scale factor, V_0, should be significantly modified. We have not studied the low temperature region. Thus our study does not address the structural properties of finite size domains indicating higher order superstructures which have been observed by electron diffraction technique [67, 68]. These superstructures, which are likely to occur at lower temperatures for thermodynamic reasons, have been accounted for by macroscopic models [69], and they may be explained by including further interaction parameters in the ASYNNNI model [70, 71]. Experimentally it is questionable whether true long range ordered phases of these superstructures can be established because of slow oxygen kinetics at low temperatures.

A comparison between the two-dimensional and the three-dimensional calculation of the peak width of the diffuse part of the structure factor at $(1/2, 0, 0)$ and $x = 0.4$ as function of temperature and direction in reciprocal space has been performed. In both cases a power law scaling behavior is observed, however with different critical exponents. The two-dimensional data are consistent with $\nu = 0.8$ suggested by Bartelt *et al.* [63], while the three-dimensional data has $\nu = 0.64$ which is much closer to the values expected from mean-field theory.

In order to gain sufficient resolution for a full three-dimensional calculation of the structure factor, we have developed a parallel updating algorithm for the three-dimensional extension of the ASYNNNI model and implemented it on a CM2 Connection Machine. Structure factor calculations have been carried out for oxygen stoichiometries, $x = 0.4$ and $x = 0.5$, on a $256 \times 256 \times 16$ system at a temperature $T = 0.15V_0/k_B$ in the tetragonal disordered phase. The anisotropy ratios $\Delta k/\Delta h$ and $\Delta l/\Delta h$ have been compared with those obtained from the two-dimensional studies and with recent experimental results at $x = 0.4$. The in-plane anisotropies obtained in the two- and three-dimensional simulations are only marginally different and there appears to be no concentration dependence. However, the difference between the interplane anisotropy ratios cannot be explained by statistical errors, but may be a consequence of the difference in the temperatures relative to T_c. Comparison with mean-field calculations and results obtained from two-dimensional Monte Carlo simulation studies suggest that the anisotropy ratios are independent of temperature, but this is not necessarily the case for temperatures close to T_c. For the $x = 0.4$ case we have compared the peak width anisotropies with similar experimental data and found excellent agreement for the in-plane anisotropy ratio, but a significant deviation for the inter-plane ratio. This discrepancy may be remedied by reducing the inter-plane interaction parameter by a factor of five.

We have investigated, by a parallel Monte-Carlo computer-simulation algorithm, the interplay between oxygen ordering and metal-ion diffusive modes in a simple lattice-gas model of the basal $(Cu_{1-y}M_yO_x)$-planes of M-ion doped $YBa_2Cu_{3-y}M_yO_{6+x}$ compounds. The main conclusion is that the value of the dopant interaction parameter has a very strong influence on the structural ordering properties in the basal plane of the superconductor. Massive metal-ion domain formation and phase separation can occur at low oxygen contents, which gives support to the interpretation of the experimental data on Fe doped materials proposed in Ref. [66].

4 Transfer Matrix Study of Metastability

In this chapter we will apply a recently developed constrained transfer-matrix (CTM) formalism to study the stationary properties of metastability in models with long-range interactions, based on the results of paper IV. We have studied an extension of the Blume-Capel model [72, 73, 74] to include weak, long-range interactions. The Blume-Capel model is an $S=1$ model and is equivalent to a three-state lattice-gas model. The reasons for studying this model are that for a certain field-range a region with two competing metastable states exists, and that the model is simple enough to allow extensive symmetry reduction of the transfer matrix, as shown in paper IV, so that large system sizes could be considered. In the CTM formalism a set of complex free-energy densities f_α arises, by reweighting the eigenvalues of the equilibrium transfer matrix, some of whose imaginary parts have been suggested to be related to the metastable decay rate [75, 76]. We have shown that f_α for a metastable state is analogous to the analytical continuation of the free energy into the region of metastability considered by Langer [77, 78], and that $\mathrm{Im}f_\alpha$ is closely related to the activation barrier height involved in the transition, even in the presence of competing metastable states, where the analytic continuation of the free energy has been argued [7] to give misleading results. When coupled with the Van't Hoff-Arrhenius law [79] of chemical reaction theory, the relation between $\mathrm{Im}f_\alpha$ and the activation barrier height provides strong evidence for the physical interpretation of $\mathrm{Im}f_\alpha$ as a decay rate. In Sec. 4.2 we briefly review the equilibrium transfer matrix formalism. We introduce the equilibrium n-point joint probability distribution functions ($n = 1, 2$), which are then generalized in Sec. 4.3 to a set of non-equilibrium constrained probability distributions, which serve as the starting point for the CTM formalism. In Sec. 4.4 we define the long-range Blume-Capel model, discuss its zero-temperature phase diagram, and calculate exactly the finite temperature mean-field spinodal surfaces. Section 4.5 contains the application of the CTM formalism to the long-range Blume-Capel model and contains our numerical results. Before discussing the CTM formalism in detail, we wish to convey a physical intuition of metastability, and in this context mention the result of Langer [77, 78]. We will then examine a simple two-state model with weak long-range forces, the quasi-one-dimensional Ising (Q1DI) model, [6, 75, 76, 80]. This model also serves as a basis for the discussion presented in Sec. 4.4 of the more general long-range Blume-Capel model, which exhibits several metastable states.

4.1 Introduction

The description of metastable states at a fundamental level has been the focus of numerous works, but it remains an unsolved problem in statistical mechanics. For reviews, see *e.g.* Refs. [81, 82, 83]. Metastable states are characterized as a thermodynamic phase, although the intensive variables of the system have values such that the equilibrium state would be in a different phase (or possible phase coexistence). By small changes of the thermodynamic variables, the metastable state responds with small reversible changes. Under large changes the system changes irreversibly (escapes) out of the metastable state. If the system is left isolated, the metastable state decays very slowly compared with the time scale for molecular processes, as a result of fluctuations. If the fluctuations are large enough, they can nucleate a droplet of the stable phase, which then grows until the entire system is dominated by the stable phase. The description of a metastable state as

being in quasi equilibrium, suggests that the procedures in equilibrium statistical mechanics might be extended to cover metastable states as well. The main idea is to consider a modified system in which nucleation is prevented by introducing a constraint, which forces the system to stay in the metastable state. This approach was followed by Langer [4] in a study of the analytical properties of free energy at the condensation point. Langer conjectured that the imaginary part of the free energy $\mathrm{Im}f$ analytically continued from the equilibrium phase across the first-order phase transition may be associated with the decay rate of the metastable phase. A dynamical investigation [77, 78] showed for a wide class of models, that the decay rate Γ may be written in terms of $\mathrm{Im}f$ as

$$\Gamma = \frac{\beta\kappa}{\pi}|\mathrm{Im}f| \,, \tag{29}$$

where $\beta = 1/k_B T$ is the inverse temperature (units are chosen so that $k_B = 1$) and κ is a kinetic prefactor that depends on the dynamics.

We will now consider a simple two-state quasi-one-dimensional Ising model, the socalled Q1D1 model. The Q1D1 model consists of a one-dimensional chain of L layers or subsystems, each containing N Ising spins $s_{i,n} = \pm 1$, where the index $i = 1, \ldots, L$ runs over the layers, and the index $n = 1, \ldots, N$ runs over the spins in a given layer. Each spin interacts ferromagnetically with each other in the adjacent layers with a coupling $J/N > 0$. Each spin also interacts with an external field H. We impose periodic boundary conditions so that $s_{i,n} = s_{L+i,n}$. The Hamiltonian can be expressed as

$$\mathcal{H} = -JN\sum_{i=1}^{L} m_i m_{i+1} - H\sum_{i=1}^{L} m_i \,, \qquad m_i = \frac{1}{N}\sum_{n=1}^{N} s_{i,n} \,. \tag{30}$$

In the mean field calculation we assume that the configurations of the system are translationally invariant, so that $m_i = m$ for all layers $i = 1, \ldots, L$. In the limit $N \to \infty$ the density m takes continuous values $m \in [-1; 1]$. The mean-field free-energy-density functional $\mathcal{F}^{\mathrm{MF}}$ can be calculated for a given m using the relation $\mathcal{F}^{\mathrm{MF}} = \mathcal{H}^{\mathrm{MF}} - T\mathcal{S}^{\mathrm{MF}}$, where $\mathcal{S}^{\mathrm{MF}}$ is the micro-canonical entropy density of the system. The functional $\mathcal{F}^{\mathrm{MF}}$ is related to the thermodynamic free energy per spin f by $f = \min_{m\in[-1;1]} \mathcal{F}^{\mathrm{MF}}(m)$. In the limit $N \to \infty$, it is shown in Ref. [6] and paper IV that $\mathcal{F}^{\mathrm{MF}}$ is given by

$$\mathcal{F}^{\mathrm{MF}} = -Jm^2 - Hm + \frac{T}{2}\left[(1+m)\ln(1+m) + (1-m)\ln(1-m) - 2\ln 2\right] . \tag{31}$$

In Fig. 12 we have plotted the free-energy-density functional from Eq. (31) versus magnetization at a temperature $T < T_c = 2J$ for two values of the H-field.

Consider first the solid curve, which corresponds to $H < H_{\mathrm{sp}}$, where H_{sp} is defined below in Eq. (34). The positions of five particular values of the magnetization have been indicated on the curve. The global minimum at $m = m_{\mathrm{eq}}$ corresponds to the equilibrium state, where the Ising spins are predominantly aligned along the external field. The local minimum at $m = m_{\mathrm{ms}}$ corresponds to the system being in a metastable state, where most of the Ising spins are aligned against the field. The two points $m = \pm m_{\mathrm{sp}}$ are inflection points of the free-energy functional, and they are located on each side of $m = m_{\mathrm{un}}$, which is a local maximum. The parts on the curve $m_{\mathrm{ms}} < m < -m_{\mathrm{sp}}$ and $m_{\mathrm{ms}} < m < m_{\mathrm{eq}}$ describe higher lying metastable states, while the part between the inflection points $-m_{\mathrm{ms}} < m < m_{\mathrm{ms}}$ describe unstable states since $\partial^2\mathcal{F}^{\mathrm{MF}}/\partial m^2 < 0$. The three magnetizations $m = m_{\mathrm{eq}}$, $m = m_{\mathrm{ms}}$, and $m = m_{\mathrm{un}}$ are determined from the stationarity condition. By setting the partial derivative of $\mathcal{F}^{\mathrm{MF}}$ with respect to m equal to zero we obtain:

$$H = -2Jm + T\tanh^{-1} m \,. \tag{32}$$

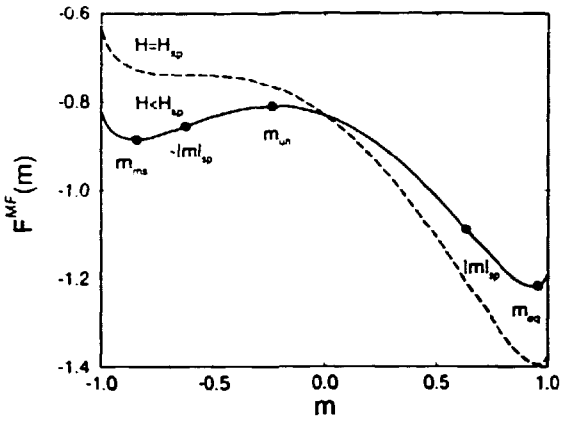

Figure 12. Mean-field free-energy density $\mathcal{F}^{MF}(m)$ for the Q1DI model as function of magnetization at $T/T_c = 0.6$. The solid curve is calculated for an H-field of $H = H_{sp}/2$, while the dashed curve corresponds to $H = H_{sp}$. The indicated positions are as follows: m_{eq} is the equilibrium magnetization, $\pm|m_{sp}|$ mark the spinodal magnetizations, m_{un} is the unstable magnetization, and m_{ms} is the metastable magnetization.

The loci of $m = \pm m_{sp}$ on the magnetization curve in Fig. 12 are called the spinodal points, and they are determined by the the condition of inflection $\partial^2 \mathcal{F}^{MF}/\partial m^2 = 0$. We obtain:

$$m_{sp} = \pm\sqrt{1 - T/2J} \,. \tag{33}$$

By inserting Eq. (33) into Eq. (32) we obtain an expression for the spinodal field H_{sp}, for which the locus of $m = m_{ms}$ is also a point of inflection:

$$H_{sp} = \pm\left[-2J\sqrt{1 - T/2J} + T\tanh^{-1}\sqrt{1 - T/2J}\right] \,. \tag{34}$$

The dashed curve in Fig. 12 is the free-energy-density functional at $H = H_{sp}$. The spinodal field $H = H_{sp}$ marks the termination of metastable states, above which no metastable states can exist. In Fig. 13 the values for the magnetization density, where $\mathcal{F}^{MF}(m)$ is extremal, *i.e.* m_{eq}, m_{ms}, and m_{un}, are plotted versus the H-field for $T/T_c = 0.6$. The solid lines represent the stable states, the long-dashed lines the metastable states, and the dashed line the unstable states. The spinodal fields H_{sp} are indicated as vertical lines.

The decay of a metastable state happens via a random formation of nuclei (spontaneous nucleation) which then grow in size. The free energy cost ΔF associated with the formation of the nucleating droplet is evaluated as the minimum barrier height for all paths in *phase space* that connect the metastable state to the stable state. In the mean-field approximation of ΔF, we assume that the magnetization of the system changes in such a way that the system remains translationally invariant. Then $\Delta F = NL\Delta\mathcal{F}^{MF}$, where $\Delta\mathcal{F}^{MF} \equiv \mathcal{F}^{MF}(m_{un}) - \mathcal{F}^{MF}(m_{ms})$ is the free-energy barrier per spin, and NL is the volume of the system. The mean-field free-energy barrier $\Delta\mathcal{F}^{MF}$ can be viewed in Fig. 12 as the barrier height which the system initially in the metastable state at $m = m_{ms}$ has to overcome in order to escape.

The expression for $\Delta\mathcal{F}^{MF}$ can be obtained analytically as an expansion around the spinodal point. For the detailed derivation the reader is referred to paper IV. We obtain

$$\Delta\mathcal{F}^{MF} = -m_{sp}(H - H_{sp}) - \frac{2\sqrt{2}}{3}\gamma^{-1/2}(H - H_{sp})^{3/2} + O(H - H_{sp})^2 \,, \tag{35}$$

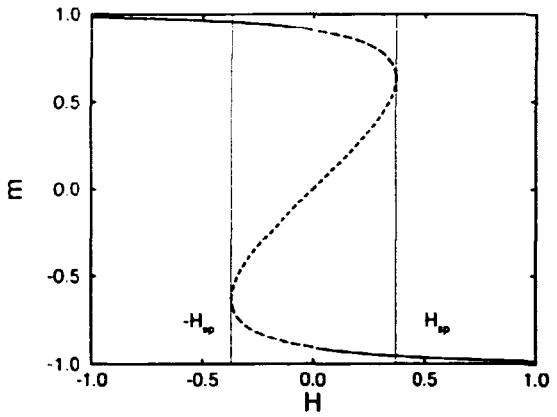

Figure 13. Magnetization for the Q1DI model plotted versus H-field at $T/T_c = 0.6$. The solid curve corresponds to the stable states, the long-dashed curves to the metastable states, and the dashed curve to the unstable states. The spinodal fields H_{sp} are indicated by vertical lines.

where $\gamma = 8J\sqrt{1 - T/2J}$. To find ΔF we must relax the assumption of translational invariance, so that a droplet of finite width is allowed to form. In Refs. [6] and [57] it was shown that the model can be mapped onto a one-dimensional field theory. We define a function $m(r)$ to be continuous in a dimensionless longitudinal coordinate r, and we force $m(r)=m_i$ at integer values $r=i$. By Taylor's theorem, if $i \leq r \leq i+1$, then $(m_{i+1} - m_i)^2=(\nabla m(r))^2 + O(\nabla m \nabla^2 m)$. Therefore, if $m(r)$ do not vary too rapidly, then the free-energy density $\mathcal{F}$ for a configuration described by $\{m_i\}$ is well approximated by the Ginzburg-Landau-Wilson form:

$$\mathcal{F} = \frac{1}{L}\int_0^L dr \left[\frac{1}{2}J(\nabla m)^2 + \mathcal{F}^{\mathrm{MF}}(m(r))\right] . \tag{36}$$

The stationary solutions for the magnetization profile is given by the Euler-Lagrange equation $\delta\mathcal{F} = 0$. In Ref. [6] it was demonstrated that this equation has three types of continuous solutions. For each local minimum m_{min} of $\mathcal{F}^{\mathrm{MF}}$, there is a uniform solution $m(r)=m_{\mathrm{min}}$, for which the free-energy density is given by the corresponding mean-field result. In addition, for each local minimum that is not the (unique) global minimum $m(r) = m_{\mathrm{ms}}$, there exists a solution that represents the lowest-lying saddle point between m_{ms} and a second minimum of equal or lower value. If the second minimum is lower, the solution, viewed as a spatial variation in m, has the shape of a "droplet" pointed toward the more stable minimum embedded in a sea of the metastable configuration m_{ms}. If the second minimum is of equal value, the solution has an "interface" shape, in which the system passes from one minimal configuration to the other. Other solutions to the Euler-Lagrange equation, which are oscillatory in space, can also exist, but we do not consider them here since their associated free-energy density is higher than that for the solutions already described. By solving the Euler-Lagrange equation for the droplet shape, see paper IV and Refs. [6, 84] the free-energy cost ΔF is determined:

$$\Delta F = \frac{48}{5}N(\sqrt{2}J)^{1/2}|\gamma|^{-3/4}|H - H_{\mathrm{sp}}|^{5/4} + O(H - H_{\mathrm{sp}})^{7/4} . \tag{37}$$

From ϕ^3 field-theory studies [85], the exponential dependence of the lifetime of a metastable state close to the spinodal point was found to scale as $|H - H_{\mathrm{sp}}|^{3/2-d/4}$ in d dimensions. The hyper-cylindrical geometry considered in the calculations has $d=1$, giving an exponent of 5/4, in agreement with Eq. (37). This is unlike that of the mean-field theory where an exponent of 3/2 was obtained (see Eq. (35)).

From the Van't Hoff-Arrhenius law [79], we expect the nucleation rate to have a "Boltzmann weight" given by the free-energy cost ΔF of forming a nucleating droplet:

$$\Gamma \propto e^{-\beta \Delta F} . \tag{38}$$

The exponent in Eq. (38) is similar in form to an escape rate for a particle in a potential well under the influence of some stochastic dynamics, [86]. From Eq. (37), it is seen that ΔF is proportional to N, which implies that in the limit $N \to \infty$ the metastable state in fact becomes a stable state. The mean-field treatment of infinite-range force models, such as the Q1DI model can easily give metastable states, probably because the relaxation time in the thermodynamic limit of infinite volume becomes infinitely long so that the metastable phase, as we have shown, becomes a stable phase. However one of the problems for a rigorous theory of metastable states comes from the fact that a general principle of statistical mechanics states that the free-energy functional in the thermodynamic limit should be an upwards concave function of the magnetization m, [87] and therefore it cannot include parts on Fig. 12 in the range $m_{\rm ms} < m < m_{\rm eq}$. This is the origin of the Maxwell construction, which connects point $m_{\rm ms}$ and $m_{\rm eq}$ by a straight line segment, in order to satisfy the above constraint.

4.2 Equilibrium Transfer Matrix Formalism

This section contains a brief review of the equilibrium transfer matrix formalism following the discussion in Ref. [88] and gives the basis for the CTM formalism (for a more extensive treatment see Refs. [87, 89]). The transfer matrix formalism is a mathematical tool to derive statistical mechanical information for d-dimensional discrete systems that are translationally invariant and infinite in one dimension and finite in $(d-1)$ dimensions. All the equilibrium information about a thermodynamic system is contained in the partition function and in the n-point joint probability distribution functions. The partition function Z is defined as

$$Z = \mathrm{Tr}\left(e^{-\beta \mathcal{H}}\right) , \tag{39}$$

where $\mathcal{H}$ is the Hamiltonian of the system. Consider a finite system, which is divided into M $(d-1)$-dimensional layers (subsystems), each containing N discrete local variables. The configuration of the m-th layer can be represented by the column vector $|X_m\rangle$, which form a complete basis set. We assume periodic boundary conditions in the longitudinal direction so that $|X_m\rangle = |X_{M+m}\rangle$. By restricting the interaction range, only to include adjacent subsystems, the Hamiltonian can be decomposed into a sum of layer Hamiltonian operators, whose form are independent of layer index:

$$\mathcal{H} = \sum_{m=1}^{M} \langle X_m | \mathcal{H}^{\rm op} | X_{m+1} \rangle . \tag{40}$$

Using the fact that a configuration $|X\rangle$ of the entire system can be written as a direct product of the M layer configurations, $|X\rangle = |X_1\rangle |X_2\rangle \cdots |X_M\rangle$, and inserting Eq. (40) into Eq. (39) we obtain for the partition function:

$$\begin{aligned} Z_M &= \mathrm{Tr} \exp\left[-\beta \sum_{m=1}^{M} \langle X_m | \mathcal{H}^{\rm op} | X_{m+1} \rangle\right] \\ &= \sum_{\{X_0\}} \langle X_0 | \mathbf{T}^M | X_0 \rangle , \end{aligned} \tag{41}$$

where the transfer matrix $\mathbf{T}$ is defined in terms of its matrix elements in the dual space of configurations of two adjacent layers:

$$\langle X_m | \mathbf{T} | X_{m+1} \rangle = \exp\left[-\beta \langle X_m | \mathcal{H}^{\rm op} | X_{m+1} \rangle\right] . \tag{42}$$

Since a layer configuration $|X_m\rangle$ can be considered as a direct product of single spin configurations in that layer: $|X_m\rangle = |s_{1,m}\rangle|s_{2,m}\rangle \cdots |s_{N,m}\rangle$, the dimension of the transfer matrix is given by p^N, where p is the number of states for a single spin. Since $\mathbf{T}$ is a finite matrix with only positive elements, the Perron-Frobenius theorem states that the largest eigenvalue λ_0 is positive and nondegenerate, and that the corresponding eigenvector can be chosen to have only positive elements [90, 91]. In addition all subdominant eigenvalues are either real or occur in complex pairs. In the following discussion we will restrict ourselves to symmetric transfer matrices $\mathbf{T}$ and we sort the eigenvalues λ_α in order of decreasing magnitude, so that $\lambda_0 > |\lambda_1| \geq |\lambda_2| \geq \cdots \geq |\lambda_{p^N-1}|$. The partition function can then be written:

$$Z_M = \mathrm{Tr}\,(\mathbf{T}^M) = \sum_{\alpha=0}^{p^N-1} \lambda_\alpha^M \,. \tag{43}$$

In the limit $M \to \infty$, the free-energy density per spin f of the system is obtained from the partition function Eq. (43), and yields:

$$f = -\frac{1}{\beta N} \lim_{M\to\infty} \frac{1}{M} \ln Z_M = -\frac{1}{\beta N} \ln \lambda_0 \,. \tag{44}$$

From Eq. (44) the order parameter and susceptibility are given from the standard statistical mechanical relations. We can also easily obtain one- and two-point probability distribution functions $P(X_m)$ and $P(X_m, X_{m+n})$ from the transfer matrix. The probability that the m-th layer in a system of length M is in a configuration $|X_m\rangle$ is given by the partial trace of the density matrix, the socalled marginal probability density, and is given by

$$P_M(X_m) = Z_M^{-1} \sum_{|X\rangle}^{(m)} \langle X|e^{-\beta\mathcal{H}}|X\rangle = Z_M^{-1} \langle X_m|\mathbf{T}^M|X_m\rangle \,. \tag{45}$$

In Eq. (45), $\sum_{|X\rangle}^{(m)}$ means that the configuration of layer m is held fixed. By expanding $|X_m\rangle$ in the orthonormal basis $\{|\alpha\rangle\}$ of eigenvectors of the transfer matrix $\mathbf{T}$, we obtain in the limit $M \to \infty$:

$$P(X_m) = \lim_{M\to\infty} P_M(X_m) = |\langle 0|X_m\rangle|^2 \,. \tag{46}$$

Thus, the probability of observing a configuration $|X_m\rangle$ is given by its projection onto the eigenvector of $\mathbf{T}$ with the largest eigenvalue. Similarly the two-layer joint probability distribution function for the m-th and the $(m+n)$-th subsystems, in the limit $M \to \infty$ can be written

$$\begin{aligned} P(X_m, X_{m+n}) &= \lim_{M\to\infty} Z_M^{-1} \sum_{|X\rangle}^{(m,m+n)} \langle X|e^{-\beta\mathcal{H}}|X\rangle \\ &= \langle 0|X_m\rangle\langle X_m|(\lambda_0^{-1}\mathbf{T})^{|n|}|X_{m+n}\rangle\langle X_{m+n}|0\rangle \,. \end{aligned} \tag{47}$$

As done previously Eq. (47) is expanded as

$$\begin{aligned} P(X_m, X_{m+n}) &= P(X_m)P(X_{m+n}) \\ &+ \langle 0|X_m\rangle\langle X_{m+n}|0\rangle \sum_{\alpha=1}^{p^N-1} \langle X_m|\alpha\rangle\langle\alpha|X_{m+n}\rangle \left(\frac{\lambda_\alpha}{\lambda_0}\right)^{|n|} \,. \end{aligned} \tag{48}$$

From Eq. (48), we see that the two-point joint probability density function for two subsystems separated by n layers, decays toward the product form characterizing statistical independence. The length scale of the decay, is given by the ratio of the two largest eigenvalues, since the terms that has an eigenvector with smaller

eigenvalues are seen to correspond to transients. We can therefore identify the correlation length ξ by

$$\xi = \left(\ln \left| \frac{\lambda_0}{\lambda_1} \right| \right)^{-1} . \tag{49}$$

All equilibrium properties can be obtained from these equations by the standard methods of equilibrium statistical mechanics. In the next section we will generalize these relations to obtain analogous quantities for the eigenstates $|\alpha\rangle$ corresponding to the smaller eigenvalues of $\mathbf{T}$, $|\lambda_\alpha| < \lambda_0$, which as we shall see will yield complex free-energy densities.

4.3 Constrained Transfer Matrix Formalism

In analogy with the expressions for the marginal and joint probability density Eqs. (46) and (47), non-equilibrium constrained probability densities associated with the α-th eigenspace of $\mathbf{T}$ are introduced:

$$\begin{aligned} P_\alpha(X_m) &= |\langle \alpha | X_m \rangle|^2 , \\ P_\alpha(X_m, X_{m+n}) &= \langle \alpha | X_m \rangle \langle X_m | (\lambda_\alpha^{-1} \mathbf{T}_\alpha)^{|n|} | X_{m+n} \rangle \langle X_{m+n} | \alpha \rangle . \end{aligned} \tag{50}$$

The constrained transfer matrices $\mathbf{T}_\alpha$ are constructed from the eigenvalues λ_α and the corresponding eigenvectors $|\alpha\rangle$ of the equilibrium transfer matrix $\mathbf{T}$. The idea is to reweight the eigenstates in a simple way, so that states near equilibrium are suppressed. The matrix $\mathbf{T}_\alpha$ is taken to commute with $\mathbf{T}$ and can be written as

$$\mathbf{T}_\alpha = \sum_{\beta=0}^{p^N-1} |\beta\rangle f_\beta(\alpha) \langle \beta| , \tag{51}$$

where $|\beta\rangle$, $(\beta = 0, \ldots, p^N - 1)$ represent the eigenvectors of $\mathbf{T}$. It was pointed out in Refs. [92, 93, 94] that the constrained marginal probability densities, $P_\alpha(X_m)$ represent actual probability densities of single layer configurations in a constrained state. In order to ensure that the entire system is characterized by $P_\alpha(X_m)$, the matrices $\mathbf{T}_\alpha$ must be chosen so that the constrained joint probability densities satisfy the following set of regularity conditions, see Refs. [75]:

(i) Relation between marginal and joint probability

$$P_\alpha(X_m) = \sum_{\{X_{m+n}\}} P_\alpha(X_m, X_{m+n}) \tag{52}$$

which is satisfied if and only if $f_\beta(\alpha) = \lambda_\alpha$ for $\beta = \alpha$.

(ii) Stochastic independence at infinite separation

$$\lim_{n \to \infty} P_\alpha(X_m, X_{m+n}) = P_\alpha(X_m) P_\alpha(X_{m+n}) , \tag{53}$$

which is satisfied if and only if $|f_\beta(\alpha)| < \lambda_\alpha$ for all $\beta \neq \alpha$ and $f_\alpha(\alpha) = \lambda_\alpha$. This condition ensures that the spatial correlation in the constrained system converge with distance to values consistent with stochastic independence.

(iii) Non-ambiguity for n=0

$$P_\alpha(X_m, X_{m+n}) = P_\alpha(X_m) , \tag{54}$$

which is satisfied if and only if $f_\beta(\alpha) \neq 0$ for all β and α. This is equivalent to requiring that those eigenvectors $|\beta\rangle$ for which $f_\beta(\alpha)$ are nonzero form a complete basis for the layer configuration space. Physically the requirement means that fluctuations into configurations which has nonzero projections onto the subspace with $|\lambda_\beta| > |\lambda_\alpha|$ are not forbidden.

(iv) Reduction to the equilibrium case

$$P_{\alpha=0}(X_m, X_{m+n}) = P(X_m, X_{m+n}) , \tag{55}$$

which is satisfied if and only if $f_\beta(\alpha) = \lambda_\beta$ for $\alpha = 0$. These conditions are satisfied by the following form, although $\mathbf{T}_\alpha$ is not uniquely defined by them:

$$\mathbf{T}_\alpha = \sum_{\beta=0}^{\alpha} |\beta\rangle \frac{\lambda_\alpha^2}{\lambda_\beta} \langle\beta| + \sum_{\beta=\alpha+1}^{p^N-1} |\beta\rangle \lambda_\beta \langle\beta| \,. \tag{56}$$

Note that, from Eq. (56) the constrained transfer matrix $\mathbf{T}_\alpha$, can only be constructed if $\lambda_\beta \neq 0$ for all $\beta < \alpha$. For $\alpha = 0$ it is obvious from Eq. (56) that $\mathbf{T}_\alpha$ reduces to the equilibrium transfer matrix.

We are now in position to define constrained, generalized thermodynamic quantities [75, 95]. The internal-energy density U_α is given by

$$U_\alpha = \frac{1}{N} \sum_{|X\rangle,|X'\rangle} \langle\alpha|X\rangle \left[\langle X|\lambda_\alpha^{-1}\mathbf{T}_\alpha|X'\rangle \langle X|\mathcal{H}_{\mathrm{I}}^{\mathrm{op}}|X'\rangle\right] \langle X'|\alpha\rangle \,, \tag{57}$$

where $\mathcal{H}_{\mathrm{I}}^{\mathrm{op}}$ is the interaction part of the layer Hamiltonian. The order parameter $\mathcal{M}_\alpha$, which is the conjugate to the H-field is given by

$$\mathcal{M}_\alpha = \frac{1}{N} \sum_{|X\rangle} \langle\alpha|X\rangle \langle X|M^{\mathrm{op}}|X\rangle \langle X|\alpha\rangle \,, \tag{58}$$

where M^{op} is the magnetization operator acting on the layer configuration $|X\rangle$. The constrained entropy density $\mathcal{S}_\alpha$ is defined in analogy with that of a stationary ergodic Markov information source [96] and it is given by

$$\mathcal{S}_\alpha = -\frac{1}{N} \sum_{|X\rangle,|X'\rangle} \langle\alpha|X\rangle \left[\langle X|\lambda_\alpha^{-1}\mathbf{T}_\alpha|X'\rangle \ln\langle X|\lambda_\alpha^{-1}\mathbf{T}_\alpha|X'\rangle\right] \langle X'|\alpha\rangle \,, \tag{59}$$

where ln is the principal branch of the complex logarithm. The branch cut is taken along the negative real axis, so that the domain of $\ln(z)$ is $|z|>0$, $-\pi<\arg(z)\leq\pi$. In analogy with equilibrium thermodynamics the free-energy density associated with the eigenstate $|\alpha\rangle$ is defined by

$$f_\alpha = U_\alpha - H\mathcal{M}_\alpha - T\mathcal{S}_\alpha \,. \tag{60}$$

Combining Langer's result (Eq. (29)) with the Van't Hoff-Arrhenius law (Eq. (38)), we expect the imaginary part of the free-energy density f_α from Eq. (60), for $\alpha \geq 1$ to be related to the free-energy cost of creating a nucleating droplet

$$\mathrm{Im} f_\alpha \propto e^{-\beta\Delta F} \,. \tag{61}$$

4.4 The Long Range Blume-Capel Model

In this section, we define a Blume-Capel model with weak, long-range interactions, and we calculate the zero-temperature phase diagram and the finite-temperature spinodal surfaces. The long-range Blume-Capel model consists of a one-dimensional chain of L layers or subsystems, each containing N spins $s_{i,n} = \{0, \pm 1\}$, where the index $i = 1, \ldots, L$ runs over the layers, and the index $n = 1, \ldots, N$ runs over the spins in a given layer. The spin-spin interaction is ferromagnetic $J/N>0$; D is an applied field that either favors ($D>0$) or disfavors ($D<0$) $s_{i,n} = 0$, and H is an applied magnetic field. We introduce the following quantities,

$$\begin{aligned} m_i &= \frac{M_i}{N} = \frac{1}{N}\sum_{n=1}^{N} s_{n,i} \\ q_i &= \frac{Q_i}{N} = \frac{1}{N}\sum_{n=1}^{N} s_{n,i}^2 \,, \end{aligned} \tag{62}$$

which are the magnetization density and the density of nonzero spins in column i, respectively. We impose periodic boundary conditions that is $m_{L+i}=m_i$ and $q_{L+i}=q_i$. The Hamiltonian for the long-range Blume-Capel model can then be written as

$$\mathcal{H} = -JN\sum_{i=1}^{L} m_i m_{i+1} + DN\sum_{i=1}^{L} q_i - HN\sum_{i=1}^{L} m_i \,, \tag{63}$$

For $D\to-\infty$, it follows that $q_i = 1$ and the long-range Blume-Capel model becomes identical to the Q1DI model discussed in the Sec. 4.1. In the mean-field calculation, we assume that the configurations of the system are translationally invariant, so that $m_i=m$ and $q_i=q$ for all columns $i=1,\ldots,L$. With this simplification, we can define a mean-field Hamiltonian $\mathcal{H}^{\mathrm{MF}}$ for the energy density as

$$\mathcal{H}^{\mathrm{MF}} = -Jm^2 + Dq - Hm \,. \tag{64}$$

In the limit $N\to\infty$, the densities m and q take on continuous values in a domain $\Omega=\{(q,m) : 0\le q\le 1, |m|\le q\}$, which defines an isosceles triangle in (q,m) space.

Before solving this mean-field model in general, let us look at its zero-temperature properties. In Fig. 14 the zero-temperature phase diagram is shown. The three stable states are $(q,m) = (0,0)$, $(1,-1)$ and $(1,1)$, which are located at the vertices of the domain Ω. In the following discussion we denote these states as (0), (−), and (+), respectively.

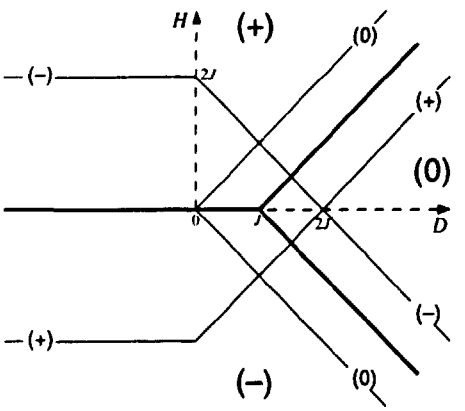

Figure 14. The zero-temperature phase diagram for the long-range Blume-Capel model. The thick solid lines are the first-order equilibrium transition lines, which divide the (D,H) plane into three regions, with stable phases (0) (+), and (−). The thin lines indicate the zero-temperature spinodals for each of the metastable phases.

The thick solid lines in Fig. 14 are first-order transition lines, which separate the (D,H) plane into three distinct regions, each corresponding to one stable phase, as indicated in the figure. The transition lines are found from a simple energy argument. From the mean-field Hamiltonian Eq. (64) we can calculate the energy of the three stable phases: $\mathcal{H}^{\mathrm{MF}}(0)=0$, $\mathcal{H}^{\mathrm{MF}}(+) = D - H - J$, and $\mathcal{H}^{\mathrm{MF}}(-) = D + H - J$. By equating these energies we obtain the transition lines. It follows from this argument that the three states have equal energy at $(D,H,T)=(J,0,0)$. The three states can also exist as metastable states for certain values of D and H outside the region where they are stable. The reason for this is that as we cross a transition line by changing the fields D and H, the previous global minimum of $\mathcal{H}^{\mathrm{MF}}$ remains as a local minimum. As we increase the fields further, we eventually reach a spinodal line where the local minimum in $\mathcal{H}^{\mathrm{MF}}$ coincides with a saddle

point, and the metastable state thus becomes unstable. The spinodal lines can be calculated by a simple stability analysis, in which we expand $\delta\mathcal{H}$ in terms of δq and δm around the stationary states and require that $\delta\mathcal{H}=0$. The spinodal lines shown in Fig. 14 are all second-order non-equilibrium transition lines. We obtain for the (0)-spinodal lines $H=\pm D$ ($D\geq 0$), for the (−)-spinodal lines $H=2J$ ($D\leq 0$) and $H = 2J - D$ ($D\geq 0$). The (+)-spinodal lines are the reflection of the (−)-spinodal lines about the D-axis.

At finite temperature the entropic contribution has to be taken into account, so the first-order phase boundaries and spinodal surfaces have to be calculated from the free energy. The mean-field free-energy-density functional can be calculated for a given m and q using the relation $\mathcal{F}^{\mathrm{MF}} = \mathcal{H}^{\mathrm{MF}} - T\mathcal{S}^{\mathrm{MF}}$, where $\mathcal{S}^{\mathrm{MF}}$ is the micro-canonical entropy density of the system. This entropy density is defined by $\mathcal{S}^{\mathrm{MF}}=(1/N)\ln g(M,Q)$, where $g(M,Q)$ is the multiplicity of spin configurations in a specific column corresponding to given values of M and Q. A simple combinatorial argument yields

$$g(M,Q) = \binom{N}{(Q+M)/2}\binom{N-(Q+M)/2}{(Q-M)/2}, \tag{65}$$

where the brackets denote the binomial coefficients. It was shown in paper IV, that in the limit $N\to\infty$, the mean-field free-energy density is given by

$$\begin{aligned}\mathcal{F}^{\mathrm{MF}} &= -Jm^2 - Hm + Dq + \frac{1}{2}T[2(1-q)\ln(1-q)\\ &\quad + (q+m)\ln(q+m) + (q-m)\ln(q-m) - 2q\ln 2]\,.\end{aligned} \tag{66}$$

In the limit $D\to-\infty$, Eq. (66) reduces to the corresponding Q1DI result Eq. (31) as expected. The equilibrium free-energy density is obtained from the global minimum of $\mathcal{F}^{\mathrm{MF}}$ within the domain Ω. By setting the partial derivatives of $\mathcal{F}^{\mathrm{MF}}$ with respect to both m and q equal to zero and defining an effective field $H_{\mathrm{eff}}=H+2Jm$, we obtain the stationarity condition as a pair of coupled equations:

$$q = \frac{m}{\tanh(H_{\mathrm{eff}}/T)} \tag{67}$$

and

$$\left[1+\frac{1}{4}\exp(2D/T)\right]q^2 - 2q + \frac{1}{4}\exp(2D/T)m^2 + 1 = 0\,. \tag{68}$$

By combining the two equations, we can write the stationarity condition as an equation only in m:

$$m = \frac{2\sinh(H_{\mathrm{eff}}/T)}{\exp(D/T) + 2\cosh(H_{\mathrm{eff}}/T)}\,. \tag{69}$$

Equations (67) and (68) are identical to the expressions found by Blume *et al.* [74]. Their common solution cannot generally be obtained in closed form. A schematic drawing of the mean-field equilibrium phase diagram can be found in Griffiths [97].

In order to calculate the spinodal surfaces, we require that the local minimum of $\mathcal{F}^{\mathrm{MF}}$ that corresponds to the metastable state is also a point of inflection. This criterion is satisfied if we require, in addition to the vanishing of the partial derivatives of $\mathcal{F}^{\mathrm{MF}}$ with respect to both m and q, that the determinant of the Hessian matrix is zero:

$$\begin{vmatrix} \mathcal{F}^{\mathrm{MF}}_{mm} & \mathcal{F}^{\mathrm{MF}}_{qm} \\ \mathcal{F}^{\mathrm{MF}}_{mq} & \mathcal{F}^{\mathrm{MF}}_{qq} \end{vmatrix} = 0\,, \tag{70}$$

where the subscripts denote partial derivatives with respect to the subscripted variables. Inserting Eq. (66) for $\mathcal{F}^{\mathrm{MF}}$ into Eq. (70), we obtain

$$2Jm^2 - 2Jq + T = 0\,. \tag{71}$$

The spinodal field is obtained by the simultaneous solution of Eqs. (67), (68), and (71), as a relation between D, H, and T. We start by using Eq. (71) to eliminate q from Eq. (68), which gives

$$m^4(16-4\eta)+m^2[-32+4\eta+(16-4\eta)T/J]+16-16T/J+(4-\eta)(T/J)^2 = 0, \quad (72)$$

where $\eta=\exp(2D/T)$. This quadratic equation in m^2 yields four solutions for m,

$$m = \pm\sqrt{\frac{1}{2}\left[\frac{4 \pm \sqrt{4(1-2T/J)\eta^2+8\eta T/J}}{4-\eta} - T/J + 1\right]}, \quad (73)$$

which we will denote $\pm m_+$ and $\pm m_-$. To get the functional relation between the fields, we use Eq. (71) again to eliminate q from Eq. (67). Isolating H from the result gives

$$H = -2Jm + T\tanh^{-1}\left[\frac{m}{m^2+T/2J}\right]. \quad (74)$$

The expression for the H-field in Eq. (74) reduces to the Q1DI result given in Eq. (32) in the limit $D\to-\infty$. This can be seen by noting that $q = m^2 + T/2J \to 1$ for $D\to-\infty$. By inserting the solution for the magnetization of Eq. (73) into Eq. (74) we obtain the desired expression for the spinodal H-field in terms of the D-field and temperature T.

A three-dimensional plot of the spinodal surface in (D, H, T) space, calculated from the above relation, is shown in Fig. 15. It is symmetric under reflection

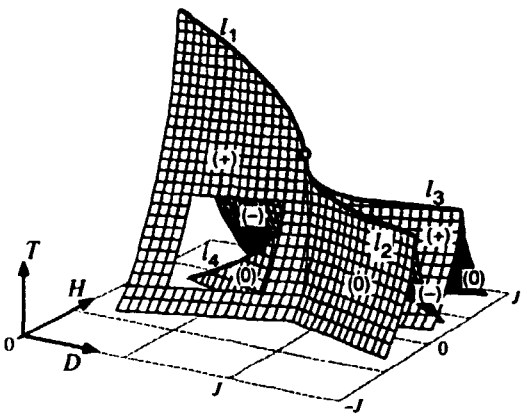

Figure 15. The spinodal surface, shown in (D, H, T) space. The whole surface is symmetric under reflection in the plane $H=0$. Only the portion for $T/J \geq 1/12$ is shown, floating above the grid at $T=0$. The two sheets that merge along the line l_1 are the (+)-spinodal in front, and the (−)-spinodal in back. This line of critical points terminates at the tricritical point $(D_t/J, H_t/J, T_t/J)=(4\ln 2/3, 0, 2/3)$, which is marked with a circle. The sheets that merge along the line l_2 are the (0)-spinodal in front and the (−)-spinodal in back. For the sheets merging along the line l_3 we have the (0)-spinodal in back and the (+)-spinodal in front. The two (0)-spinodal sheets intersect and cross the (+)- and (−)-spinodal surfaces, and merge along the line l_4. This line connects the point $(D, H, T) = (0, 0, 0)$ with the tricritical point.

about the plane $H=0$, due to the symmetry of the Hamiltonian Eq. (63) under the transformation $(s_{n,i}, H)\to(-s_{n,i}, -H)$. Due to the singular behavior of Eq. (74) at $T=0$, the bottom edge of the surface pictured lies at $T/J=1/12$. At $T=0$, the spinodal surfaces are anchored to the zero-temperature spinodal lines shown in Fig. 14. Starting from large positive D, we have four spinodal sheets corresponding

to the four solutions. These are indicated at the right-hand side of the figure. The (0)-spinodal sheets in front and in back merge with the (−)- and (+)-spinodal sheets along the lines l_2 and l_3, respectively. Below we obtain analytic expressions for the lines l_1, l_2, l_3, and l_4, including the tricritical point where all four lines meet. As we reduce D past $D=2J$, the (+)- and (−)-spinodal sheets intersect and cross. The line of intersection becomes l_1 above the tricritical point. The (0)-spinodal sheets pass inside the (+) and (−) sheets and merge along the line l_4, as can be seen through the rectangular window in the (+) sheet.

Obtaining analytical expressions for the four lines of critical points is quite simple using Eq. (73) for the spinodal magnetizations. The lines are parameterized by the appropriate critical temperature T_c. The line l_1 is derived by setting $m_-=0$ yielding

$$l_1 : \begin{cases} D_c = T_c \ln\left[\frac{3\cdot 2J - T_c}{T_c}\right] \\ H_c = 0 \end{cases} \tag{75}$$

for $2/3 \le T_c/J \le 2$. Similarly, l_2 is obtained from the condition $m_- = m_+$:

$$l_2 : \begin{cases} D_c = \frac{T_c}{2} \ln\left[\frac{8T_c}{2T_c - J}\right] \\ H_c = -2J\sqrt{-3T_c/2J + 1} + T_c \tanh^{-1}\left[\frac{\sqrt{-3T_c/2J+1}}{-T_c/J+1}\right] \end{cases} \tag{76}$$

for $1/2 \le T_c/J \le 2/3$. The line l_3 is the mirror image of l_2 about the plane $H=0$. The line l_4 is determined by setting $m_-=0$ as was the case for l_1. The result for l_4 is given in Eq. (75) for $0 \le T_c/J \le 2/3$ and it is a continuation of l_1 below the tricritical point. The magnetization m_c along the lines of critical points is easily found using Eq. (73). Along l_1 and l_4 obviously $m_c=0$, since $H=0$ along these lines, whereas along l_2 and l_3 we have $m_c^2 = 1 - 3T_c/2J$. The tricritical point is found as the intersection of the lines l_1 and l_2: $T_t/J = 2/3$, $D_t/J = 4\ln(2)/3$ and $H_t = 0$. These analytic expressions for the critical lines agree with the results obtained by Blume *et al.* [74], which were derived from the Landau expansion of the free energy to sixth order.

In Fig. 16 the region of competing metastability at a temperature $T/J = 0.25$ (well below T_t) is shown. The thick solid lines are first-order transition lines, and the thin solid lines are spinodal lines. The figure is similar to the zero-temperature phase diagram in Fig. 14, except for the curvature in the (0)-spinodals near $H=0$. The lines separate the (D, H) plane into 17 regions, in each of which we have drawn the free-energy-density functional schematically along the most probable mean-field escape path, or mean-field reaction path (MFRP), joining the three states. Since the MFRP must go through the saddle points of $\mathcal{F}^{\mathrm{MF}}$, it can be shown from the stationarity condition of Eq. (68) that, for the range of fields shown on the figure, each MFRP is very close to the border of Ω defined by $q = \pm m$. The global minimum represents the equilibrium phase, whereas the remaining local minima represent metastable states. For the D and H values inside the large central diamond-shaped region, two competing metastable states are present. As we cross a spinodal line, the metastable state associated with that spinodal vanishes. The thick dotted lines indicate where the free-energy functional for two competing metastable states become degenerate. The thin dotted line for $H \ge 0$ indicates points where the barrier heights $\Delta\mathcal{F}^{\mathrm{MF}}_{(-)-(0)}$ and $\Delta\mathcal{F}^{\mathrm{MF}}_{(0)-(+)}$ are equal, and analogously for the dotted line for $H \le 0$. All lines except the exactly obtained spinodal lines have been calculated numerically from Eq. (66) since they involve finding the extrema of $\mathcal{F}^{\mathrm{MF}}$, which has not been done in closed form.

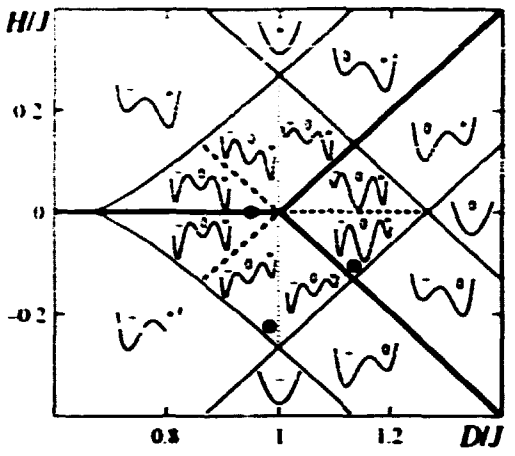

Figure 16. Finite-temperature phase diagram, showing the region of competing metastability, where the spinodal and equilibrium surfaces intersect the plane $T/J = 0.25$. Thick solid lines represent the first-order equilibrium transition lines; and thin solid lines show the spinodal lines. The thick dashed lines represent transitions between two metastable states, and the dotted vertical line is the locus of equal barrier heights. In each separate region, the free-energy-density functionals are drawn schematically along the mean-field reaction path. The global minimum corresponds to the stable phase, and local minima represent metastable states. Solid points indicate parameter sets for which dynamical Monte Carlo simulations of the decay of metastable states were performed (see paper IV).

4.5 Transfer-matrix Results

We will apply the formalism described in Sec. 4.3 to the long-range Blume-Capel model Hamiltonian of Eq. (63). From the definition in Eq. (62) it follows that $M_i = \langle N_i | M^{op} | N_i \rangle$ and $Q_i = \langle N_i | Q^{op} | N_i \rangle$. The layer Hamiltonian matrix element is written in the symmetrized form

$$\langle N_i | \mathcal{H}^{op} | N_{i+1} \rangle = -\frac{J}{N} M_i M_{i+1} + \frac{D}{2}(Q_i + Q_{i+1}) - \frac{H}{2}(M_i + M_{i+1}) , \qquad (77)$$

so that we obtain a symmetric transfer matrix from Eq. (42). As can be seen from Eq. (77) the layer Hamiltonian is invariant under all permutations of the individual spins, since it only depends on the total magnetizations, M_i and M_{i+1}, and the total numbers of nonzero spins, Q_i and Q_{i+1}. This implies that the transfer matrix can be contracted to a reduced basis set consisting of states $|M_i Q_i\rangle$, as described in detail in paper IV. The dimension of the contracted transfer matrix is easily seen to be

$$\dim = \sum_{Q=0}^{N} (Q+1) = \frac{1}{2}(N+1)(N+2) , \qquad (78)$$

and the elements of the contracted transfer matrix are given by

$$\langle MQ|\mathbf{T}|M'Q'\rangle = \sqrt{g(M,Q)g(M',Q')} \times \exp\left(-\beta\left[-\frac{J}{N}MM' + \frac{D}{2}(Q+Q') - \frac{H}{2}(M+M')\right]\right) , \qquad (79)$$

where $g(M,Q)$ is the multiplicity factor given in Eq. (65). The internal-energy density U_n is given by

$$U_n = -\frac{J}{N^2} \sum_{|MQ\rangle |M'Q'\rangle} MM' \langle \alpha | MQ \rangle \langle MQ | \lambda_\alpha^{-1} \mathbf{T}_n | M'Q' \rangle \langle M'Q' | \alpha \rangle . \qquad (80)$$

In the Blume-Capel model we have two fields, H and D. Consequently we have two field contributions in addition to the interaction part of the Hamiltonian. The order parameter $\mathcal{M}_\alpha$, which is the conjugate to the H-field is given by

$$\mathcal{M}_\alpha = \frac{1}{N} \sum_{|MQ\rangle} M \, |\langle MQ|\alpha\rangle|^2 \quad . \tag{81}$$

Similarly the order parameter conjugate to the D-field is given by

$$\mathcal{Q}_\alpha = \frac{1}{N} \sum_{|MQ\rangle} Q \, |\langle MQ|\alpha\rangle|^2 \quad . \tag{82}$$

The expression for the constrained entropy $\mathcal{S}_\alpha$ is given by

$$\begin{aligned} \mathcal{S}_\alpha &= -\frac{1}{N} \sum_{|MQ\rangle} \sum_{|M'Q'\rangle} \langle \alpha|MQ\rangle \\ &\times \left[\langle MQ|\lambda_\alpha^{-1}\mathbf{T}_\alpha|M'Q'\rangle \ln \left(\frac{\langle MQ|\lambda_\alpha^{-1}\mathbf{T}_\alpha|M'Q'\rangle}{\sqrt{g(M,Q)g(M',Q')}} \right) \right] \langle M'Q'|\alpha\rangle \quad . \end{aligned} \tag{83}$$

In addition to the fact that the transfer matrix $\mathbf{T}$ is invariant under the spin permutations, which led to the above contraction, other more complex symmetries may be present. This is the case for the long-range Blume-Capel model since we have shown in paper IV, that the rank of the matrix is $(2N+1)$, which is much smaller than the dimension of the contracted matrix. This means that most of the eigenvalues are zero, and that the matrix can be reduced further by projecting out the null space. This further reduction is important, since in order to define the CTM it suffices to diagonalize the reduced matrix. In the numerical computation a reduction of the matrix size from $(N+1)(N+2)/2$ to $(2N+1)$ is obviously a great advantage, because much larger system sizes can be studied.

The numerical calculations proceed by using Eq. (79) to set up a symmetric transfer matrix. This matrix is then reduced to a $(2N+1)\times(2N+1)$ matrix preserving its symmetry, and diagonalized. The constrained transfer matrices $\mathbf{T}_\alpha$ $(\alpha=0,\ldots,2N)$ are constructed from the eigenvalues λ_α and eigenvectors $|\alpha\rangle$ using the definition given in Eq. (56). Using this form for $\mathbf{T}_\alpha$ we calculated the constrained free-energy densities

$$f_\alpha = U_\alpha - H\mathcal{M}_\alpha + D\mathcal{Q}_\alpha - T\mathcal{S}_\alpha \, , \tag{84}$$

using Eqs. (80)-(83). In Figs. 17 and 18, the real and imaginary parts of the constrained free energies are shown as functions of the D-field for $0.6 \le D/J \le 1.4$ for $N=18$ and $H/J=0.1$ at $T/J=0.25$, giving rise to a total of 37 branches. By drawing a line segment in Fig. 16 representing the D-scan, we obtain values of D corresponding to the following transitions: $D_1/J \approx 0.82$ for the (0)-spinodal, $D_2/J \approx 0.90$ for the exchange of metastable states, $D_3/J \approx 0.99$ for the equal barrier height, $D_4/J \approx 1.10$ for the equlibrium transition, $D_5/J \approx 1.17$ for the (−)-spinodal, and $D_6/J \approx 1.37$ for the (+)-spinodal. These values are indicated as vertical lines. In Fig. 17 we show $\mathrm{Re} f_\alpha/J$ together with bold curves indicating the mean-field results for the stable, metastable and unstable states. The states can be identified from the slopes of their branches due to the identity

$$-\frac{T}{N} \frac{\partial \ln|\lambda_\alpha|}{\partial D} = \mathcal{Q}_\alpha \, . \tag{85}$$

Thus both the (+) and the (−) branches have slopes near unity, while the (0) state has a slope near zero. For $D \le D_4$, the (+) state is stable, while for $D \ge D_4$, it remains metastable until the (+)-spinodal at $D=D_6$. The thick line parallel to the (+) branch is the (−) branch, which terminates at the (−)-spinodal at $D=D_5$. The horizontal thick line is the (0) state, which is metastable for $D_1 \le D \le D_4$ and

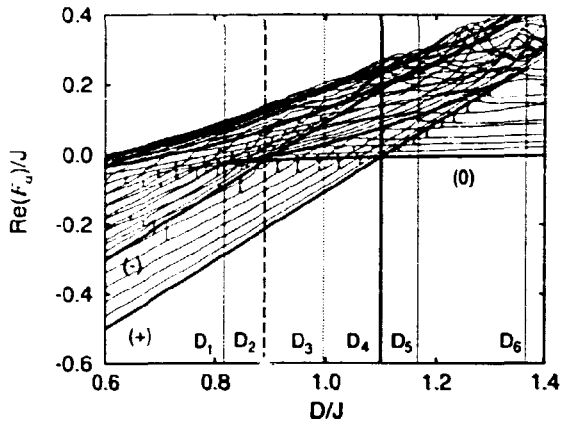

Figure 17. The real parts of the constrained free-energy density $\mathrm{Re}f_\alpha/J$ *for* $N=18$, $H/J=0.1$, *and* $T/J=0.25$, *shown as a function of* D/J *for* $0.6\leq D/J\leq 1.4$. *The vertical transition lines are the (-) spinodal at* $D_1/J\approx 0.82$, *the exchange of metastable states at* $D_2/J\approx 0.90$, *the line of equal barrier heights at* $D_3/J\approx 0.99$, *the equilibrium transition at* $D_4/J\approx 1.10$, *the (−)-spinodal at* $D_5/J\approx 1.17$, *and the (+)-spinodal at* $D_6/J\approx 1.37$. *Also included are bold curves representing the stationary points of the mean-field free-energy functional. The virtually straight lines correspond to the stable and metastable states (0), (+), and (−), and the upward-concave curves represent the uniform unstable stationary points.*

stable for $D>D_4$. Exchange of the metastable (−) state and the metastable (0) state occurs at $D=D_2$, as seen by the crossing of the two corresponding thick lines.

The imaginary part of the constrained free energy $\mathrm{Im}f_\alpha$ is shown on a logarithmic scale in Fig. 18. The data extends over 55 decades. The solid lines for

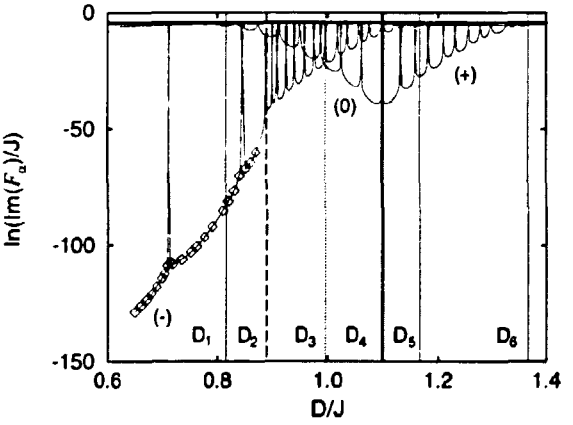

Figure 18. The imaginary parts of the free-energy density $\mathrm{Im}f_\alpha/J$ *shown on a logarithmic scale. The parameters are the same as in Fig. 17, and the vertical lines have the same meaning. The lobe structures correspond to different metastable states. Diamonds are data points obtained using extended numerical precision (128 bit). See the detailed description in the text.*

$\ln(\mathrm{Im}f_\alpha/J)\geq -60$ were calculated with 64-bit precision on a HP9000/735 workstation. Extended precision (128-bit) was used for the remaining parts. These data points, shown as diamonds, were calculated on a Cray Y-MP/432 supercomputer. The lobe structure is identified as follows. The set of lobes which increase in value with increasing D for $D_4\leq D\leq D_6$ corresponds to the (+) metastable state, whereas

those that decrease in value for $D_1 \leq D \leq D_4$ correspond to the (0) metastable state. The remaining lobes for $D \leq D_5$ correspond to the (−) metastable state. Note that the lobe structures corresponding to the (−) and (0) metastable states intersect at $D \approx D_3$, which is approximately equidistant from the (−)- and (0)-spinodals, as can be seen in Fig. 16. The barrier heights $\Delta F_{(-)\to(0)}$ and $\Delta F_{(0)\to(+)}$ are therefore equal to leading order in the expansion about the spinodals, just as their mean-field counterparts $\Delta \mathcal{F}^{\mathrm{MF}}$, even though the H-field dependence for the mean-field barriers are quite different. Further, we have for $D_1 < D < D_3$, $\Delta F_{(-)\to(0)} > \Delta F_{(0)\to(+)}$ and $\mathrm{Im} f_{(-)} < \mathrm{Im} f_{(0)}$, whereas for $D_3 < D < D_5$ we have $\Delta F_{(-)\to(0)} < \Delta F_{(0)\to(+)}$ and $\mathrm{Im} f_{(-)} > \mathrm{Im} f_{(0)}$. These results give strong evidence that $\mathrm{Im} f_\alpha$ for the metastable state is related to the free-energy barrier height involved in the transition in agreement with Eq. (61). More quantitative evidence was given in paper IV where we applied finite-range scaling to $|\mathrm{Im} f_\alpha|$. We found good agreement between the finite-range scaling of $|\mathrm{Im} f_\alpha|$ and the free-energy barrier height. Further evidence is given by the sudden change in behavior for the (−) metastable branch at $D = D_2$. This can be explained by the fact that the magnetization profile of the critical droplet undergoes a drastic change as one metastable state becomes more favored than the other. For $D_2 < D < D_4$, the critical droplet is one through which the (−) metastable state decays into the (0) metastable state before it has a chance to decay finally to the stable state. However, for $D_1 < D < D_2$, the (0) metastable state becomes too costly for a system in the (−) metastable state to decay into it, so the critical droplet is one that allows the (−) metastable state to pass directly to the stable state. This droplet is somewhat larger and hence more costly to form.

4.6 Discussion

We have studied an extension of the Blume-Capel model to include weak, long-range interactions. The reason being that for a certain field-range a region with two competing metastable states exist, but also that the model is simple enough to allow extensive symmetry reduction of the transfer matrix. An exact analytic expression for the four sheets, which constitute the spinodal surface has been obtained. By analytic continuation of the equilibrium free-energy density $\mathcal{F}$ near the spinodal we have calculated the free-energy cost ΔF of creating a nucleating droplet in the Q1DI model. However, the formula remains valid for the long-range Blume-Capel model provided that γ is replaced by $\gamma = 8 m_{\mathrm{sp}} J^2 (m_{\mathrm{sp}}^2 - 1 + 3T/2J)/T$. Thus it follows that the dominant H-field dependence scales as $|H - H_{\mathrm{sp}}|^{5/4}$, also in this case.

The study of metastability via the constrained transfer matrix formalism is particularly attractive. One reason is that the real part of the constrained free-energy density $\mathrm{Re} f_\alpha$ display branches, which in the intervals between crossings correspond to the metastable states. Thus the associated eigenvectors represent spin configurations that show important characteristics of metastability. In addition, the metastable states, are uniquely characterized by the extreme smallness of the imaginary part of the constrained free-energy density $\mathrm{Im} f_\alpha$. We have demonstrated that for any pure metastable state, the value of $|\mathrm{Im} f_\alpha|$ is in agreement with the Van't Hoff-Arrhenius law for the decay rate of that particular metastable state. Another reason is, that in the case where two metastable states are present as in the long-range Blume-Capel model, the CTM method gives a distinct value for $|\mathrm{Im} f_\alpha|$ for each state, which can easily be continued through points where these states are degenerate. The usual procedure of analytic continuation of the free energy [7], on the other hand, has no mechanism for distinguishing coexisting metastable states, and thus gives an imaginary part related only to the lowest activation barrier separating any one of the coexisting states and the equilibrium state.

5 Driven Lattice Gas Models

A unifying theory which explains $1/f$-noise in temporal fluctuating signals is still lacking. Recently Bak, Thang, and Wiesenfeld [8, 98, 99] introduced a new concept, which they called self-organized criticality (SOC), which was an attempt to find such a theory. They used a cellular automaton, to illustrate the idea, but unfortunately, the model turned out to have an $1/f^2$ power spectrum [20, 21, 100]. Later a deterministic lattice gas model [101], very much in the spirit of the self-organized-critical models studied by Bak, Thang, and Wiesenfeld, was shown to have $1/f$-noise when driven by a white noise boundary condition.

In this chapter we will discuss the deterministic lattice gas model, based on the results of paper V. Two versions of the model are studied. In one case we consider a finite open system in which particles are injected stochastically. In the other case we use periodic boundary conditions. In both cases the power spectrum of the density fluctuations $S(f)$ and the lifetime distribution $D(t)$ display power law scaling, $S(f) \propto 1/f^{\beta}$ and $D(t) \propto 1/t^{\alpha}$, with α=3/2 and β=1. This is remarkable since α=3/2 is the expected behavior of particles as non-interacting random walkers, which gives rise to β=3/2 due to the scaling relation [20] $\alpha + \beta = 3$. The deviation from the scaling relation indicates that important correlations exist between the particles even after many collisions. In order to understand this behavior we have developed a macroscopic theory in the framework of a Langevin description, which reproduces our numerical findings.

Before concentrating on the details of the deterministic lattice gas model, we will briefly introduce the general concept of self-organized criticality. The reason being that the self-organized critical state exhibits scale invariance both spatially and temporally, which immediately implies power law behavior. Following Ref. [102], we will then proceed by analyzing a class of models for dissipative transport in the framework of Langevin equations, which are capable of producing $1/f^{\alpha}$ power spectra for the density fluctuations.

5.1 Introduction

Many phenomena in nature exhibits self-similarity spatially and temporally over a wide range of scales. However a proper understanding of the origin is still lacking. This led Bak, Thang, and Wiesenfeld (BTW) [8] to introduce the concept of self-organized criticality (SOC) as a possible explanation of $1/f$-noise. The idea is that driven systems with many spatial degrees of freedom never reach equilibrium, but rather jump from one metastable state to another. In the words of BTW, the driven system self-organizes into a critical state, which then corresponds to motion on an attractor in phase space, under the random driving force. The important point of SOC is that the "energy release" in the transition from one metastable state to another, is characterized both by spatial and temporal scale invariance. Although scale invariance also arises in the theory of equilibrium phase transitions, the difference is that the driven system self-organizes into the critical state, without the need to fine-tune system parameters. BTW studied a simple cellular automaton (the sand pile model), where the perturbation consists of random addition of sand grains. When the local slope exceeds a threshold value, sand tumbles down the slope, which can trigger additional sand grains *etc.* The energy release considered above was then measured as the total mass involved in an avalanche of sand tumbling down. BTW found that the system indeed evolves into a statistically stationary state, characterized by power law scaling of both the lifetime distribution and the size distribution of the avalanches. The cellular automaton was believed to describe quantitatively the flow of sand in real sand

piles. The applicability of SOC was subsequently questioned by Jaeger *et al.* [103], who performed an experiment on real sand piles and did not find a $1/f$ power spectrum. Later it was shown in Refs. [20, 21, 100] that the power spectrum of the BTW cellular automaton, was mistakenly reported to be $1/f$, but rather behaved as $1/f^2$ in 1,2,3,4, and 5 dimensions. Motivated by a Langevin treatment (see below), Jensen [104] considered the original BTW cellular automaton again, while only perturbing the system at the boundary. In this case the power spectrum behaved as $1/f$.

We will now attempt to describe driven diffusive lattice gas models from a macroscopic point of view in the framework of diffusive Langevin-like equations, Ref. [86]. In a Langevin description, the variables of the system, are separated according to their time scales and wavelengths. The slow varying variables (low frequency, long wavelengths) of the system are typically the order parameter, and other quantities that obey a conservation law. The fast variables (high frequency, small wavelengths) are then taken into account as a noise term, that appears in the Langevin equation, see Eq. (87). The application of such a model to discrete lattice gas models is only valid at a coarse-grained level, where the microscopic motion of the particles has been averaged out. We therefore proceed by coarse graining the discrete occupation numbers, to obtain a local density field $n(\mathbf{r},t)$ which denotes the number density of particles in a volume element around $\mathbf{r}$ at time t and which is continuous in both space and time. The coarse-grained hydrodynamic equations, in which all fluctuations are integrated out, can then be established by considering the symmetries and conservations of the system, and assuming the existence of an appropriate regularity of the problem so that gradient expansions are possible [105]. This leads to partial differential equations like the ordinary diffusion equation, for example, of the form

$$\frac{\partial n(\mathbf{r},t)}{\partial t} = \gamma\nabla^2 n(\mathbf{r},t) + F[n,\nabla n]\,, \tag{86}$$

where $F[n,\nabla n]$ denotes some general function which takes care of higher order terms in the expansion in $n(\mathbf{r},t)$ and $\nabla n(\mathbf{r},t)$. The fundamental problem arises when one wants to account for the remaining fast variables. This is most often done by adding some kind of noise ρ, consistent with the symmetries and conservations of the system, to the right hand side of the diffusion equation

$$\frac{\partial n(\mathbf{r},t)}{\partial t} = \gamma\nabla^2 n(\mathbf{r},t) + F[n,\nabla n] + \rho\,. \tag{87}$$

Generally the nature of the noise term ρ is unknown. Therefore one normally assumes ρ to be a delta function correlated (in-time as well as in-space) Gaussian process [106, 107]. Though power law distributed noise has recently been considered [108], the important point is that the assumed form of the noise term determines the fluctuations of the system described by Eq. (87). This makes it particularly unsatisfactory that we do not know how to determine the form of the fluctuating source term from the microscopic properties of the considered many body system.

We will now analyze a class of linear dissipative transport processes following the discussion of Ref. [102]. We consider a d-dimensional semi-infinite system, where particles are injected at the boundary, move dissipatively through the system and are removed at infinity. Positions are denoted, using the notation of Ref. [102], $\mathbf{r} = (r_\parallel, \mathbf{r}_\perp)$, where $\parallel$ and $\perp$ denote the direction transverse or parallel to the $(d-1)$-dimensional hyperplane at $r_\parallel = 0$. Periodic boundary conditions in the transverse ($\perp$) direction are imposed. We want to drive the system by injecting particles stochastically, so that the density field is fixed at the boundary $r_\parallel = 0$ to $n(r_\parallel = 0, \mathbf{r}_\perp) = \delta(r_\parallel)\eta(\mathbf{r}_\perp, t)$, where η is a white noise random variable, with correlations $\langle\eta(\mathbf{r}_\perp,t)\eta(\mathbf{r}'_\perp,t')\rangle = 2\Gamma\delta(\mathbf{r}_\perp - \mathbf{r}'_\perp)\delta(t-t')$, and Γ is constant. Consider

first the case where the motion in the bulk is deterministic, in which case there is no bulk noise. We allow for a driving force, which pushes the particles from left to right. This introduces an additional term $-\kappa\partial n(\mathbf{r},t)/\partial r_{\|}$ on the right hand side of Eq. (87). For an infinite system we need a constraint, to prevent the density field from growing without bound. The solution suggested in Ref. [102], is to include a pinning term $-r\delta(r_{\|})n(\mathbf{r},t)$, where r is a positive constant. In this context it is important to note that the inclusion of the pinning term is an analytical trick which allows the solution of the Langevin equation to be obtained by a Fourier transformation. A solution without the inclusion of the pinning term is much more complicated and was obtained in Ref. [104], using an explicit formula for the Green's function propagator for a d-dimensional semi-infinite system. The Langevin equation without bulk noise can therefore be written:

$$\frac{\partial n(\mathbf{r},t)}{\partial t} = \gamma\nabla^2 n(\mathbf{r},t) - \kappa\frac{\partial n(\mathbf{r},t)}{\partial r_{\|}} - r\delta(r_{\|})n(\mathbf{r},t) + \delta(r_{\|})\eta(\mathbf{r}_{\perp},t)\,. \tag{88}$$

In the analytical formulas that follows it is convenient to make use of the cyclic frequency ω, related to the frequency f by $\omega = 2\pi f$. The solution of Eq. (88) can be obtained by a Fourier transformation which yields

$$n(\mathbf{k},\omega) = \frac{g_0(\mathbf{k},\omega)\eta(\mathbf{k}_{\perp},\omega)}{1 + rI(\mathbf{k}_{\perp},\omega)}\,, \tag{89}$$

where $g_0(\mathbf{k},\omega) = (-i\omega + i\kappa k_{\|} + \gamma k^2)^{-1}$, and $I(\mathbf{k}_{\perp},\omega) = \int dk_{\|} g_0(\mathbf{k},\omega)/2\pi$. The power spectrum $S(\omega)$ for the total number of particles $N(t) = \int n(\mathbf{r},t)d^d\mathbf{r}$ in the system is defined in terms of the ensemble average of the product $\langle N(\omega)N^*(\omega')\rangle$ as:

$$S(\omega)\delta(\omega - \omega') = \langle N(\omega)N^*(\omega')\rangle\,. \tag{90}$$

The delta function in the definition in Eq. (90) represents the ω=0 component of $N(\omega) = n(\mathbf{k} = 0,\omega)$. Direct evaluation gives

$$S(\omega) = \frac{|\eta(\mathbf{k}_{\perp} = 0,\omega)|^2}{\omega^2}\left|\frac{1}{1 + r(\kappa^2 - 4i\omega\gamma)^{-1/2}}\right|^2\,. \tag{91}$$

From Eq. (91) it follows that if there is no driving force (κ=0) the low frequency behavior is given by $S(\omega) \sim \omega^{-1}$, while if we include a driving force (κ>0) we get $S(\omega) \sim \omega^{-2}$. In the case where the particles move stochastically through the system, a white noise term that conserves the particle number has to be included on the right hand side of Eq. (88). Such a term can be represented as the divergence of a random vector function, $\nabla\cdot\boldsymbol{\eta}(\mathbf{r},t)$, with correlations $\langle\eta_i(\mathbf{r},t)\eta_j(\mathbf{r}',t')\rangle = 2\Gamma\delta_{i,j}\delta(\mathbf{r} - \mathbf{r}')\delta(t - t')$. It can be shown [102], that for (κ=0) this gives $S(\omega) \sim \omega^{-3/2}$, while if ($\kappa$>0) we obtain $S(\omega) \sim \omega^{-2}$ as before.

The exponent 3/2 for the power spectrum in the case of conserving bulk noise can be understood very simply by an elegant argument given in Ref. [109]. For a gas of non-interacting random walkers, the temporal fluctuation in the particle density within a subsystem scales as $\Delta N(\tau) \sim \tau^{1/4}$, since obviously the number of particles involved in diffusion scales with the diffusion length $l_\tau \propto \tau^{1/2}$, and the fluctuations involved for a Gaussian process is just given by the square root. From the Wiener-Khintchin theorem [11] the power spectrum is obtained as the cosine transform

$$S(\omega) = \int d\tau(\Delta N(\tau)^2)\cos(\omega\tau)\,, \tag{92}$$

independent of dimensionality. By counting of powers, we obtain $S(\omega) \sim \omega^{-3/2}$.

5.2 Deterministic Lattice Gas Model

The deterministic lattice gas model, originally proposed in Ref. [101], is constructed to simulate particles which follow Stokesian dynamics. That is, the equation of motion has the form $\eta \mathbf{v} = \mathbf{F}$, where η is the friction coefficient, $\mathbf{v}$ the velocity and $\mathbf{F}$ the total force acting on the particle. Consider a two dimensional lattice with $N_x \times N_y$ sites. We will restrict ourselves to a square lattice *i.e.* $N_x = N_y = N$. Each site can be empty or occupied. Particles on *nearest neighbor* sites repel each other with a central force of unit strength. The dynamics is deterministic and defined in the following way. For each particle we sum up all the forces acting upon the particle in the normal vectorial fashion. If the resulting force is non zero, we move the particle, one lattice site in the direction according to the resulting force (diagonal moves are accepted). In case of competition where two particles which are acted upon by a force of equal strength, wants to move into the same site, none of the particles move. This will be termed the *blocking mechanism*. Finally, if two particles want to move to the same site but are acted upon by a force of unequal strength the particle with the largest force wins. The whole lattice is simultaneously updated. The updating rules are illustrated in Fig. 19 in the case of an 8×8 lattice. The boundary drive acts as a particle reservoir which sets up an external

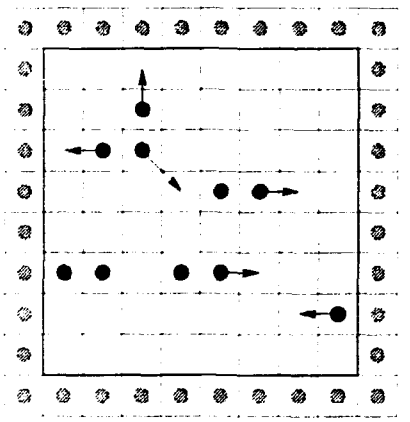

Figure 19. Updating rules for the deterministic lattice gas model. The arrows on the particles indicate where the particles move to in the next iteration. The particles without any arrow do not move. The case where two or more particles want to enter the same site, need special consideration. First, competition between two particles which are acted upon by a force of equal strength, no particle moves. This is shown for the four particles occupying the third row from the bottom. Secondly, if two particles want to move to the same site but are acted upon by a force of unequal strength the particle with the largest force wins, as shown for the particle with the diagonal arrow.

pressure, by occupying the outer boundary by fixed particles (the cross-hatched particles in Fig. 19), which tends to push particles on neighboring sites into the lattice. In each iteration, the particles at the boundary sites (*i.e.* the particles which are nearest neighbor to the cross-hatched particles) are annihilated, and new particles are introduced at all the boundary sites with a probability p per site.

We will now attempt to describe the lattice gas from a macroscopic point of view. The simplest possible description one can think of is a Langevin-like linear diffusion equation. As discussed in Sec. 5.1 we introduce a coarse-grained density

$n(\mathbf{r},t)$, which denotes the number density of particles, in a volume element around r at time t. We will concentrate on two properties, the power spectrum $S(\omega)$ of the total number of particles on the lattice and the lifetime distribution $D(t)$. For a discussion of the correlation function, the reader is referred to paper V. In order to calculate these quantities only the fluctuations in $n(\mathbf{r},t)$ around its average value $\langle n(\mathbf{r},t)\rangle$ enters the calculation. Thus the absolute value of $\langle n(\mathbf{r},t)\rangle$ is irrelevant and for convenience we will take this as zero. The appropriate boundary condition on $n(\mathbf{r},t)$ should be taken such as to mimic the boundary drive on the lattice gas model. In the lattice gas model, the particle density at the boundary varies in a stochastic manner, which is characterized by the lack of long time correlations. Thus it is natural to apply a white noise boundary condition on $n(\mathbf{r},t)$. The diffusion equation should be solved in a bounded region Ω, where $\Omega = \{(x,y)|0 \le x \le L,\ 0 \le y \le L\}$. The side length $L = Na_0$ is measured in units of the lattice spacing a_0. Hence

$$\frac{\partial n(\mathbf{r},t)}{\partial t} = \gamma\nabla^2 n(\mathbf{r},t) + \rho(\mathbf{r},t)\,, \qquad (\mathbf{r}\in\Omega, t>0) \tag{93}$$

$$n(\mathbf{r},t) = \eta(\mathbf{r},t)\,, \qquad (\mathbf{r}\in S, t>0)\,, \tag{94}$$

where S denotes the surface of Ω. The Dirichlet condition consists of fixing $n(\mathbf{r},t)$ to take the value $\eta(\mathbf{r},t)$, which is a white noise boundary term [110]. The solution to Eqs. (93) and (94) can be expressed in terms of the appropriate Green's function $G(\mathbf{r},t|\mathbf{r}_0,t_0)$. The Green's function is the propagator of a pulse at $\mathbf{r}_0\in\Omega$ at time t_0. The causality condition forces $G(\mathbf{r},t|\mathbf{r}_0,t_0) = 0$ when $t < t_0$. The Green's function is a solution to the problem involving an impulsive point source

$$\frac{\partial G(\mathbf{r},t|\mathbf{r}_0,t_0)}{\partial t} - \gamma\nabla^2 G(\mathbf{r},t|\mathbf{r}_0,t_0) = \delta(\mathbf{r}-\mathbf{r}_0)\delta(t-t_0) \quad (\mathbf{r}\in\Omega,\ t>0)\,, \tag{95}$$

where the Green's function should be chosen to satisfy the homogeneous boundary condition $G(\mathbf{r},t|\mathbf{r}_0,t_0) = 0$ when $\mathbf{r}_0\in S_0$ or $\mathbf{r}\in S$. The Green's function is now used to construct the solution for the particle density $n(\mathbf{r},t)$ (see [111] chap. 7). Hence, in general,

$$n(\mathbf{r},t) = \gamma\int_0^t\int_{S_0}[G(\mathbf{r},t|\mathbf{r}_0,t_0)\nabla_0 n(\mathbf{r}_0,t_0) - n(\mathbf{r}_0,t_0)\nabla_0 G(\mathbf{r},t|\mathbf{r}_0,t_0)]\,dS_0dt_0$$
$$+\int_0^t\int_{\Omega_0} G(\mathbf{r},t|\mathbf{r}_0,t_0)\rho(\mathbf{r}_0,t_0)d\Omega_0dt_0 + \int_\Omega G(\mathbf{r},t|\mathbf{r}_0,0)n(\mathbf{r}_0,0)d\Omega_0\,. \tag{96}$$

The third term in Eq. (96) represents the response of a bulk noise term, which we will *disregard* because we are only concerned with the deterministic lattice gas model. The fourth term represents the effect of having an initial condition on $n(\mathbf{r},t)$. However, this can be ignored, because we are only interested in ensemble properties which we assume to be independent of the initial condition. Finally using the homogeneous condition of the Green's function, the first part in the first term vanishes. Hence,

$$n(\mathbf{r},t) = -\gamma\int_0^t\int_{S_0} n(\mathbf{r}_0,t_0)\nabla_0 G(\mathbf{r},t|\mathbf{r}_0,t_0)dS_0dt_0\,. \tag{97}$$

The solution to Eq. (95) may be obtained by the method of eigenfunction expansion, whereby we expand the Green's function on the eigenfunctions to the Laplacian ∇^2 on the domain Ω subject to zero homogeneous Dirichlet condition Ref. [112]. The power spectrum $S(\omega)$ of the total number of particles is evaluated from Fourier transformation of the integrated particle density given by

$$N(\omega) = \int_{-\infty}^{\infty} dt\exp(i\omega t)\int_\Omega d\Omega n(\mathbf{r},t)\,, \tag{98}$$

by inserting Eq. (98) into Eq. (90). For a detailed derivation of the power spectrum, the reader is referred to paper V. We obtain:

$$S(\omega) \simeq \frac{64\pi L^2 p \Delta t}{a_0^2} \left[1 + \frac{\omega^2 L^4}{\pi^4 \gamma^2}\right]^{-1/2} , \tag{99}$$

where Δt is the time unit. We define a characteristic frequency ω_c from Eq. (99) that will be especially important in our subsequent discussion of our computer simulations as follows:

$$\omega_c = \gamma \left(\frac{\pi}{L}\right)^2 . \tag{100}$$

From Eq. (99) it follows that for $\omega \ll \omega_c$, $S(\omega)$ is almost constant which gives rise to white noise, while for $\omega \gg \omega_c$, we obtain $S(\omega) \propto 1/\omega$. Notice that $S(\omega = 0)$ scales with the volume of the system. This is to be expected for the following reasons. The average of the total number of particles on the lattice scales with the volume of the system, *i.e.* $\langle N(t) \rangle \propto L^2$. Hence the fluctuations in $N(t)$ is of the order of $\Delta N(t) \sim \sqrt{\langle N(t) \rangle} \propto L$. The power spectrum is expressible as the cosine transform of $\langle \Delta N(t)^2 \rangle$ (Eq. (92)), and it is seen to scale with L^2. As discussed in Sec. 5.1, it was pointed out that an $1/\omega$ power spectrum would result from a diffusion-like equation without bulk noise [102]. However this analysis was restricted to a semi-infinite system, and does not have the cross-over to white noise at low frequencies. In addition the *ad hoc* inclusion of a pinning term $-r\delta(r_\parallel)n(\mathbf{r},t)$ is not necessary for a finite system. In computer simulations, the finite size behavior is of particular importance because the cross-over frequency ω_c is readily determined and finite-size scaling can be checked.

The behavior of the individual particles can for instance be characterized by the lifetime distribution $D(t)$, which is the ensemble average of the time the particles spend on the lattice from they are injected until they leave. The lifetime distribution can only be calculated in a probabilistic manner, that is to say, we treat the particles as individual random walkers. We consider a delta function spike at $\mathbf{r}_0$ at time $t_0 = 0$ in the particle density, represented by $G(\mathbf{r}, t|\mathbf{r}_0, 0)$, and follow how the particle probability leaks out of the domain Ω. The lifetime distribution is calculated from

$$D(t) = -\frac{\partial}{\partial t} \int_\Omega d\Omega \, G(\mathbf{r}, t|\mathbf{r}_0, 0) . \tag{101}$$

The expression Eq. (101) can be simplified by introducing the diffusion equation Eq. (93) for the partial derivative. Hence,

$$\begin{aligned} D(t) &= -\gamma \int_\Omega d\Omega \, \nabla^2 G(\mathbf{r}, t|\mathbf{r}_0, 0) \\ &= -\gamma \int_S d\vec{S} \cdot \nabla G(\mathbf{r}, t|\mathbf{r}_0, 0) . \end{aligned} \tag{102}$$

The lifetime distribution $D(t)$ is then averaged along the particle injection point $\mathbf{r}_0 \in S_0$. For a detailed derivation of $D(t)$, the reader is referred to paper V. We obtain as an asymptotic expansion

$$D(t) \propto \exp(-2t/t_c) \left(\frac{t}{t_c}\right)^{-3/2} , \tag{103}$$

where $t_c = 1/\omega_c$ is the reciprocal of the cross-over frequency introduced in Eq. (100). From Eq. (103) we see that there exists a region where the lifetime distribution follows an algebraic scaling law with exponent 3/2, independent of lattice size. For times t larger than the characteristic value t_c, the distribution falls off exponentially. This cross-over comes from the finite-size of the system and t_c is seen to scale with the volume of the lattice.

The lifetime distribution and the power spectrum are not independent. In the approximation, where the particles can be considered as independent random walkers, the total number of particles on the lattice $N(t)$ is given as a sum of square-box signals:

$$N(t) = \sum_{\tau_i} f_{\tau_i, t_i}(t - \tau_i) \,, \tag{104}$$

where the box function $f_{\tau_i,t_i}(t-\tau_i)$ contributes with unity to $N(t)$ in the interval $[\tau_i, \tau_i + t_i]$ and zero otherwise. The sum in Eq. (104) corresponds to summation over individual particles injected at $t = \tau_i$ and leaving at $t = t_i + \tau_i$. Evidently the lifetime distribution is given by $D(t) = \sum_i \delta(t - t_i)$. Assuming that the injection times τ_i are uncorrelated, the power spectrum for a random linear superposition of signals, can be calculated by methods analogous to those of the structure factor presented in paper II. In Ref. [20] power law distributed lifetimes $D(t) \propto t^{\alpha}$ was considered. In this work $S(\omega) \sim \omega^{-(3-\alpha)}$, was obtained for $(\alpha > 1)$, and $S(\omega) \sim \omega^{-2}$ otherwise.

5.3 Numerical Results

We have obtained the power spectrum by Fourier transformation of the time signal for the total number of particles on the lattice. In order to obtain sufficient statistics, it is necessary to perform an ensemble average containing several independent runs. In Fig. 20 are shown the power spectra for the lattice gas for different lattice sizes, where the boundary drive is fixed to $p = 10^{-1}$. The power spectra are presented as function of frequency $f = \omega/2\pi$, rather than $S(\omega)$ to conform with usual practice.

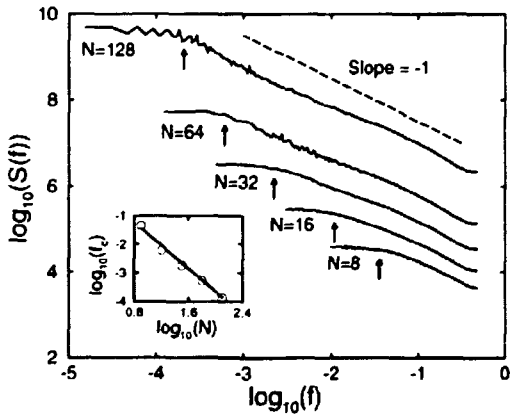

Figure 20. The power spectra $S(f)$ for the deterministic lattice gas model shown for different lattice sizes. It is seen to satisfy algebraic scaling with exponent $\beta = 1$. The cross-over frequency to white noise f_c has been indicated by small arrows, and it follows from the inset that f_c scales inversely with the volume of the system. The boundary drive is fixed to $p = 10^{-1}$ in all simulations.

The power spectrum satisfies an algebraic scaling law $S(f) \propto 1/f^{\beta}$, with the exponent $\beta = 1$. For the largest lattice of size 128×128, the scaling region extends for over almost three orders of magnitude. The deviation from $\beta = 1$ at high frequencies is just an artifact of the finite time resolution, which produces aliasing [113]. The low frequency deviation, is caused by the finite system size, which gives rise to a cross-over to white noise; as the system size increases, the cross-over frequency is reduced. In Eq. (99) the power spectrum was obtained from a linear

Langevin equation. The result showed that the power spectrum should scale as $S(f) \propto 1/f$ for f larger than a characteristic frequency $f_c = \omega_c/2\pi$, which is in good agreement with the computer simulations. From Eq. (100) we see that f_c should scale inversely with the volume of the lattice. The cross-over frequency f_c can be obtained from the numerical simulations in Fig. 20, by locating the characteristic frequency where the power spectrum exhibits a cross-over from $1/f$ noise to white noise, as indicated by the small arrows in Fig. 20. Good agreement with the scaling relation is observed.

The value of the exponent β depends on the strength of the boundary drive. In Fig. 21 the lattice size is fixed to 16×16 while p is varied. As can be seen from the figure, the power spectrum scales as $S(f) \propto 1/f^{\beta}$ at frequencies which are large compared to f_c. However, the exponent exhibits a cross-over from $\beta = 1$ to

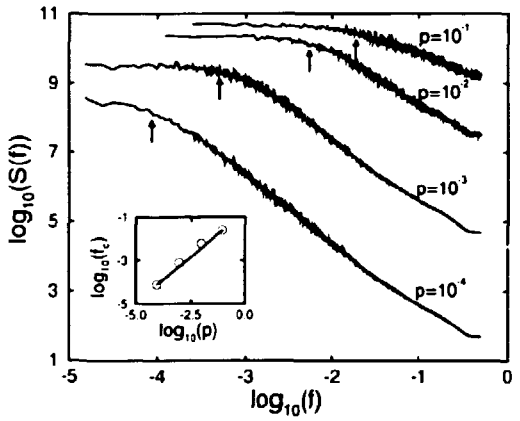

Figure 21. Power spectra $S(f)$ for the deterministic lattice gas model. The boundary drive is varied between $p = 10^{-1}$ and $p = 10^{-4}$. Note that the critical exponent exhibits a cross-over from $\beta = 1$ to $\beta = 2$ as the boundary drive vanishes. The cross-over frequency to white noise f_c has been indicated by small arrows, and it follows from the inset that f_c scales with the boundary drive p. In all simulations we have used a 16×16 lattice.

$\beta = 2$ as the boundary drive is reduced from $p = 10^{-1}$ to $p = 10^{-4}$. This result cannot be explained from the Langevin equation, where we obtained an exponent $\beta = 1$ independently of the free parameters γ and p. Thus, when p is reduced below $p \approx 10^{-2}$, the diffusion equation does not offer an adequate description of the lattice gas. The reason for this breakdown in the diffusive description, can be understood by considering the limit $p \to 0$. As the boundary drive vanishes, no particle needs to have any nearest neighbor, and hence the particle system cannot lower its density further by its own repulsive interactions. The particle system is therefore not able to support density waves across the system. Another way of describing this breakdown, is through the formation of damage clusters. For details the reader is referred to paper V.

The dependence of the cross-over frequency f_c on p can be obtained from Fig. 21. The cross-over frequency is determined as before, and we have indicated f_c with small arrows. We get $f_c \propto p$, which is to be expected from the following simple minded argument. Consider the situation where the boundary drive is reduced from p_1 to p_2. Then the number of particles which is injected into the lattice is reduced by this ratio p_2/p_1. If we now assume that the qualitative behavior of the lattice gas is unaffected, this reduction can be thought of as redefining our time unit by the reciprocal of this ratio. From this the frequency dependence of p follow. It is interesting that f_c continues to be proportional to p with the same

proportionality constant through the region where β changes from 1 to 2.

The lifetime distribution is obtained by labeling the particles, and following them through each iteration. We record the number of iterations each particle survives in a subsystem of the lattice and calculate a histogram. Thus if the particle trajectory is given by $\mathbf{r}(t)$, where $\mathbf{r}(t=0) \in \partial\Omega_{sub}$, we set $t = 0$ when the particle passes over the boundary of the subsystem; the lifetime of the particle is defined as $t' = \max\{t \mid \mathbf{r}(t) \in \Omega_{sub}\}$. In the numerical simulation, there is no need to average over independent runs, because the system itself is self-averaging, in the sense that new particles are continuously supplied at the boundary, which are incorporated in the statistics. It is important to use a subsystem because the activity at the boundary is much higher than the bulk, due to the white-noise boundary condition. This will overestimate $D(t)$ for small values of t, and lead to a too-high value for the α exponent. It should be recognized that the use of subsystems is a computational trick to mask out the initial transient behavior, and that the correct α exponent would show up for large system sizes. In all simulations the subsystem chosen is $\Omega_{sub} = \{(x,y) | L/4 \le x \le 3L/4,\ L/4 \le y \le 3L/4\}$. In Fig. 22 is shown the lifetime distribution $D(t)$ for different subsystem sizes. The

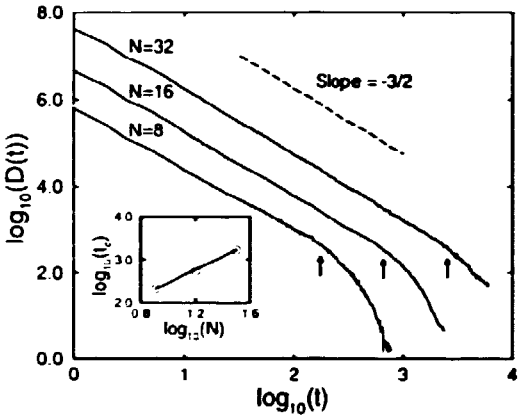

Figure 22. The lifetime distribution $D(t)$ for different subsystem sizes, with a fixed boundary drive of $p = 10^{-1}$. The lifetime distribution scales as a power law with exponent $\alpha = 3/2$ for $t < t_c$, while for $t > t_c$ we observe an exponential decay. The inset shows the size dependence on the cross-over times t_c which have been marked by small arrows.

lifetime distribution was insensitive to the strength of the boundary drive; the data presented are for $p = 10^{-1}$. We observe that $D(t)$ follows a power law $D(t) \propto 1/t^{\alpha}$ when t is smaller than some cross-over time constant t_c, which is indicated by small arrows. For t larger than t_c we see an exponential decay. The exponent α approaches a constant value $\alpha = 3/2$ independent of the lattice size in agreement with Eq. (103). However, some transient behavior is observed for the small systems. In Sec. 5.2 we defined $t_c = 1/\omega_c$. Thus the cross-over time t_c is expected to scale with the volume of the lattice. From the inset of Fig. 22, we see that this is indeed the case.

The periodic lattice gas model is defined in analogy with the previous lattice gas model, with the exception that the open boundary is substituted by periodic boundary conditions. In this manner we obtain a homogeneous model without a surface, and with translational symmetry, both vertically and horizontally. The total number of particles is conserved, and it should be noticed that when $\langle n(\mathbf{r},t) \rangle \le 0.5$, there is a possibility that the activity stops, because no particle repels any other. However this is not likely to happen and was only observed for

$\langle n(\mathbf{r},t)\rangle > n_c$, where $n_c \approx 0.3$. The situation $\langle n(\mathbf{r},t)\rangle < n_c$ is trivial in the sense that the density is so low that no density fluctuations can be supported, due to the lack of dynamical connectivity in the system. The power spectrum $S(f)$ is calculated as the Fourier transform of the total number of particles inside a subsystem, while the life-time distribution is calculated as before. The size of the subsystem is chosen to $\Omega_{sub} = \{(x,y)\, L/4 \le x \le 3L/4,\ L/4 \le y \le 3L/4\}$. In the simulations we have used a fixed particle density $\langle n(\mathbf{r},t)\rangle = 0.3$ which corresponds to the density for the boundary driven system at $p = 10^{-1}$. The results for the power spectra and the life-time distribution resemble closely the data presented in Fig. 20 and Fig. 22.

5.4 Discussion

The dynamics of a driven diffusive lattice gas models have been investigated in terms of a Langevin equation. The result for the power spectra $S(\omega)$ of the spatial integral of the density field are independent of dimensionality and possible non-linear correction terms [102]. The picture that emerged from this analysis can be summarized as follows: (a) white noise boundary condition gives $S(\omega) \sim 1/\omega$; (b) particle conserving bulk noise gives $S(\omega) \sim 1/\omega^{3/2}$; (c) a drift term as a density gradient gives $S(\omega) \sim 1/\omega^2$. In the case where several of the above mentioned noise terms are present, the resulting power spectrum $S(\omega)$ corresponds to the one that is fastest diverging.

Computer simulation studies of driven lattice gas models, *e.g.* the deterministic lattice gas model, have been particularly useful for the characterization of the relevant micro-dynamics that leads to the above universality classes (a), (b), and (c). The reason is that lattice gas models are discrete in time and space, so that we can afford to follow the evolution of the systems over the very long time intervals, that are required for determination of the low frequency behavior of the power spectra. As discussed, the deterministic lattice gas model for moderate boundary drive and the boundary driven BTW cellular automaton gave $S(\omega) \sim 1/\omega$, corresponding to class (a). Monte Carlo simulation studies was considered in Refs. [109, 114], where it was found that the particle number fluctuations in a gas of non-interacting random walkers behaved as $S(\omega) \sim 1/\omega^{3/2}$, corresponding to class (b). This implies that a Brownian gas is to be described with a conserving bulk noise term. By inclusion of a drift term, a cross-over to $S(\omega) \sim 1/\omega^2$ (class (c)) was observed both for the deterministic lattice gas model [101], and in the Monte Carlo study considered in Ref. [114]. An exception to the classifications presented above was discussed in Ref. [115]. The model was defined as a one-dimensional version of the deterministic lattice gas model considered in Sec. 5.2. It turned out that for boundary conditions yielding a non-uniform density profile, the power spectrum behaved as $S(\omega) \sim 1/\omega^{3/2}$, corresponding to class (b). However, since no bulk noise was present, class (a) was expected theoretically.

Although the deterministic and the stochastic lattice gasses have different density fluctuations, the individual particles do, in both cases asymptotically, perform ordinary random walks. The difference between the two models consists in different correlations among the particles. In the deterministic models, the particles remain correlated, whereas in the stochastic case, correlations are lost with time. This shows up in the following way. Strictly independent particles will fulfill the scaling relation $\alpha + \beta = 3$ [20]. This scaling relation is found to be fulfilled for the stochastic lattice gas, whereas the deterministic gas has $\alpha = 3/2$ and $\beta = 1$.

The observation of $1/\omega$ fluctuations in the particle number of a subvolume in the completely deterministic periodic lattice gas raises serious questions about the applicability of the Langevin description. If we assume that the observed power spectrum also in this case is a consequence of boundary driven diffusion, we need

we include that the surrounding system effectively produces a white noise drive $f(\mathbf{r},t)$ at the boundary of the subsystem[5]. However, since the boundary is arbitrarily chosen, a white noise boundary condition for the subsystem seems to be equivalent to a white noise bulk term in the diffusion equation. This lead to an inconsistency since we know that a white noise bulk term produces a $1/\omega^{3/2}$ spectrum. We have not yet been able to argue in a convincing way for the form of noise terms to be included in the Langevin equation describing the periodic lattice gas model. Also, it is not understood completely how one from the nature of the micro-dynamics decides whether a conserving bulk noise term should be included in the Langevin description. This point became especially clear in a series of computer simulation on variants of the deterministic lattice gas model, where a stochastic element is included in the dynamics. We considered two versions. In model (i), we introduced stochasticity, by updating the lattice in a Monte Carlo fashion, by a random selection of which particle should be updated. The particle then decides where to move based on the *local* arrangements of the neighboring particles according to the above mentioned deterministic rules. In model (ii) the stochastic element is introduced into the dynamics. Instead of the *blocking mechanism*, we randomly chose which particle should move in case of competition. From the Langevin treatment as discussed above, we would expect a change in scaling behavior of the power spectrum from $1/\omega$ to $1/\omega^{3/2}$, for both models. It turned out that model (i) produces an $1/\omega^{3/2}$ power spectrum in accordance with the expectations, while model (ii) conserves the $1/\omega$ power spectrum. The absence of change in scaling behavior for model (ii) is remarkable, because it shows, that the strength of the bulk noise are important for determining whether a conserving bulk noise term should be included at the coarse-grained description assumed in the Langevin treatment.

[5] This is certainly consistent with the numerically observed spectrum for the boundary values of $n(\mathbf{r},t)$, because the power spectrum for the local quantity $n(\mathbf{r},t)$ at some fixed $\mathbf{r}$ always numerically appears to be white.

Acknowledgements

I would like to use this oppunity to express my gratitude to my primary supervisor Dr. P.-A. Lindgård at Risø National Laboratory for his support and encouragement during my Ph.D. study. His inspiration and good advice has been a great help. My sincere thanks to my second supervisor Prof. O. G. Mouritsen at the Technical University of Denmark, for many fruitfull discussions, and for arranging all formalities in connection with my study. Also I would like to thank him for arranging access to the Connection Machine at Uni-C, and for his hospitality during my stay in the fall of 1991. I am very greatful to Dr. N. H. Andersen at Risø National Laboratory, who has been a most pleasant and encouraging person to collaborate with. I am indebted to him for his careful reading an useful coments. Thanks to Profs. P. A. Rikvold and M. Novotny for creating an extremly active scientific environment, and for hospitality during my stay at the Supercomputer Computations Research Institute (SCRI) at Florida State University in 1993. Everything I know about the transfer matrix formalism, I have learned from them. A special thank is due to C. Grüther and B. Gorman, whom I have been collaborating with at SCRI, for many useful discussions. I would like to thank for their help and friendship. Also I would like to thank the system administrator on the Connection Machine Dr. J. Berlin at SCRI, with whom I have been collaborating on the oxygen ordering process in $YBa_2Cu_3O_{6+x}$. Thanks to Dr. H. J. Jensen, now at Imperial College in London, who taught me all I know about driven diffusive systems. His enthusiasm and encouragement have been of great importance. Thanks to S. Mannstaedt, who performed the numerical calculations on the CM200 on the metal-ion doped systems. I would like to thank my family, especially Annette for patience and moral support during my Ph.D. study. Finally, I would like to thank the Danish Research Academy for financial support.

References

[1] K. Binder. *Monte Carlo Methods in Statistical Physics.* Springer, Berlin, 1979.

[2] K. Binder and D. W. Heermann. *Monte Carlo Simulation in Statistical Physics.* Springer-Verlag, Berlin, 1988.

[3] O. G. Mouritsen. *Computer Studies of Phase Transitions and Critical Phenomena.* Springer-Verlag, Berlin, 1984.

[4] J. S. Langer. *Ann. Phys.*, 41:108, 1967.

[5] C. M. Newman and L. S. Schulman. *J. Math. Phys.*, 18:23, 1977.

[6] B. M. Gorman, P. A. Rikvold, and M. A. Novotny. to be published.

[7] B. Gaveau and L. S. Schulman. *Lett. Math. Phys.*, 18:201, 1989.

[8] P. Bak, C. Thang, and K. Wiesenfeld. *Phys. Rev. Lett.*, 59:381, 1987.

[9] M. A. Krivoglaz. *Theory of X-Ray and Thermal-Neutron Scattering by Real Crystals.* Plenum Press, New York, 1969.

[10] H. Jagodzinski and F. Frey. In U. Shmueli, editor, *International Tabels for Crystallography, Volume B.* Kluwer Academic Publishers, Dordrecht, 1993.

[11] D. K. C. MacDonald. *Noise and Fluctuations: an Introduction.* John Wiley & Sons, Inc., New York, 1962.

[12] D. C. Champeney. *Fourier Transforms and their Physical Applications.* Academic Press, London, 1973.

[13] I. S. Gradshteyn and I. M. Ryzhik. *Tables of Integrals, Series, and Products.* Academic Press Inc., London, 1980.

[14] G. Uimin. to be published.

[15] G. Porod. *Colloid-Zeitschrift*, 124:83, 1951.

[16] G. Porod. *Colloid-Zeitschrift*, 125:51, 1952.

[17] R. L. Pego. *Proc. Roy. Soc.*, 422:261, 1989.

[18] P. Fratzl, J. L. Lebowitz, O. Penrose, and J. Amar. *Phys. Rev. B*, 44:4794, 1991.

[19] A. Guinier. *X-Ray Diffraction.* W. F. Freeman and Co., San Fransisco, 1963.

[20] H. J. Jensen, K. Christensen, and H. C. Fogedby. *Phys. Rev. B*, 40:7425, 1989.

[21] K. Christensen, H. C. Fogedby, and H. J. Jensen. *J. Stat. Phys.*, 63:653, 1991.

[22] T. Freltoft. *Neutron Study of Aggregate Structure and Kinetics.* Ph.D Thesis, Risø National Laboratory, Denmark, 1986.

[23] K. M. Wu, J. R. . Lburn, C. J. Torng, P. H. Hor, R. L. Meng, L. Goa, Z. J. Huang, Y. Q. Wang, and C. W. Chu. *Phys. Rev. Lett.*, 58:908, 1987.

[24] R. J. Cava, B. Batlogg, R. B. van Dover, D. W. Murphy, S. Sunshine, T. Siegrist, J. P. Remeika, E. A. Reitmann, S. Zahurak, and G. P. Espinosa. *Phys. Rev. Lett.*, 58:1676, 1987.

[25] R. J. Cava, A. W. Hewat, E. A. Hewat, B. Batlogg, M. Marezio, K. M. Rabe, J. J. Krajewski, W. F. Peck Jr., and L. W. Rupp Jr. *Physica C*, 165:419, 1990.

[26] B. W. Veal, A. P. Paulikas, H. You, H. Shi, Y. Fang, and J. W. Downey. *Phys. Rev. B*, 42:6305, 1990.

[27] J. D. Jorgensen, S. Pei, P. Lightfood, H. Shi, A. P. Paulikas, and B. W. Veal. *Physica C*, 167:571, 1990.

[28] B. W. Veal, H. You, A. P. Paulikas, H. Shi, Y. Fang, and J. W. Downey. *Phys. Rev. B*, 42:4770, 1990.

[29] D. de Fontaine, L. T. Wille, and S. C. Moss. *Phys. Rev. B*, 36:5709, 1987.

[30] L. T. Wille, A. Berera, and D. de Fontaine. *Phys. Rev. Lett.*, 60:1065, 1988.

[31] J. Stoltze. *Phys. Rev. Lett.*, 64:970, 1990.

[32] P. A. Sterne and L. T. Wille. *Physica C*, 162-164:223, 1989.

[33] D. de Fontaine, M. Asta, G. Ceder, and R. McCormack. *Europhys. Lett.*, 19:229, 1992.

[34] D. K. Hilton, B. M. Gorman, P. A. Rikvold, and M. A. Novotny. *Phys. Rev. B*, 46:381, 1992.

[35] V. E. Zubkus, P. J. Kundrotas, and A. S. Orliukas. *J. Phys. Cond. Matter*, 4:83, 1992.

[36] J. V. Andersen. *Non-Equlibrium Phase Transitions and Ordering Pocesses in Lattice Gas Models*. Ph.D Thesis, The Technical University of Denmark, 1991.

[37] H. F. Poulsen. *Oxygen Ordering and Superconductivity in the High T_c Superconductor $YBa_2Cu_3O_{6+x}$*. Ph.D Thesis, Risø National Laboratory, Denmark, 1991.

[38] A. A. Aligia, H. Bonadeo, and J. Garcés. *Phys. Rev. B*, 43:542, 1991.

[39] A. A. Aligia. *Europhys. Lett.*, 18:181, 1992.

[40] H. F. Poulsen, N. H. Andersen, J. V. Andersen, H. Bohr, and O. G. Mouritsen. *Nature*, 349:595, 1991.

[41] T. Zeiske, R. Sonntag, D. Hohlwein, N. H. Andersen, and T. Wolf. *Nature*, 353:542, 1991.

[42] P. R. Schleger et al. unpublished.

[43] J. Karpinski, S. Ruseicki, E. Kaldis, and E. Jilek. In H.-U. Habermeier, E. Kaldis, and J. Schoenes, editors, *Proceedings of E-MRS Spring Conference Symposium A: High T_c Superconductor Materials*, Strassburg, 1990.

[44] J. D. Jorgensen, B. W. Veal, W. K. Kwok, G. W. Crabtree, A. Umenzawa, L. J. Nowicki, and A. P. Paulikas. *Phys. Rev. B*, 36:5731, 1987.

[45] H. Casalta et al. unpublished.

[46] D. de Fontaine, L. T. Wille, and S. C. Moss. *Phys. Rev. B*, 41:8698, 1987.

[47] H. F. Poulsen, N. H. Andersen, J. V. Andersen, H. Bohr, and O. G. Mouritsen. *Phys. Rev. Lett.*, 66:465, 1991.

[48] D. de Fontaine, G. Ceder, and M. Asta. *J. Less-Common Met.*, 164/165:108, 1990.

[49] D. W. Heermann and A. N. Burkitt. *Parallel Algorithms in Computational Science*. Springer-Verlag, Berlin, 1991.

[50] K. Binder. In K. Binder, editor, *Monte Carlo Methods in Statistical Physics*. Springer, Berlin, 1979.

[51] A. M. Ferrenberg and R. Swendsen. *Phys. Rev. Lett.*, 61:2635, 1988.

[52] A. M. Ferrenberg and R. Swendsen. *Phys. Rev. Lett.*, 63:1195, 1989.

[53] R. Swendsen, J. S. Wang, and A. M. Ferrenberg. *The Monte Carlo Method in Condensed Matter Physics*. Springer-Verlag, Berlin, 1992.

[54] W. H. Press, S. A. Teukolsky, W. T. Vetterling, and B. P. Flannery. *Numerical Recipes in C*. Cambridge University Press, Cambridge, 1992.

[55] N. H. Andersen, B. Lebech, and H. F. Poulsen. *Physica C*, 172:31, 1990.

[56] T. Aukrust, M. A. Novotny, P. A. Rikvold, and D. P. Landau. *Phys. Rev. B*, 41:8772, 1990.

[57] P. A. Rikvold, B. M. Gorman, and M. A. Novotny. *Phys. Rev. E*, 47:1474, 1993.

[58] C. C. A. Günther, P. A. Rikvold, and M. A. Novotny. *Phys. Rev. B*, 42:10738, 1990.

[59] P. A. Lindgård. Phase transitions and critical phenomena. In H. Dachs, editor, *Neutron Diffraction*. Springer-Verlag, Berlin, 1978.

[60] P. A. Lindgård and O. G. Mouritsen. *Phys. Rev. B*, 41:668, 1990.

[61] L. E. Reichl. *A Modern Course in Statistical Mechanics*. University of Texas Press, Texas, 1980.

[62] D. McLachlan Jr. *X-ray Crystal Structure*. McGraw Hill, New York, 1957.

[63] N. C. Bartelt, T. L. Einstein, and L. T. Wille. *Phys. Rev. B*, 40:10759, 1989.

[64] J. V. Andersen, N. H. Andersen, O. G. Mouritsen, and H. F. Poulsen. *Physica C*, 214:143, 1993.

[65] N. H. Andersen, J. V. Andersen, L. B. Börjesson, R. Hadfield, M. Kakihana, R. McGreevy, O. G. Mouritsen, and H. F. Poulsen. *J. Alloys and Compounds*, 195:327, 1993.

[66] S. Katsuyama, Y. Ueda, and K. Kosuge. *Physica C*, 165:404, 1990.

[67] G. Van Tendeloo and S. Amelinckx. *J. Less-Common Met.*, 164,165:92, 1990.

[68] R. Beyers, B. T. Ahn, G. Gorman, V. Y. Lee, S. S. P. Parkin, M. L. Ramirez, K. P. Roche, J. E. Varzques, T. M. Gür, and R. A. Huggins. *Nature*, 340:619, 1989.

[69] A. G. Khachaturyan and J. W. Morris Jr. *Phys. Rev. Lett.*, 61:215, 1988.

[70] G. Ceder, M. Asta, and D. de Fontaine. *Physica C*, 177:106, 1991.

[71] D. de Fontaine, G. Ceder, and M. Asta. *Nature*, 343:544, 1990.

[72] M. Blume. *Phys. Rev.*, 141:517, 1966.

[73] H. W. Capel. *Physica*, 32:966, 1966.

[74] M. Blume, V. J. Emery, and R. B. Griffiths. *Phys. Rev. A*, 4:1071, 1971.

[75] P. A. Rikvold. *Prog. Theor. Phys. Suppl.*, 99:95, 1989.

[76] P. A. Rikvold, B. M. Gorman, and M. A. Novotny. *AIP Conf. Proc.*, 256:549, 1992.

[77] J. S. Langer. *Phys. Rev. Lett.*, 21:973, 1968.

[78] J. S. Langer. *Ann. Phys.*, 54:258, 1969.

[79] P. Hänggi, P. Talkner, and M. Borkovec. *Rev. Mod. Phys.*, 62:251, 1990.

[80] M. A. Novotny, W. Klein, and P. A. Rikvold. *Phys. Rev. B*, 33:7729, 1986.

[81] J. D. Gunton, M. San Miguel, and P. S. Sahni. In C. Domb and J. L. Lebowitz, editors, *Phase Transitions and Critical Phenomena, Vol. 8*. Academic, New York, 1976.

[82] K. Binder. *Rep. Prog. Phys.*, 50:783, 1987.

[83] O. Penrose and J. L. Lebowitz. In E. W. Montroll and J. L. Lebowitz, editors, *Fluctuation Phenomena*, chapter 5, page 293. North-Holland, Amsterdam, 1979.

[84] L. S. Schulman. *Techniques and Applications of Path Integration*, chapter 29. Wiley, New York, 1981.

[85] C. Unger and W. Klein. *Phys. Rev. B*, 29:2698, 1984.

[86] N. G. van Kampen. *Stochastic Processes in Physics and Chemistry*. North-Holland, New York/Amsterdam, 1981.

[87] H. E. Stanley. *Introduction to Phase Transitions and Critical Phenomena*. Oxford, New York, 1971.

[88] P. A. Rikvold. *Scaling Analysis and Pattern Formation in some Equilibrium and Nonequilibrium Systems*. Ph.D Thesis, Temple University, 1984.

[89] K. Huang. *Statistical Mechanics*. Wiley, New York, 1987.

[90] C. Domb. *Adv. Phys.*, 9:149, 1960.

[91] M. Marcus and H. Minc. *A Survey of Matrix Theory and Matrix Inequalities*. Dover Publications, New York, 1964.

[92] R. J. McCraw and L. S. Schulman. *J. Stat. Phys.*, 18:293, 1978.

[93] V. Privman and L. S. Schulman. *J. Phys. A*, 15:L231, 1982.

[94] V. Privman and L. S. Schulman. *J. Stat. Phys.*, 31:205, 1982.

[95] P. A. Rikvold. *Physica Scripta*, T38:36, 1991.

[96] R. E. Blahut. *Principles and Practice of Information Theory*. Addison-Wesley, Reading, 1987.

[97] R. B. Griffiths. *Phys. Rev. Lett.*, 13:715, 1970.

[98] C. Thang, K. Wiesenfeld, and P. Bak. *Phys. Rev. Lett.*, 58:1161, 1987.

[99] P. Bak, C. Thang, and K. Wiesenfeld. *Phys. Rev. A*, 38:364, 1988.

[100] J. Kertéz and L. B. Kiss. *J. Phys. A*, 23:L433, 1990.

[101] H. J. Jensen. *Phys. Rev. Lett.*, 64:3103, 1990.

[102] G. Grinstein, T. Hwa, and H. J. Jensen. *Phys. Rev. A*, 45:R559, 1992.

[103] H. M. Jaeger, C. Liu, and S. R. Nagel. *Phys. Rev. Lett.*, 61:40, 1989.

[104] H. J. Jensen. *Physica Scripta*, 43:593, 1991.

[105] D. Forster. *Hydrodynamic Fluctuations, Broken Symmetry, and Correlation Functions*. W. A. Benjamin, Inc., London, 1975.

[106] T. Hwa and M. Kadar. *Phys. Rev. Lett.*, 62:1813, 1989.

[107] G. Grinstein, D.-H. Lee, and S. Sacdev. *Phys. Rev. Lett.*, 64:1927, 1990.

[108] Y.-C. Zhang. *Physica A*, 170:1, 1990.

[109] H. C. Fogedby, M. H. Jensen, Y.-C. Zhang, T. Bohr, H. J. Jensen, and H. H. Rugh. *Mod. Phys. Lett. B*, 5:1837, 1991.

[110] S. H. Liu. *Phys. Rev. B*, 16:4218, 1977.

[111] P. M. Morse and H. Feshbach. *Methods of Theoretical Physics*. McGraw-Hill Book Company, New York, 1953.

[112] P. Duchateau and D. W. Zachmann. *Partial Differential Equations*. McGraw-Hill Book Company, New York, 1986.

[113] R. N. Bracewell. *The Fourier Transform and Its Applications*. McGraw-Hill Book Company, New York, 1986.

[114] J. V. Andersen, H. J. Jensen, and O. G. Mouritsen. *Phys. Rev. B*, 44:439, 1991.

[115] H. J. Jensen. *Mod. Phys. Lett. B*, 5:625, 1991.

Paper I

Theory and Computer Simulation of Diffuse Scattering from Lattice Gas Models

Structure factor calculations for the high-temperature superconductor $YBa_2Cu_3O_{6+x}$

Theory and Computer Simulation of Diffuse Scattering from Lattice Gas Models — Structure factor calculations for the high-temperature superconductor $YBa_2Cu_3O_{6+x}$*

T. Fiig,[1] N.H. Andersen,[1] J. Berlin,[2] P. A. Lindgård,[1]
and O.G. Mouritsen[3]

[1] Department of Solid State Physics
Risø National Laboratory,
DK-4000 Roskilde, Denmark

[2] Thinking Machines Corporation
245 First Street
Cambridge, Massachusetts 02142-1264, USA

[3] Department of Physical Chemistry,
The Technical University of Denmark
DK-2800 Lyngby, Denmark

March 18, 1994

*Submitted to Physical Review B.

Abstract

The computational aspects of calculations of the structure factor $S(\mathbf{q})$ for lattice gas models are reviewed. For one-dimensional ordered structures the relation between $S(q)$, the correlation function $C(r)$, and the cluster size distribution $\mathcal{D}(n)$ is discussed. For a number of one-dimensional models the problem of excluded volume related to densely packed ordered structures is treated exactly and the corresponding line shapes are found. The possibilities for having line shapes of Lorentzian, square Lorentzian and multi peaked form for the diffuse scattering are discussed. We also discuss the possible decomposition of $S(q)$ into contributions from domains of differently ordered structures, as well as the application of symmetries in reciprocal space. The oxygen order in $YBa_2Cu_3O_{6+x}$ has been investigated by Monte Carlo simulation using an extension to three dimensions of the well known two-dimensional anisotropic next nearest neighbor lattice gas model (the ASYNNNI model). The calculation of the structure factor in three spatial dimensions has been implemented on a massively parallel computer, the Connection Machine. Our results for the widths of the structure factor at the (1/2,0,0) superstructure reflection are compared with recent neutron diffraction measurements.

1 Introduction

The diffuse scattering of X-rays and neutrons provides a powerful tool to investigate disorder and defects in structure at a microscopic level in condensed matter physics. In recent years attempts have been made to use inverse Monte Carlo (MC) techniques on Ising or lattice gas representations for the atomic arrangements [1, 2], in order to determine the micro structure of alloys from the observed diffuse scattering. In the high T_c superconducting materials of the $YBa_2Cu_3O_{6+x}$ family the representation is in the form of the anisotropic next nearest neighbor (ASYNNNI) lattice gas model [3] with several interaction parameters. Inverse transfer matrix calculations have been performed on this model by Hilton *et al.* [4] in order to determine a set of effective interaction parameters by fitting the calculated phase diagram to the experimental data. The theory of diffuse scattering is very similar to that of small angle scattering, which in recent years has been subject to intensive studies in the investigations of for example polymers and biological substances, which have complex imperfect structures [5, 6, 7, 8]. The reciprocal space scattering methods do not give the direct real space information as for example electron microscopy or tunneling microscope techniques. In order to fill in this gap computer simulations are of increasing importance. The real space information is in particular useful for obtaining a physical and intuitive understanding, whereas the reciprocal space description of correlation functions is superior for describing disorder in a well-defined quantitative way. However, a number of questions cannot be resolved uniquely. In particular questions, concerning whether the diffuse scattering arises from a substantial randomness in large domains of structures (with for example different anti-phases or competing structures) or the diffuse scattering results from a random collection of small domains of the structures. In the $YBa_2Cu_3O_{6+x}$ materials, where the superconducting properties depend strongly on the structural properties and in particular on the details of the oxygen ordering, an elucidation of this question is very important. Since dissimilar structural models can give almost identical results for the integrated scattering intensities, we discuss the scattering line shape as obtained from different models. From this analysis, it has become clear that the diffuse scattering cannot always provide a unique distinction between the different structural models. A better approach is therefore to simulate a model numerically, compute the structure factors directly in reciprocal space, and then compare with the experimental data. The problem with this approach is that in order to obtain a satisfactory resolution in reciprocal space very large model systems in real space are required. It is therefore an advantage to make use of optimized computer programs on parallel computers. We shall describe the results and implementation of a three-dimensional structure factor calculation for $YBa_2Cu_3O_{6+x}$ on the Connection Machine, based on a three-dimensional extension of the ASYNNNI model. A comparison with recent experiments [9] will also be made.

The paper is organized in the following way. A discussion of the division of $S(\mathbf{q})$ into the long-range Bragg scattering and the diffuse part, and of the q-values

that are physical relevant in finite size lattice gas model calculations are given in Sec. 2. The use of symmetries in order to reduce the computational efforts and reduce the statistical uncertainty of the structure factor are discussed in Sec. 2.1. In Sec. 2.2 a detailed analytical account is given for the line shapes that result from different assumed distributions of one-dimensional lattice gas structures and possible extensions to higher dimensions are discussed. We analyze the oxygen ordering of $YBa_2Cu_3O_{6+x}$ in Sec. 3. In Sec. 4 we describe how the Monte Carlo calculations are implemented on a Connection Machine (CM2). Section 5 contains the results of the numerical calculations and a comparison with recent experimental data. A summary and a conclusion are given in Sec. 6.

2 Theory of structure factor calculations

In this section, we will briefly review some of the fundamental concepts and basic results on structure factor calculations for lattice gas models. The unit cell of the crystal is spanned by the primitive vectors $\mathbf{a}_1$, $\mathbf{a}_2$, and $\mathbf{a}_3$, along the crystallographic axis. If we have p atomic sites in the unit cell, the atomic sites are given by $\mathbf{r} + \mathbf{d}_j$, $j = 1, \ldots, p$, where $\mathbf{r} = n_1\mathbf{a}_1 + n_2\mathbf{a}_2 + n_3\mathbf{a}_3$, with n_1, n_2 and n_3 being integers, and $\mathbf{d}_j$ denote position vectors in the unit cell. The crystal system is treated as a lattice gas, where the occupation numbers are $\sigma(\mathbf{r} + \mathbf{d}_j) = 1, 0$ depending on whether the site is occupied or not. Primitive vectors in reciprocal space can then be defined as $\mathbf{b}_1 = 2\pi(\mathbf{a}_2 \times \mathbf{a}_3)/(\mathbf{a}_1 \cdot \mathbf{a}_2 \times \mathbf{a}_3)$, and analogously for $\mathbf{b}_2$ and $\mathbf{b}_3$ by cyclic permutation of the indices. The density-density correlation function is defined as

$$C_{jj'}(\mathbf{r}, \mathbf{r}') = \langle \sigma(\mathbf{r} + \mathbf{d}_j)\sigma(\mathbf{r}' + \mathbf{d}_{j'}) \rangle \,, \tag{1}$$

where $\mathbf{r} + \mathbf{d}_j$ and $\mathbf{r}' + \mathbf{d}_{j'}$ denotes particle sites, and $\langle \cdots \rangle$ denotes ensemble average over independent configurations. Experimentally this average has its origin in the experimental conditions of conventional X-ray and neutron diffraction studies, where the finite experimental resolution restricts the coherence of the diffracted beam to a length scale, that is several orders of magnitude smaller than the spatial extension of the physical sample. This means that the number of averages over independent realizations in an experimental situation is tremendous. The structure factor is defined as the Fourier transform of the density-density correlation $C_{j,j'}(\mathbf{r}, \mathbf{r}')$:

$$\begin{aligned} S(\mathbf{q}) &= \frac{1}{N} \sum_{\mathbf{r}} \sum_{j=1}^{p} \sum_{\mathbf{r}'} \sum_{j'=1}^{p} e^{i\mathbf{q}\cdot(\mathbf{r}+\mathbf{d}_j-\mathbf{r}'-\mathbf{d}_{j'})} b_j b_{j'} C_{jj'}(\mathbf{r}, \mathbf{r}') \\ &= \frac{1}{N} \left\langle \left| \sum_{\mathbf{r}} \sum_{j=1}^{p} e^{i\mathbf{q}\cdot(\mathbf{r}+\mathbf{d}_j)} \sigma(\mathbf{r} + \mathbf{d}_j) b_j \right|^2 \right\rangle \,, \end{aligned} \tag{2}$$

where b_j for neutron diffraction is the coherent scattering amplitude. The structure factor has been normalized by the number of unit cells N. Equation (2) is also valid

for X-ray diffraction provided that b_j is replaced by the atomic form factor $f_j(\mathbf{q})$. The derivation of the second equality in Eq. (2), which assumes translational invariance, can be found in Ref. [10]. Obviously in computer simulations the formulation of the structure factor as a single summation greatly reduces the computational work. Thermal motion of the atoms in the crystal around their equilibrium positions gives rise to a reduction in the intensities of the Bragg reflections, and to inelastic and quasi-elastic diffuse scattering at the non Bragg positions in the rest of reciprocal space, provided that the conditions for true elastic scattering are not fulfilled. However, contributions from thermal motion are absent in the lattice gas approximation considered in this paper, because the atoms are assumed to occupy fixed positions.

In the computer simulations, we will consider a finite crystal system with $N = N_1 \times N_2 \times N_3$ unit cells, subject to periodic boundary conditions. In order to remove the shape dependence of the geometry used in the structure factor calculation, the finite system is extended by periodic boundary conditions to a system of $P(P \rightarrow \infty)$ replica of our original finite system on a superlattice with lattice spacing $N_1\mathbf{a}_1$, $N_2\mathbf{a}_2$, and $N_3\mathbf{a}_3$. Let $\mathbf{R}$ be a vector pointing to the origin of the different replica, then the occupation numbers are periodic $\sigma(\mathbf{r} + \mathbf{R} + \mathbf{d}_j) = \sigma(\mathbf{r} + \mathbf{d}_j)$. The structure factor $S(\mathbf{q})$ of such a system has been considered in Ref. [11], where it was shown that it reduces to

$$\begin{aligned} S(\mathbf{q}) &= \frac{1}{NP}\left\langle \left| \sum_{\mathbf{R}} \sum_{\mathbf{r}} \sum_{j=1}^{P} e^{i\mathbf{q}\cdot(\mathbf{R}+\mathbf{r}+\mathbf{d}_j)} \sigma(\mathbf{R}+\mathbf{r}+\mathbf{d}_j) b_j \right|^2 \right\rangle \\ &= \frac{1}{NP}\left\langle \left| \sum_{\mathbf{R}} e^{i\mathbf{q}\cdot\mathbf{R}} \sum_{\mathbf{r}} \sum_{j=1}^{P} e^{i\mathbf{q}\cdot(\mathbf{r}+\mathbf{d}_j)} \sigma(\mathbf{r}+\mathbf{d}_j) b_j \right|^2 \right\rangle \\ &= \frac{1}{N}\left\langle \left| \sum_{\mathbf{r}} \sum_{j=1}^{P} e^{i\mathbf{q}\cdot(\mathbf{r}+\mathbf{d}_j)} \sigma(\mathbf{r}+\mathbf{d}_j) b_j \right|^2 \right\rangle \sum_{h,k,l=-\infty}^{\infty} \delta_P\left(\mathbf{q} - \frac{h}{N_1}\mathbf{b}_1 - \frac{k}{N_2}\mathbf{b}_2 - \frac{l}{N_3}\mathbf{b}_3\right) \end{aligned} \quad (3)$$

where for $P \rightarrow \infty$, $\delta_P(\mathbf{q})$ is given by the delta function $((2\pi)^3/V_0)\delta(\mathbf{q})$, with V_0 as the cell volume. The result in Eq. (3) shows that $S(\mathbf{q})$ is independent of the shape of the finite system. However, the presence of the delta functions due to the replica shows that only the discrete set of $\mathbf{q}$-vectors given by

$$\mathbf{q} = \frac{h}{N_1}\mathbf{b}_1 + \frac{k}{N_2}\mathbf{b}_2 + \frac{l}{N_3}\mathbf{b}_3 , \quad (4)$$

have non-zero structure factors, with h, k, and l being integers. It is important to note that this result implies that the resolution in $\mathbf{q}$-space is given *a priori* by the system size of the finite crystal system, and that the resolution can only be enhanced by increasing the system size. It is conventional in computer simulation to define the structure factor $S(\mathbf{q})$ as the first term in Eq. (3) where the delta function restriction has been removed. This is also done in the present work.

In the special case where the crystal structure itself can be described by a Bravais lattice, then the number of atoms in the unit cell is $p = 1$ and $\mathbf{d}_1 = 0$. Hence $S(\mathbf{q})$ is a periodic function with periodicity given by the primitive reciprocal lattice vectors. Assuming that no other symmetry element exists, the structure factor $S(\mathbf{q})$ can then be uniquely specified by the q-vectors in the first Brillouin zone. For a general crystal system with several atoms in the unit cell, the structure factor $S(\mathbf{q})$ will posses translational symmetry if and only if the basis vectors occupy rational fractional positions, as is the case for the oxygen sites in the basal plane of the high temperature superconductor $YBa_2Cu_3O_{6+x}$ (see Sec. 3).

2.1 Symmetry considerations

In this section we will show that symmetries of the crystal structure in real space can be used to greatly simplify the calculation of the structure factor. Also the symmetries may be used to improve the statistics in the calculation.

The symmetry elements of the space group for a crystal structure are symmetry transformations of the crystal onto itself. The symmetry transformations consist of a rotation, or mirror rotation (the point group transformations), which is expressible as a matrix operator $\mathbf{A}$, followed by a subsequent translation $T_{\mathbf{t}_0}$, through a vector $\mathbf{t}_0$. As described in Ref. [12] the symmetry element g of the space group G, can then be written $g = T_{\mathbf{t}_0}\mathbf{A}$, with an inverse g^{-1} given by $g^{-1} = T_{-\mathbf{A}^{-1}\mathbf{t}_0}\mathbf{A}^{-1}$.

Let us first consider the case where the occupation numbers $\{\sigma(\mathbf{r} + \mathbf{d}_j)\}$ are invariant under g, so that $\sigma(g(\mathbf{r} + \mathbf{d}_j)) = \sigma(\mathbf{r} + \mathbf{d}_j)$. Using this identity and by inserting the unity operator $g^{-1}g$ in Eq. (3) we have

$$\begin{aligned} S(\mathbf{q}) &= \langle \left| \sum_{\mathbf{r}} \sum_{j=1}^{p} e^{i\mathbf{q}\cdot g^{-1}g(\mathbf{r}+\mathbf{d}_j)} \sigma(g(\mathbf{r}+\mathbf{d}_j)) b_j \right|^2 \rangle , \\ &= \langle \left| \sum_{\mathbf{r}} \sum_{j=1}^{p} e^{-i\mathbf{q}\cdot\mathbf{A}^{-1}(\mathbf{t}_0)} e^{i\mathbf{q}\cdot\mathbf{A}^{-1}g(\mathbf{r}+\mathbf{d}_j)} \sigma(g(\mathbf{r}+\mathbf{d}_j)) b_j \right|^2 \rangle , \\ &= \langle \left| e^{-i\mathbf{q}\cdot\mathbf{A}^{-1}(\mathbf{t}_0)} \sum_{\mathbf{r}} \sum_{j=1}^{p} e^{i[(\mathbf{A}^*)^{-1}\mathbf{q}]\cdot g(\mathbf{r}+\mathbf{d}_j)} \sigma(g(\mathbf{r}+\mathbf{d}_j)) b_j \right|^2 \rangle , \\ &= S(\mathbf{A}q) . \end{aligned} \tag{5}$$

In Eq. (5) $\mathbf{A}^*$ denotes the adjoint of the operator $\mathbf{A}$. In the last derivation we have used the fact that $\mathbf{A}$ is a unitary operator an hence $(\mathbf{A}^*)^{-1} = \mathbf{A}$. The fact that $\mathbf{A}$ is unitary can be understood from the fact that rotations and mirror rotations are angle preserving. The result above can be expressed as: ***the point group symmetry of a crystal structure and that for its reciprocal structure are the same.*** However no such analogous statement exists for space group symmetries.

Consider now the more general situation where the occupation numbers $\{\sigma(\mathbf{r}+\mathbf{d}_j)\}$ are variable. The space group G of the crystal structure is determined from the

average occupation c_j on site j in the unit cell. As before let $g = T_{t_g}\mathbf{A} \in G$ be a symmetry element. Then in the computer simulation a configuration $\{\sigma(\mathbf{r}+\mathbf{d}_j)\}$ and the symmetry related configuration $\{\sigma(g(\mathbf{r}+\mathbf{d}_j))\}$ have exactly the same statistical weight. Since the structure factor is defined as an ensemble average, the result for $S(\mathbf{q})$ in Eq. (5) remains unchanged.

2.2 Diffuse scattering from disordered structures

Diffuse scattering is due to disorder phenomena, which result from deviations from perfectly translational invariant scattering objects and from long range correlations in space and time. Fluctuations in scattering amplitudes and phase shifts reduce the intensities of the Bragg reflections, and they are responsible for the diffuse scattering at the non-Bragg positions in reciprocal space. Consider the situation where the unit cell is not translationally invariant due to spatial inhomogeneities in the material composition. The average occupation of an atom at site j is given by the number of atoms on equivalent sites j divided by the number of available sites:

$$c_j = \frac{1}{N}\langle\sum_{\mathbf{r}}\sigma(\mathbf{r}+\mathbf{d}_j)\rangle, \quad j = 1,\ldots,p\,. \tag{6}$$

The occupation numbers may be separated into two terms $\sigma(\mathbf{r}+\mathbf{d}_j) = c_j + \Delta\sigma(\mathbf{r}+\mathbf{d}_j)$, where the first term is the average occupation at the atomic site j, and $\Delta\sigma(\mathbf{r}+\mathbf{d}_j)$ is the deviation from the average occupation. From these basic concepts, the generally adopted method in a disorder problem [13, 14, 15] is to separate the structure factor into two parts: $S(\mathbf{q}) = S_{\mathrm{Bragg}}(\mathbf{q}) + S_{\mathrm{dif}}(\mathbf{q})$, given by

$$\begin{aligned} S_{\mathrm{Bragg}}(\mathbf{q}) &= \frac{1}{N}\left|\sum_{\mathbf{r}}\sum_{j=1}^{p} e^{i\mathbf{q}\cdot(\mathbf{r}+\mathbf{d}_j)} c_j b_j\right|^2, \\ S_{\mathrm{dif}}(\mathbf{q}) &= \frac{1}{N}\left\langle\left|\sum_{\mathbf{r}}\sum_{j=1}^{p} e^{i\mathbf{q}\cdot(\mathbf{r}+\mathbf{d}_j)}\Delta\sigma(\mathbf{r}+\mathbf{d}_j) b_j\right|^2\right\rangle, \end{aligned} \tag{7}$$

where the cross terms containing $c_j\Delta\sigma(\mathbf{r}+\mathbf{d}_{j'})$ vanish by definition. The first part represents the coherent contribution from the average atomic configuration. Because c_j is periodic $S_{\mathrm{Bragg}}(\mathbf{q})$ describes Bragg diffraction and may be decomposed into a sum over the ordering $\mathbf{Q}$-vectors. Direct evaluation yields

$$S_{\mathrm{Bragg}}(\mathbf{q}) = \sum_{\mathbf{Q}} \theta_{\mathbf{Q}}^2 \delta_{\mathbf{q},\mathbf{Q}}\,, \tag{8}$$

where the Kronecker delta function $\delta_{\mathbf{q},\mathbf{Q}}$ represents the contribution corresponding to a non-zero order parameters $\theta_{\mathbf{Q}}$, for an ordered structure, which interferes constructively upon scattering of a plane wave with momentum transfer $\mathbf{Q}$. The second term in the structure factor $S_{\mathrm{dif}}(\mathbf{q})$ is the diffuse part, which carries information about the

fluctuations of the atomic configurations from the average, and hence the correlation lengths.

In many cases diffuse scattering is centered exactly at the Bragg positions. This is the case for the oxygen disordered diffuse scattering in the high temperature superconducting compound $YBa_2Cu_3O_{6+x}$. It is then a difficult experimental problem to deconvolute the Bragg contribution and isolate the diffuse part.

2.3 Analytical considerations

The full treatment of the theoretical background for the diffuse diffraction pattern lies beyond the scope of this paper. A discussion of the diffuse scattering arising from elastic deformations, defects, impurities and other imperfections of the lattice has been presented by Krivoglaz [13]. We will only consider the situation where the diffuse scattering is due to variation in the material composition described by clusters with a given distribution in a periodic lattice. Most of the discussion will be restricted to one dimension, with comments on the consequences in higher dimensions. The remaining part of the present section is divided into three parts. In the first part we calculate the one-dimensional structure factor in the dilute limit where the lattice is sparsely filled with clusters. In this limit the results may be generalized to higher dimensions. In the second part the dilute one-dimensional case is generalized to higher densities of non-interacting clusters by taking into account that different clusters cannot overlap. This result is then applied to a calculation of the structure factor for a variety of different cluster distributions. Finally we consider a simple one-dimensional model for the oxygen ordering process in $YBa_2Cu_3O_{6+x}$. We discuss the situation when two types of clusters with different internal structure are present.

2.4 Structure factor calculations in the dilute limit

Let Ω be the set of real space lattice points with the lattice spacing a in an undistorted, infinite one-dimensional system, which we treat as a chain with N sites for $N \to \infty$. We have $N_p \leq N$ identical particles, each with scattering amplitude b. A single cluster $f_{R,n}(r)$ can be represented as a box $A_{R,n}(r)$ of unit height and length na centered at R containing n delta functions with spacing a:

$$\begin{aligned} f_{R,n}(r) &= \sum_{j=0}^{n-1} \delta\left\{r - R + \left(\frac{n-1}{2} - j\right) a\right\} = A_{R,n}(r) D(r). \\ D(r) &= \sum_{j=-\infty}^{\infty} \delta\{r - ja\}\,. \end{aligned} \tag{9}$$

The Fourier transform of $f_{R,n}(r)$, is given by a folding of the Fourier transform of the box function $A_{R,n}(r)$ and that of the perfect structure $D(r)$, [16]. Thus $f_{R,n}(q) = A_{R,n}(q) \otimes D(q)$. The Fourier transform of $f_{R,n}(r)$ can also be evaluated directly [16]

and yields

$$f_{R,n}(q) = \frac{\sin(qan/2)}{\sin(qa/2)} e^{iqR} . \tag{10}$$

Consider a distribution of randomly placed clusters $f_{R,n}(r)$ with a size distribution $\mathcal{D}(n)$. The distribution is normalized, so that the concentration of particles is $x = \lim_{N\to\infty}(N_p/N)$ which gives the constraint: $\sum_{n=1}^{\infty} n\mathcal{D}(n) = x$. In the approximation where we neglect interference phenomena between clusters (*i.e.* overlapping clusters are accepted), we can apply Campbell's theorem, which determines the power spectrum of a function consisting of a random repetition of elementary signals (see appendix L in Ref. [16]). In the following discussion we will only be interested in diffuse scattering, so that q does not coincide with the Bragg positions $q \neq Q_m = 2\pi m/a$, where m is an integer. By restricting the q values in this fashion, we can replace $\Delta\sigma(\mathbf{r})$ by $\sigma(\mathbf{r})$ in the definition of the diffuse structure factor in Eq. (7). The structure factor normalized to one lattice site can then be written as

$$S_{\mathrm{dif}}(q) = b^2 \sum_{n=0}^{\infty} \mathcal{D}(n)|f_{R,n}(q)|^2 , \tag{11}$$

which is just a weighted average of the structure factors arising from a single cluster containing n delta functions. Equation (11) is valid without any restriction of dimensionality. In one dimension the applicability of Eq. (11) is restricted to the limit $x\to 0$, since overlapping clusters are not physically acceptable. In higher dimensions, for $\mathbf{q}$ in the direction where all mass points in planes perpendicular to $\mathbf{q}$ can be projected onto the delta functions of a linear chain, overlap naturally arises and the modification is simply that instead of using $f_{R,n}(q)$ as evaluated from Eq. (10) we have to consider the folding $f_{R,n}(q) = A_{R,n}(q) \otimes D(q)$, with $A_{R,n}(q)$ replaced by the Fourier transform of the projected shape function.

Naturally it is interesting to be able to invert Eq. (11) so that given $S_{\mathrm{dif}}(q)$ we are able to determine the cluster size distribution function $\mathcal{D}(n)$. If we assume that the projected shape function is that of a box function which leads to Eq. (10), this can be done analytically. By expressing $|f_{R,n}(q)|^2$ from Eq. (10) as $|f_{R,n}(q)|^2 = (1-\cos(qan))/(2\sin^2(qa/2))$, we see that the sum in Eq. (11) corresponds to a Fourier expansion in cosines (the sines in the expansion are absent, since $S_{\mathrm{dif}}(q)$ is even in q). The Sturm-Liouville theory (see Ref. [17], p. 760) can then be applied and yields

$$\mathcal{D}(n) = \frac{-2}{\pi b^2} \int_0^{2\pi} dk\, S_{\mathrm{dif}}(k) \sin^2\left(\frac{k}{2}\right) \cos(nk) , \quad (n \geq 1) . \tag{12}$$

Traditionally the structure factor $S(q)$ is expressed in terms of the density-density correlation function $C(r,r')$. Again, if we assume translational invariance *i.e.* $C(r,r') = C(r-r')$, the structure factor is determined from the Wiener-Khinchin theorem (see *e.g.* Ref. [18]). In the one-dimensional case where $r = na$ is restricted to the lattice

sites of Ω, this theorem is expressed as:

$$S_{\rm dif}(q) = b^2 \sum_{n=-\infty}^{\infty} C(na) e^{iqna} \,. \tag{13}$$

In exactly the same way this equation can be inverted to yield the correlation function $C(r - r')$ in terms of the structure factor $S_{\rm dif}(q)$. We obtain

$$C(na) = \frac{1}{2\pi b^2} \int_0^{2\pi} dk \cos(nk) S_{\rm dif}(k) \,. \tag{14}$$

Thus in the approximation, where the clusters are assumed to be non-interacting, we have obtained analytically a complete description of the system in terms of any of the functions $\mathcal{D}(n)$, $S_{\rm dif}(q)$, and $C(na)$, since each one can be found from the knowledge of one of the other, by Eqs. (11)–(14).

In the case where the density of the clusters become so high that they are no longer independent, Eq. (11) becomes more complicated, as discussed below, so that inversion of the series cannot be done in closed form. The results presented is valid for a lattice gas model, where the particles occupy fixed positions. It follows from Eqs. (10) and (11) that the structure factor is periodic, *i.e.* $S_{\rm dif}(q + Q_m) = S_{\rm dif}(q)$. A continuum formulation can be obtained by considering the lattice spacing $a \to 0$. The relation between the correlation function $C(\mathbf{r})$ and the structure factor is then found from a d-dimensional Fourier transform $C(\mathbf{r}) = \int d^d q S_{\rm dif}(\mathbf{q}) e^{-i\mathbf{q}\cdot\mathbf{r}}$. It should be noted that $S_{\rm dif}(\mathbf{q})$ from the continuum formulation is *not* a periodic function, since all Bragg positions except Q_0 moves to infinity in the limit $a \to 0$. In a simple mean-field theory the correlation function is determined from the Ornstein-Zernike approximation, which amounts to assuming that $S_{\rm dif}(q)$ is a Lorentzian, independent of dimensionality d [10]. For an isotropic system the Fourier transform can be performed and yields for $T \to T_c^+$, $(\kappa \to 0)$:

$$C(r) \propto \begin{cases} e^{-\kappa r} & d = 1 \\ \ln(r) e^{-\kappa r} & d = 2 \\ \frac{e^{-\kappa r}}{r^{d-2}} & d \geq 3 \end{cases} \,. \tag{15}$$

Data from diffraction experiments are often fitted to a Lorentzian or a Lorentzian square. In this context, it is interesting to notice that if the correlation function in three dimensions is modified to be $C(r) \propto \exp(-\kappa r)$, the one obtains a Lorentzian square instead.

2.4.1 Delta function distributed cluster sizes

Assuming that the clusters are of equal size ℓ, the normalized cluster size distribution function is given by $\mathcal{D}(n) = \mathcal{N}\delta_{n,\ell}$, with $\mathcal{N} = \frac{x}{\ell}$. By evaluating the sum in Eq. (11) the structure factor becomes

$$S_{\rm dif}(q) = x b^2 \frac{\sin^2(qa\ell/2)}{\ell \sin^2(qa/2)} \,. \tag{16}$$

In higher dimensions, the result resembles that of Eq. (16), in particular with respect to having vanishing intensities at certain q-values, which is due to the sharp cut-off in the projected shape function $A_{R,n}(r)$.

2.4.2 Exponentially distributed cluster sizes

Let us assume that the cluster size is exponentially distributed $\mathcal{D}(n) = \mathcal{N}e^{-\kappa n a}$. Normalization gives $\mathcal{N} = x[e^{\kappa a} - 1]^2/e^{\kappa a}$. The parameter κ measures the width of the distribution and is analogous to an inverse correlation length $\kappa = 1/\xi$. The sum in Eq. (11) can easily be evaluated after expressing $\sin^2(qan/2)$ in terms of exponentials. We obtain for the structure factor

$$\begin{aligned} S_{\rm dif}(q) &= xb^2 \frac{(\alpha^2 - 1)}{1 + \alpha^2 - 2\alpha\cos(qa)} , \\ \alpha &= e^{\kappa a} . \end{aligned} \tag{17}$$

We notice that Eqs. (16) and (17) are proportional to x and not $x(1-x)$ as normally expected for impurity scattering [15]. Therefore, they are only valid to first order in x. The structure factor Eq. (17) is periodic and may be written

$$S_{\rm dif}(q) = xb^2 \sum_{n=-\infty}^{\infty} \frac{(\alpha^2 - 1)}{(1-\alpha)^2 + \alpha a^2 (q - Q_n)^2} \approx xb^2 \frac{1}{a} \sum_{n=-\infty}^{\infty} \frac{2\kappa}{\kappa^2 + (q - Q_n)^2} . \tag{18}$$

It is interesting that the structure factor Eq. (17) is exactly a sum of Lorentzian line shapes over the Bragg positions. The second expression for the more familar form of the Lorentzian line shape follows by an expansion to second order in κ. In this fashion we obtain a direct linkage between the full-width-half-maximum (FWHM) of the structure factor 2κ and the width of the cluster size distribution.

2.4.3 Cluster distribution for a Lorentzian square

It is interesting to determine the cluster size distribution $\mathcal{D}(n)$ that gives rise to a Lorentzian square. An infinite sum of Lorentzians was obtained from Eq. (17), so by analogy we have for the infinite sum of square Lorentzians:

$$\begin{aligned} S_{\rm dif}(q) &= xb^2 \frac{C}{(1 + \alpha^2 - 2\alpha\cos(qa))^2} , \\ \alpha &= e^{\kappa a} . \end{aligned} \tag{19}$$

where the normalization constant C is to be determined from the sum rules of the cluster distribution. From Eq. (12) we obtain

$$\mathcal{D}(n) = \frac{-2xC}{\pi} \int_0^{2\pi} dt \frac{\sin^2(t/2)\cos(nt)}{(1 + \alpha^2 - 2\alpha\cos(t))^2} . \tag{20}$$

This integral can be solved by means of the following formula (see Ref. [19] p. 369)

$$I_n \equiv \int_0^{2\pi} dt \frac{\cos(nt)}{(1+\alpha^2-2\alpha\cos(t))^2} = \frac{2\pi}{\alpha^n(\alpha^2-1)^3}(2+(n+1)(\alpha^2-1)) . \qquad (21)$$

By expressing the numerator in Eq. (20) entirely in cosines we obtain

$$\begin{aligned} \mathcal{D}(n) &= \frac{-2x\mathcal{C}}{\pi}\left(\frac{1}{2}I_n - \frac{1}{4}(I_{n-1}+I_{n+1})\right) \\ &= x\mathcal{C}\frac{\alpha^{-1-n}(-2\alpha-n+\alpha^2 n)}{(\alpha+1)^2(\alpha^2-1)} . \end{aligned} \qquad (22)$$

By requiring that $\sum_{n=1}^{\infty} n\mathcal{D}(n) = x$ it follows that $\mathcal{C} = (\alpha^2-1)^3/(1+\alpha^2)$. Thus we obtain for the normalized cluster size distribution:

$$\begin{aligned} \mathcal{D}(n) &= x\left(\frac{(\alpha+1)(\alpha-1)^3}{\alpha(1+\alpha^2)}\right)\alpha^{-n}(n(\alpha^2-1)-2\alpha) . \\ \alpha &= e^{\kappa a} . \end{aligned} \qquad (23)$$

The cluster distribution Eq. (23), unlike the exponential distribution, is suppressed

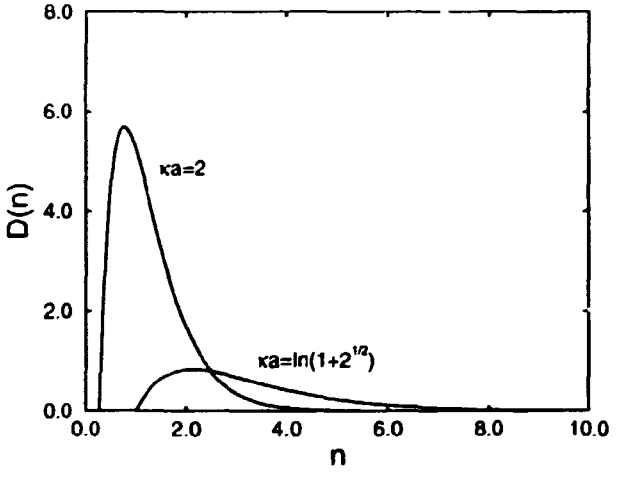

Figure 1: The cluster size distribution $\mathcal{D}(n)$ that arises for a Lorentzian square lineshape for the diffuse part of the structure factor. The distributions shown have been calculated from Eq. (23) for $\kappa a = \ln(1+\sqrt{2})$ and $\kappa a = 2$, respectively.

at small n and has a maximum at $n_{max} = (-1+\alpha^2+2\alpha\ln\alpha)/((-1+\alpha^2)\ln\alpha)$. For $n \gg n_{max}$ it decays exponentially. Since for a proper distribution we must have $\mathcal{D}(n) \geq 0$, it follows that $\kappa a \geq \ln(1+\sqrt{2})$. In Fig. 1, the distribution function has

been plotted versus n for $\kappa a = \ln(1+\sqrt{2})$, which is the limiting value for κa, and for $\kappa a = 2$, respectively. It can be seen, that for larger values of κ, the distribution becomes more narrow, and the maximum of the distribution moves towards smaller cluster sizes. This shows that only a narrow distribution around small cluster sizes is compatible with a Lorentzian square. At lower temperatures the cluster sizes become larger and the correlation length diverges ($\kappa \rightarrow 0$), in which case the criterion for a non-negative distribution is violated, and the Lorentzian square line shape is not supported. In other words if an experiment results in a Lorentzian square it implies that only short range order is present.

2.5 Structure factor calculations with excluded volume

The problem of the 'excluded volume' effect originates in that of hard sphere liquids [8]. It was discussed by Fratzl *et al.* [5] with respect to scaling relations of $S_{\rm dif}(q)$. Recently it was considered by Uimin [20] in a context of introducing the fermionic degrees of freedom into randomly placed non-overlapping copper-oxide chain fragments in $YBa_2Cu_3O_{6+x}$. Uimin has formulated the solution in a form, which is useful for the present discussion. The problem for a one-dimensional system is stated as follows: determine $S_{\rm dif}(q)$ for a distribution of unequally sized clusters $f_{R,n}(r)$ separated by vacancies, not allowing overlaps. A simple solution is to include a vacancy to the right of the cluster in the definition. Since the vacancies do not contribute to the scattering amplitude, the correlation between them is not important and they can be treated as 'zero' length clusters. A problem with this approach arises, since it cannot account for the observed interconnected, sponge like domain structures which occur in simulations as well as in experiments in many systems of phase separation. This feature can only be included, if correlations between the distribution of the ordered and the vacant regions are taken into account. Experimentally these correlations give rise to a characteristic limiting behavior: $S_{\rm dif}(q) \propto q^{-4}$ for large q, called Porod's law [6, 7] and $S_{\rm dif}(q) \propto q^4$ for small q, (for mesoscopic domains and narrow line widths $q \ll 2\pi/a$) called Pego's law [21].

This problem has not been solved in general, even in the one dimensional case. However, in Ref. [5] it was shown that by filling the boxes $A_{R,n}(r)$ symmetrically around R and leaving the remaining part as vacancies at $x = 1/2$, one captures sufficient of the required correlation to obtain the expected limiting behavior of $S_{\rm dif}(q)$. However, the two methods of including the vacancies yield qualitatively identical results for intermediate q-values. For mathematical simplicity we will follow the approach of including vacancies to the right of a cluster. This means that the cluster size distribution, in addition to the normalization $\sum_{n=1}^{\infty} n\mathcal{D}(n) = x$, has to satisfy the constraint $\sum_{n=0}^{\infty} \mathcal{D}(n) = 1 - x$. The structure factor for the diffuse scattering can be determined exactly [8, 20] and takes the form

$$S_{\rm dif}(q) = b^2(1-x)\frac{1-u^2}{1+u^2-2u\cos(\phi)},\ ue^{i\phi} = \frac{1}{1-x}\sum_{n=0}^{\infty}\mathcal{D}(n)e^{iq(n+1)a}\,, \qquad (24)$$

where ϕ and u are real variables defined as the phase and the modulus of the complex number from the summation over the cluster size distribution in Eq. (24). The normalization conditions give the following constraint: $0 \leq u \leq 1$. There is a complete symmetry between x and $(1-x)$ in Eq. (24), which can be seen from the following general argument. We denote the entire set of box functions by $A(r)$, which is then a sum of individual non-overlapping box functions $A_{R,n}(r)$. The remaining space can be considered to be a distribution of boxes $B(r) = 1 - A(r)$. The structure in $B(r)$ interferes with that of $A(r)$, contrary to the dilute limit considered previously, and the distribution of $B(r)$ carries important correlations. The diffuse structure factor $S_{\rm dif}(q)$ in Eq. (24) can then be calculated as $S_{\rm dif}(q) = b^2|A(q) \otimes D(q)|^2$, where $A(q)$ and $D(q)$ are the Fourier transform of the collection of box functions and that of the perfect structure. From $A(r) + B(r) = 1$ for all r it follows that $B(q) = -A(q)$, for $q \neq Q_m$. This means that we get the same $S_{\rm dif}(q)$ whether we fill the A-boxes or the B-boxes with the structure and the rest with vacancies; small islands of a structure and small lacunas in a structure give the same diffuse scattering. Therefore a complete symmetry between x and $1-x$ must exist. Below we calculate the structure factor for different cluster size distributions.

2.5.1 Delta function distributed cluster sizes

It is interesting to investigate the 'excluded volume' effect in a simple example with clusters of equal length ℓ. The distribution function is now generalized to include the vacancies $\mathcal{D}(n) = \mathcal{V}\delta_{n,0} + \mathcal{N}\delta_{n,\ell}$, with $\mathcal{V} = 1 - x(1 + \frac{1}{\ell})$ and $\mathcal{N} = \frac{x}{\ell}$. Since the distribution must be non-negative $\mathcal{D}(n) \geq 0$, it follows that $x \leq \ell/(1+\ell)$. The general result can be written similar to Eq. (16)

$$\begin{aligned} S_{\rm dif}(q) &= x(1-x)b^2 \frac{(\ell - x - x\ell)\sin^2(qa\ell/2)}{[\ell^2(1-x)^2 - x\alpha_q]\sin^2(qa/2) + x\beta_q}\,, \\ \alpha_q &= 2\ell(1-x)\sin^2(qa\ell/2)\,, \\ \beta_q &= \ell(1-x)\sin(qa)\sin(qa\ell)/2 + x\sin^2(qa\ell/2)\,. \end{aligned} \tag{25}$$

For $x \to 0$ Eq. (25) reduces to Eq. (16) as expected. The line shape is displayed in Fig. 2 on a linear scale versus the q-vector in the first Brillouin zone $q \in [-\pi/a; \pi/a]$. It should be noted, that since the cluster size distribution is normalized, the integrated intensities of the different structure factors for a particular value of the particle concentration x, are also the same. The line shapes presented are calculated for $\ell = 5$, and particle concentrations of $x = 0.1$ (a), $x = 0.3$ (b), and $x = 0.5$ (c), respectively. It is interesting to note that the 'excluded volume' effect does not prohibit the intensity to vanish at certain wave vectors ($q = 4\pi m/\ell a$). For small particle concentration $x \leq x_{\rm delta} \approx 0.22$, $S_{\rm dif}(q)$ has a maximum at $q = 0$, decays smoothly for increasing q and becomes zero at $q = 4\pi/\ell a$. By comparison with a Lorentzian line shape for $\kappa = 1/\ell$, it is seen that $S_{\rm dif}(q)$ is much broader. For larger concentrations, $S_{\rm dif}(q)$ develops a satellite peak at a wave vector $q_{\rm sat}$. The position of $q_{\rm sat}$ is related to the

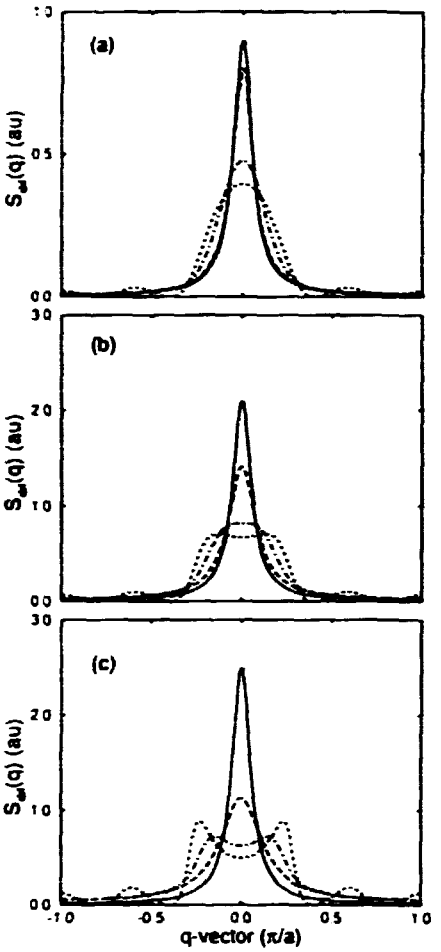

Figure 2: Lineshapes of the structure factor from one-dimensional distributions of non-overlapping clusters. The cluster distributions are indicated as follows: exponential distribution (long-dashed line), delta function distribution (dashed line), Poisson distribution (dashed-dotted line), and Lorentzian lineshape (solid line). The parameters used are: $\ell = 5$ and $\kappa a = \ell^{-1}$. The panels (a), (b), and (c) show the behavior for a particle concentration of $x = 0.1$, $x = 0.3$, and $x = 0.5$ respectively.

inverse length $1/\ell a$ of the clusters because the cluster length results in a characteristic separation between the clusters and therefore gives rise to a pseudo periodicity. This behavior has been discussed by Guinier [8], who called it the formation of a 'para-lattice'. The relation between q_{sat} and $1/\ell a$ is not trivial and depends on the value of x. This is demonstrated in Fig. 3 (a), where the position of q_{sat} is plotted versus x in the range $0 \leq x \leq \ell/(1+\ell)$. The upper bound on x comes from the requirement of a non-negative distribution function. The position of q_{sat} is shown for the delta function distribution for $\ell = 5, 10$, and 20. It is seen that q_{sat}=0 for $x \leq x_{delta}$, and q_{sat} becomes non-zero for $x > x_{delta}$. Thus for $x \leq x_{delta}$ there is no characteristic length scale in the problem except the cluster size ℓa. For $x > x_{delta}$ a new length

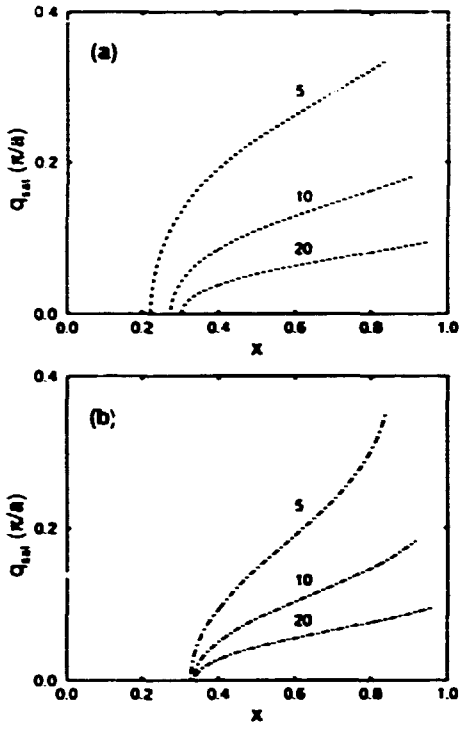

Figure 3: The location of the first maximum q_{sat} of the structure factor $S(q)$ within the Brillouin zone. The satellite positions q_{sat} are displayed as function of particle concentration x, for different values of the average cluster size $\ell = 5, 10$, and 20. In panel (a) and (b) are shown the results obtained from the delta function distribution (dashed line), and the Poisson distribution (dashed-dotted line) respectively. Notice that q_{sat} is consistently below $2\pi/\ell a$, which is the expected characteristic q-value.

scale enters: the characteristic separation between clusters given by $1/q_{sat}$. It should be noted that q_{sat} is consistently smaller than $2\pi/\ell a$, which from an experimental point of view is often taken to be the average separation between the clusters. The satellite position q_{sat} increases monotonically with x, since the distance between clusters becomes smaller at higher particle concentration. It is seen that (apart from the ℓ dependence of x_{delta}) the functional form of q_{sat} scale with ℓ. This has important consequences for the experimental situation, since it allows for a determination of the average cluster size from the knowledge of the particle concentration. In Fig. 4, we have for $\ell = 5$, and as a function of x plotted the width $\Delta(x)$ of $S_{dif}(q)$ defined as the half-width-half-maximum (HWHM), where the maximum is taken at the satellite position in case of splitting. As can be seen $\Delta(x)$ increases almost linearly, with a slight change in slope at $x = x_{delta}$.

2.5.2 Exponentially distributed cluster sizes

Let us derive the result for the exponential distribution of clusters. With the distribution function generalized to include vacancies we have $\mathcal{D}(n) = \mathcal{V}\delta_{n,0} + \mathcal{N}e^{-\kappa n a}$, where $\mathcal{V} = 1 - xe^{\kappa a}$ and $\mathcal{N} = x(e^{\kappa a} - 1)^2/e^{\kappa a}$. The condition for a non-negative

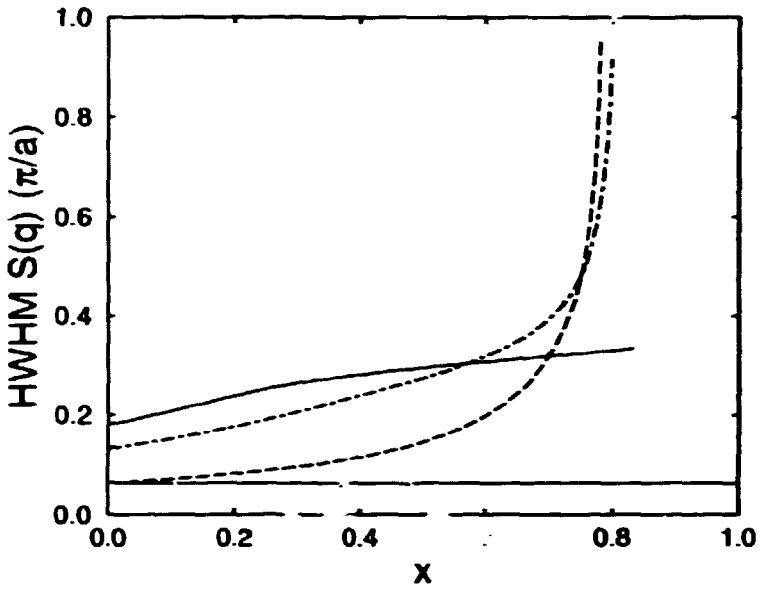

Figure 4: The width of the structure factors calculated from different cluster distributions are displayed as function of particle concentration x. The width of $S_{dif}(q)$ is measured as the half-width-half-maximum (HWHM), where the maximum is defined as $S_{dif}(q_{max})$ is case of splitting. The cluster distributions are indicated as follows: exponential distribution with $\kappa = 1/5a$ (long-dashed line); delta function distribution, $\ell = 5$, (dashed line); Poisson distribution, $\ell = 5$, (dashed-dotted line). The width of the Lorentzian, $\kappa = 1/5a$ (solid line), is independent of the particle concentration and is included for comparison.

distribution function yields $x \leq 1/(2 - e^{\kappa a})$. The general result can be written in a form similar to Eq. (17):

$$\begin{aligned} S_{dif}(q) &= b^2 x(1-x) \frac{(\alpha^2 - 1 - x\beta)}{(1-\alpha)^2 + (2\alpha(1-x)^2 - \beta x)(1 - \cos(qa))} , \\ \alpha &= e^{\kappa a} \\ \beta &= 2(1-x)\alpha(\alpha - 1) . \end{aligned} \tag{26}$$

Equation (26) reduces to Eq. (17) for $x \to 0$. However for finite x there are important corrections. The line shape remains Lorentzian around each Bragg point Q_m and can be expanded for small κ and q as

$$S_{dif}(q) \approx \frac{x(1-x)b^2}{a} \sum_{n=-\infty}^{\infty} \frac{2\kappa/(1-x)}{(\kappa/(1-x))^2 + (q - Q_n)^2} . \tag{27}$$

This shows that the FWHM of $S_{dif}(q)$ is increased, yielding $\kappa_{eff} = \kappa/(1-x)$. The line shape from Eq. (26) is plotted in Fig. 2 for $\kappa = 1/5a$ at particle concentrations $x = 0.1$

(a), $x = 0.3$ (b), and $x = 0.5$ (c) in the q-range $q \in [-\pi/a; \pi/a]$. In Fig. 4 we have plotted the width $\Delta(x)$ versus x as defined above. In the limit $x \to 0$, $\Delta(x)$ reduces to that of a Lorentzian $\Delta(x) \to \kappa$. For x not too large $x \lesssim 0.3$, the effective width κ_{eff} is rather well approximated by $\kappa_{\text{eff}} = \kappa/(1-x)$. However since $\Delta(x)$ diverges at $x = 1/(2 - e^{\kappa a})$, while κ_{eff} diverges at $x = 1$, the expansion, which gives rise to Eq. (27) is not valid for high particle concentrations.

2.5.3 Poisson distributed cluster sizes

The Poisson distribution function is given by $\mathcal{D}(n) = \mathcal{V}\delta_{n,0} + \mathcal{N}\ell^n/n!$, where ℓa is the average length of the cluster. The Poisson distribution appears to be a very plausible distribution of clusters in real physical systems with weak interactions, *e.g.* it would arise if the particles randomly occupy the lattice sites for small x. Normalization yield $\mathcal{V} = 1 - x(1 + \frac{1}{\ell})$ and $\mathcal{N} = \frac{x}{\ell}e^{-\ell}$. The condition for a non-negative distribution function is identical with that of the delta function distribution $x \leq \ell/(1+\ell)$. The expression for $S_{\text{dif}}(q)$ is more complicated than Eq. (26) and Eq. (25). The structure factor can be expressed as

$$
\begin{aligned}
S_{\text{dif}}(q) &= b^2 x(1-x)\frac{2\ell(1-x)(1-\alpha_q) - x(1+\beta_q - 2\alpha_q)}{x\lambda_q + x^2(1+\beta_q-2\alpha_q) + (2\ell x(1-x)\alpha_q + \gamma)(1-\cos(qa))} \\
\alpha_q &= e^{\ell\cos(qa)-\ell}\cos(\ell\sin(qa)) \\
\beta_q &= e^{2\ell\cos(qa)-2\ell} \\
\gamma &= 2\ell(1-x)(\ell - \ell x - x) \\
\lambda_q &= 2\ell(1-x)e^{\ell\cos(qa)-\ell}\sin(qa)\sin(\ell\sin(qa)) \,. \qquad (28)
\end{aligned}
$$

The line shape from Eq. (28) is plotted in Fig. 2 for $\ell = 5$ at particle concentrations $x = 0.1$ (a), $x = 0.3$ (b), and $x = 0.5$ (c) in the q-range $q \in [-\pi/a; \pi/a]$. Comparing with the delta distribution, we see that due to the variation of cluster lengths around ℓa, the intensity does not vanish at any q-vector. For small particle concentration $x \leq x_{\text{Poisson}} \approx 0.33$, $S_{\text{dif}}(q)$ has a maximum at $q = 0$, while for larger concentration, $S_{\text{dif}}(q)$ develops a satellite peak at a wave vector q_{sat}, as was the case for delta function distributed clusters. In the case of a Poisson distribution the particle concentration is much higher for a satellite to appear. In Fig. 3 (b), the position of q_{sat} is plotted versus x for $\ell = 5, 10$, and 20 in the range $0 \leq x \leq \ell/(1+\ell)$. The upper bound on x is the same as for the delta function distribution. Apart from the fact that x_{Poisson} shows much less ℓ dependence, the results are qualitatively the same as those for the delta function distribution. In Fig. 4, we have for $\ell = 5$ and as a function of x, plotted the width $\Delta(x)$ of $S_{\text{dif}}(q)$ as calculated from Eq. (28). The width Unlike the behavior for delta distributed $\Delta(x)$ diverges for $x \to \ell/(1+\ell)$ unlike the behavior for delta distributed clusters.

2.6 One-dimensional model for $YBa_2Cu_3O_{6+x}$

For a one-dimensional model to have relevance for a real material like $YBa_2Cu_3O_{6+x}$, we assume the existence of a direction or a plane where the ordering is predominant and chose our one-dimensional model system Ω perpendicular to this direction. In $YBa_2Cu_3O_{6+x}$ the oxygen ordering takes place in the basal CuO_x plane. Due to the large separation between these planes, the oxygen ordering has a pseudo-two-dimensional character. A predominant tendency towards formation of copper-oxide chains along one of the crystallographic axis (the b-axis) makes a one-dimensional description of the chain ordering with Ω along the a-axis appropriate (cf. Sec. 3.2, Fig. 5 and [22]). The two cluster types considered are composed of oxygen ordered

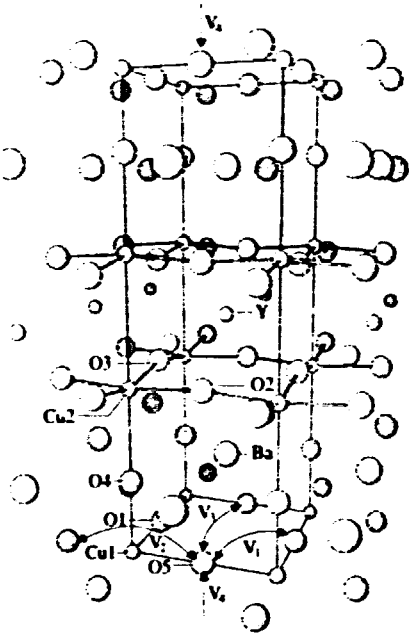

Figure 5: The crystallographic structure of $YBa_2Cu_3O_{6+x}$. The unit cell, which has almost ideal $1\times1\times3$ dimensions, is indicated by solid lines. All oxygen sites assume perovskite positions located halfway between the copper atoms along the square edges. The variable oxygen stoichiometry occur at the O1 and O5 sites in the basal planes, which are separated by $|c| = 11.7$ Å along the c-axis. The oxygen pair interaction parameters V_1, V_2, V_3, and V_4 are defined as follows: V_1 is the nearest neighbor repulsion, V_2 is the next nearest neighbor attraction between pairs bridged by Cu, V_3 is the next nearest neighbor repulsion between pairs not bridged by Cu, and V_4 is the nearest neighbor attraction between pairs on adjacent basal planes.

domains of ortho-I and ortho-II, which will be denoted type $t = \mathrm{I}, \mathrm{II}$ respectively. We wish to discuss the situation of perfectly ordered clusters of type $t = \mathrm{I}, \mathrm{II}$ with the same lattice, but different structures, distributed at random along Ω with an exponential size distribution $\mathcal{D}_t(n)$. The distance between the particles in the clusters is $s_t a$, where $s_{\mathrm{I}} = 1$ for ortho-I and $s_{\mathrm{II}} = 2$ for ortho-II. The ideal ortho-I structure consists

of an infinite sum of delta functions separated by $s_I a$ and is denoted $D_I(r)$. For the ideal ortho-II structure, the separation between the delta functions is $s_{II} a$, which gives rise to two possibilities. The situation where the delta functions occupy sites $2ma$ is denoted $D_{II}(r)$, while its anti-phase occupying the sites $(2m+1)a$ is denoted $D_{II}^{anti}(r)$. This means that the ordered structure has Bragg peaks at positions $Q_I = 2\pi m/a$ for ortho-I and $Q_{II} = \pi m/a$ for ortho-II, where m is an integer. The one-dimensional structure consists of clusters $f_{R,n}^t(r)$ of type $t = I, II$ and a zero background (vacancies) between the clusters. Let p_t be the fraction of particles in clusters of type $t = I, II$ so that $p_I + p_{II} = 1$; then x remains the total concentration of particles. An obvious generalization of Eq. (18) to the case of clusters with different structures yields:

$$S_{dif}(q) \approx xb^2 \sum_{t=I,II} \frac{p_t}{s_t a} \sum_{n_t} \frac{2\kappa_t}{\kappa_t^2 + (q - Q_{n_t})^2} . \tag{29}$$

Notice from the definition of $\mathcal{D}_t(n)$ that the correlation length in real space is s_t/κ_t. For $YBa_2Cu_3O_{6+x}$ this means that if $\kappa_I = \kappa_{II}$ the correlation for Ortho-II is twice that of Ortho-I. This has important consequences for the interpretation of the structure factor since Eq. (29) is often used experimentally to determine the correlation lengths of the individual domain structures. From Eq. (29) it follows that the relative amount of particles participating in the structures p_t is given by the relative *integrated* intensities of the characteristic Bragg positions. For $YBa_2Cu_3O_{6+x}$ the relative integrated intensity around Q_{II} and Q_I is $(1 - p_I)/(1 + p_I)$, whereas the relative peak intensity, on the other hand, depends on κ_t and is in this case $S_{dif}(Q_{II})/S_{dif}(Q_I) = (1 - p_I)/[1 + p_I((2\kappa_{II}/\kappa_I) - 1)]$.

Finally, we will consider situations with a dense packing of the two structures with $t = I, II$ (we indicate this case by a superscript 'dense'). We denote as before the collection of box functions by $A(r)$, and the remaining space by $B(r) = 1 - A(r)$. The interference effects are most clearly seen if we fill both the A-boxes and the B-boxes with the same of one of the structures $t = I, II$. Then the Fourier transform of the structure is a folding $\mathcal{F}(q) = D_t(q) \otimes A(q) + D_t(q) \otimes B(q) = 0$, *i.e.* complete destructive interference of the diffuse scattering, as expected. Then, consider A-boxes filled with structure $t = II$ and B-boxes filled with its anti-phase. The structure can be written $\mathcal{F}(r) = A(r)D_{II}(r) + B(r)D_{II}^{anti}(r)$. Apart from a phase factor e^{iqa} the Fourier transform of the phase and the anti-phase are the same, as can be judged from Eq. (10). Then, the total Fourier transform is $\mathcal{F}(q) = D_{II}(q) \otimes A(q) + D_{II}^{anti}(q) \otimes B(q) = D_{II}(q) \otimes A(q)(1 - e^{iqa})$, and therefore $S_{dif}^{dense}(q) = b^2|\mathcal{F}(q)|^2 = 2[1 - \cos(qa)]S_{dif}(q)$ is modulated with twice the period of the Bragg points relative to $S_{dif}(q)$ as found in Eq. (24). Next consider A-boxes having a structure $t = II$ and B-boxes filled with a $t = I$ structure. This situation can be regarded as a case with complete $t = II$ structure superimposed with the anti-phase in the B-boxes. The structure can be written $\mathcal{F}(r) = D_{II}(r) + B(r)D_{II}^{anti}(r)$. Then $\mathcal{F}(q) = D_{II}(q) + B(q) \otimes D_{II}(q)e^{iqa}$. Since $D_{II}(q)$ only contributes at the Bragg positions, $S_{dif}^{dense}(q) = S_{dif,II}(q)$. This means that

only the diffuse scattering from type t = II A-boxes remains. Other situations can easily be calculated along the same lines.

3 Structure factor of $YBa_2Cu_3O_{6+x}$

The crystallographic structure of $YBa_2Cu_3O_{6+x}$ is based on a unit cell, which consists of a stack of three perovskite cubes. The unit cell has almost ideal $1 \times 1 \times 3$ dimensions. The primitive unit vectors of the unit cell are $|\mathbf{a}| = 3.9$ Å, $|\mathbf{b}| = 3.9$ Å, and $|\mathbf{c}| = 11.7$ Å, and they are mutually orthogonal. The essential features of the crystal structure are described in Fig. 5, where the unit cell is indicated by solid lines. The interaction parameters V_1, V_2, V_3, and V_4 are discussed in Sec. 3.2. The notation $A(x, y, z)$ denotes that atom A is located at (x, y, z) in the unit cell in the basis of the primitive vectors, with the site nomenclature from Jorgensen *et al.* [23]. The unit cell is generated by Y(1/2, 1/2, 1/2), Ba(1/2, 1/2, 0.19), Cu1(0, 0, 0), Cu2(0, 0, 0.36), O1(0, 1/2, 0), O2(1/2, 0, 0.38), O3(0, 1/2, 0.38), O4(0, 0, 0.15), and O5(1/2, 0, 0), and using the mirror plane symmetry at the level of the yttrium atom. All oxygen atoms assume perovskite positions located halfway between the copper atoms along the cube edges. There are no oxygens at the level of the Y atom, but the oxygen sites O2 and O3 at the level of Cu2 are fully occupied. From single crystal neutron diffraction measurements it is known that only the oxygen sites O1 and O5 have a variable occupation [24]. Writing the total number of oxygen atoms in the unit cell as $c_{ox} = 6 + x$, it follows that the oxygen stoichiometry x is given by

$$x = \langle \sigma(\mathrm{O1}) \rangle + \langle \sigma(\mathrm{O5}) \rangle \,. \tag{30}$$

Experimentally the oxygen stoichiometry x can only be varied between $x = 0$ and $x = 1$. Under high pressure the compound is unstable towards formation of the superconducting material $YBa_2Cu_4O_8$. The compound exhibits two structural phases at high temperature [25]. For small x-values, the oxygen atoms are equally distributed between the sites O1 and O5, and the compound is tetragonal with space group P4/mmm. For low temperatures the compound becomes orthorhombic with space group Pmmm, due to oxygen chain formation in the basal plane, where the oxygen atoms preferentially occupy the O1 sites, while the O5 sites become depleted. At high concentration x, where almost all O1 sites are occupied the orthorhombic phase is known as the ortho-I phase. The stoichiometric composition of the ortho-I phase is $x = 1$, which corresponds to a two fold degenerate oxygen structure. At lower concentrations the next nearest neighbor repulsion V_3 (see Sec. 3.2) between the oxygen atoms becomes important and the compound develops an oxygen structure known as the ortho-II phase. At the stoichiometric composition the ortho-II phase has $x = 1/2$ and it corresponds to is a four fold degenerate oxygen structure.

As discussed in Sec. 2 we need only be concerned with the atomic sites, which have a variable occupation in the structure factor calculation. Therefore only the

oxygen atoms located at the O1 and O5 sites are taken into account. From Eq. (7) the diffuse part of $S(\mathbf{q})$ for the oxygen atoms reduces to

$$S_{dif}(\mathbf{q}) = \langle \left| \sum_{\mathbf{r}} \sum_{j=1}^{2} e^{i\mathbf{q}\cdot(\mathbf{r}+\mathbf{d}_j)} \Delta\sigma(\mathbf{r}+\mathbf{d}_j) b_{ox} \right|^2 \rangle \,, \tag{31}$$

where b_{ox} is the scattering cross section for an oxygen atom. The basis vectors for the oxygen atoms in the unit cell are given by $\mathbf{d}_1 = (1/2, 0, 0)$ and $\mathbf{d}_2 = (0, 1/2, 0)$. In the next section we will discuss applications of symmetry to reduce the computational work in connection with calculations of the structure factor.

3.1 Application of symmetry

As discussed in Sec. 2.1, the symmetries of a crystal play an important role in structure factor calculations. In this section we will consider the symmetry reduction of the structure factor in the case of $YBa_2Cu_3O_{6+x}$. The orthorhombic $YBa_2Cu_3O_{6+x}$ compound is topologically almost identical to the tetragonal form. The a and b axis generally differ less than 2%, giving rise to a pseudo-tetragonal unit cell. In the computer simulations we will ignore this small difference and always consider the compound to be tetragonal using the symmetries of the space group P4/mmm. In Fig. 6 (a) is shown the basal plane of $YBa_2Cu_3O_{6+x}$ with the c axis perpendicular to the plane. The point group symmetries corresponding to P4/mmm consist of three perpendicular rotors 2_x, 2_y, and 2_z, in addition to a four fold rotor 4_{xy} as indicated on the figure. The symmetry elements are indicated by the conventional crystallographic symbols. In Fig. 6 (b) are shown the corresponding symmetries in reciprocal space, which were derived using results from Sec. 2.1. In general the structure factor will not have the periodicity of the first Brillouin zone. However in the P4/mmm space group, the basis vectors $\mathbf{d}_1$ and $\mathbf{d}_2$ occupy high symmetry positions, leading to the following translational symmetry: $S(\mathbf{q} + 2\mathbf{b}_j) = S(\mathbf{q})$, for $j = 1,2$ and $S(\mathbf{q} + \mathbf{b}_j) = S(\mathbf{q})$ for $j = 3$. The translational periodicity gives rise to an additional symmetry element, which is a mirror plane perpendicular to the endpoint of the primitive reciprocal lattice vectors for $j = 1,2$. This can be understood as follows: For $j = 1,2$ we have $S(\mathbf{q} + \mathbf{b}_j) = S(-\mathbf{q} - \mathbf{b}_j) = S(-\mathbf{q} - \mathbf{b}_j + 2\mathbf{b}_j) = S(-\mathbf{q} + \mathbf{b}_j)$, where the inversion symmetry and the translational symmetry have been used. The symmetry elements define a minimal zone, the *irreducible zone*, in reciprocal space, which generates the entire structure factor by repetitive use of symmetries. In Fig. 6 (b) the irreducible zone is shown as the cross hatched triangle. Thus in the computer calculation of the structure factor only the $\mathbf{q}$-vectors in this zone need to be calculated.

3.2 Modeling of oxygen order

The model used in the calculations is an extension to three dimensions of the well known two-dimensional locally anisotropic lattice gas model, which includes near-

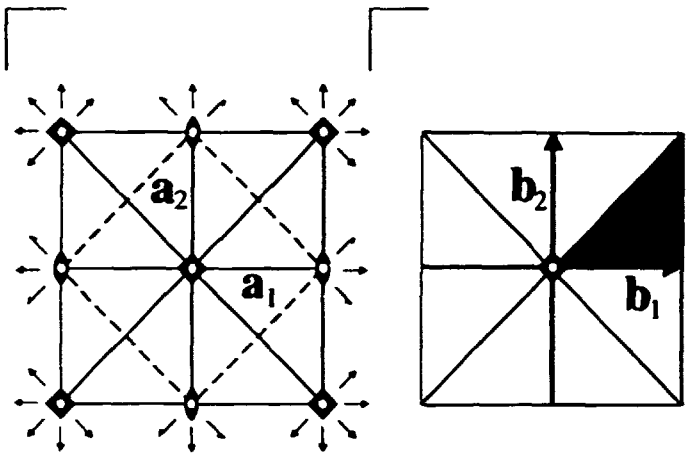

Figure 6: In (a) is shown the projection of the space group $P4/mmm$ along the c-axis (from Ref. [34]). The symmetry elements are indicated with the conventional crystallographic symbols. In (b) is shown the corresponding symmetries in reciprocal space. The irreducible zone is shown as the cross-hatched triangle.

est neighbor and next nearest neighbor interactions (the ASYNNNI model). The two-dimensional model, originally proposed by de Fontaine *et al.* [3], describes the ordering of oxygen atoms in the basal CuO_x plane of $YBa_2Cu_3O_{6+x}$. From Fig. 5 the basal planes are seen to consist of a square lattice of copper atoms, with oxygen sites located halfway between the copper atoms along the square edges. The pair interaction parameters V_1, V_2, V_3, and V_4 are defined as follows, see Fig. 5: V_1 is the nearest neighbor repulsion between to oxygen atoms; V_2 is the next nearest neighbor attractive interaction between pairs of oxygen atoms, that are bridged by a copper atom (NNNCu), while V_3 a repulsive interaction between oxygen atoms which are not bridged by a copper atom (NNNV). The three-dimensional extension of the ASYNNNI model is introduced as a nearest neighbor attractive interaction V_4 between pairs of oxygen atoms located on adjacent basal planes vertically above and below each other (NNPl).

In the computer simulations it is convenient to introduce an orthogonal basis $\mathbf{e}_1$, $\mathbf{e}_2$, and $\mathbf{e}_3$, which is rotated 45° around the crystallographic c-axis. The primitive tetragonal oxygen lattice, which constitutes the O1 and O5 sites, is then given by

$$\mathbf{e}_1 = (\mathbf{a}_1 + \mathbf{a}_2)/2, \quad \mathbf{e}_2 = (\mathbf{a}_2 - \mathbf{a}_1)/2, \quad \mathbf{e}_3 = \mathbf{a}_3. \tag{32}$$

Equivalently in Eq. (32), we could interchange $\mathbf{a}_1$ and $\mathbf{a}_2$ due to symmetry. In this basis, the positions of the oxygen atoms at the O1 and O5 sites are written

$$\mathbf{r} = n_1\mathbf{e}_1 + n_2\mathbf{e}_2 + n_3\mathbf{e}_3 \,, \tag{33}$$

where n_1, n_2, and n_3 are integers. This leads to a three-dimensional Hamiltonian of the following form:

$$\begin{aligned}\mathcal{H} \;=\; & -V_1 \sum_{\langle \mathbf{r}\mathbf{r}' \rangle}^{NN} \sigma(\mathbf{r})\sigma(\mathbf{r}') - V_2 \sum_{\langle \mathbf{r}\mathbf{r}' \rangle}^{NNNCu} \sigma(\mathbf{r})\sigma(\mathbf{r}') - V_3 \sum_{\langle \mathbf{r}\mathbf{r}' \rangle}^{NNNV} \sigma(\mathbf{r})\sigma(\mathbf{r}') \\ & -V_4 \sum_{\langle \mathbf{r}\mathbf{r}' \rangle}^{NNPl} \sigma(\mathbf{r})\sigma(\mathbf{r}') - \mu \sum_{\mathbf{r}} \sigma(\mathbf{r}) \,,\end{aligned} \tag{34}$$

where $\sigma(\mathbf{r})$ is the site occupation variable for the oxygen atom. Thus $\sigma(\mathbf{r}) = 1$ if the site is occupied and zero otherwise. The sum runs over all oxygen pairs $(\mathbf{r}, \mathbf{r}')$, that are nearest neighbor (NN and NNPl) or next nearest neighbors (NNNV and NNNCu), respectively. The chemical potential μ acts as an external field, which is related to the equilibrium oxygen partial pressure in the sample [22, 25]. We have used the following values for the normalized interaction parameters,

$$(V_1, V_2, V_3, V_4) = (-1, 0.36, -0.12, 0.02) \,, \tag{35}$$

which are brought on an absolute energy scale by multiplication with the normalization constant $V_0/k_B = 4470\text{K}$ [26]. The set of normalized two-dimensional lattice gas interaction parameters (V_1, V_2, V_3) comes from Refs. [27, 28, 29]. The inter-plane attractive parameter V_4 has been suggested by de Fontaine *et al.* [30]. The stoichiometric factor x is related to the average number of oxygen atoms on the lattice by

$$x = \frac{2}{N_{\text{tot}}} \langle \sum_{\mathbf{r}} \sigma(\mathbf{r}) \rangle \,, \tag{36}$$

where N_{tot} is the number of available oxygen sites. The statistical thermodynamic calculation of the oxygen ordering properties is performed by Monte Carlo simulation of the Hamiltonian Eq. (34) with the interaction parameters Eq. (35), using the Metropolis algorithm [31, 32, 33]. In the computer simulation the structure factor $S_{\text{dif}}(\mathbf{q})$ has been calculated from Eq. (7). In the next section we discuss the algorithms used in the implementation of the extension of the ASYNNNI model to three dimensions and the calculation of the structure factor on the Connection Machine.

4 Implementation on the Connection Machine

The main drawback of the Monte Carlo technique is that it is extremely time consuming (running several weeks on a workstation is not uncommon). Vectorizing the

procedure is not easy, because the Monte Carlo algorithm is an inherently sequential process, where the basic computational step as discussed previously consists of randomly selecting a lattice site and updating it according to some transition probability. Nevertheless, in recent years several vectorized and parallel updating algorithms have been devised for speeding up the convergence. One of the problems arising from the use of parallel updating methods is the necessary redefinition of the time variable. However, as far as equilibrium properties are concerned, the sequential and the parallel updating methods lead to the same results. In the present study we have developed a parallel updating algorithm for the three-dimensional extension of the ASYNNNI model, which naturally maps onto the underlying architecture of the Connection Machine (CM2). The Connection Machine is a SIMD computer with 65536 bit-processors and a hyper-cubic data router. In our simulations we have used 16384 processors. The program was implemented in Connection Machine Fortran (CMF) with calls to the Connection Machine Scientific Software Library (CMSSL).

To update the lattice we have used the Metropolis algorithm employing the standard method of dividing the lattice into non-interacting sublattices. We have used four sublattices within each a-b plane. However, due to the inter-plane coupling, two alternating sets are used along the c-axis, giving a total of eight sublattices. Since only one of the chosen sublattices is updated at a time, each one has been spread across all the available processors of the CM2.

Using the data layout described above, each oxygen site interacts with ten neighboring oxygen sites located on four different sublattices. This somewhat complicates the gathering of neighbors. The complication is, however, almost purely in programming effort, and does only marginally affect the performance of the local stencil. The performance gained by being able to keeping all processors active at all times, far outweighs the loss from using a more complicated stencil. To maximize the bandwidth of the inter-processor communication needed to implement the stencil we have used communication commands from CMSSL.

The data organization used for Monte Carlo updating is, however, not the optimal one for calculating the structure factor. Before each calculation of the structure factor the different sublattices are therefore reassembled into the full lattice. By aligning the different sublattices and the full lattice properly, and using the communication commands from CMSSL, this reassembling process can be carried out without making necessary any data transfer between processors. After the data reordering, the structure factor is calculated using a standard fast Fourier transform.

5 Numerical results

For the results of the structure factors presented we have used 10^4 Monte Carlo steps per site (MCSS) for equilibration, followed by $5 \cdot 10^4$ MCSS with averaging taken every 10 MCSS. In all simulations we have used periodic boundary conditions. By

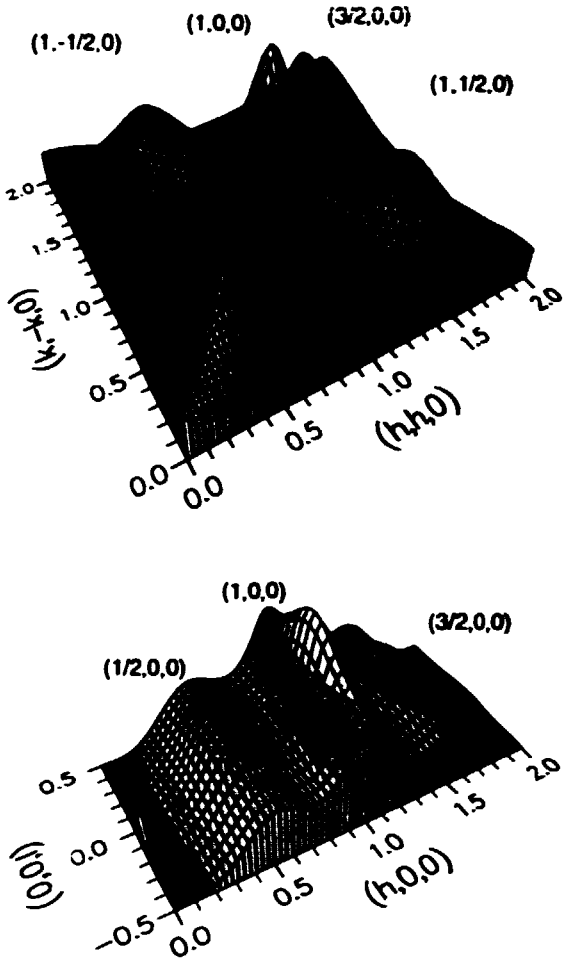

Figure 7: Structure factor for an $256\times256\times16$ system with $x = 0.4$ at $T = 0.15V_0/k_B$ which is above T_c for $x = 0.4$ ($T_c = 0.13V_0/k_B$). Vertically, the logarithm of the intensity of the structure factor $S(\mathbf{q})$ is shown in arbitrary units. See detailed description in text.

using 16384 processors on the CM2 we have achieved a maximum performance of $8.7 \cdot 10^6$ MCSS/sec.

The results for the structure factor are shown in Fig. 7 for $x = 0.4$ and in Fig. 8 for $x = 0.5$. The structure factors have been calculated for a $256\times256\times16$ system at $T = 0.15V_0/k_B$, which is above the critical temperature [26]: $T_c(x = 0.4) = 0.13V_0/k_B$ and $T_c(x = 0.5) = 0.14V_0/k_B$. Vertically, the logarithm of the intensity of the structure factor $S(\mathbf{q})$ is shown in arbitrary units. In panel (a) is shown the result for the $l = 0$ plane in q-space, which extends over four Brillouin zones. The q_x axis along $(h, h, 0)$ and the q_y axis along $(k, -k, 0)$ in the plot are rotated 45° around the crystallographic c-axis. The numbers on the axis indicate the values of h and k respectively. The five peaks shown are, using notation (h, k, l): $(1/2, 0, 0)$, $(1, 0, 0)$, $(3/2, 0, 0)$, $(1, -1/2, 0)$,

and $(1, 1/2, 0)$. The delta function contributions at $(0,0,0)$ and $(2,0,0)$ have been removed for clarity. In panel (b) is shown the corresponding $k = 0$ plane in q-space extending over two Brillouin zones. The axis in the plot are $(h,0,0)$ and $(0,0,l)$. The three peaks shown are: $(1/2,0,0)$, $(1,0,0)$, and $(3/2,0,0)$. The line scan at $l = 0$, for $0 \leq h \leq 2$ in panel (b) can be identified with the diagonal line through the peaks: $(1/2,0,0)$, $(1,0,0)$, and $(3/2,0,0)$ in panel (a). Again the delta function contributions at $(0,0,0)$ and $(2,0,0)$ have been removed for clarity.

By fitting the $(1/2,0,0)$ peak to a three-dimensional Lorentzian line shape for the diffuse part of the structure factor (including a fitted Lorentzian at the $(1,0,0)$ position and a background term), we have determined the widths Δh, Δk, and Δl along the main crystallographic axis. For the structure factor presented in Fig. 7 at $x = 0.4$ we obtain $\Delta h = 0.2738$, $\Delta k = 0.1285$, and $\Delta l = 0.530$, which gives the following values for the anisotropy $\Delta k/\Delta h = 0.47$ and $\Delta l/\Delta h = 1.94$. In the same fashion we obtain for the structure factor presented in Fig. 8 at $x = 0.5$, $\Delta h = 0.1274$, $\Delta k = 0.0645$, and $\Delta l = 0.297$, which gives the following values for the anisotropy $\Delta k/\Delta h = 0.51$, and $\Delta l/\Delta h = 2.33$. By comparison of the individual widths Δh, Δk, and Δl for the two oxygen stoichiometries, we see that the values for $x = 0.5$ are smaller than those for $x = 0.4$ by a factor of roughly two. This difference can be attributed to the curvature of the tetragonal/ortho-II phase boundary, see Ref. [22], which implies that the phase boundary for the $x = 0.4$ case is much further away than for the $x = 0.5$ case and the system is therefore stronger ordered.

The results for the anisotropy $\Delta k/\Delta h = 0.47$ at $x = 0.4$ for the three-dimensional calculation, can be compared with the corresponding result for the two-dimensional calculation with the same intra-plane interaction parameters. In Ref. [22] we obtained $\Delta k/\Delta h = 0.50$. Hence we find, that the inclusion of a weak inter-plane interaction only marginally affects the anisotropy. From mean-field theory [26], and as verified by Monte Carlo simulations in Ref. [22] the anisotropy is known to be almost temperature independent at least not too close to the critical temperature. Therefore, even though the individual widths cannot be compared as discussed above, we can use our results to determine the oxygen concentration dependence on the anisotropies. For the anisotropy within the basal plane, there appears to the no concentration dependence, as can be realized from the almost identical values $\Delta k/\Delta h = 0.47$ for $x = 0.4$ and $\Delta k/\Delta h = 0.51$ for $x = 0.5$. For the inter-plane anisotropy, the difference between the results $\Delta l/\Delta h = 1.93$ at $x = 0.4$ and $\Delta l/\Delta h = 2.33$ at $x = 0.5$ seems to be too large to be explained by the statistical uncertainty and it is probably due to the weak temperature dependence.

Recently, Zeiske *et al.* [9] measured the oxygen ordering in $YBa_2Cu_3O_{6+x}$ ($x = 0.4$) by neutron diffraction. By measuring the structure factor at room temperature, they observed diffuse superstructure reflections (h,k,l) at $(1/2,0,0)$. By fitting the profile of the superstructure reflections to a Gaussian, they determined the widths Δh, Δk and Δl. They obtained $\Delta h = 0.099$, $\Delta k = 0.049$ and $\Delta l = 0.52$, which gives the following values for the anisotropies: $\Delta k/\Delta h = 0.50$ and $\Delta l/\Delta h = 5.25$.

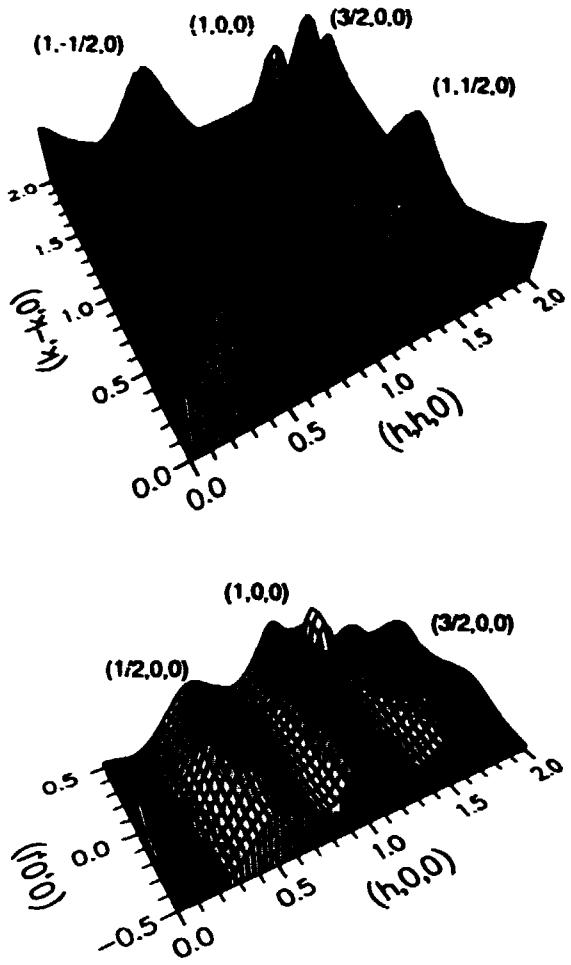

Figure 8: Structure factor for an $256 \times 256 \times 16$ system with $x = 0.5$ at $T = 0.15V_0/k_B$ which is above T_c for $x = 0.5$ ($T_c = 0.14V_0/k_B$). Vertically, the logarithm of the intensity of the structure factor $S(\mathbf{q})$ is shown in arbitrary units. See detailed description in text.

By comparing with the corresponding results from the three-dimensional calculation; $\Delta k/\Delta h = 0.47$ and $\Delta l/\Delta h = 1.93$, we see that while the intra-plane anisotropy are in excellent agreement with experiment, the inter-plane anisotropy is too large. The result implies that for particular values of the correlation lengths ξ_a and ξ_b, the correlation length ξ_c along the c-axis in our Monte Carlo simulation is too large as compared to the experimental data. Therefore, the attractive inter-plane interaction parameter V_4 used in the model should be reduced. This is in agreement with our mean-field analysis [26], where we obtain $|V_4| = |V_3|/(\Delta l/\Delta h)^2 = 0.0044V_0$. It should be mentioned that the experimental data are measured at room temperature, while the numerical data were obtained above the ortho-II ordering temperature. The rational for this comparison is the observation that only short-range ordering was

observed experimentally, which indicates that short-range ordered domain structures are frozen in at the tetragonal to orthorhombic phase transition [22].

6 Summary and conclusions

In the present paper we have developed the scattering formalism for lattice gas models with special emphasis on the diffuse part of the structure factor, $S_{dif}(\mathbf{q})$. Analytical solutions are presented for one-dimensional lattice gas models, and numerical results of the three-dimensional oxygen ordering in the high temperature superconductor $YBa_2Cu_3O_{6+x}$ have been calculated from Monte Carlo simulation studies.

In the one-dimensional case we have considered a lattice gas with only one atomic species and computed $S_{dif}(q)$ analytically for random distributions of perfectly ordered clusters with different size distribution functions, $\mathcal{D}(n)$. The analysis has been carried out in the case of low average coverage of species on the lattice, $x \ll 1$ (the dilute limit), and for larger concentrations where interference between the randomly distributed ordered clusters and the intervening vacancy regions, the so-called 'excluded volume' effect, cannot be neglected. The size distribution functions considered are the delta function distribution (equal size), exponential distribution, and the Poisson distribution. In the dilute limit a one to one correspondence between either two of $S_{dif}(q)$, $\mathcal{D}(n)$, and $C(na)$ (the correlation function) has been established analytically. From these relations it is shown that a Lorentzian squared line shape of the structure factor corresponds to a narrow distribution of small cluster sizes. Therefore, this lineshape cannot occur in extended short-range ordered one-dimensional systems. For the exponential distribution function we find that $S_{dif}(q)$ is well described by a simple Lorentzian line-shape for all q-vectors and a large range of correlation lengths.

For larger concentrations satellite peaks develop in $S_{dif}(q)$ for the delta function distributed and the Poisson distributed cluster sizes. These distribution functions have a maximum weight for finite chain length, and as a consequence of the 'excluded volume' effect they give rise to the formation of a para-lattice for particle concentrations exceeding a critical value, x_{sat}, that depends on the details in the distribution function. The basic reason for the formation of the para-lattice is the tendency for the finite size clusters to pack in the lattice with a characteristic separation. The separation is determined by the average cluster length and the particle density. It should be noted that the satellite position is consistently smaller than $2\pi/\ell a$, where ℓa is the average cluster length.

Based on the tendency towards oxygen chain formation in the basal CuO_x plane of $YBa_2Cu_3O_{6+x}$ we have mapped the oxygen ordering properties of this material onto a one-dimensional model and analysed $S_{dif}(q)$ for structures that are composed of vacancies and of oxygen ordered domains of the two orthorhombic structural phases ortho-I and ortho-II, respectively. In the dilute limit, where the lineshapes are Lorentzians, we establish relations between the ratios of the intensities (peak as well as integrated) of the structure factor centered at the Bragg positions, Q_I for the ortho-I phase and

Q_{II} for the ortho-II phase. Further, it is shown, that the correlation length of the ortho-II structure resulting from an analysis of the peak width of $S_{dif}(q)$ is twice as large as that of the ortho-I for the same peak width. Structure factor calculation of densely packed ortho-I and ortho-II domains are also presented.

In the dilute limit it is argued that the results may be generalized to higher dimensions by considering the shape function obtained by projecting the scattering density onto the line defined by the scattering q-vector. However, the effect of the 'excluded volume' cannot be solved analytically for densely packed structures in higher dimensions, and it should be realized that the correlations between different types of ordered and disordered structures cannot in general be neglected.

With special emphasis on the three-dimensional oxygen ordering of $YBa_2Cu_3O_{6+x}$ we have extended the two-dimensional ASYNNNI model to three dimensions and carried out such studies numerically by Monte Carlo simulation technique using the following values for the interaction parameters $(V_1, V_2, V_3, V_4) = V_0(-1, 0.36, -0.12, 0.02)$ with $V_0 = 4470$K. From the formal analysis of the structure factor, $S_{dif}(\mathbf{q})$, we show that the resolution, which may be accomplished by the simulation studies, is intrinsically related to the system size. As a consequence it is only possible to carry out a detailed analysis of the line shape on large model systems. In order to gain sufficient resolution we have developed a parallel updating algorithm for the three-dimensional extension of the ASYNNNI model and implemented it on a CM2 Connection Machine. Structure factor calculations have been carried out for oxygen stoichiometries, $x = 0.4$ and $x = 0.5$, on a $256\times256\times16$ system at a temperature $T = 0.15V_0/k_B$ in the tetragonal disordered phase ($T_c = 0.13V_0/k_B$ for $x = 0.4$, and $T_c = 0.14V_0/k_B$ for $x = 0.5$). By application af the symmetry relations pertinent to the oxygen lattice of $YBa_2Cu_3O_{6+x}$, we have reduced the computational efforts of calculating the structure factors to an irreducible zone of reciprocal space which is 1/16 of the Brillouin zone. The structure factor have been fitted excellently by a three-dimensional Lorentzian and the peak widths along the three major crystallographic axes have been determined. The anisotropy ratios $\Delta k/\Delta h = 0.47$ and $\Delta l/\Delta h = 1.94$ for $x = 0.4$ and $\Delta k/\Delta h = 0.51$ and $\Delta l/\Delta h = 2.33$ for $x = 0.5$ have been compared with those obtained from previous two-dimensional studies and with recent experimental results for $x = 0.4$. The in-plane anisotropies obtained in the two- and three-dimensional simulations are only marginally different and there appears to be no concentration dependence. However, the difference between the interplane anisotropy ratios $(\Delta l/\Delta h)$ for $x = 0.4$ and $x = 0.5$ cannot be explained by statistical errors, but may be a consequence of the difference in the temperatures relative to T_c. Comparison with mean-field calculations and results obtained from two-dimensional Monte Carlo simulation studies suggest that the anisotropy ratios are independent of temperature, but this is not necessarily the case for temperatures close to T_c. Further studies of these properties are in progress. For the $x = 0.4$ case we have compared the peak width anisotropies with similar experimental data and found excellent agreement for the in-plane anisotropy ratio, but a significant deviation for the inter-plane ratio. This

discrepancy may be remedied by reducing the inter-plane interaction parameter V_4 by a factor of five.

The present and previous Monte Carlo simulation studies have shown that the ASYNNNI model, in its original form and by the extension to three dimensions, may be used to account for many of the oxygen ordering properties in the basal CuO_x plane of $YBa_2Cu_3O_{6+x}$. The prospects of such studies are appealing because the superconducting properties are known to depend critically on details in the oxygen ordering. Many studies have focused on the structural phase transition temperatures, $T_c(x)$, between the tetragonal disordered and the orthorhombic ordered phases, for which reliable experimental data are available. However, since the $T_c(x)$ curve is essentially a straight line it is not surprising that it may be successfully established for different values of the three model parameters in the two-dimensional ASYNNNI model. Away from the phase transition line the available experimental structural data are in qualitative agreement with the model predictions, but they are not sufficiently detailed that the validity of the ASYNNNI model and the appropriate interaction parameters may be estimated in more extended parts of the phase diagram. Generally $S_{dif}(\mathbf{q})$ may supply structural information in a larger part of the phase diagram, and additional details about the ordering properties and the interaction parameters are contained in the line shape profiles and intensities. In particular one may study $S_{dif}(\mathbf{q})$ in the critical region in order to establish the universality class. The high resolution experiments and simulations needed for such studies are becoming available by the development of new diffraction techniques and massive parallel computers. In the present work we have initiated such studies of the three-dimensional oxygen ordering in $YBa_2Cu_3O_{6+x}$ by the use of a simple extension of the two-dimensional ASYNNNI model. Our results indicate that such studies may be used to determine the effective interaction parameters in the model. They also show that the anisotropy in the in-plane correlation lengths are little affected by the inter-plane coupling. However, our initial studies of the structural phase diagram indicate that the energy scale factor, V_0, should be significantly modified. More detailed analysis are in progress and will be presented elsewhere.

Acknowledgments

Stimulating discussions with Prof. G. Uimin, who has kindly supplied a preprint of his unpublished work, are greatly acknowledged. T.F. is supported by The Danish Research Academy. The work is supported by the Danish Ministry of Energy, the Danish Natural Science Research Council, and the CEC Science and Esprit programs. The simulations were carried at the Supercomputer Computations Research Institute located at the Florida State University. The research institute is partially funded by the U.S. Department of Energy under contract number DE-FC05-85ER250000.

References

[1] W. Schweika and H. G. Houbold, Phys. Rev. B **37**, 9240 (1991).

[2] L. Reinhard, B. Schönfeld, and G. Kostorz, Phys. Rev. B **41**, 1727 (1990).

[3] D. de Fontaine, L. T. Wille, and S. C. Moss, Phys. Rev. B **41**, 8698 (1987).

[4] D. K. Hilton, B. M. Gorman, P. A. Rikvold, and M. A. Novotny, Phys. Rev. B **46**, 381 (1992).

[5] P. Fratzl, J. L. Lebowitz, O. Penrose, and J. Amar, Phys. Rev. B **44**, 4794 (1991).

[6] G Porod, Colloid-Zeitschrift **124**, 83 (1951).

[7] G. Porod, Colloid-Zeitschrift **125**, 51 (1952).

[8] A. Guinier, *X-Ray Diffraction* (W. F. Freeman and Co., San Francisco, 1963).

[9] T. Zeiske *et al.*, Nature **353**, 542 (1991).

[10] H. E. Stanley, *Introduction to Phase Transitions and Critical Phenomena* (Oxford, New York, 1971).

[11] E. Vives and P. A. Lindgård, Phys. Rev. B **44**, 1318 (1991).

[12] O. V. Kovalev, *Irreducible Representations of the Space Groups* (Gordon and Breach, Science Publishers, New York, 1965).

[13] M. A. Krivoglaz, *Theory of X-Ray and Thermal-Neutron Scattering by Real Crystals* (Plenum Press, New York, 1969).

[14] H. Jagodzinski and F. Frey, in *International Tables for Crystallography, Volume B*, edited by U. Shmueli (Kluwer Academic Publishers, Dordrecht, 1993).

[15] S. W. Lovesey, *Theory of Neutron Scattering from Condensed Matter* (Oxford University Press, New York, 1984).

[16] D. C. Champeney, *Fourier Transforms and their Physical Applications* (Academic Press, London, 1973).

[17] G. Arfken, *Mathematical Methods for Physicists* (Academic Press Inc., Boston, 1985).

[18] D. K. C. MacDonald, *Noise and Fluctuations: an Introduction* (John Wiley & Sons, Inc., New York, 1962).

[19] I. S. Gradshteyn and I. M. Ryzhik, *Tables of Integrals, Series, and Products* (Academic Press Inc., London, 1980).

[20] G. Uimin, (unpublished).

[21] R. L. Pego, Proc. Roy. Soc. **422**, 261 (1989).

[22] T. Fiig *et al.*, Physica C **217**, 34 (1993).

[23] J. D. Jorgensen *et al.*, Phys. Rev. B **36**, 5731 (1987).

[24] H. Casalta *et al.*, (unpublished).

[25] N. H. Andersen, B. Lebech, and H. F. Poulsen, Physica C **172**, 31 (1990).

[26] T. Fiig *et al.*, (unpublished).

[27] J. V. Andersen, *Non-Equilibrium Phase Transitions and Ordering Processes in Lattice Gas Models* (Ph.D Thesis, The Technical University of Denmark, 1991).

[28] H. F. Poulsen, *Oxygen Ordering and Superconductivity in the High T_c Superconductor $YBa_2Cu_3O_{6+x}$* (Ph.D Thesis, Risø National Laboratory, Denmark, 1991).

[29] H. F. Poulsen *et al.*, Phys. Rev. Lett. **66**, 465 (1991).

[30] D. de Fontaine, G. Ceder, and M. Asta, J. Less-Common Met. **164/165**, 108 (1990).

[31] D. W. Heermann and A. N. Burkitt, *Parallel Algorithms in Computational Science* (Springer-Verlag, Berlin, 1991).

[32] K. Binder, in *Monte Carlo Methods in Statistical Physics*, edited by K. Binder (Springer, Berlin, 1979).

[33] K. Binder and D. W. Heermann, *Monte Carlo Simulation in Statistical Physics* (Springer-Verlag, Berlin, 1988).

[34] U. Shmueli, *International Tables for Crystallography, Volume A* (Kluwer Academic Publishers, Dordrecht, 1993).

Paper II

Oxygen Ordering Phenomena in $YBa_2Cu_3O_{6+x}$ Studied by Monte Carlo Simulation:

Phase Diagram, Structure Factor and Oxygen Equilibrium Pressure

Physica C 217 (1993) 34–52
North-Holland

PHYSICA C

Oxygen-ordering phenomena in $YBa_2Cu_3O_{6+x}$ studied by Monte Carlo simulation

Phase diagram, structure factor and oxygen equilibrium pressure

T. Fiig [a], J.V. Andersen [b], N.H. Andersen [a], P.A. Lindgård [a], O.G. Mouritsen [c] and H.F. Poulsen [d]

[a] *Department of Solid State Physics, Risø National Laboratory, DK-4000 Roskilde, Denmark*
[b] *Department of Physics, McGill University, Montreal, Que., Canada H3A 2T8*
[c] *Department of Physical Chemistry, The Technical University of Denmark, DK-2800 Lyngby, Denmark*
[d] *HASYLAB, Notkestrasse 85, D-2000 Hamburg 52, Germany*

Received 25 June 1993
Revised manuscript received 6 September 1993

The oxygen order in $YBa_2Cu_3O_{6+x}$ has been investigated by Monte Carlo simulation with the two-dimensional anisotropic next-nearest-neighbor lattice gas model, the ASYNNNI model. For a specific set of interaction parameters we have calculated the structural phase diagram, the chemical potential, and the structure factor as a function of temperature and wave vector for $x=0.4$. The phase diagram has been determined from an ivestigation of the order parameters and their fluctuations as well as by the use of an improved version of the Ferrenberg-Swendsen method. The calculated phase diagram and the widths of the structure factors are in excellent agreement with measured neutron-diffraction data. We suggest that the observation of an orthorhombic distortion, simultaneously with only short-range oxygen order at $T=25$ °C, is due to the freezing-in of an ortho-II domain state with a preferred oxygen chain direction and accordingly only two types of domains. Using thermodynamic relations the chemical potential has been related to the measured oxygen-gas pressure, and it is discussed why only qualitative agreement with experimental data is established.

1. Introduction

The oxygen-ordering properties of the high-temperature superconductor $YBa_2Cu_3O_{6+x}$ have attracted considerable interest since the discovery of this material [1,2]. A major reason is the experimental evidence that not only the oxygen content [3], but also the oxygen-ordering configurations [4–6] are important for the superconducting transition temperature, T_c.

It is of further interest to note that $YBa_2Cu_3O_{6+x}$ appears to be an ideal model system for studies of two-dimensional structural ordering phenomena. The variable amount of oxygen ($0<x<1$) is located in the widely separated (≈ 11.7 Å) CuO_x basal planes of the structure and it is generally accepted that the oxygen ordering in the basal plane is the driving force for the majority of the observed structural transformations and local ordering phenomena. For this reason it is natural that two-dimensional lattice-gas models [7–17], and notably the anisotropic nearest- and next-nearest-neighbor interaction model, the ASYNNNI model [7–15], has attracted considerable interest.

In the present paper we have used a Monte Carlo simulation to study how applicable the ASYNNNI model is in accounting for the structural and thermodynamic properties of oxygen ordering in $YBa_2Cu_3O_{6+x}$. For the three interaction parameters in the ASYNNNI model, the nearest neighbor V_1 and the two locally anisotropic next-nearest-neighbor interaction parameters, V_2 and V_3, we have used the values estimated from a preliminary analysis and comparison with the structural phase diagram [14,15,18]. In this paper we make a complete study and establish that our model accounts for the experimental phase boundary between the tetragonal disordered phase and the two orthorhombic ordered

0921-4534/93/$06.00 © 1993 Elsevier Science Publishers B.V. All rights reserved.

phases, ortho-I and ortho-II. As a subject of particular interest we have calculated the structure factor $S(q)$ from the statistics of the oxygen-ordering properties. The aim has been to study whether the ASYNNNI model can account for recent neutron-diffraction results [19], which show splitting of the (2, 0, 0) and (0, 2, 0) Bragg peaks compatible with long-range orthorhombic order in a twinned crystal, while the diffuse scattering at $(\frac{1}{2}, 0, 0)$ indicates only a short-range oxygen ortho-II superstructure.

From many studies on $YBa_2Cu_3O_{6+x}$ it is now well established that the CuO_x basal plane of the structure acts as the charge reservoir creating the necessary holes in the superconducting CuO_2 planes. The oxygen ordering properties in the CuO_x basal plane, and how they influence the charge transfer and electronic structure in a way that leads to superconductivity in $YBa_2Cu_3O_{6+x}$, have been the subject of many studies [3–6,14,15,18,20–27], but despite the significant efforts there is not yet a satisfactory microscopic understanding of the relation. From phenomenological models it has been possible to establish close relations between T_c and the effective charge-transfer mechanisms, which have been derived from experimental structural data [3–6] or from model calculations of the structural ordering phenomena [14,15,18,20–22]. The hole-doping mechanism has also been studied by model calculations of the electronic structures [23–27]. In most of these calculations the observed oxygen-ordering properties are taken into account but not with the degree of structural details which the combined experimental and phenomenological model results suggest to be important [3–6,18,20–22].

More detailed experimental structural data and reliable models for the description of the oxygen-ordering properties seem imperative for developing the microscopic understanding of superconductivity in $YBa_2Cu_3O_{6+x}$. The increased size and improved quality of single crystals, which have become available, open the way for this development and for tests of the structural models. The ASYNNNI model has proven to account for many of the structural ordering properties [11–13,15,28]. From studies based on the mean-field cluster variational method [11] and interaction parameters determined from electron-band structure calculations [10], it has been shown that the experimental results for the structural phase transition line separating the tetragonal disordered and the orthorhombic ordered structures in the x–T phase diagram may be accounted for the ASYNNNI model without adjustable parameters. However, Hilton et al. [12] have suggested by calculating the structural phase diagram with the transfer-matrix technique, that this remarkable agreement may be fortuitous. We shall comment on this aspect in a forthcoming paper which includes the three-dimensional structural ordering properties of $YBa_2Cu_3O_{6+x}$ [29].

The paper is organized in the following way: In section 2 we present the ASYNNNI model and the interaction parameters used in the model studies. In section 3 we account for the Monte Carlo methods (3.1) and define the order parameters being used (3.2), and in section (3.3) we discuss the the applicability of the Ferrenberg–Swendsen method [30–32] for Monte Carlo simulation studies of the ASYNNNI model. The structural phase diagram resulting from the model calculations is presented and compared with experimental data in section 4. The model results of the chemical potential are compared with experimental oxygen equilibrium pressure data in section 5. Section 6 contains the structure-factor calculations of the oxygen-ordering properties and the results are discussed in relation to the neutron-diffraction data. Conclusions on the study are given in section 7.

2. Model hamiltonian

The model used in the calculations is a two-dimensional locally anisotropic lattice-gas model, which includes nearest-neighbor and next-nearest-neighbor interactions (the ASYNNNI model). This model, originally proposed by de Fontaine et al. [7], describes the ordering of oxygen atoms in the CuO_x basal plane of $YBa_2Cu_3O_{6+x}$. The basal plane consists of a square lattice of oxygen atoms embedded in a fixed lattice of copper atoms. The oxygen sites are located between the copper atoms as shown in fig. 1. The pair interaction parameters V_1, V_2 and V_3 are defined as follows. V_1 is the nearest-neighbor repulsion between two oxygen atoms. V_2 is the attractive next-nearest-neighbor interaction between pairs of oxygen atoms, which are bridged by a copper atom

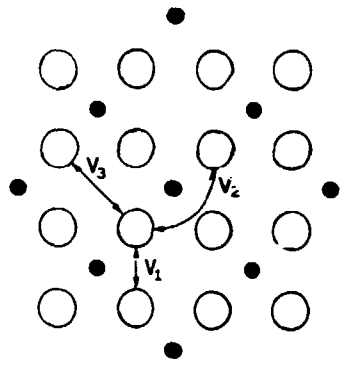

Fig. 1. Schematic illustration of the basal plane of $YBa_2Cu_3O_{6+x}$. The dots denote the copper atoms, while the open circles denote the oxygen sites. The pair interaction parameters V_1, V_2 and V_3 are indicated on the figure.

(NNNCu), while V_3 is the similar repulsive interaction between oxygen atoms which are not bridged by a copper atom (NNNV). This leads to a grand canonical hamiltonian

$$H-\mu N=-V_1\sum_{\langle ij\rangle}^{\mathrm{NN}}\sigma_i\sigma_j-V_2\sum_{\langle ij\rangle}^{\mathrm{NNNCu}}\sigma_i\sigma_j$$
$$-V_3\sum_{\langle ij\rangle}^{\mathrm{NNNV}}\sigma_i\sigma_j-\mu\sum_i\sigma_i, \qquad (1)$$

where σ_i is the site-occupation variable for the oxygen atoms at site i. This means $\sigma_i=1$ in the presence of an oxygen atom at the site i, while $\sigma_i=0$ if the oxygen atom is absent at site i. The rum runs over all oxygen pairs (i,j), which are nearest neighbor (NN) or next-nearest neighbors (NNNV and NNNCu), respectively. The chemical potential μ acts as an external field, which is related to the equilibrium oxygen pressure in the sample [28] as discussed in section 5. We have used the following values for the normalized interaction parameters:

$$(V_1, V_2, V_3)=(-V_0, 0.36V_0, -0.12V_0), \qquad (2)$$

with the energy scale given by $V_0=5430k_B$ K. The relative magnitude of the parameters is suggested by Poulsen et al. [18] to be $V_0/k_B=4300$ K. The stoichiometric factor x can experimentally be varies from ≈ 0 to ≈ 1. and is related to the average number of oxygen atoms on the lattice by

$$x=\frac{2}{N}\left\langle\sum_i\sigma_i\right\rangle, \qquad (3)$$

where N is the number of available oxygen sites.

3. Computational methods

3.1. Monte Carlo simulation methods

The Monte Carlo simulation is a standard method for studying the ASYNNNI model hamiltonian (1) using the Metropolis algorithm [33–35]. We have used both Glauber and Kawasaki dynamics. The Monte Carlo simulation with Glauber dynamics is performed in the usual manner, where a single process is proposed at each step, corresponding to removing or inserting an oxygen atom at random. The equilibrium properties obtained in this fashion correspond to an ensemble average taken from the grand canonical ensemble. In a Monte Carlo simulation process the emphasis is to achieve a realistic statistical distribution of the configurations at a given temperature. However, the updating procedure needs not be physically realistic – except for fulfillment of certain constraints. Such constraints could be to preserve the number of oxygen atoms at every new Monte Carlo step (MCS). A simple way of doing this is to use Kawasaki dynamics, which only allows for interchange of particles and vacancies.

In the real physical system the oxygen atoms have to jump from place to place. It might be a good approximation to consider only jumps to vacant nearest-neighbor and next-nearest-neighbor sites. This can easily be simulated using the Kawasaki dynamics which allows for only such interchanges; let us call this updata (A). After many MCS's it is expected that the phase space will be properly visited. However, a much faster method (B) is obtained by allowing oxygen atoms to "jump" over arbitrary distances. This should not be considered as modeling the real oxygen diffusion, but rather an efficient sampling procedure of other relevant independent configurations. The point is that as far as equilibrium properties are concerned, there should be no difference between (A) and (B), but clearly the equilibrium condition is much easier obtained by (B). The ensemble properties obtained by both

methods correspond to the canonical ensemble. An exception to this behavior may be introduced at the surface where a direct exchange of adsorbed oxygen atoms and the oxygen-gas phase is possible. In this case the Glauber dynamics is realistic with a grand canonical hamiltonian including a chemical potential for the oxygen exchange.

In all the simulations we have enforced periodic boundary conditions (PBC) and the linear extensions of the lattice of $L=32$, 50, 100 or 200 were used. The total number of Monte Carlo steps per site (MCSS) used in the calculations varied between 2×10^4 and 2×10^5. The grand canonical average $\langle A\rangle_{T,\mu}$ of an operator A, which depends on the entire oxygen configuration $\{\sigma_i\}$ in addition to the external parameters T and μ, was calculated both as an ensemble average over independent runs, typically 8, and as time average over each individual run. The time average is performed after the system has reached equilibrium by taking a simple average over the value of the operator A for every 100th oxygen configuration. By systematically varying the external parameters, the dependence of $\langle A\rangle_{T,\mu}$ on the temperature and chemical potential was determined. To check that $\langle A\rangle_{T,\mu}$ really represented equilibrium properties of the system, the whole calculation was redone by varying the external parameters in the opposite direction.

3.2. Order parameters

The ground-state oxygen configurations in the basal plane of $YBa_2Cu_3O_{6+x}$ can be calculated exactly from eq. (1) and are shown in fig. 2. The ortho-I phase, which at perfect order corresponds to $x=1$, is a two-fold degenerate oxygen structure. The ortho-II phase, which at perfect order corresponds to $x=\frac{1}{2}$ is a four-fold degenerate oxygen structure. The ideal tetragonal phase consists of an empty oxygen lattice ($x=0$). At finite stoichiometry ($0<x<0.3$), randomly oriented small oxygen chain segments are formed. For stoichiometries deviating from the ideal ones ($x=0, \frac{1}{2}, 1$) the majority phase with long-range order of either ortho-I or ortho-II coexist dynamically at high temperatures with short-range ordered domains of the other type – or regions with disordered oxygen chain segments, i.e. the tetragonal phase. Following Aukrust [36] we can define order

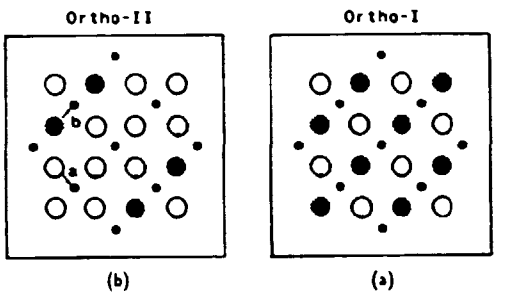

Fig. 2. Schematic presentation of the two ideal orthorhombic phases, (a) the ortho-I phase ($x=1$) and (b) the ortho-II phase ($x=0.5$). In (b) the domain shown is of the b-type with oxygen chains in the b-direction. There are two possible b-type ortho-II domains and two a-type ortho-II domains. In (a) the grey sub-lattice represents a b-domain, while the white sub-lattice represents an a-domain.

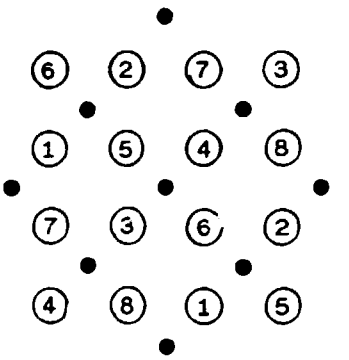

Fig. 3. The eight sub-lattices of oxygen sites used in defining the order parameters for the two orthorhombic phases are shown. The numbering convention is equivalent to that of Aukrust et al. [36].

parameters for both the ortho-I and the ortho-II phase. This is done by sub-division of the lattice into eight interpenetrating sub-lattices as shown in fig. 3. The concentration of oxygen atoms on the sub-lattice α is defined by

$$\theta_\alpha=\frac{8}{N}\left\langle\sum_{i\in\alpha}\sigma_i\right\rangle, \tag{4}$$

where ($\alpha=1, \ldots, 8$) and N is the number of oxygen sites. In terms of the sub-lattice concentrations, the order parameter for the ortho-I phase can be written

$$\theta_1=\tfrac{1}{4}|\theta_1+\theta_2+\theta_3+\theta_4-\theta_5-\theta_6-\theta_7-\theta_8|, \tag{5}$$

and similarly for the ortho-II phase

$$\theta_{II} = \tfrac{1}{4}|\theta_1 + \theta_2 - \theta_3 - \theta_4 + \theta_5 + \theta_6 - \theta_7 - \theta_8| \,. \qquad (6)$$

The behavior of θ_I and θ_{II} with respect to variation in the chemical potential at a constant temperature of $T = 0.083 V_0/k_B$ can be seen in fig. 4. The system size used in this calculation is 60×60. At low chemical potential μ the system is in the disordered (tetragonal) region of the phase diagram fig. 5 and both θ_I and θ_{II} are approximately zero. Upon increasing the chemical potential a rapid increase in the order parameters results, signaling ordering of the oxygen atoms. This is accompanied by a structural phase transition, where the system becomes orthorhombic (the ortho-II phase) and the basal plane lattice parameters become different ($a < b$, see fig. 2). This happens at about $\mu = -0.36 V_0$ where the ortho-II order parameter increases to $\theta_{II} \approx 1.0$. This corresponds to almost perfect occupation on one of the four sub-lattices $\alpha = \{1, 2\}$, $\{3, 4\}$, $\{5, 6\}$ or $\{7, 8\}$ from which it follows that $\theta_I \approx 0.5$. Increasing the chemical potential even further, a second structural phase transition takes place at about $\mu = -0.12 V_0$, where the system enters into the ortho-I phase with occupation on one of the two sub-lattices $\alpha = \{1, 2, 2, 4\}$ or $\{5, 6, 7, 8\}$ which corresponds to $\theta_I \approx 1.0$ and $\theta_{II} \approx 0.0$. Thus θ_{II} in contrast to θ_I is an order parameter in the normal sense. In principle a proper order parameter can be defined as $\theta_I^* = \theta_I - \frac{1}{2}\theta_{II}$ but we have refrained from this for historical reasons [36]. A feature of the θ_I and θ_{II} order parameters is that they cannot distinguish between the different degenerate ground-state configurations. This drawback may easily be remedied by introducing vector order parameters in the following manner:

$$\boldsymbol{\Theta}_I = \tfrac{1}{4}\begin{pmatrix} \theta_1 + \theta_2 + \theta_3 + \theta_4 \\ \theta_5 + \theta_6 + \theta_7 + \theta_8 \end{pmatrix}, \quad \boldsymbol{\Theta}_{II} = \tfrac{1}{2}\begin{pmatrix} \theta_1 + \theta_2 \\ \theta_3 + \theta_4 \\ \theta_5 + \theta_6 \\ \theta_7 + \theta_8 \end{pmatrix}. \qquad (7)$$

In the following, $\boldsymbol{\Theta}_I(n)$ $(n = 1, 2)$ and $\boldsymbol{\Theta}_{II}(n)$ $(n = 1, 2, 3, 4)$ denote the components of the vector order parameters. This formulation is particularly useful in non-equilibrium studies, where the relaxation times toward equilibrium are studied. By comparing figs. 2 and 3 it is clear that the depicted ortho-II phase corresponds to having the sites $\{1\}$ and $\{2\}$ occupied, and all other empty. In other words $\theta_1 + \theta_2 = 2$. In eq. (7), $\boldsymbol{\Theta}_{II}(1)$ and $\boldsymbol{\Theta}_{II}(2)$ are thus the order parameters for the domains with oxygen chains in the b-direction (b-domains). They are related to one another by a translation of the oxygen chains by one lattice unit along the a-direction. Similarly $\boldsymbol{\Theta}_{II}(3)$ and $\boldsymbol{\Theta}_{II}(4)$ are order parameters for the domains with chains in the a-direction (a-domains). In the ortho-I phase either the b-axis chains $\boldsymbol{\Theta}_I(1)$ or the a-axis chains $\boldsymbol{\Theta}_I(2)$ of domains are simultaneously occupied, in the same region of space. This gives the two ortho-I sub-lattices, grey and white, in fig. 2. A structure consisting of, for example, small ortho-II b-domains separated in space with $\boldsymbol{\Theta}_{II}(1) \sim \boldsymbol{\Theta}_{II}(2) \neq 0$, will again decorate only the grey $\boldsymbol{\Theta}_I(1)$ ortho-I sub-lattice. Thus also this structure contributes to the structure factor $S(q)$ at the (1, 0, 0) peak which is characteristic for the ortho-I structure. By a uniform distribution of the a-domains ($\boldsymbol{\Theta}_{II}(3)$ and $\boldsymbol{\Theta}_{II}(4)$) and b-domains ($\boldsymbol{\Theta}_{II}(1)$ and $\boldsymbol{\Theta}_{II}(2)$) both the grey and white ortho-I sub-lattices become occupied and both the (1, 0, 0) and (0, 1, 0) peaks diminish by destructive interference.

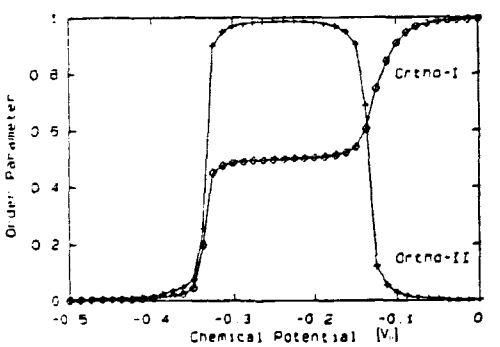

Fig. 4. The order parameters for the ortho-I phase and the ortho-II phase as a function of the chemical potential. The temperature is fixed at $T = 0.0831 V_0/k_B$.

3.3. The Ferrenberg-Swendsen method

The main drawback of the standard Monte Carlo simulation is its large demand for computer resources. The demand grows proportionally to the system size, but more seriously the time for reaching equilibrium also grows with the system size. Even for moderately small systems sizes several hours of CPU

time are usually needed for each data point. Therefore, the development of more efficient Monte Carlo schemes has attracted a lot of interest. Recently Ferrenberg and Swendsen [30–32] proposed a reweighting technique for studying phase transitions. The idea is to calculate the energy histogram $H_n(E)$ at different temperatures T_n. Typically in standard MC implementations only the first few moments of the histogram are stored. The histograms are combined in a self-consistent way to obtain the probability distribution $P(E, T)$ in the following way. The energy histograms $H_m(E)$ at a particular temperature T_m with $(m=1, ..., R)$ are most easily accumulated by initially calculating the total energy E_{tot} of the start configuration. Subsequently for each Metropolis proposal E_{tot} is updated by the energy difference ΔE (which is calculated anyway) between successive oxygen configurations. Then the total energy and the histograms are updated according to

$$E_{tot} \Rightarrow E_{tot} + \Delta E , \tag{8}$$

$$H_m(E_{tot}) \Rightarrow H_m(E_{tot}) + 1 . \tag{9}$$

We will assume that all the histograms contain the same number of Monte Carlo updates n. Then the sum of all histograms normalized by the number of updates can be written

$$H(E) = \frac{1}{n} \sum_{m=1}^{R} H_m(E) . \tag{10}$$

The multiple histograms equations, as formulated in the original work by Ferrenberg and Swendsen [30–32] are very troublesome in numerical calculations. This is due to the fact that the solutions of the equations cannot be represented within the range of floating point numbers on the computer. The numerical problem resembles that of stiff differential equations, where the solutions comprise both exponential growth and decay. However, some of the numerical problems can be by-passed by rewriting the equations in a slightly different manner. The multiple histogram equations then take the following form

$$P(E,T) = \frac{H(E)}{\Sigma_{m=1}^{R} \exp\left[E\left(\frac{1}{kT} - \frac{1}{kT_m}\right) - f_m \right]} , \tag{11}$$

where the free-energy term f_m is to be calculated self-consistently. The normalization condition gives rise to the following equations for determining f_m:

$$\sum_E \frac{H(E)}{\Sigma_{m=1}^{R} \exp\left[E\left(\frac{1}{kT_n} - \frac{1}{kT_m}\right) - f_m + f_n \right]} = 1 ,$$

$$n = 1, ..., R . \tag{12}$$

From eq. (12) we see that only the difference $(f_m - f_n)$ enters in the equation. As a result only $R-1$ equations are independent. Equation (12) was solved iteratively by the Newton–Raphson algorithm [37]. The convergence of the algorithms depends crucially on how close the initial guess is to the solution. Therefore, the equations were solved iteratively by first solving for $n=2$, and then we use the solutions as the starting point for solving the equations with $n=3$, and so on.

In figs. 5(a) and (b) are shown the mean energy $\langle E \rangle_T$ and the heat capacity $C_V(T)$ for a temperature scan at $x=0.4$. The system size is 32×32 and the energy histograms $H_m(E)$ were accumulated at temperatures $T_m = (0.09 + 0.02m) V_0/k_B$. In each of the histograms 3×10^5 MCS's were used. The diamonds are the conventional Monte Carlo data points obtained by utilizing only the first and the second moments of the histograms, while the solid curve represents the Ferrenberg–Swendsen interpolation formula (11). In fig. 5(a) we see that the interpolating curve and the data points for $\langle E \rangle_T$ agree well, while this is not the case in (b) for $C_V(T)$. The reason for this is that whereas the average of a distribution is obtained quite accurately; the higher moments require much better statistics in the tails of the distribution. This accounts for the fact that the data points in fig. 5(b) are much more scattered around the interpolating curve. Therefore, the interpolation curve allows the numerical position of the peak in C_V to be determined very accurately to be $T_c = 0.1052 V_0/k_B$. We shall see that this agrees very well with the T_c estimated from the behavior of other quantities.

4. Phase diagram

In this section we report on the calculation of the phase diagram using a Monte Carlo simulation (MC). Several other methods have previously been

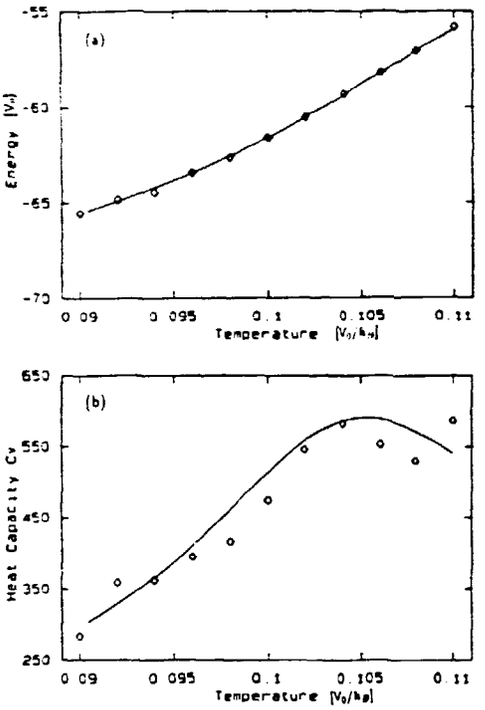

Fig. 5. In (a) is shown the mean internal energy $\langle E \rangle_T$ as a function of the temperature. The oxygen stoichiometric factor is fixed to $x=0.4$. The diamonds are the data points obtained from a Monte Carlo simulation with the Kawasaki dynamics model (B), and the solid line represents the results using the Ferrenberg-Swendsen interpolation formula. In (b) is shown the corresponding heat capacity $C_V(T)$ (arbitrary units) from which the phase boundary can be determined numerically accurate.

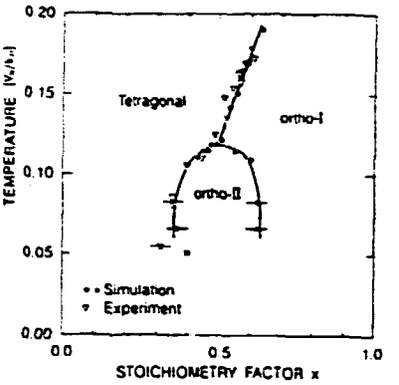

Fig. 6. The phase diagram in the x–T plane obtained by Monte Carlo simulation. Solid circles represent data obtained by Glauber dynamics, while the diamonds represents results obtained with Kawasaki dynamics. The triangles are the experimental data points [28]. The interaction parameters used are $V_1=-V_0$, $V_2=0.36V_0$ and $V_3=-0.12V_0$. All phase transition lines shown are of second order. The location of the points were obtained from the position of the peak in the fluctuation of the relevant order parameter. The (*) indicates the position in phase space where the neutron-diffraction data by Zeiske et al. [19] were obtained.

applied to the ASYNNNI model; the most important ones are the cluster variation method (CVM), which is mean-field-type of calculation, and the transfer-matrix (TM). Because of the different accuracy of the methods there exist several sets of values for the interaction parameters describing the oxygen ordering phenomena in $YBa_2Cu_3O_{6+x}$. The transfer-matrix and Monte Carlo method give the most reliable statistical results.

We have calculated the phase diagram by Monte Carlo simulation of the hamiltonian (1) with the interaction parameters given in eq. (2). The resulting x–T phase diagram is shown in fig. 6. Here x is the stoichiometric factor given by eq. (3). The location of the phase boundary was determined by calculating the position of the peak in the fluctuations of the relevant order parameters. In the case of Glauber dynamic x is only indirectly determined from the x–μ relation. The x–μ relation is particularly important because it can be compared directly with the experimental measurements of the oxygen equilibrium partial pressure. We will return to this in section 5.

The solid circles in fig. 6 are the actual data points obtained with Glauber dynamics. The horizontal error bars are the total error, representing the combined uncertainty from determining the peak position of the susceptibility of the order parameter and the uncertainty in the x–μ relation. The solid diamonds represent results obtained by Kawasaki dynamics. All the Monte Carlo data points have been calculated with a 60×60 system, where sufficiently good statistics could be obtained as will be discussed in section 3.3. To check the finite size dependence of the results larger system sizes, 100×100 and 200×200, were applied at $x=0.4$ and $x=0.5$ for a complete temperature scan across the phase boundary. The differences in T_c were small and within the computational uncertainty. The triangles are the experimental points from Andersen et al. [28]. By fitting at $x=0.4$ the calculated $T_c=0.105V_0/k_B$ to the experimental $T_c=570$ K we determine the normal-

ization factor $V_0/k_B = 5430$ K. Since the phase diagram is more accurately obtained than the preliminary result published by Poulsen et al. [18] we obtain a more reliable value than their quoted value of the scale factor ($V_0/k_B = 4300$ K).

As already discussed, the phase diagram contains the high-temperature oxygen-disordered tetragonal phase and the two low-temperature oxygen-ordered orthorhombic phases, the ortho-I and ortho-II phase. The three lines shown in the phase diagram are all consistent with being of second order as expected from finite-size scaling analysis of the order parameter discussed by Aukrust et al. [36]. The three lines merge at a multicritical point separating the tetragonal phase from the ortho-I and ortho-II phases. The multicritical point is for our interaction parameters located at $T_t = 0.115 V_0/k_B$ and $x_t = 0.46$.

5. Chemical potential

In this section we discuss the chemical potential $\mu(x, T)$ as a function of oxygen stoichiometry x and temperature T predicted by the ASYNNNI model from Monte Carlo calculations with Glauber dynamics of the grand canonical hamiltonian (1). The results are important not only for determining the structural phase diagram, as described in section 4, but also because the chemical potential may be related to the oxygen equilibrium partial pressure, which can be observed experimentally.

In fig. 7(a) we show isotherms of $\mu(x)$ in reduced units for six different temperatures between $T = 100$°C and $T = 700$°C using the normalization factor $V_0/k_B = 5430$ K determined from the fit at $x = 0.4$ and $T = 0.105 V_0/k_B$ to the structural phase diagram. In the isotherms for $T \leq 300$°C a step-like increase is observed in the chemical potential at $x = 0.5$, and $x = 1.0$. The general features can be understood as follows, cf. fig. 1: For $x \leq 0.5$ the oxygen energy is reduced by V_2 per site by chain formation, whereas the repulsive interactions, V_1 and V_3, may both be avoided because only the oxygen sites on every second chain need to be occupied in the ortho-II ground state, see fig. 2. For $x > 0.5$ oxygen sites on the intervening chains start to be populated at the expense of an energy increase of $2|V_3|$ per occupied site; and so on. Accordingly, one finds

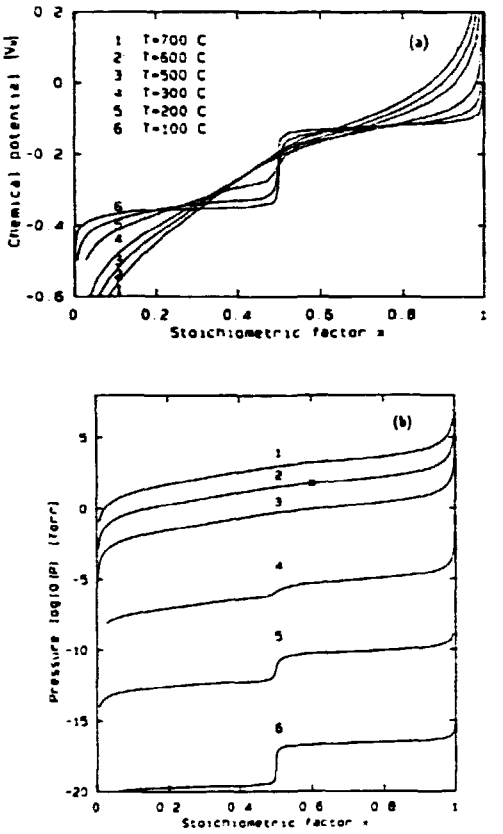

Fig. 7. (a) Monte Carlo simulation results of isotherms of the chemical potential μ as a function of the oxygen stoichiometric contents x. The temperature used are $T = 700$°C, $T = 600$°C, $T = 500$°C, $T = 300$°C, $T = 200$°C and $T = 100$°C. In (b) is shown the calculated partial oxygen pressure, using eq. (20) which has been adjusted to the experimental pressure in fig. 8 (a) at $T = 600$°C and $x = 0.6$, indicated by (*).

that the chemical potential at $T = 0$ K has a step-like variation with $\mu = -\infty$ for $x = 0$, $\mu = -V_2 = -0.36 V_0$ for $0 < x < 0.5$, $\mu = -(V_2 + 2V_3) = -0.12 V_0$ for $0.5 < x < 1.0$, and $\mu = -(4V_1 + V_2) = 3.64 V_0$ for $1.0 < x < 1.5$, and finally $\mu = -(4V_1 + V_2 + 2V_3) = 3.88 V_0$ for $1.5 < x < 2$. For finite temperatures the steps are smeared by thermal excitations and for temperatures above the multicritical point the jump at $x = 0.5$ disappears because the ortho-II phase is not thermodynamically stable for any x-values. At the high temperatures the isotherms seem to have a rather featureless increase with oxygen stoichiometry, x. A closer analysis shows,

however, that the derivative, $(\partial x/\partial\mu)_T$, called the *non-ordering susceptibility* [36,38] has a peak at the structural phase transitions. It may be shown that the non-ordering susceptibility is a thermodynamic response function related to the particle number fluctuations;

$$\left(\frac{\partial x}{\partial \mu}\right)_T = \frac{1}{k_B T}(\langle x^2\rangle - \langle x\rangle^2)\,. \tag{13}$$

Equation (13) is the lattice-gas analogue of the magnetic susceptibility of the equivalent spin-½ Ising model, but since the particle stoichiometric factor x is not an order parameter in the phases of the present model, it is called a non-ordering susceptibility.

5.1. Oxygen equilibrium pressure

The chemical potential entering the grand canonical hamiltonian of the ASYNNNI model (1) is equal to that of atomic oxygen in the surrounding oxygen gas. Assuming that the diatomic oxygen molecules constitute an ideal gas of non-interacting particles we may calculate the chemical potential, $\mu(O_2)$, from standard statistical mechanics. Following Landau and Lifshitz [39] the free energy for a gas in a volume V_0 containing N_0 molecules of O_2 may be expressed as

$$F = F_t + F_{el} + F_{rot} + F_{vib}\,, \tag{14}$$

where

$$F_t = -N_0 k_B T\left[\log_e\left(\frac{eV_0}{N_0}\right) + \frac{3}{2}\log_e\left(\frac{mk_BT}{2\pi\hbar^2}\right)\right] \tag{15}$$

is the translational part of the free energy, m is the mass of the O_2 molecule and e is the base of the natural logarithm.

$$F_{el} = -N_0 k_B T \log_e(g_e) + N_0\epsilon_0 \tag{16}$$

is the contribution from the electronic ground state of the O_2 molecule with energy ϵ_0 and degeneracy g_e (the higher electronic states may be neglected).

$$F_{rot} = -N_0 k_B T \log_e\left(\frac{Ik_BT}{\hbar^2}\right) \tag{17}$$

is the rotational free energy of a diatomic molecule of identical atoms. I is the moment of inertia for the rotation perpendicular to the bond.

$$F_{vib} = N_0 k_B T \log_e\left[1-\exp\left(-\frac{\hbar\omega_0}{k_BT}\right)\right] + N_0\frac{\hbar\omega_0}{2} \tag{18}$$

is the free energy of the internal vibrations of the O_2 molecule with the frequency ω_0. Using the standard thermodynamic relations $\mu(O_2) = (\partial F/\partial N_0)_{V_0,T}$ and $PV_0 = N_0 k_B T$ the resulting chemical potential of the oxygen molecule is

$$\mu(O_2) = k_B T \log_e\left[\frac{P(1-\exp(-\hbar\omega_0/(k_BT)))}{\xi_0(k_BT)^{7/2}}\right] + \epsilon_0 + \frac{\hbar\omega_0}{2}\,, \tag{19}$$

where

$$\xi_0 = \left(\frac{m}{2\pi\hbar^2}\right)^{3/2}\frac{Ig_e}{\hbar^2}\,.$$

Equating the chemical potential μ of atomic oxygen in $YBa_2Cu_3O_{6+x}$ with that of the gas gives the relation between the chemical potentials, $\mu = \frac{1}{2}\mu(O_2)$. Thus eq. (19) may be converted into

$$\log_{10}(P) = \frac{2\mu - \epsilon_0 - \hbar\omega_0/2}{\log_e(10)k_BT} - \log_{10}\left[\frac{1-\exp(-\hbar\omega_0/(k_BT))}{\xi_0(k_BT)^{7/2}}\right]. \tag{20}$$

with this relation and the appropriate values for the oxygen molecule, $m = 5.312\times10^{-26}$ kg, $g_e = 3$, $I = 1.938\times10^{-46}$ kg m^2, and $\omega_0 = 2.978\times10^{14}$ s^{-1} we have expressed the chemical potential, μ, calculated from the ASYNNNI model, fig. 7(a), in terms of the equivalent pressure isotherms shown in fig. 7(b). The only adjustable parameter ϵ_0 sets the absolute energy scale for the electronic ground-state energy of molecular oxygen relative to the zero-energy level of the ASYNNNI model. ϵ_0 has been determined by comparing the Monte Carlo simulation with the experimental data in fig. 8(a) at $x = 0.60$ and $T = 600$°C, where a high accuracy of the oxygen equilibrium pressure is obtained, and equilibrium conditions are most likely established in the experimental sample. Using $\log_{10}(P) = 1.8$ we obtain $\epsilon_0 = 1.83$ eV. The pressure isotherms thus predicted on the basis of eq.

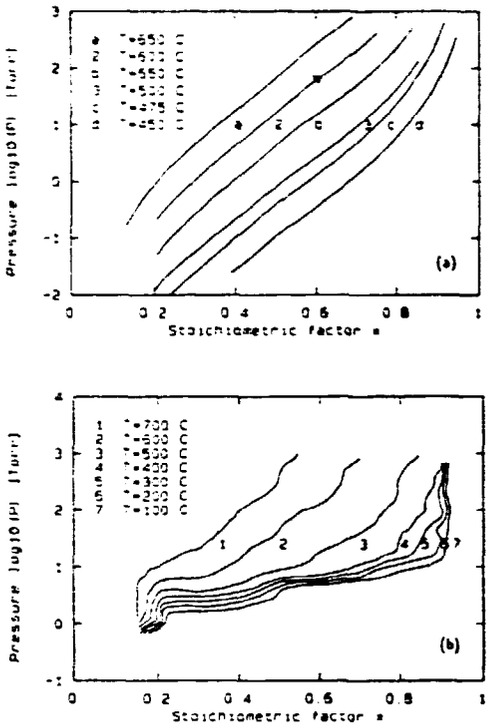

Fig. 8. (a) The experimental results by Schleger et al. [41,42] for the oxygen partial pressure are presented as isotherms for the indicated temperatures. The data point (*) is used as a fix point for the theoretical calculation of the equilibrium pressures in fig. 7 (b). The panel (b) shows the corresponding data by Andersen et al. [28] at the indicated temperatures.

(20) by the ASYNNNI model for other temperatures are shown in fig. 7(b).

We have compared the theoretical expression for the chemical potential, eq. (19), with the similar expression [28] derived from the semi-empirical thermodynamic data of molecular oxygen collected by Barin and Knacke [40], and found that they are in agreement to within 1 meV in the temperature range considered.

For a comparison, we have reproduced the experimental data of the oxygen equilibrium pressures measured by Schleger et al. [41,42] in fig. 8(a) and by Andersen et al. [28] in fig. 8(b). Both sets of data have been obtained by the use of a gasvolumetric technique. The data in fig. 8(a) are the result of titration experiments at constant temperatures. For the data in fig. 8(b) the sample has been cooled in a closed volume of oxygen with interpolation between the pressure data obtained from sixteen different values of the starting pressure. In both cases the decay in the oxygen pressure has been monitored to test that equilibrium has been established. The two data sets are in fair agreement at equilibrium pressures above 10 Torr provided that the nominal oxygen stoichiometry x of the data in fig. 8(a) is reduced by $\Delta x=0.065$. In this context it should be mentioned that a comparable reduction ($\Delta x=0.035$) is needed in the nominal oxygen stoichiometries when the structural phase-transition line separating the tetragonal disordered and the orthorhombic ordered ortho-I phases from the same two studies are compared. The difference between the data sets at low pressures is not necessarily a result of the different measuring techniques, but rather due to the level of accuracy aimed at in the two studies. Probably, the data presented in fig. 8(a) are the more accurate, but these data have not been recorded down to the low temperatures where the jump at $x=0.5$ related to the ortho-II ordering develops. It is obvious that the oxygen equilibrium pressures predicted by the ASYNNNI model, fig. 7(b), are not in quantitative agreement with the experimental data measured by the gasvolumetric technique, figs. 8(a) and (b). The most significant deviations appear at low temperatures. The predicted equilibrium pressures are very low and outside the measurable range. It may be argued that the oxygen diffusion kinetics at these temperatures is too slow to allow for oxygen diffusion, and thereby it prevents thermodynamics equilibrium to be established. It should be mentioned, however, that pressure relaxations are observed in the experiments leading to the data in fig. 8(b) [28,43]. Although gas impurities and minor leaks in this experiment may result in equilibrium pressures which are far too high, the observed pressure decays in the gasvolumetric system and the associated oxygen uptake by the sample are inconsistent with an oxygen equilibrium pressure below 10^{-16} Torr.

The experimental data in fig. 8(b) reveal the predicted jump in the pressure isotherms at $x=0.5$, cf. fig. 7(b), at least in the $T=100$°C isotherm, but it is significantly smaller, $\Delta\log_{10}(P)\approx 0.4$, than the value predicted by the ASYNNNI model, $\Delta\log_{10}(P)\approx 2.7$. This difference may be real and may indicate that the interaction parameter, V_3, used in the pres-

ent ASYNNNI model study is too large (recall that the jump is approximately $\Delta \log_{10}(P) = 4|V_3|/\log_e(10)k_BT$ at low temperatures). Alternatively, it may result from the limited accuracy in the oxygen-pressure measurements at low pressures. In order to establish an appropriate value for V_3 it would be highly recommendable to perform more accurate low-temperature oxygen equilibrium pressure studies.

The significant deviations, which result from the comparison between the measured and the calculated thermodynamic properties, are not surprising considering that the ASYNNNI model includes only the static ordering properties of the oxygen in the basal plane. It is obvious that the dynamics of the lattice vibrations and the degrees of freedom related to the electronic charge transfer should be included in order to establish realistic thermodynamic response functions. These additional contributions to the hamiltonian are not necessarily significant for the structural ordering properties. We have analyzed how the lattice vibrations of the variable amount of oxygen in the basal CuO_x plane influence the chemical potential and the oxygen equilibrium pressures. We have chosen a simple approach with three independent Einstein oscillators with frequencies ω_x, ω_y and ω_z for the oxygen vibrations along the x-, y- and z-axes. This adds the term

$$\Delta\mu_{vib} = k_BT\left\{\log_e\left[1-\exp\left(-\frac{\hbar\omega_x}{k_BT}\right)\right] + \log_e\left[1-\exp\left(-\frac{\hbar\omega_y}{k_BT}\right)\right] + \log_e\left[1-\exp\left(-\frac{\hbar\omega_z}{k_BT}\right)\right]\right\} + \frac{\hbar}{2}(\omega_x+\omega_y+\omega_z) \quad (21)$$

to the chemical potential μ of the ASYNNNI model entering eq. (20). Using experimentally determined values for the oscillator frequencies: $\omega_x = 6.89\times10^{12}$ s^{-1}, $\omega_y = 1.71\times10^{13}$ s^{-1} and $\omega_z = 1.21\times10^{13}$ s^{-1} [44], and the fix point, $T = 600$°C, $x = 0.6$ where $\log_{10}(P) = 1.8$ as in fig. 7(b), we have calculated the resulting pressure isotherms and determined the adjustable parameter to be $\epsilon_0 = 1.5$ eV. The reduction of ϵ_0 is a direct consequence of the additional degrees of freedom, which increases the chemical potential of the CuO_x basal plane oxygen relative to the ground-state energy. As a result of the temperature dependence of the chemical potential of the Einstein oscillators (21), the calculated oxygen pressures are significantly larger at low temperatures. For the $T = 100$°C isotherm we find pressures which are five decades higher. This is not enough to establish satisfactory agreement with the experimental data, but the anticipated effect of the additional degrees of freedom is confirmed.

At high temperatures close to the fitting point there is qualitative agreement. However, the average slopes of the measured isotherms at $T = 600$°C in fig. 8(a) are somewhat larger than the calculated ones. Similar discrepancies are observed by the analysis of the non-ordering susceptibility, $(\partial x/\partial\mu)_T$, eq. (13), which may be related to the oxygen equilibrium pressures through eq. (20). From such studies it is found that the peak in $(\partial x/\partial\mu)_T$ predicted by the ASYNNNI model, at the structural phase transition from the tetragonal disordered to the orthorhombic ordered ortho-I phase, is significantly larger than the experimentally observed one [38,41,42]. In this context it should be mentioned that the addition of single site terms to the ASYNNNI model hamiltonian do not influence the non-ordering susceptibility. From analysis of the non-ordering susceptibility of eq. (13) and its relation to the oxygen equilibrium partial pressure, eq. (20) it is therefore possible to obtain important information about the concentration-dependent variations of the static and dynamic properties of the oxygen ordering and the associated electronic charge transfers. Such studies have been carried out by other groups [41,42,45], and is beyond the scope of the present paper. Considering that the ASYNNNI model (1) does not account satisfactorily for the chemical potential and the equilibrium pressure, it is not surprising that it cannot account for derivatives such as the non-ordering susceptibility.

6. Structure factor

Recently, Zeiske et al. [19] measured the oxygen ordering in $YBa_2Cu_3O_{6+x}$ ($x = 0.4$) by neutron diffraction. The measurement was performed at room temperature and in fig. 6 the corresponding position

in the phase diagram, indicated by an (*), makes it evident that the measurement was expected to be taken well within the ortho-II phase at $T=25$°C. By measuring the structure factor they observed diffuse superstructure reflections (h, k, l) at $(\frac{1}{2}, 0, 0)$, fig. 9. This superstructure reflection corresponds to a doubling of the unit cell along the crystallographic a-axis (see fig. 2), but the finite width, and the fact that there was no evidence for a Bragg peak show that only short-range ordered ortho-II domains are formed. By fitting the profile of the superstructure reflections to a gaussian [46], they determined the widths Δh, Δk and Δl, where (h, k, l) are the reduced reciprocal lattice units. They obtained $\Delta h=0.099$, $\Delta k=0.049$ and $\Delta l=0.52$ and deduced the correlation lengths $\xi_a=10a$, $\xi_b=24b$ and $\xi_c=2c$ showing a strong anisotropy of the correlation lengths ξ_a and ξ_b in the basal plane. The small value of the inter-plane correlation length ξ_c shows that the oxygen order is predominantly two-dimensional and supports the rationale for the 2D lattice-gas hamiltonian (1) used in the calculations.

The simultaneous observation of a splitting of the (2, 0, 0) peak proves that the crystal has an orthorhombic distortion, i.e. $a \neq b$. This indicates the presence of oxygen chains in a preferred direction. However, there is no long-range correlations between the chains, as would have been expected from the fact that the measurements were performed deep into the ortho-II phase. The experimental results are puzzling and in order to elucidate the problem we have calculated the structure factor from the simulations of the ASYNNNI model and compared this with the above experimental values.

The structure factor $S(q)$ is defined as the Fourier transform of the density–density correlation function

$$\langle \sigma(r)\sigma(r') \rangle = C(r,r') + \langle \sigma(r) \rangle \langle \sigma(r') \rangle ,$$

$$C(r,r') = \langle [\sigma(r) - \langle \sigma(r) \rangle][\sigma(r') - \langle \sigma(r') \rangle] \rangle . \quad (22)$$

Here r and r' denote the positions of the oxygen atoms, while $\langle \ldots \rangle$ denotes the ensembles average over independent system. In terms of the fluctuations in the density–density correlation function the diffuse part of the structure factor for N sites can be written

$$S_{\text{diff}}(q) = \frac{1}{N^2} \sum_r \sum_{r'} \exp[-i2\pi q \cdot (r-r')] C(r,r') . \quad (23)$$

For convenience we use reduced units for r and q. The structure factor $S(q)$ can in principle be evaluated for all q vectors, but if the finite system with $N=L\times L\times L$ sites is extended to infinity by means of periodic boundary conditions, it can easily be shown [47] that only the q-vectors $q=(h,k,l)$, where $(h=0/L, \ldots, (L-1)/L)$, $(k=0/L, \ldots, (L-1)/L)$

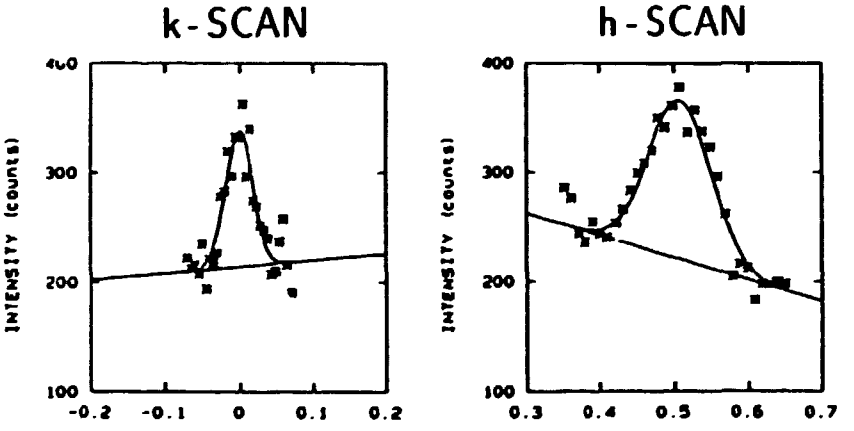

Fig. 9. Profiles of the $(\frac{1}{2}, 0, 0)$ superstructure reflections for a scan in the h (a-axis) and k (b-axis) directions in reciprocal space, from Zeiske et al. [19]. The (*) are the measured data points, while the solid curve is a best fit to a gaussian profile including a background term.

and ($l=0/L$, ..., $(L-1)/L$)) have non-zero structure factors. It could be mentioned, however, that when Fourier transforming a finite system (even if this is calculated with PBC) the structure factor is non-zero for all q-values, with amplitudes which depend on the actual geometry of the sample. Accordingly, they do not supply reliable information about the structure, even on a small length scale compared with the sample size. At the proper q-values given above, the structure factor amplitudes do not depend on the shape of the lattice.

In the computer simulations it is more convenient to formulate the structure factor in a slightly different way, requiring only a single summation over $\{\sigma_i\}$. Following Stanley [48] the structure factor can be written (assuming translational invariance)

$$S(q)=\frac{1}{N^2}\left\langle\left|\sum_r \exp(-i2\pi q\cdot r)\sigma(r)\right|^2\right\rangle. \qquad (24)$$

The analysis of the structure factor of eq. (24) is commonly carried out by decomposing $S(q)$ into the diffuse and the coherent parts in the following manner:

$$S(q)=S_{dif}(q)+\theta_{Q_0}^2\delta(q-Q_0), \qquad (25)$$

where Q_0 is the ordering q-vector. For the ortho-II phase the two equivalent ordering q-vectors are $Q_0=(\frac{1}{2},0,0)$ and $Q_0=(0,\frac{1}{2},0)$, while for the ortho-I phase the two ordering q-vectors are $Q_1=(1,0,0)$ and $Q_1=(0,1,0)$. The second term in eq. (25) is the Bragg peak containing the delta function which represents the coherent contribution from the average ordered oxygen structure corresponding to a non-zero order parameter θ_{Q_0}. This is equal to the order parameter components in eq. (7) $\Theta_{II}(n)$, where $n=1,2$ for $Q_0=(\frac{1}{2},0,0)$ and $n=3,4$ for $Q_0=(0,\frac{1}{2},0)$. The first term $S_{dif}(q)$ is the diffuse part of the structure factor which carries the information about the *fluctuations* in the oxygen configurations, and hence the correlation lengths. The formation of domains of orthorhombic symmetry in the ortho-II phase shows up as a peak in $S(q)$ for $q=Q_0$. Therefore, the important information about the structural ordering phenomena is obtained by calculating $S(q)$ for a scan along the main axis in reciprocal space through $q=Q_0$.

In fig. 10 the columns (a) and (b) show the profiles of the $(\frac{1}{2},0,0)$ superstructure reflections for scans along the a-axis (h-scan) and b-axis (k-scan) at the temperatures $T=0.1250V_0/k_B$ ($T\gg T_c$), $T=0.1175V_0/k_B$ ($T\gtrsim T_c$), $T=0.1025V_0/k_B$ ($T\approx T_c$) and $T=0.080V_0/k_B$ ($T\ll T_c$). Column (c) in fig. 10 shows snap-shots of the corresponding real-space oxygen configurations. The system size used in the calculations is 200×200 and the oxygen concentration is kept fixed at a value $x=0.4$ corresponding to that of Zeiske et al. [19]. The points indicate the actual data points. In order to gain sufficient statistics in the calculation, the structure factors has been averaged over 100 configurations. In addition the symmetry properties of the lattice was utilized by taking into account that the reflections $(\frac{1}{2},0,0)$ and $(0,\frac{1}{2},0)$ are equivalent which means that an additional factor of 2 was gained in the statistics by the averaging.

The solid line through the data points represents the best fit to a two-dimensional lorentzian line shape for the diffuse part of the structure factor (including a fitted lorentzian at the (1, 0, 0) position and a background term). From the fit the amplitude A and the widths Δh and Δk along the main axis are determined. The amplitude is very small in comparison to a Bragg peak as will be further discussed below. At $T=0.1175V_0/k_B$ the line shapes and widths of the diffuse scattering, $\Delta h=0.100\pm0.004$ and $\Delta k=0.050\pm0.001$ agree very well with the experimental values in fig. 9. In the simulations a similar width is obtained at $T=0.0800V_0/k_B$, as is also shown. However, in the simulated results the presence of an additional strong Bragg peak is found.

A more extensive series of data showing the width of the diffuse scattering at $q=Q_0$ as a function of temperature is presented in fig. 11. The widths Δh (h-scan, fig. 11(a)) and Δk (k-scan, fig. 11(b)) have an approximately temperature-independent ratio $\Delta h/\Delta k\sim2$. The magnitude of this ratio depends strongly on the anisotropy of the interaction constants V_2/V_3. The updating has been performed with Kawasaki dynamics model (A) and (B) for system sizes $L\times L$ for $L=60$, 100 and 200. For the Kawasaki dynamics model (A) the time to reach equilibrium is approximately ten times longer than the corresponding model (B). However, the equilibrium results for the different updating methods agree both in value and in the trend of the finite size effects. Above T_c the width Δh for the 60×60 system is consistently larger

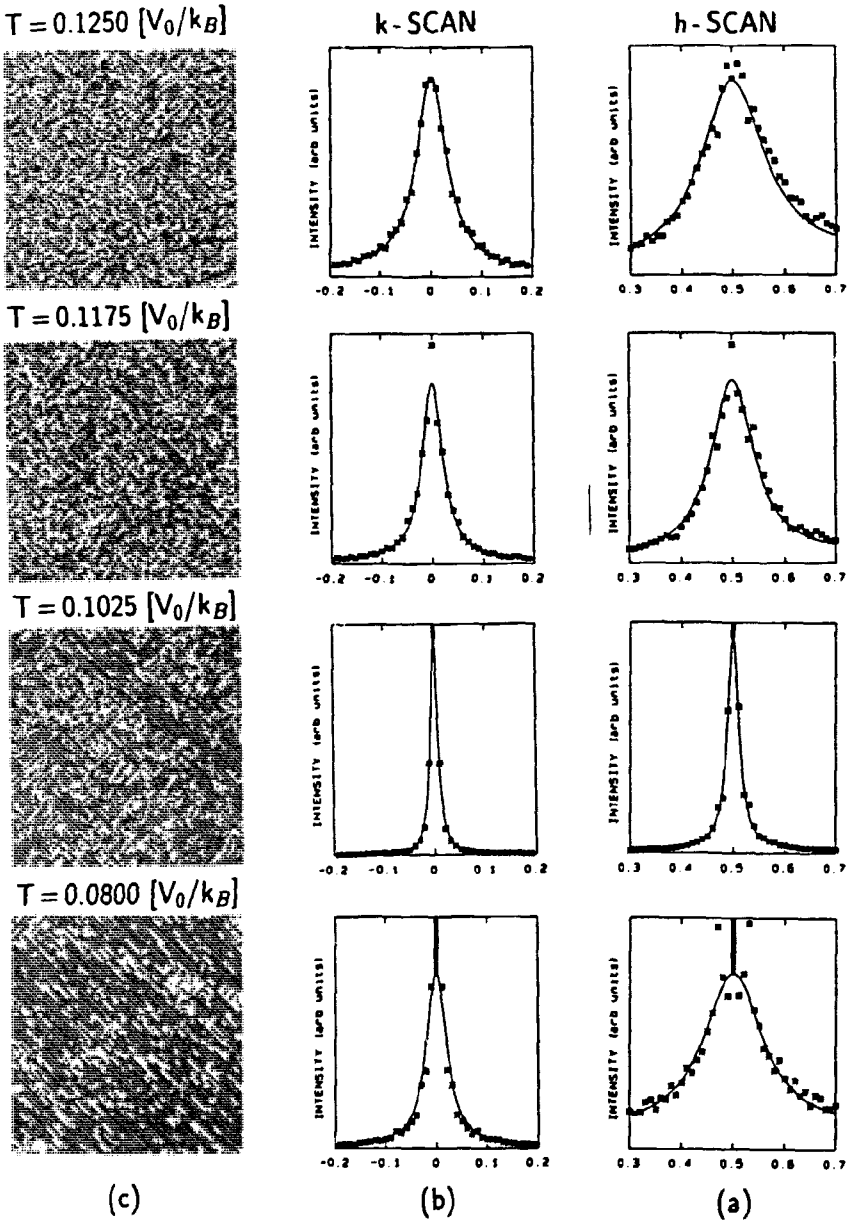

Fig. 10. In (a) and (b) are shown a gallery of the profiles of the $(\frac{1}{2}, 0, 0)$ superstructure reflections along the a-axis (h-scan) and along the b-axis (k-scan) for different temperatures. In (c) are shown the corresponding real-space snapshots of the oxygen configurations. The system size used in the MC calculation is 200×200 and the updating is performed by the Kawasaki model (B), with a fixed oxygen concentration $x = 0.4$ corresponding to that of the experimental sample, cf. fig. 9.

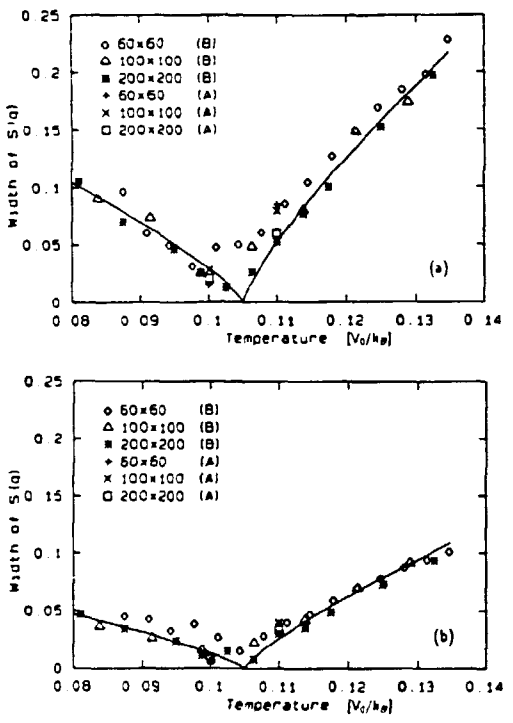

Fig. 11. In (a) and (b) are shown the peak width of the diffuse structure factor $S_{diff}(q)$ at $(\frac{1}{2}, 0, 0)$ as a function of the temperature for the h-scan and the k-scan, respectively. The solid points are the actual data points, indicating the results for the different system sizes and from the Monte Carlo Kawasaki updating method (A) and (B). The solid curve represents the best fit to the data.

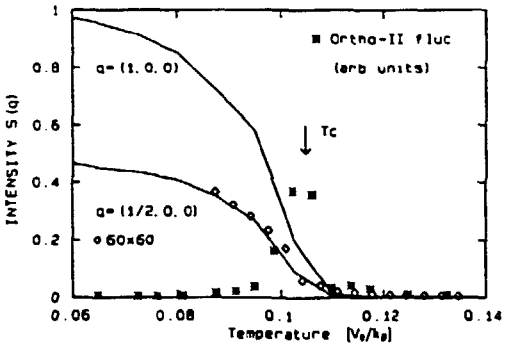

Fig. 12. The peak amplitude of structure factors at (1, 0, 0) and $(\frac{1}{2}, 0, 0)$ as a function of the temperature for a 200×200 system (line), and for a 60×60 system (◇). The fluctuations in the order parameter (θ_{II}) for the 200×200 system is shown as (•).

than Δh for the larger system, whereas for $T < T_c$ the width Δk is larger. This will be discussed further below.

Figure 12 shows the peak intensity (line) of the symmetrized, normalized structure factor $S(Q_0)$ and $S(Q_1)$ for the 200×200 systems. For a perfect ortho-II domain the ratio in intensity is 2 at $T=0$ K. This ratio is found for the 200×200 systems even for $T \gtrsim T_c$. For the 60×60 system the intensity ratio is two for $T < T_c$; however, for $T \gtrsim T_c$ it is approximately three. This will be further discussed below. We have also indicated on fig. 12 the behavior of the fluctuations in the ortho-II order parameter. This is proportional to the intensity of the diffuse scattering. We remark that this intensity is very small for $T > T_c$. For the temperatures $T=0.1250V_0/k_B$, $0.1175V_0/k_B$, $0.1025V_0/k_B$ and $0.0800V_0/k_B$, for which the diffuse peaks are shown in fig. 10, the peak values are $S(\frac{1}{2}, 0, 0) = 0.00076$, 0.00142, 0.00781 and 0.00070, respectively. The temperature of the divergence of the fluctuations agrees well with the T_c determined from the specific heat calculated using the Ferrenberg–Swendsen method, as shown in fig. 6(b).

From the theory of critical phenomena it is expected that the correlation lengths ξ_a and ξ_b should scale with the reduced temperature as a power law with critical exponent ν, which leads to the following temperature dependence of the line widths

$$\Delta h(T) \propto \Delta k(T) \propto |T - T_c(x)|^{\nu}. \qquad (26)$$

Although the ASYNNNI model equation (1) is of the Ising type (for which the exponents are $\nu = 1$ and $\beta = \frac{1}{8}$), the universality class of the tetragonal-to-orthorhombic ortho-II phase transition has been suggested by Bartelt et al. [49] to be that of the XY-model with cubic anisotropy, with an exponent $\nu \approx 0.8$ which depends on the oxygen concentration. The solid line in figs. 11(a) and (b), represents a fit to the 200×200 data using $\nu = 0.8$, and using the value for $T_c = 0.1052V_0/k_B$ obtained from the peak position of C_V as explained in section 3.3. The data are consistent with this value of ν, but might also be consistent with $\nu = 1$, i.e. a straight line. However, the temperature variation of the order parameter is not consistent with the Ising exponent; an approximate value of $\beta \gtrsim 0.2$ is found.

6.1. Equilibrium, non-equilibrium, finite size and strain

In the simulations we have made serious efforts in attempting to reach thermodynamic equilibrium. Tests have been made showing that the results are independent of whether a temperature is reached from above or from below. However, for the present anisotropic system difficulties arise. If we compare the results of the 200×200 and the 60×60 system for $T>T_c$, in fig. 11(a), the too large width in the h-scan for the 60×60 systems indicates a too narrow width of the domains perpendicular to the oxygen chain direction. The increased ratio $S(1,0,0)/S(\frac{1}{2},0,0)\sim3$ in fig. 12 for the 60×60 systems indicates furthermore a predominance of either a-domains or b-domains in a given member of an ensemble, as discussed in section 3. The reason is simply that when the correlation length along the chain direction becomes of the order of the system size, percolating domains are formed, and only if these have the same chain direction, they can coexist. Consequently either of the two a-type domains (with order parameters $\Theta_{II}(3)$ or $\Theta_{II}(4)$) or the two b-type domains (with order parameters $\Theta_{II}(1)$ or $\Theta_{II}(2)$) are selected (cf. eq. (7) and fig. 3). A look at the real-space snapshot confirms this picture, see fig. 13. Here one can identify two percolating domains with the same oxygen chain direction, here b-type domains. The snapshot for the 200×200 systems, fig. 10, on the other hand, shows a uniform distribution of domains at $T=0.1175V_0/k_B$, and the intensity ratio is accordingly close to two. We remark that there is no sign of domains of the ortho-I type. At $T=0.1025V_0/k_B$ there are signs of a predominant direction, which is fully developed for $T=0.0800V_0/k_B$. Because of the finite-size effects (percolation) it is impossible in the simulation to maintain a distribution of all types of domains, although this presumably is the true equilibrium state for a macroscopic system at elevated temperatures, $T\lesssim T_c$, as is found in other systems [50]. The simulations in the ordered phase, even for the 200×200 systems represent therefore the equilibrium behavior of a *single domain* sample. The fluctuations in a b-type domain are those of small inclusions of either of the two a-type domains, but not of the other b-type domain.

Fig. 13. A snapshot of a 60×60 system for $T=0.1175V_0/k_B$ showing two percolating domains with preferred oxygen chain direction in the b-direction. The percolating domains dominate the domain pattern. There is no longe-range order and yet a preferred oxygen chain direction.

The experimental samples are orthorhombically distorted on length scales much larger than these domains. How can we understand this? Let us assume that the strain favors one direction of the oxygen chains, i.e. for example domains of the b-type. Although strain is not included in the ASYNNNI model a similar effect is seen in the finite-size effect for the 60×60 system. The energy reduction for having percolating clusters in a 60×60 ensemble is the energy cost of the energy of one domain wall or $2V_2/60\approx60k_B$K per atom for each percolating chain. This favors a disordered state with a predominant oxygen chain direction, fig. 13. In the experiments the oxygen diffusion is slow for T approaching T_c due to critical slowing down, and at room temperature it is very slow mainly because the jump frequency is proportional to $\exp(-U_{barrier}/k_BT)$, where $U_{barrier}$ is the barrier height, typically of the order of eV. Thus, if the system in a praticable time after being cooled below $T=0.1175V_0/k_B$ can perform only a small number of jumps per site, the system would be trapped in the domain state with preferred chain orientation, but there would be no long-range order. This state is, with respect to the orthogonal strain, equally favorable as a single-domain ortho-II state. Because a Bragg peak at (1, 0, 0) coincides with a strong Cu-contribution, the neutron-diffraction experiments cannot determine if long-range order is present in the sense of only a-type or b-type domains. The stabilization of chains by means of percolation for small clusters is a somewhat artificial method of introducing strain effects. However, it has the virtue of being self-consistent, non-local and only effective after a certain

statistical organization of the oxygen chains. Such a self-consistent strain mechanism is difficult to include as a field term in the hamiltonian.

The picture which has emerged from this is that due to the very slow oxygen kinetics at low temperature, the oxygen order in the experimental sample was frozen in at $T=0.1175V_0/k_B$ above the phase transition into a two domain state with preferred oxygen chain direction. This would explain why only diffuse superstructure reflections was observed.

7. Conclusion

In the present work we have added further support to the conclusion that the ASYNNNI model accounts for many of the structural properties of $YBa_2Cu_3O_{6+x}$ such as the presence of the tetragonal disordered, and the two major orthorhombic ordered structural phases, ortho-I and ortho-II. We have not studied the low-temperature region. Thus our study does not address the problem that finite-size domains indicating higher order superstructures have been observed by the electron diffraction technique [51,52]. These superstructures, which are likely to occur at lower temperatures for thermodynamic reasons, have been accounted for by macroscopic models [53], and they may be explained by including further interaction parameters in the ASYNNNI model [54,55]. Experimentally it is questionable whether true long-rang ordered phases of these superstructures can be established because of slow oxygen kinetics at low temperatures. Further, the presence of a $2\sqrt{2}a\times\sqrt{2}a$-type superstructure has been observed in the tetragonal disordered phase [56–58] by different structural techniques. It has been argued that these structures most likely are stabilized by electronic properties in the CuO_2 planes [51], and they are therefore not directly significant for the oxygen ordering in the CuO_x basal plane.

In our ASYNNNI model studies, the Monte Carlo simulation technique has been used with both the Kawasaki and the Glauber dynamics, yielding the same phase diagram – although with quite different amounts of computer time. The order parameters, their fluctuations and the fluctuation in the number of oxygen atoms have been calculated and used for the determination of the phase boundaries as a function of temperature and oxygen stoichiometry. The Ferrenberg–Swendsen method has also been used and improved slightly in order to make it more stable numerically. The transition temperature obtained in this way from the specific heat can be determined very accurately; it agrees with that obtained by analysis of the other quantities. The oxygen-ordering structure factor has been calculated with good statistics and for large 200×200 systems and yields the correlation length as a function of temperature and direction in the CuO_x basal plane. The widths of the structure factors are in good agreement with those measured by neutron scattering for the oxygen stoichiometry $x=0.4$. The puzzling feature has been discussed that the experimental results at room temperature show orthorhombic lattice distortions and simultaneously that the oxygen-ordering structure factors are similar to the calculated ones at $T\approx600$°C, i.e. above the ordering temperature at $T=500$°C. It is suggested that the experimentally observed state is a disordered ortho-II domain state in which only two out of the four possible domains are selected. These have a predominant common oxygen chain direction and are thus not in contradiction with a larger-scale lattice strain. In the simulation the strain effects are not included, but can be illustrated using the finite size effects.

We have also calculated the chemical potential μ, and by using a thermodynamic model we have related μ to the corresponding oxygen pressure of an external O_2 gas in equilibrium with $YBa_2Cu_3O_{6+x}$. The calculated oxygen pressure has been compared with experimental data. The ASYNNNI model accounts only qualitatively for the experimental results. Using a chemical shift of $\epsilon_0=1.83$ eV for the difference between the zero energy of the oxygen molecule in the O_2 gas and the atomic oxygen in the CuO_x basal plane, reasonable agreement between the calculated and measured pressure isotherms is obtained at $T\approx600$°C. However the pressure at low temperatures is much too low compared with the experiments. This is presumably mostly due to effects not included in the ASYNNNI model, rather than experimental difficulties in measuring extremely low pressures. In agreement with the conclusions of a recent study [41,42,45] we have found that additional degrees of freedom should be included in the ASYNNNI model to account for the detailed behav-

ior of the chemical potential and oxygen pressure.

Acknowledgements

TF is supported by The Danish Research Academy. The work is supported by the Danish Ministry of Energy, the Danish Natural Science Research Council, and the CEC Science and Esprit programs.

References

[1] M.K. Wu, J.R. Ashburn, C.J. Torng, P.H. Hor, R.L. Meng, L. Gao, Z.J. Huang, Y.Q. Wang and C.W. Chu, Phys. Rev. lett. 58 (1987) 908.
[2] R.J. Cava, B. Batlogg, R.B. van Dover, D.W. Murphy, S. Sunshine, T. Siegrist, J.P. Remeika, E.A. Rietmann, S. Zahurak and G.P. Espinosa, Phys. Rev. Lett. 58 (1987) 1676.
[3] R.J. Cava, A.W. Hewat, E.A. Hewat, B. Batlogg, M. Marezio, K.M. Rabe, J.J. Krajewski, W.F. Peck Jr. and L.W. Rupp Jr., Physica C 165 (1990) 419.
[4] B.W. Veal, H. You, A.P. Paulikas, H. Shi, Y. Fang and J.W. Downey, Phys. Rev. B 42 (1990) 4770.
[5] J.D. Jorgensen, S. Pei, P. Lightfoot, H. Shi, A.P. Paulikas and B.W. Veal, Physica C 167 (1990) 571.
[6] B.W. Veal, A.P. Paulikas, H. You, H. Shi, Y. Fang and J.W. Downey, Phys. Rev. B 42 (1990) 6305.
[7] D. de Fontaine, L.T. Wille and S.C. Moss, Phys. Rev. B 36 (1987) 5709.
[8] L.T. Wille, A. Berera and D. de Fontaine, Phys. Rev. Lett. 60 (1988) 1065.
[9] J. Stolze, Phys. Rev. Lett. 64 (1990) 970.
[10] P.A. Stern and L.T. wille, Physica C 162 (1989) 223.
[11] D. de Fontaine, M. Asta, G. Ceder, R. McCormack and G. van Tendeloo. Europhys. Lett. 19 (1992) 229.
[12] D.K. Hilton, B.M. Gorman, P.A. Rikvold and M.A. Novotny, Phys. Rev. B 46 (1992) 381.
[13] V.E. Zubkus, P.J. Kundrotas and A.S. Orliukas, J. Phys. Cond. Matt. 4 (1992) 83.
[14] J.V. Andersen, Non-equilirbrium Phase Transitions and Ordering Processes in Lattice Gas Models, PhD. thesis, The Technical University of Denmark (1991).
[15] H.F. Poulsen, Oxygen Ordering and Superconductivity in the High-T_c Superconductor $YBa_2Cu_3O_{6+x}$, PhD. thesis, Risø National Laboratory, Denmark (1991).
[16] A.A. Aligia, H. Bonadeo and J. Garcés, Phys. Rev. B 43 (1991) 542.
[17] A.A. Aligia, Europhys. Lett. 18 (1992) 181.
[18] H.F. Poulsen, N.H. Andersen, J.V. Andersen, H. Bohr and O.G. Mouritsen, Phys. Rev. Lett. 66 (1991) 465.
[19] T. Zeiske, R. Sonntag., D. Hohlwein, N.H. Andersen and T. Wolf, Nature (London) 353 (1991) 542.
[20] H.F. Poulsen, N.H. Andersen, J.V. Andersen, H. Bohr and O.G. Mouritsen, Nature (London) 349 (1991) 595.
[21] R. McCormack, D. de Fontaine and G. Ceder, Phys. Rev. B 45 (1992) 12976.
[22] S. Lapinskas, A. Rosengren and E.E. Tornau, Physica C 199 (1992) 91.
[23] J. Zaanen, A.T. Paxton, O. Jepsen and O.K. Andersen, Phys. Rev. Lett. 60 (1988) 2685.
[24] S. Modak and J.L. Marán-López, Phys. Rev. B 40 (1989) 8933.
[25] A. Latgé, E.V. Anda and J.L. Morán-López, Phys. Rev. B 42 (1990) 4288.
[26] A.A. Aligia, Solid State Commun. 78 (1991) 739.
[27] V.Z. Kresin and S.A. Wolf, Phys. Rev. B 46 (1992) 6458.
[28] N.H. Andersen, B. Lebech and H.F. Poulsen, Physica C 172 (1990) 31.
[29] T. Fiig, J.V. Andersen, N.H. Andersen, P.-A. Lindgård, O.G. Mouritsen and H.F. Poulsen, to be published.
[30] A.M. Ferrenberg and R. Swendsen, Phys. Rev. Lett. 61 (1988) 2635.
[31] A.M. Ferrenberg and R. Swendsen, Phys. Rev. Lett. 63 (1989) 1195.
[32] R. Swendsen, J.S. Wang and A.M. Ferrenberg, in: The Monte Carlo Method in Condensed Matter Physics, ed. K. Binder (Springer, Berlin, 1992).
[33] D.W. Heermann and A.N. Burkitt, Parallel Algorithms in Computational Science (Springer, Berlin, 1991).
[34] K. Binder, in: Monte Carlo Methods in Statistical Physics, ed. K. Binder (Springer, Berlin, 1979).
[35] K. Bindr and D.W. Heermann, Monte Carlo Simulation in Statistical Physics (Springer, Berlin, 1988).
[36] T. Aukrust, M.A. Novotny, P.A. Rikvold and D.P. Landau, Phys. Rev. B 41 (1990) 8772.
[37] W.H. Press, B. Flannery, S.A. Teukolsky and W.T. Vetterling, Numerical Recipes (Cambridge University, Cambridge, 1986).
[38] P.A. Rikvold, M.A. Novotny and T. Aukrust, Phys. Rev. B 43 (1991) 202.
[39] L.D. Landau and E.M. Lifschitz, Statistical Physics, Part 1 (Pergamon, Oxford, 1980).
[40] I. Barin and O. Knacke, Thermochemical properties of inorganic substances (Springer, Berlin, 1973).
[41] P.R. Schleger, Thermodynamics of oxygen ordering in $YBa_2Cu_3O_{6+x}$, PhD. thesis, The University of British Columbia (1992).
[42] P. Schleger, W.N. Hardy and B.X. Yang, Physica C 176 (1991) 180.
[43] H.F. Poulsen, N.H. Andersen and B. Lebech, Physica C 173 (1991) 387.
[44] J. Humlicek, A.P. Litvinchuk, W. Kress, B. Lederle, C. Thomsen, M. Cardona, H.-U. Habermeier, I.E. Trofimov and W. König, Physica C 206 (1993) 345.
[45] P. Schleger, W.N. Hardy and H. Casalta, preprint.
[46] It should be noticed that in order to obtain the width of the structure factor, a gaussian line shape waas chosen in the fit of the experimental data, while the numerical data obtained

from the Monte Carlo simulation was fitted by a lorentzian line shape.
[47] E. Vives and P.A. Lindgård, Phys. Rev. B 44 (1991) 1318.
[48] H.E. Stanley, Introduction to Phase Transitions and Critical Phenomena (Oxford University, Oxford, 1971).
[49] N.. Bartelt, T.L. Einstein and L.T. Wille, Phys. Rev. B 40 (1989) 10759.
[50] T. Castan and P.-A. Lindgård, Phys. Rev. B 43 (1991) 956.
[51] S. Van Tendeloo and S. Amelinckx, J. Less Common Met. 164–165 (1990) 92.
[52] R. Beyers, B.T. Ahn, G. Gorman. V.Y. Lee, S.S.P. Parkin, M.L. Ramirez, K.P. Roche, J.E. Varzques, T.M. Gür and R.A. Huggins, Nature (London) 340 (1989) 619.
[53] A.G. Khachaturyan and J.W. Morris Jr., Phys. Rev. Lett. 61 (1988) 215.
[54] G. Ceder, M. Asta and D. de Fontaine, Physica C 177 (1991) 106.
[55] D. de Fontaine, G. Ceder and M. Asta, Nature (London) 343 (1990) 544.
[56] R. Sonntag, D. Hohlwein, T. Brückei and G. Collin, Phys. Rev. Lett. 66 (1991) 1497.
[57] T. Krekels, T.S. Shi, J. Reyes-Gasga, G. Van Tendeloo, J. Van Landuyt and S. Amelinckx, Physica C 167 (1990) 677.
[58] T. Zeiske, D. Hohlwein, R. Sonntag, F. Kubanek and G. Collin, Z. Physik B 86 (1992) 11.

Paper III

Monte Carlo Simulation of a Two-Species Diffusive Lattice Gas in Optimized C* on the Connection Machine:

Metal-Ion Doping Effects in the High-Temperature Superconductor $YBa_2Cu_{3-y}M_yO_{6+x}$ (M = Co, Fe, Al)

Monte Carlo Simulation of a Two-Species Diffusive Lattice Gas in Optimized C* on the Connection Machine*

Metal-Ion Doping Effects in the High-Temperature Superconductor
$YBa_2Cu_{3-y}M_yO_{6+x}$ (M = Co, Fe, Al)

S. Mannstaedt
Department of Physical Chemistry, The Technical University of Denmark
Building 206, DK-2800 Lyngby, Denmark

T. Fiig and N. H. Andersen and P.-A. Lindgård
Department of Solid State Physics, Risø National Laboratory
DK-4000 Roskilde, Denmark

O. G. Mouritsen
Department of Physical Chemistry, The Technical University of Denmark
Building 206, DK-2800 Lyngby, Denmark

March 22, 1994

Abstract

With a view to determine the effect on the material properties of the interplay between oxygen ordering and the diffusive motion of metal-ion dopants in $YBa_2Cu_{3-y}M_yO_{6+x}$ (M = Co, Fe, Al) we have developed, for a specific statistical mechanical model, a Monte Carlo computer-simulation algorithm in optimized C* and implemented the program on a 8192-processor CM200 Connection Machine. The algorithm, which allows for the simultaneous diffusive motion of oxygen atoms and metal ions, takes full advantage of all single-bit processors available on a CM200. Performance on the CM200 is compared with that on a 65536-processor CM2 as well as various serial workstations. The simulation results on the physical model show in the case of small oxygen concentrations significant metal-ion domain-formation effects related to phase separation into a phase with dense packing of oxygen and metal-ion dopants. At high oxygen concentration, a dispersed phase is found with a strong tendency towards formation of extended O-M-O-M chains. The results are briefly discussed in relation to experiments on $YBa_2Cu_{3-y}Fe_yO_{6+x}$.

*Submitted to Computational Materials Science

1 Introduction

The simulation of the material properties of solids, that are predominantly controlled by long-range correlations and strong spatial fluctuations, usually proceeds by the use of simplified statistical mechanical models. In these models, the particles are arrayed on regular lattices and the interaction is given by an effective Hamiltonian [1, 2]. The effective Hamiltonian often contains some model parameters which are not known from first-principles calculations and which typically have to be determined by fitting simulation results to experimental data. In the case of classical particle systems with strongly fluctuating modes due to ordering processes and phase transitions, the effective Hamiltonian is often tailored on the basis of a lattice-gas or Ising formalism which captures the essential structural properties of a cooperative many-body system. The lattice-gas formulation implies some major computational advantages over molecular dynamics [3]. This permits large-scale Monte Carlo simulations on particle assemblies that are sufficiently large to permit accurate description of the cooperative phenomena. In the present paper we study some structural properties in ceramic high-temperature superconductors by means of a simple lattice-gas formalism using Monte Carlo simulation on a massively parallel computer, the Connection Machine.

The structural properties of the ceramic high-temperature superconductor, $YBa_2Cu_{3-y}M_yO_{6+x}$ (M = Co, Fe, Al), and the way the structural properties relate to superconductivity, lends itself to a model-simulation study which uses an effective Hamiltonian in a simple lattice-gas formalism. A number of different properties of statistical models of this material has already been studied by simulation techniques using serial computers [4, 5, 6, 7, 8, 9, 10, 11, 12, 13, 14, 15, 16, 17, 18, 19] and a preliminary report on the use of the CM200 has appeared [20].

In Monte Carlo simulations of lattice-gas models the particle positions and the occupancy on the lattice points are governed by stochastic dynamics. For descriptions within the grand canonical ensemble, where the particle number is a fluctuating quantity controlled by a chemical potential, the dynamics is most often taken to be the Glauber mechanism which implies independent single-site particle creation or annihilation processes. In the case of systems with conserved particle density (described within the canonical ensemble) the diffusive dynamics is usually taken to be that of two-site exchange of particles on nearest- or next-nearest neighbor sites. The Kawasaki dynamics, which is a faithful description of the local diffusive modes, is more demanding computationally compared with the Glauber dynamics since each excitation of the lattice involves correlated sites. A number of papers have been devoted to a description of how Kawasaki dynamics for Ising models can be implemented on vector computers using various generalized versions of the checkerboard principle [21, 22, 23, 24]. Furthermore, a LISP program developed for the Connection Machine has previously been described for implementation of nearest-neighbor Kawasaki exchange for the ferromagnetic Ising model in order to describe spinodal decomposition [25, 26].

In the present paper we develop a parallel program to account for the simultaneous diffusion of two different particle species on a two-dimensional lattice using a Monte Carlo method based on single-site Glauber dynamics as well as two-site Kawasaki exchange dynamics. The particular model used describes the interaction and diffusion of oxygen atoms and mobile metal ions in the basal $(Cu_{1-y}M_yO_x)$-plane of the $YBa_2Cu_{3-y}M_yO_{6+x}$ superconductor. The program can easily be extended to lattices of higher spatial dimension.

The statistical mechanical lattice model, *i.e.* the effective Hamiltonian, and the particle dynamics are described in Sec. 2. The parallel algorithm written in optimized C* for the CM200 is described in Sec. 3, which also contains the results of a performance test and a comparison of the efficiency with that of the earlier version of the Connection Machine CM2 as well as serial workstations. Section 4 is devoted to a description of some of the results obtained from the simulations with emphasis on the influence of metal-ion diffusion on the M-dopant clustering and the

oxygen-ordering properties of $YBa_2Cu_{3-y}M_yO_{6+x}$. The results are discussed in Sec. 5 in relation to experimental observations in M=Fe-doped systems.

2 The lattice-gas model and its dynamics

The statistical mechanical lattice model we have used to study the effect of metal-ion doping in $YBa_2Cu_{3-y}M_yO_{6+x}$ is a modified version [12, 13] of the original two-dimensional ASYNNNI model proposed by de Fontaine *et al.* [27]. The ASYNNNI model is known to account quantitatively for the structural properties of $YBa_2Cu_3O_{6+x}$ [15]. Within the ASYNNNI model the sites available to the oxygen atoms in the basal CuO_x plane constitute a square lattice embedded with another square lattice of Cu atoms, as shown in Fig. 1.

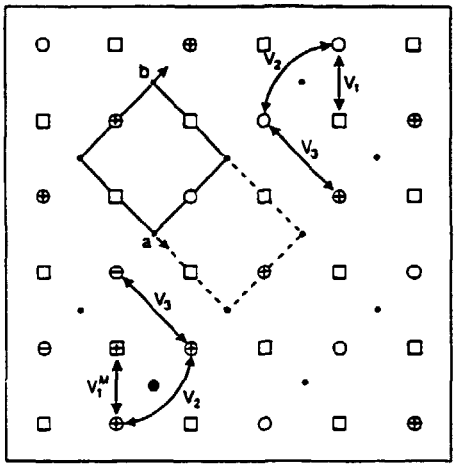

Figure 1: Schematic presentation of the $(Cu_{1-y}M_yO_x)$ basal plane defining the atomic configurations, the structural ordering configurations, and the oxygen interaction parameters of the modified ASYNNNI model. • are Cu atoms, and ● an M-atom. The crystallographic unit cell of the ortho-I structure is drawn with full lines. In the perfect ortho-I structure all the circles are occupied and the squares (□) are empty oxygen sites. In the perfect ortho-II structure only the ⊕ are occupied. It results in the doubling of the unit cell along the a-axis, indicated by the extension with dashed lines. M-doping, indicated by ●, increases the probability of occupation on the □ type oxygen sites, but will in consequence cause depletion on the ⊖ sites. The interaction parameters of the modified ASYNNNI model include the nearest-neighbor oxygen interactions around Cu, V_1, and M, V_1^M, and the anisotropic next-nearest-neighbor oxygen interactions, V_2 and V_3. The parameters V_1, V_2, and V_3 are adopted from the original ASYNNNI model for $YBa_2Cu_3O_{6+x}$ without modifications.

The ASYNNNI model is an effective model in the sense that it only accounts directly for the interactions between the oxygen atoms on the lattice, and the coupling to the other atoms is hidden in the effective coupling constants. The grand canonical Hamiltonian of the ASYNNNI model is given by

$$\mathcal{H}_{\text{ASYNNNI}} = -V_1 \sum_{i,j}^{\text{NN}} n_i n_j - V_2 \sum_{i,j}^{\text{NNN(Cu)}} n_i n_j - V_3 \sum_{i,j}^{\text{NNN}} n_i n_j - \mu \sum_i n_i \,, \qquad (1)$$

where $n_i = 1,0$ is the oxygen occupation variable of the ith site, and μ is the chemical potential. The interaction parameters are defined as follows: V_1 is the nearest-neighbor (NN) coupling, and V_2 and V_3 are the locally anisotropic couplings between next-nearest-neighbor (NNN) pairs, as shown

in Fig. 1. These interactions are attractive or repulsive depending on whether or not the oxygen pair is bridged by a Cu atom. The interaction constants have been determined for the undoped system from simulation studies of the structural phase diagram and subsequent comparison with experimental data [10, 15] to be $V_1 < 0$, $V_2/V_1 = -0.36$, and $V_3/V_1 = 0.12$. The equilibrium phase diagram contains an oxygen-disordered tetragonal phase and two oxygen-ordered phases: ortho-I which at perfect order corresponds to $x = 1$, and ortho-II which at perfect order corresponds to $x = 1/2$. Both oxygen-ordered phases consist of CuO-chains aligned along one of the crystallographic axes, usually taken as the b axis, and with essentially no oxygen atoms on the available sites on the a axis, as indicated in Fig. 1. The perfect ortho-I structure has all CuO chains fully occupied with oxygen. In the perfect ortho-II structure only every second chain is occupied.

In the absence of a detailed model for the covalent oxygen-metal interactions one has to look for a way of describing phenomenologically the fact that Co, Fe, and Al have higher oxidation and coordination numbers than Cu. We have chosen the simplest possible formulation [12] which can be made within a pairwise interaction scheme and which accounts for the tendency towards increased oxygen coordination around the M-sites. We assume the M-species to be distributed on the Cu sites, and adopt the model Hamiltonian given by Eq. (1) and the interaction parameters for the undoped material except for the nearest-neighbor interaction parameter for oxygen atoms around the M-atoms, V_1^{M}, which we assume to be less repulsive than V_1. The Hamiltonian of the modified ASYNNNI model is then given by

$$\mathcal{H} = \mathcal{H}_{\mathrm{ASYNNNI}} - (V_1^{\mathrm{M}} - V_1) \sum_{i,j}^{\mathrm{NN(M)}} n_i n_j \,. \tag{2}$$

The Monte Carlo simulation uses a simple Metropolis algorithm, and the equilibrium of the model is obtained by using Glauber dynamics or Kawasaki exchange dynamics for the oxygen atoms and Kawasaki exchange dynamics for the dopant ions, each on their respective lattice, *cf.* Fig. 1. Specifically in the case of Kawasaki dynamics, the oxygen atoms can jump to nearest as well as next-nearest vacant sites on the oxygen lattice with equal attempt frequency. The M-ions can exchange with nearest-neighbor Cu atoms on the metal-ion lattice. The dynamics for the two-species diffusive motion is discussed in relation to the experimental system in Sec. 5.

3 A parallel computer-simulation program for CM200

In the Connection Machine system, the front-end is a standard serial workstation, which is connected to the parallel processors. Programs for the CM200 reside and run on the front end. Serial parts of the program are executed on the workstation in the usual manner; parallel parts of the program are executed on the parallel processors. The CM200 is a single instruction multiple data (SIMD) computer containing modules of 8192 (2^{13}) single bit-processors, and a hyper-cubic data router. Each processor has 128 kb local memory available, giving a total of 1Gb memory/module. In our simulations we have used one module. The processors are gathered in groups of 32 bit-processors in addition to a Weitek vector floating point processor to form a processing element. All floating points and integer operations are performed through this group of processors. Unlike a CM5 Connection Machine, the CM200 only operates on whole arrays at a time, yet with a possibility to mask out inactive elements of the array. However, the processors assigned to the masked out elements, are still performing the computations, but not storing the result in their local memory. The total number of sites in the array have to be a multiplum of the total number of physical processors (8192, 16384, *etc.*). The parallel program is written in C* which has a syntax similar to C. The C*

compiler translates this program into a pseudo-language called C/Paris, which is then translated by a standard C-compiler.

All commands passing between the serial workstation (front-end) and the Connection Machine are performed by library function calls defined in C/Paris.

It should be noted that it is difficult from FORTRAN or LISP languages to access the single-bit processors directly, because all floating point operations are performed by the Weitek group, in a socalled "slice-wise mode". Programs which rely heavily on bit-manipulations will therefore have a clear advantage of using C* where all single bit-processors are directly accessible.

When the C* compiler translates the parallel C* program into C/Paris, almost no optimization is performed. Several redundant assignments may therefore exist in the C/Paris program. The non-optimized C/Paris program is transferred to a standard C compiler. However, since the C compiler is not able to detect what the C/Paris program actually is doing, it will not be able to optimize it. Until a dedicated optimizer for C* has been written, it may therefore be an advantage to write parts of the code directly in C/Paris as done in the present work.

3.1 The energy table

The ASYNNNI model is a lattice gas model, which makes it possible to perform all updates of the lattice in a manner which only depends on the configuration of the neighbors. An oxygen site in the ASYNNNI model interacts with eight neighbors on a two-dimensional lattice. The contribution from each neighbor to the energy depends on the specific type of neighbor relation, see Fig. 1. The energy associated with a given site can be precalculated for all possible neighbor configurations. This will lead to an energy table, which can be indexed by the relevant configuration of neighbors. The index can be calculated by use of bit manipulation [28], since each of the two types of neighbor sites can only be in two states: oxygen sites occupied or vacant, and Cu or M on the copper sites.

An array in C* is normally stored as a copy in the memory of each processor, but it is also possible to store an array in a memory-efficient way (in the Weitek group) by a socalled "shared table" [29] which has been done for the energy table. This implies a 32 times reduction of the memory needed, compared with a normal C* array.

3.2 Updating principles

The Monte Carlo simulation of a statistical mechanical model with a Hamiltonian $\mathcal{H}$ provides a sequence of configurations of the system, which are distributed according to the appropriate Boltzmann probability. The resulting determination of physical quantities corresponds to a time-averaging process by which the system evolves according to stochastic dynamics. In the Metropolis algorithm the successive configurations are not chosen independently of each other, but rather constructed as a Markov chain, in which the transition probability for going from ω to ω' is given by

$$W(\omega \to \omega') = \begin{cases} \exp[-\{\mathcal{H}(\omega') - \mathcal{H}(\omega)\}/k_B T], & \text{if } \mathcal{H}(\omega') \geq \mathcal{H}(\omega) \\ 1 & \text{otherwise.} \end{cases} \quad (3)$$

In the case of Glauber dynamics the transition probabilities are precalculated and arranged into a table similar to the energy table. However, for Kawasaki dynamics there are too many configurations to make such a table practicable. Hence, the transition probability in this case is only partially precalculated by splitting the transition probability into two factors which each only depends on a single site. When a single site is considered for updating by the Metropolis algorithm Eq. (3), it is necessary to calculate the energy difference associated with the change of state. Only after having decided whether this update is performed or not we are free to consider updating of

neighboring sites. Simultaneous updating of neighboring (*i.e.* physically interacting) sites is not allowed because the Boltzmann distribution is violated. This problem relevant for simulations on a parallel computer, may be solved by generating a mask which is a modification of the simple checkerboard principle. The mask selects a subsystem of independent or groups of independent lattice sites. For the model considered this leads to a partition of the lattice into four independent subsystems. However, calculations on only one subsystem at a time imply that only one fourth of the processors are active. All the available processors may be activated by performing calculations on four *different* physical systems at the same time, which leads to a four times increase in the amount of statistical data.

Figure 2 illustrates the Glauber dynamics procedure for updating of the oxygen sites.

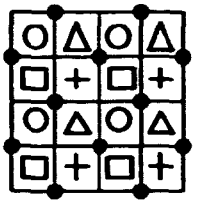

Figure 2: The layout of the parallel processors in the case of Glauber dynamics. Symbols represent sites of different physical systems which are labeled by ○, □, +, and △. The metal-ion sites are denoted by •. There are four possible ways of making this composite labeling of the lattice. See detailed description in text.

The oxygen sites of the four different physical systems are labeled by ○, □, +, and △. The layout of the parallel processors is illustrated as a 4×4 array, where the labels above denotes which physical system each processor is updating. By arranging the subsystems of the different physical systems in this manner all sites are non-interacting and can therefore be updated simultaneously. The updating of the other subsystems of the different physical systems is performed in an analogous manner. The updates of the metal-ion sites, denoted by •, are performed by randomly selecting between different types of Kawasaki pair exchanges between the metal-ion sites, as described below in connection with Fig. 3 (only Kawasaki updates are relevant for the non-volatile metal-ion system).

Figure 3 illustrates in the upper panel specific types of updates with pair exchange using Kawasaki dynamics in the physical lattice and the associated pair subsystems. As for the case of Glauber dynamics the oxygen sites of the four different physical systems are labeled by ○, □, +, and △. In the lower panel the layout of the parallel processors is shown. For the oxygen system, where exchange between both nearest and next-nearest neighbors are considered, there are eight different directions in which a given oxygen atom, in a pair subsystem may exchange with a vacancy, ●→ ○, on neighboring sites. Both diagonal (Fig. 3 (a)) and axial (Fig. 3 (b)) directions are considered. By inter mixing the oxygen sites from different physical systems as described all processors can be activated. For the metal-ion lattice only nearest neighbor diagonal updates are considered. Clearly, the diagonal update scheme developed for the oxygen system may be used also for the metal-ions, which gives a total of four independent metal-ion update types. Since there are no direct interaction between the metal-ions, all the metal-ions shown in the lower part of Fig. 3 (c), may in principle be updated simultaneously. In practice they are updated like the oxygen atoms because of the reduced programming effort. The update of an entire physical system is performed by randomly selecting between all different oxygen and metal-ion update types.

The data organization used for the Monte Carlo updating is, however, not the optimal one for

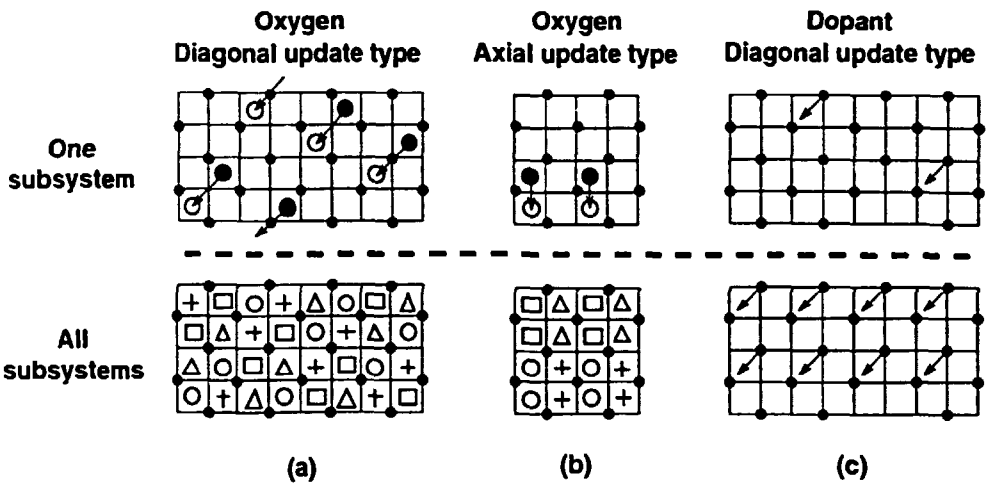

Figure 3: The oxygen sites of the four different physical systems are labeled by ○, □, +, and △. The layout of the parallel processors is illustrated in the lower panel. For two examples of a diagonal (figure 3 (a)) and an axial (figure 3 (b)) oxygen update it is shown how the oxygen subsystems of the four different physical systems are arranged with respect to the parallel processors. For the oxygen system, where exchange between both nearest and next-nearest neighbors are considered, there are eight different directions in which a given oxygen atom, ●, in a pair subsystem may exchange with a vacancy, ○, on neighboring sites. For the metal-ion lattice only nearest neighbor diagonal updates are considered as shown in panel (c).

calculation of physical quantities, especially for the Kawasaki algorithm. Before each calculation of the quantities, the different subsystems are therefore reassembled into the full lattice.

3.3 Performance test

We have conducted a performance test of the MC-simulation program by comparing the performance on the CM200 with that of the CM2 and different serial workstations. The results of the performance test are given in Table 1.

Computer\Algorithm	Kawasaki +M	Kawasaki −M	Glauber +M	Glauber −M
HP/705	$1.36 \cdot 10^4$	-	-	$4.15 \cdot 10^3$
Apollo/Dn10000	$1.59 \cdot 10^4$	-	-	$2.99 \cdot 10^3$
HP/750	$3.11 \cdot 10^4$	-	-	$8.13 \cdot 10^3$
HP/735	$5.13 \cdot 10^4$	-	-	$5.40 \cdot 10^4$
CM-200 8192 proc.	$1.29 \cdot 10^6$	$2.05 \cdot 10^6$	$3.08 \cdot 10^6$	$3.24 \cdot 10^7$
CM-2 65536 proc.	$1.37 \cdot 10^6$	$2.25 \cdot 10^6$	$3.34 \cdot 10^6$	$3.01 \cdot 10^7$

Table 1: Results of performance tests indicated by the number of attempted updated lattice sites per second on a lattice with 256×256 sites. All Kawasaki tests have been done for a fully oxygenated system, $x = 1$. The symbols $\pm$M indicate whether or not the system is doped by M-ions. In the case of doping, the results of the table refer to a dopant concentration of $y = 0.15$.

The Kawasaki updating is considerably slower than that for Glauber updating on the Connection Machines, simply because the calculation of the transition probabilities are more involved for Kawasaki updating. The speed of the program can be compared with that of a somewhat similar program by Amar and Sullivan [25, 26] who have reached $1.3 \cdot 10^8$ attempted spin-exchanges

per second on the two-dimensional ferromagnetic Ising model with nearest-neighbor interactions. The higher speed is probably mainly due to the simplicity of the Ising model compared with our modified ASYNNNI model.

The results of speed tests of our MC-simulation programs obtained on different serial workstations are also given in Table 1. It should be noted that the speed depends significantly on the oxygen and the dopant concentration for the Kawasaki case. The lower the oxygen content and the smaller the dopant concentration, the faster the serial program runs for the Kawasaki case, because only exchange of particle-vacancy pairs need to be considered. This is the reason why the Kawasaki updates mentioned in Table 1 are faster than those obtained by Glauber updates. On the parallel machines all the redundant exchanges (particle-particle and vacancy-vacancy) have to be calculated.

We have furthermore analyzed how the system size influences the speed of the program. The total time spent in the central part of the MC-program has been measured for 1000 updates per lattice site for different lattice sizes. The results for systems without metal-ion doping using Glauber dynamics, and the corresponding results for Kawasaki dynamics with mobile metal-ion dopants are shown in Fig. 4.

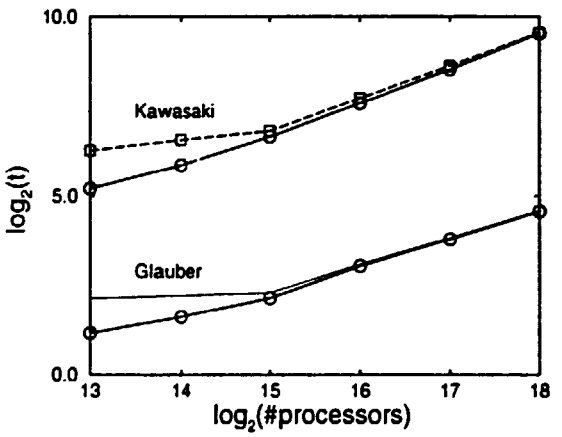

Figure 4: Double-logarithmic plot of the time spent in the central Monte Carlo core in the parallel program shown as a function of system size for both Glauber and Kawasaki dynamics. Symbols are the actual data points. The solid line represents the CM200 busy time, while the dashed line represents the total time.

The figure demonstrates that the total time spent by the program is rather insensitive to the lattice size up to about 2^{15} sites on the 8192-processor CM200. Figure 4 also shows the busy-time contributions to the total time. The observed variation of the total time and busy-time indicates that the time spent on communication between the front-end and the CM is determining the speed of the program for small systems. For larger systems the analysis of the size dependence shows an increased utilization of the CM. Only when each processor is handling four sites or more does the Connection Machine start to be a limiting factor for the computational speed.

We have found that when both the oxygen and the dopant ions are allowed to diffuse simultaneously, the system approaches thermodynamic equilibrium very slowly. The reason for this is apparently due to the use of our particular parallel algorithm by which the particles only are moved to neighboring sites and are furthermore moved in the same direction. This is particularly troublesome for the equilibration process if the dopant ions tend to cluster in a compact manner, as

will be described in Sec. 4. The formation and equilibration of such clusters and large domains are only slowly acquired by our parallel algorithm since the oxygen and dopant-ion motions in this case are strongly correlated. Typically, the number of updates per site required to reach equilibrium on the CM, in cases where compact clustering occurs, may be 10-100 times larger than on a serial workstation which allows ions on different sites to move in independent directions.

Hence, the performance of the CM relative to that of a serial workstation on the present type of physical problem depends critically on the actual way the two diffusing species organize themselves on the lattice.

4 Simulation results

In this section we report on preliminary results [30] of an extensive series of simulations on the model in Eq. (2) using the parallel algorithm described above. Particular emphasis will be put on the generic behavior of the system and its lateral organization, specifically the variation of the system properties as a function of the dopant coupling constant, V_1^{M}. These results will serve as the necessary basis for a detailed analysis in relation to experimental observations on M-doped $YBa_2Cu_{3-y}M_yO_{6+x}$ prepared under different conditions [30].

In Fig. 5 is shown the average internal energy, $E/|V_1|$, per oxygen atom as a function of dopant coupling parameter, $V_1^{\mathrm{M}}/|V_1|$.

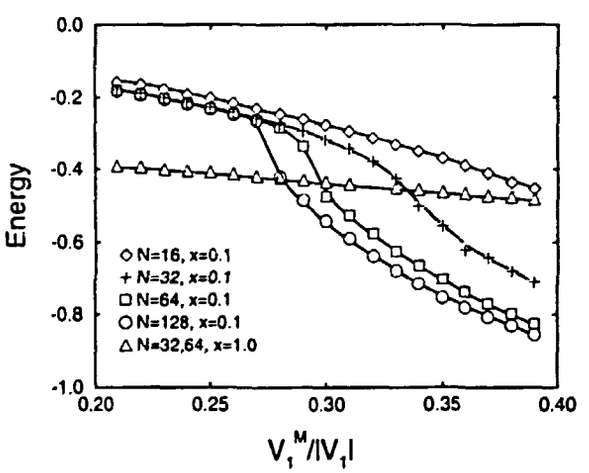

Figure 5: Average internal energy, $E/|V_1|$, per oxygen atom as a function of reduced dopant coupling constant, $V_1^{\mathrm{M}}/|V_1|$, shown for four different lattice sizes. In all simulations the temperature was fixed to $k_BT/|V_1| = 0.15$ and the dopant-ion concentration was $y = 0.15$. For an oxygen content of $x = 0.1$ the symbols refer to the following lattice sizes: $N = 16 \times 16\,(\diamond)$, $32 \times 32\,(+)$, $64 \times 64\,(\square)$, and $128 \times 128\,(\bigcirc)$. For an oxygen content of $x = 1$ the data points $(\triangle)$ for lattice sizes 32×32 and 64×64 yield almost identical results. The solid lines are guides to the eye.

The figure demonstrates that in the case of low oxygen concentration, the energy has a dramatic dependence on system size for high values of the coupling parameter, whereas at low values there is no significant size dependence. In contrast, for large oxygen contents the energy displays only a weak size dependence as a function of V_1^{M}. The data for low oxygen contents display an inflection point which occurs at a lower value of the coupling parameter the larger the size of the lattice is. For the largest lattice sizes, the energy displays a rather strong variation within a narrow range of the coupling parameter. This suggests that a phase-separation process occurs at low oxygen contents

for increasing coupling parameter values. The phase-separated state is the stable phase beyond the inflection point in the energy. Consistent with this interpretation the specific heat is found to have a peak where the phase separation sets in. For lower temperatures, the phase transition point is, for a given system size, shifted to lower values of V_1^M, simple because the entropy contribution in the dispersed non-phase separated state is smaller.

The occurrence of a phase separation is supported by the snapshots in Fig. 6 which indeed show that a domain formation sets in at low oxygen contents and for large values of the coupling parameter, V_1^M, and that these domains at late times, *cf.* Fig. 6 (e) form a separate phase.

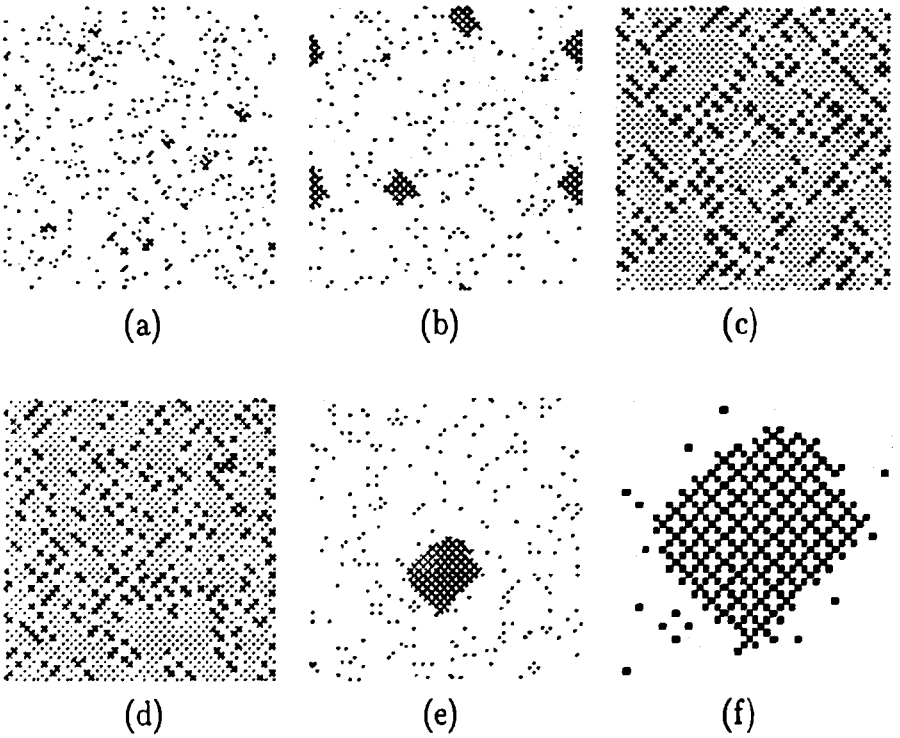

Figure 6: Selected snapshots of oxygen and dopant ion configurations. Red dots denote oxygen atoms, black dots denote the dopant metal ions, and blue denote vacant oxygen sites. The configurations correspond to typical equilibrium states for a lattice with 128 × 128 oxygen sites at a temperature $k_B T/|V_1| = 0.15$ and a dopant concentration of $y = 0.15$. The configurations correspond to an equilibration time of $4 \cdot 10^4$ MCSS. (a) $x = 0.1$ and $V_1^M/|V_1| = 0.2$. (b) $x = 0.1$ and $V_1^M/|V_1| = 0.4$. (c) $x = 1$ and $V_1^M/|V_1| = 0.2$. (d) $x = 1$ and $V_1^M/|V_1| = 0.4$. (e) Same as (b) but after a much longer equilibration time corresponding to $4 \cdot 10^5$ MCSS. (f) Enlargement of a section of the snapshot in (e).

This phase is a dense (1 × 1) oxygen structure in which all metal-ion sites are occupied by the dopant ions, as illustrated in the blow-up snapshot in Fig. 6 (f). The M-dense domains coexist with an oxygen-poor phase (a gas) with a certain dispersed fraction of the remaining M-ions. The strong size dependence of the energy, *cf.* Fig. 5, in the phase-separated phase can be rationalized by a simple rescaling of the size-dependent energy by a correction term which accounts for the surface-to-volume ratio of the M-dense, almost circular (1 × 1) oxygen domain that occurs at late times. Not all of the dopant ions take part in the phase separated domain, because for low values

of the oxygen content, shown in Fig. 6 (b), there is simply not enough oxygen to get all the M-ions together. A substantial part of the M-ions therefore remain dispersed in the oxygen-poor phase.

The formation of the dense metal-ion cluster structure is a result of the interface energy which is high at low oxygen contents. At high oxygen contents, the interfacial energy is low, and the metal ions are effectively absorbed into the oxygen phase. The metal-ions are divided among the largest possible number of oxygen atoms, as shown in Fig. 6 (c) and (d), and correspondingly only a weak dependence of V_1^M is observed.

We now turn to a more detailed analysis of the lateral organization of the doped system in terms of domains of M-ions. A domain (cluster) is defined as a structure of M-ions connected by nearest or next-nearest bonds on the metal-ions lattice. The size, Ω, of a domain is defined as the number of M-ions in the domain. In order to characterize the shape of the domain, we calculate also a linear extension, R in units of the oxygen lattice constant. R is defined as the largest edge of the smallest rectangle which, when aligned along the axis of the oxygen lattice, circumscribes the domain. Together, these two measures of a domain will describe possible shape transitions of domains from chain structures to compact disc-like structures. Single-ion "domains" are not included in the calculation of average domain properties.

In Fig. 7 (a) and (b) are shown the results for the average domain size, Ω, and the average linear domain extension, R, respectively, corresponding to the data for the internal energy given in Fig. 5.

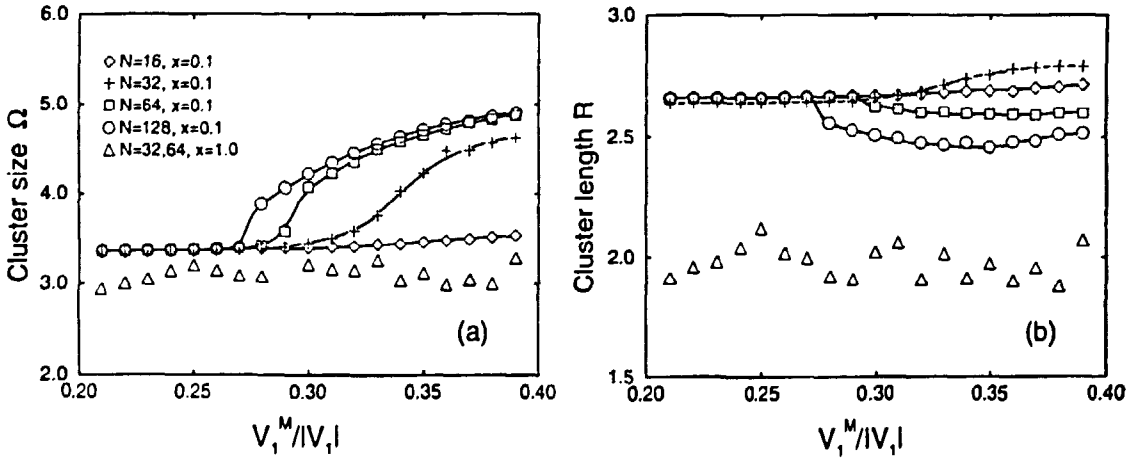

Figure 7: In panel (a) is shown the average M-dopant cluster size, Ω, as measured from the number of M-dopant ions that participate in a cluster, while in panel (b) is shown the corresponding linear average M-dopant cluster extension, R. Both quantities have been calculated as a function of reduced dopant coupling constant, $V_1^M/|V_1|$. In all simulations the temperature was fixed to $k_BT/|V_1| = 0.15$ and the dopant-ion concentration to $y = 0.15$. For an oxygen content of $x = 0.1$ the symbols refer to the following lattice sizes: $N = 16 \times 16$ (◇), 32×32 (+), 64×64 (□), and 128×128 (○). For an oxygen content of $x = 1$ the data points (△) for lattice sizes 32×32 and 64×64 yield almost identical results. The solid lines are guides to the eye.

Both these figures show a behavior of the measures of the domains that is consistent with the onset of phase separation at low oxygen contents and the absence of phase separation for high oxygen contents. The smallest system size studied, $N = 16 \times 16$, has not entered the phase separated state for the coupling-constant values studied. The domains which can be formed in a system of this size are simply not large enough to overcome the unfavorable interface energy. In contrast to

the finite-size scaling of the internal energy, there is no straightforward way of describing the size dependence of the cluster sizes in Fig. 7 (a). The occurrence of a number of small domains along with the large phase-separated domains has a strong influence on the average properties which depends on the actual size-distribution function.

The clear onset of the formation of domains of large size seen in Fig. 7 (a), for the large systems $N = 64, 128$ in the case of low oxygen contents, is accompanied by a simultaneous decrease in the average linear domain extension, R. This signals a compactification of the domains. The average domain size is increased due to the fact that there are only few domains in the dilute gas phase. Below the phase separated region, the domains are linear consisting of single O-M-O-M chains, which is also obvious from the snapshots in Fig. 6 (a). In the non phase-separated state and as V_1^{M} tends to V_1 (decreasing $V_1^M/|V_1|$), the average domain size and the average linear domain extension are approaching those for a completely random configuration at the given dopant concentration. For the small system sizes, R in Fig. 7 (b) has a special behavior. Since there is no phase separation in the $N = 16 \times 16$ lattice, all domains are small O-M-O-M chains and R does only depend weakly on V_1^{M}.

5 Discussion and comparison with experiments

In the present paper we have investigated, by a parallel Monte-Carlo computer-simulation algorithm, the interplay between oxygen ordering and metal-ion diffusive modes in a simple lattice-gas model of the basal $(Cu_{1-y}M_yO_x)$-planes of M-ion doped $YBa_2Cu_3O_{6+x}$ compounds. Results were obtained for different values of the dopant coupling parameter. The range of parameters investigated should cover a range of metal-ion dopants, including Co, Fe, and Al, which all are supposed selectively to substitute for Cu in the basal planes. Our work may be seen as an extension of a previous model calculation by Andersen *et al.* [12] that was based on the same Hamiltonian in Eq. (2) but with randomly distributed non-mobile dopant ions. The extension was made in order to account for the experimental observation for M=Fe which indicates that the Fe-ions are mobile at high temperatures [31].

The experiments on the Fe-doped system [31] have also indicated that the structural oxygen ordering increases and the superconducting properties are improved when the system is brought to equilibrium at high temperature in an atmosphere with low oxygen pressure, and subsequently cooled down into the orthorhombic phase and annealed in a one bar oxygen atmosphere. This procedure can be compared with equivalent experiments, starting with a high oxygen pressure [31]. The experimental results may be interpreted to result from dopants that are mobile at high temperatures since the dopants somehow seem to arrange themselves better at low oxygen pressure than at high oxygen pressure. The computer simulation approach presented in this paper is a simulation of this type of experiments [30] and our findings lend support to the interpretation of the experimental data proposed in Ref. [31].

The main conclusion of the present work is that the value of the dopant interaction parameter has a very strong influence on the structural ordering properties in the basal plane of the superconductor. Massive domain formation and phase separation can occur at low oxygen contents. If the system is quenched in temperature, and the dopant ions hence are made immobile, a subsequent annealing in high oxygen pressure may result in orthorhombic oxygen-ordered phases that are highly spatially coherent, producing a high superconducting transition temperature [12]. This is contrary to the ordered states that are formed when the annealing is performed in high oxygen pressure and at higher temperatures where the dopant ions are mobile. The complex phenomena are intimately related to the subtle interplay between the oxygen ordering, and the competition for oxygen between Cu and the dopant metal ions. It is likely that simple model simulations of the

type described in the present paper will prove useful in guiding experiments on doped materials with an aim to produce materials with improved superconducting properties [30].

Acknowledgments

Access to the CM200 Connection Machine at UNI·C was provided via a grant from the Danish Natural Science Research Council (J.no. 11-0491). TF is supported by the Danish Research Academy. The work was furthermore supported by the Danish Ministry of Energy, by the Danish Natural Science Research Council (J.no. 11-0065-1), and by the EEC SCIENCE and ESPRIT programs. One of the authors (SM) wishes to thank Malcolm Brown for his help and inspiration during the development of the computer program. TF wishes to thank J. Berlin at the Supercomputer Computations Research Institute (Florida State University) for assistance with the CM2.

References

[1] K. Binder and D. W. Heermann, *Monte Carlo Simulation in Statistical Physics* (Springer-Verlag, Berlin, 1988).

[2] O. Mouritsen, *Computer Studies of Phase Transitions and Critical Phenomena* (Springer-Verlag, Berlin, 1984).

[3] D. C. Rapaport, in *Computer Physics Communications, Vol. 8*, edited by P. G. Burke (Elsevier Science Publisher B. V., Amsterdam, 1993), p. 301.

[4] N. C. Bartelt, T. L. Einstein, and W. L. T., Phys. Rev. B **40**, 10759 (1989).

[5] Z.-X. Cai and Mahanti, Phys. Rev. B **40**, 6563 (1989).

[6] C. P. Burmester, L. T. Wille, and R. Gronsky, Phys. Rev. B **40**, 8795 (1989).

[7] T. Aukrust, M. A. Novotny, P. A. Rikvold, and D. P. Landau, Phys. Rev. B **41**, 8772 (1990).

[8] C. P. Burmester, L. T. Wille, and R. Gronsky, Solid State Comm. **77**, 693 (1991).

[9] J. V. Andersen, H. Bohr, and O. G. Mouritsen, Phys. Rev. B **41**, 283 (1990).

[10] H. F. Poulsen *et al.*, Phys. Rev. Lett. **66**, 465 (1991).

[11] H. F. Poulsen *et al.*, Nature **349**, 595 (1991).

[12] J. V. Andersen, N. H. Andersen, O. G. Mouritsen, and H. F. Poulsen, Physica C **214**, 143 (1993).

[13] N. H. Andersen *et al.*, J. Alloys and Compounds **195**, 327 (1993).

[14] J. V. Andersen, H. Bohr, and O. G. Mouritsen, Comp. Mat. Sci. **1**, 25 (1992).

[15] T. Fiig *et al.*, Physica C **217**, 34 (1993).

[16] P. A. Rikvold, M. A. Novotny, and T. Aukrust, Phys. Rev. B **43**, 202 (1991).

[17] R. McCormack, D. de Fontaine, and G. Ceder, Phys. Rev. B **45**, 12976 (1992).

[18] D. K. Hilton, B. M. Gorman, P. A. Rikvold, and M. A. Novotny, Phys. Rev. B **46**, 381 (1992).

[19] W. Selke and G. V. Uimin, Physica C **214**, 37 (1993).

[20] T. Fiig *et al.*, in *Ann. Rep. Supercomp. UNI·C*, edited by P. C. Hansen (Dth, Lyngby, Denmark, 1991).

[21] P. J. Shah and O. G. Mouritsen, Phys. Rev. B **41**, 7003 (1990).

[22] O. G. Mouritsen, P. J. Shah, and J. V. Andersen, Phys. Rev. B **42**, 4506 (1990).

[23] O. Paetzold, in *Computer Simulation Studies in Condensed Matter Physics III*, edited by D. P. Landau, K. K. Mon, and H. B. Schüttler (Springer Verlag, Berlin, 1991), p. 197.

[24] W. Schleier, G. Besold, and K. Heinz, J. Stat. Phys. **66**, 2941 (1992).

[25] J. G. Amar, F. E. Sullivan, and R. D. Mountain, Phys. Rev. B **37**, 196 (1988).

[26] J. G. Amar and F. E. Sullivan, Comp. Phys. Comm. **55**, 287 (1989).

[27] D. de Fontaine, L. T. Wille, and S. C. Moss, Phys. Rev. B **36**, 5709 (1987).

[28] The bit manipulation can technically be performed by arranging all the possible neighbors in a programming structure that shares memory address with the energy index. This programming structure called 'bit-fields' is, however, not implemented in C* for parallel variables, which makes use of bit manipulations difficult.

[29] The proper command is not implemented in C*, but it can be accessed through the C/Paris commands 'aref32-shared' and 'aset32-shared'.

[30] S. Mannstaed *et al.*, a full report of results obtained by the present approach will be given elsewhere with particular focus on comparison with experimental results on $YBa_2Cu_{3-y}M_yO_{6+x}$ (M=Fe, Co, and Al) (unpublished).

[31] K. S., Y. Ueda, and K. Kosuge, Physica C **165**, 404 (1990).

Paper IV

Numerical Transfer-matrix Study of a Model with Competing Metastable States

Numerical transfer-matrix study of a model with competing metastable states*

T. Fiig†

Supercomputer Computations Research Institute,
Florida State University
Tallahassee, Florida 32306-4052
and Department of Solid State Physics,
Risø National Laboratory
DK-4000 Roskilde, Denmark

B. M. Gorman and P. A. Rikvold

Supercomputer Computations Research Institute,
Center for Materials Research and Technology
and Department of Physics,
Florida State University
Tallahassee, Florida 32306-4052

M. A. Novotny

Supercomputer Computations Research Institute,
Florida State University
Tallahassee, Florida 32306-4052

March 21, 1994

*Submitted to Physical Review E.

†Present address: Department of Solid State Physics, Risø National Laboratory, DK-4000 Roskilde, Denmark.

Abstract

The Blume-Capel model, a three-state lattice-gas model capable of displaying competing metastable states, is investigated in the limit of weak, long-range interactions. The methods used are scalar field theory, a numerical transfer-matrix method, and dynamical Monte Carlo simulations. The equilibrium phase diagram and the spinodal surfaces are obtained by mean-field calculations. The model's Ginzburg-Landau-Wilson Hamiltonian is used to expand the free-energy cost of nucleation near the spinodal surfaces to obtain an analytic continuation of the free-energy density across the first-order phase transition. A recently developed transfer-matrix formalism is applied to the model to obtain complex-valued "constrained" free-energy densities f_α. For particular eigenvectors of the transfer matrix, the f_α exhibit finite-range scaling behavior in agreement with the analytically continued metastable free-energy density. This transfer-matrix approach gives a free-energy cost of nucleation that supports the proportionality relation for the decay rate of the metastable phase $\Gamma \propto |\mathrm{Im} f_\alpha|$, even in cases where two metastable states compete. The picture that emerges from this study is verified by Monte Carlo simulation.

PACS Number(s): 64.60.My, 64.60.Qb, 02.70.Rw, 03.50.Kk

1 Introduction

The investigation of metastable states and their decay through thermally activated nucleation has been the focus of numerous works. (For reviews, see *e.g.* Refs. study of the analytic properties of the free energy at the condensation point, Langer [3] conjectured that the imaginary part of the free energy $\tilde{F}$ analytically continued from the equilibrium phase across the first-order phase transition may be associated with the decay rate of the metastable phase. A dynamical investigation [4, 5] showed for a wide class of models that the decay rate Γ may be written in terms of $\mathrm{Im}\tilde{F}$ as

$$\Gamma = \frac{\beta\kappa}{\pi}|\mathrm{Im}\tilde{F}|\,, \tag{1}$$

where β is the inverse temperature and κ is a kinetic prefactor that depends on the dynamics. (We set k_B=1 throughout this work.) Subsequently, Binder and collaborators [6, 7, 8] developed a scaling theory using a nonequilibrium relaxation function to define the metastable states and tested the theory by Monte-Carlo simulation on the two-dimensional Ising model. Schulman and collaborators studied by various methods metastability in the two-dimensional Ising model [9], in the one-dimensional Kac model with algebraically decaying interactions [10], in the Curie-Weiss model [11], and in a droplet-like "urn" model [12]. In addition, Büttiker and Landauer [13, 14] studied nucleation in the over-damped one-dimensional sine-Gordon chain, and Klein and Unger [15, 16] studied classical metastability in systems with long-range interactions using a ϕ^3 field theory. Each of these studies supported the validity of Langer's treatment. More recently Gaveau and Schulman [17] determined a rigorous upper bound for the decay rate for a larger class of models than that considered by Langer, and used it not only to explain why Eq. (1) is usually valid, but also provided an example in which Eq. (1) may not appropriately describe the decay rate of the metastable state.

One method for studying metastability that has been used previously is the transfer-matrix approach. Privman and Schulman [18, 19] obtained an indication of metastability in their transfer-matrix treatment of the two-dimensional Ising model. Rikvold *et al.*, [20, 21, 22] studied the stationary properties of metastability in a two-state model with weak, long-range forces, the quasi-one-dimensional Ising (Q1DI) model [23], with a constrained-transfer-matrix (CTM) formalism. This method produces a set of "constrained" free-energy densities f_α, some of whose imaginary parts have been demonstrated to be related to the metastable decay rate [24]. In particular, strong quantitative agreement was found between the imaginary part of the constrained free-energy density and the analytically continued free-energy density. Recent studies of the two-dimensional Ising model with nearest-neighbor interactions, also using the CTM method [25, 26], found that the imaginary part of the constrained free-energy density is consistent with Monte-Carlo estimates of the metastable lifetime [27] and agrees well with field-theoretical droplet-model calculations [1, 3, 4, 5, 28, 29].

Our previous studies of metastability [20, 21, 22, 23, 24, 25, 26, 27] have focused on systems with one single metastable state. In the present paper we examine a system with two competing metastable states using scalar field theory, the CTM method, and dynamical Monte Carlo simulations. The purpose is two-fold: to test the applicability of the CTM formalism to a system with a more complicated metastability structure and to obtain a clearer understanding of the implications of a recent result of Gaveau and Schulman [17].

This result of Ref. [17] can be summarized as follows. Consider a three-state system with two degenerate metastable phases, A and B, and an equilibrium phase C, and assume that the reaction path in phase space connects the states only in the following way: $A \to B \to C$. According to the Van't Hoff-Arrhenius law [30], the decay rate of A is $\Gamma_A \propto \exp(-\beta \Delta F_{A \to B})$, where $\Delta F_{A \to B}$ is the height of the free-energy barrier on the path $A \to B$. Gaveau and Schulman argued that the procedure of analytically continuing the free energy for such a system from C into A gives $\mathrm{Im}(\bar{F}) \propto \exp(-\beta \Delta F_{B \to C})$, where $\Delta F_{B \to C}$ is defined analogously as above, which when coupled with Eq. (1) does not appropriately describe the decay rate of A. Such a discrepancy would give rise to a fundamental question about the physical interpretation of the imaginary part of the constrained free-energy density $\mathrm{Im} f_\alpha$ in our CTM formalism. Is $\mathrm{Im} f_\alpha$ related to the decay rate in a system with competing metastable states? Based on our analytic and numerical results in this paper, we will argue that $\mathrm{Im} f_\alpha$ does indeed give the correct decay rate of A.

The system we have chosen is a variant of the Blume-Capel model [31, 32, 33] with weak, long-range interactions. The Blume-Capel model is an $S=1$ Ising model and is equivalent to a particular three-state lattice-gas model. This model and its generalizations have been studied extensively in the literature, and they have been applied to a variety of different systems (see *e.g.* Ref. [34] for some chemical applications) and have been studied with different techniques, including mean-field approximations [31, 32, 33], position-space renormalization group [35], transfer-matrix and Monte-Carlo finite-size scaling methods [36], and Monte-Carlo renormalization group [37].

The Hamiltonian for the original ferromagnetic nearest-neighbor Blume-Capel model is given by

$$\mathcal{H} = -J \sum_{(\alpha,\beta)} s_\alpha s_\beta + D \sum_\alpha s_\alpha^2 - H \sum_\alpha s_\alpha \,, \tag{2}$$

where the local spin variables s_α at site α can take three values, $s_\alpha = \{0, \pm 1\}$. The spin-spin interaction is ferromagnetic ($J>0$), D is an applied field that either favors ($D>0$) or disfavors ($D<0$) $s_\alpha=0$, and H is an applied magnetic field. The indices α and β run over a lattice, and the sum $\sum_{(\alpha,\beta)}$ runs over nearest neighbors. Unfortunately, the transfer matrix for this model is so complicated that extending it to long-range interactions would be impractical. We therefore introduce a new model, the long-range Blume-Capel model, which we define in Sec. 2 in analogy with the Q1DI model [23].

Systems with long-range interactions are often useful to study since they share many characteristics of mean-field models, which are often exactly soluble. Among these characteristics are the presence of metastable and unstable stationary states, which exist for external fields that lie between the first-order phase boundary and a sharp spinodal. (In contrast, in systems with short-range interactions, the spinodal is replaced by a smooth crossover.) In addition, a number of physical systems display behavior characteristic of long-range interactions. Examples include supercooled water [38], superfluid ^{3}He [39], superconductors [40], and long-chain polymer mixtures [41].

The remainder of this paper is organized as follows: In Sec. 2 we define the long-range Blume-Capel model, discuss its zero-temperature phase diagram, and calculate exactly the finite-temperature mean-field spinodal surfaces. The analytic continuation of the free-energy density is considered in Sec. 3. The constrained-transfer-matrix formalism is briefly reviewed in Sec. 4, and its application to the long-range Blume-Capel model is described. Our numerical CTM results are presented in Sec. 5, and the finite-range scaling of the constrained free energy is discussed in Sec. 6. Section 7 contains Monte-Carlo simulation studies of the decay of metastable states, and Sec. 8 contains discussions and conclusions.

2 Phase Diagram and Spinodal Surfaces

In this section, we define a Blume-Capel model with weak, long-range interactions, and we calculate the zero-temperature phase diagram and the finite-temperature spinodal surfaces. The system consists of a one-dimensional chain of L layers, each of which contains N spins. The long-range Blume-Capel model is defined by assuming that a given spin $s_{n,i}$, where $i=1,\ldots,L$ and $n=1,\ldots,N$, interacts with each spin in the two adjacent layers with an equal interaction strength J/N. We thus replace J with J/N in the first term of the Hamiltonian of Eq. (2), and we allow the sum to range over all spins in adjacent layers. We introduce the following quantities,

$$\begin{aligned} m_i &= \frac{M_i}{N} = \frac{1}{N}\sum_{n=1}^{N} s_{n,i} \\ q_i &= \frac{Q_i}{N} = \frac{1}{N}\sum_{n=1}^{N} s_{n,i}^2 , \end{aligned} \tag{3}$$

which are the magnetization density and the density of nonzero spins in layer i, respectively. The Hamiltonian for the long-range Blume-Capel model can then be written as

$$\mathcal{H} = -JN\sum_{i=1}^{L} m_i m_{i+1} + DN\sum_{i=1}^{L} q_i - HN\sum_{i=1}^{L} m_i , \tag{4}$$

where periodic boundary conditions are imposed, that is $(\forall i)\ m_{L+i}=m_i$ and $q_{L+i}=q_i$.

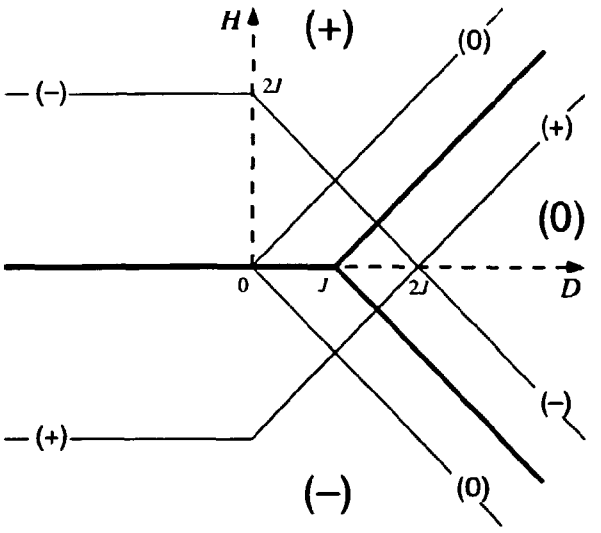

Figure 1: The zero-temperature phase diagram for the long-range Blume-Capel model. The thick solid lines are the first-order equilibrium transition lines, which divide the (D, H) plane into three regions, with stable phases (0), (+), and (−). The thin lines indicate the zero-temperature spinodals for each of the metastable phases.

In the mean-field calculation, we assume that the configurations of the system are translationally invariant, so that $m_i{=}m$ and $q_i{=}q$ for all layers $i{=}1,\ldots,L$. With this simplification, we can define a mean-field Hamiltonian $\mathcal{H}^{\mathrm{MF}}$ for the energy density as

$$\mathcal{H}^{\mathrm{MF}} = -Jm^2 + Dq - Hm\,. \tag{5}$$

In the limit $N{\to}\infty$, the densities m and q take on continuous values in a domain $\Omega{=}\{(m,q) : |m|{\le}q, 0{\le}q{\le}1\}$, which defines an isosceles triangle in (m,q) space.

Before solving this mean-field model in general, we consider its zero-temperature properties. In Fig. 1 the zero-temperature phase diagram is shown. The three stable states are $(m,q) = (0,0)$, $(-1,1)$ and $(1,1)$, which are located at the vertices of the domain Ω. In the following discussion we denote these states as (0), (−), and (+), respectively. The thick solid lines in Fig. 1 are first-order transition lines, which separate the (D,H) plane into three distinct regions, each corresponding to one stable phase, as indicated in the figure. The transition lines are found from a simple energy argument. From the mean-field Hamiltonian of Eq. (5) we can calculate the energy of the three stable phases: $\mathcal{H}^{\mathrm{MF}}(0){=}0$, $\mathcal{H}^{\mathrm{MF}}(+) = D-H-J$, and $\mathcal{H}^{\mathrm{MF}}(-) = D+H-J$. By equating these energies we obtain the transition lines. It follows from this argument that the three states have equal energy at $(D,H,T){=}(J,0,0)$. The three states can also exist as metastable states for certain values of D and H outside the region where they are stable. The reason for this is that as we cross a transition line by changing the fields D and H, the previously global minimum of $\mathcal{H}^{\mathrm{MF}}$ remains as

a local minimum. As we increase the fields further, we eventually reach a spinodal where the local minimum in $\mathcal{H}^{\mathrm{MF}}$ coincides with a saddle point, and the metastable state thus becomes unstable. The spinodal lines at T=0 can be calculated by a simple stability analysis, in which we expand $\delta\mathcal{H}$ in terms of δq and δm around the stationary states and require that $\delta\mathcal{H}$=0. The spinodal lines shown in Fig. 1 are all second-order nonequilibrium transition lines. We obtain for the (0)-spinodal $H=\pm D$ ($D\geq 0$), for the (−)-spinodal $H=2J$ ($D\leq 0$) and $H=2J-D$ ($D\geq 0$), and the (+)-spinodal is the reflection of the (−)-spinodal about the D-axis.

At finite temperatures the entropic contribution has to be taken into account, so the first-order phase boundaries and spinodal surfaces have to be calculated from the free energy. The mean-field free-energy-density functional can be calculated for a given m and q using the relation $\mathcal{F}^{\mathrm{MF}}=\mathcal{H}^{\mathrm{MF}}-T\mathcal{S}^{\mathrm{MF}}$, where $\mathcal{S}^{\mathrm{MF}}$ is the Boltzmann entropy density of the system, defined by $\mathcal{S}^{\mathrm{MF}}=(1/N)\ln g(M,Q)$, where $g(M,Q)$ is the multiplicity of spin configurations in a specific layer corresponding to given values of M and Q. A simple combinatorial argument yields

$$g(M,Q)=\binom{N}{(Q+M)/2}\binom{N-(Q+M)/2}{(Q-M)/2}\,. \tag{6}$$

Strictly speaking, $\mathcal{F}^{\mathrm{MF}}$ is a functional, but it is related to the thermodynamic free-energy density f by $f=\min_{(q,m)\in\Omega}\mathcal{F}^{\mathrm{MF}}(m,q)$. In the limit $N\to\infty$, $\mathcal{F}^{\mathrm{MF}}$ is given to the leading order of Stirling's approximation as

$$\begin{aligned}\mathcal{F}^{\mathrm{MF}} &= -Jm^2-Hm+Dq+\tfrac{1}{2}T[2(1-q)\ln(1-q)\\ &\quad+(q+m)\ln(q+m)+(q-m)\ln(q-m)-2q\ln 2]\,.\end{aligned} \tag{7}$$

The equilibrium free-energy density is obtained from the global minimum of $\mathcal{F}^{\mathrm{MF}}$ within the domain Ω. By setting the partial derivatives of $\mathcal{F}^{\mathrm{MF}}$ with respect to both m and q equal to zero and defining an effective field $H_{\mathrm{eff}}=H+2Jm$, we obtain the stationarity condition as a pair of coupled equations:

$$q=\frac{m}{\tanh(H_{\mathrm{eff}}/T)} \tag{8}$$

and

$$\left[1+\tfrac{1}{4}\exp(2D/T)\right]q^2-2q+\tfrac{1}{4}\exp(2D/T)m^2+1=0\,. \tag{9}$$

By combining the two equations, we can write the stationarity condition as an equation only in m:

$$m=\frac{2\sinh(H_{\mathrm{eff}}/T)}{\exp(D/T)+2\cosh(H_{\mathrm{eff}}/T)}\,, \tag{10}$$

Equations (8) and (10) are identical to the expressions found by Blume, *et al.*, [33]. Their simultaneous solution cannot generally be obtained in closed form. A schematic drawing of the mean-field equilibrium phase diagram can be found in Ref. [42].

In order to calculate the spinodal surfaces, we require that the local minimum in $\mathcal{F}^{\rm MF}$ that corresponds to the metastable state is also a point of inflection. This criterion is satisfied if we require, in addition to the vanishing of the partial derivatives of $\mathcal{F}^{\rm MF}$ with respect to both m and q, that the determinant of the Hessian matrix is zero:

$$\begin{vmatrix} \mathcal{F}^{\rm MF}_{mm} & \mathcal{F}^{\rm MF}_{qm} \\ \mathcal{F}^{\rm MF}_{mq} & \mathcal{F}^{\rm MF}_{qq} \end{vmatrix} = 0 \,, \tag{11}$$

where the subscripts denote partial derivatives with respect to the subscripted variables. Inserting Eq. (7) for $\mathcal{F}^{\rm MF}$ into Eq. (11), we obtain

$$2Jm^2 - 2Jq + T = 0 \,. \tag{12}$$

The spinodal field is obtained by the simultaneous solution of Eqs. (8), (9), and (12), as a relation between D, H, and T. We start by using Eq. (12) to eliminate q from Eq. (9), which gives

$$m^4(16-4\eta) + m^2[-32+4\eta+(16-4\eta)T/J] + 16 - 16T/J + (4-\eta)(T/J)^2 = 0 \,, \tag{13}$$

where η=exp$(2D/T)$. This quadratic equation in m^2 yields four solutions for m,

$$m = \pm\sqrt{\frac{1}{2}\left[\frac{4 \pm \sqrt{4(1-2T/J)\eta^2 + 8\eta T/J}}{4-\eta} - T/J + 1\right]} \,, \tag{14}$$

which we denote $\pm m_+$ and $\pm m_-$. To get the functional relation between the fields, we use Eq. (12) again to eliminate q from Eq. (8). Isolating H from the result gives

$$H = -2Jm + \frac{T}{2}\ln\left[\frac{2Jm + 2Jm^2 + T}{-2Jm + 2Jm^2 + T}\right] \,. \tag{15}$$

By inserting the solution for the magnetization from Eq. (14) into Eq. (15) we obtain the desired expression for the spinodal field H in terms of the field D and temperature T.

A three-dimensional plot of the spinodal surface in (D, H, T) space, calculated from the above relation, is shown in Fig. 2. It is symmetric under reflection about the plane H=0, due to the symmetry of the Hamiltonian, Eq. (4), under the transformation $(s_{n,i}, H) \rightarrow (-s_{n,i}, -H)$. Due to the singular behavior of Eq. (15) at T=0, the bottom edge of the surface pictured lies at T/J=1/12. At T=0, the spinodal surfaces are anchored to the zero-temperature spinodal lines shown in Fig. 1. Starting from large positive D, we have four spinodal sheets corresponding to the four solutions. These are indicated at the right-hand side of the figure. The (0)-spinodal sheets in front and in back merge with the (−)- and (+)-spinodal sheets along the lines l_2 and l_3, respectively. Below we obtain analytic expressions for the lines l_1, l_2, l_3, and l_4, including the tricritical point where all four lines meet. As we reduce D past

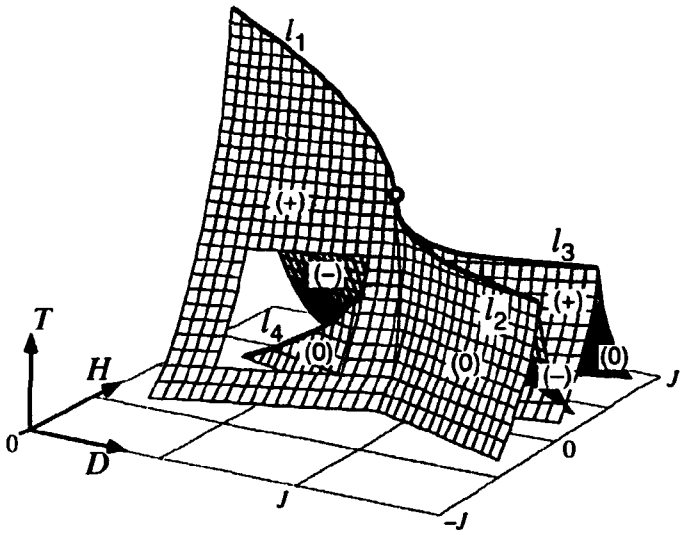

Figure 2: The spinodal surface, shown in (D, H, T) space. The whole surface is symmetric under reflection in the plane H=0. Only the portion for $T/J \geq 1/12$ is shown, floating above the grid at T=0. The two sheets that merge along the line l_1 are the (+)-spinodal in front, and the (−)-spinodal in back. This line of critical points terminates at the tricritical point $(D_t/J, H_t/J, T_t/J)=(\frac{4}{3}\ln 2, 0, 2/3)$, which is marked with a circle. The sheets that merge along the line l_2 are the (0)-spinodal in front and the (−)-spinodal in back. For the sheets merging along the line l_3 we have the (0)-spinodal in back and the (+)-spinodal in front. The two (0)-spinodal sheets intersect and cross the (+)- and (−)-spinodal surfaces, and merge along the line l_4. This line connects the point $(D, H, T) = (0, 0, 0)$ with the tricritical point.

D=$2J$, the (+)- and (−)-spinodal sheets intersect and cross. The line of intersection becomes l_1 above the tricritical point. The (0)-spinodal sheets pass inside the (+) and (−) sheets and merge along the line l_4, as can be seen through the rectangular window in the (+) sheet.

Obtaining analytical expressions for the four lines of critical points is quite simple using Eq. (14) for the spinodal magnetizations. The lines are parameterized by the appropriate critical temperature T_c. The line l_1 is derived by setting m_-=0 yielding

$$l_1 : \begin{cases} D_c = T_c \ln\left[\frac{2(2J-T_c)}{T_c}\right] \\ H_c = 0 \end{cases} \tag{16}$$

for $2/3 \leq T_c/J \leq 2$. Similarly, l_2 is obtained from the condition m_-=m_+:

$$l_2 : \begin{cases} D_c = \frac{T_c}{2} \ln\left[\frac{8T_c}{2T_c - J}\right] \\ H_c = -2J\sqrt{-3T_c/2J+1} + T_c \tanh^{-1}\left[\frac{\sqrt{-3T_c/2J+1}}{-T_c/J+1}\right] \end{cases} \tag{17}$$

for $1/2 \leq T_c/J \leq 2/3$. The line l_3 is the mirror image of l_2 about the plane H=0. The line l_4 is determined by setting m_-=0 as was the case for l_1. The result for l_4 is

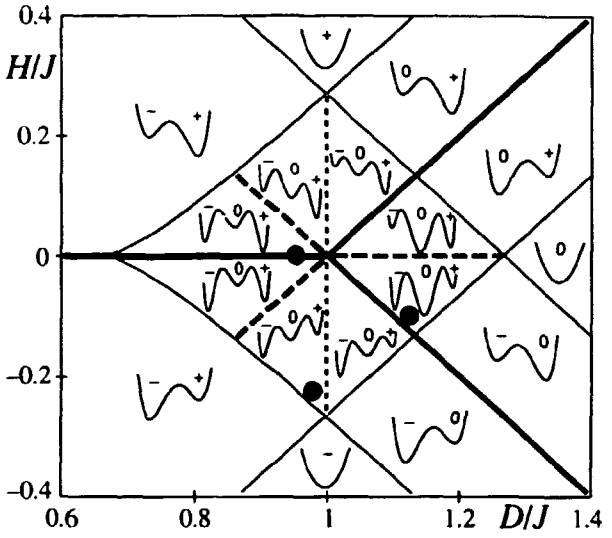

Figure 3: Finite-temperature phase diagram, showing the region of competing metastability, where the spinodal and equilibrium surfaces intersect the plane T/J=0.25, well below the tricritical temperature. Thick solid lines represent the first-order equilibrium transition lines, and thin solid lines are the spinodal lines. The thick dashed lines represent transitions between two metastable states, and the thin dotted vertical line is the locus of equal barrier heights. In each separate region, the free-energy-density functionals are drawn schematically along the mean-field reaction path. The global minimum corresponds to the equilibrium phase, and local minima represent metastable states. Solid dots indicate parameter sets for which dynamical Monte Carlo simulations of the decay of metastable states were performed (see Fig. 11).

given by Eq. (16) for $0 \leq T_c/J \leq 2/3$ and is a continuation of l_1 below the tricritical point. The magnetizations m_c along the lines of critical points are easily found using Eq. (14). Along l_1 and l_4 obviously m_c=0, since H=0 along these lines, whereas along l_2 and l_3 we have $m_c^2 = 1 - 3T_c/2J$. The tricritical point is found as the intersection of the lines l_1 and l_2: T_t/J=2/3, $D_t/J = \frac{4}{3}\ln 2$ and H_t=0. These analytic expressions for the critical lines are identical to the results obtained by Blume, *et al.* [33], which in that study were derived from the Landau expansion of the free energy to sixth order.

In Fig. 3 the region of competing metastability at a temperature T/J=0.25 (well below T_t) is shown. The thick solid lines are first-order transition lines, and the thin solid lines are spinodal lines. The figure is similar to the zero-temperature phase diagram in Fig. 1, except for the smaller area of the central diamond-shaped region and the curvature in the (0)-spinodals near H=0. The lines separate the (D, H) plane into 17 regions, in each of which we have drawn the free-energy-density functional schematically along the most probable mean-field escape path, or mean-field reaction path, joining the three states. Since this path must go through the saddle points of $\mathcal{F}^{\mathrm{MF}}$, it can be shown from the stationarity condition of Eq. (9) that, for the range of fields shown in the figure, each mean-field reaction path is very close to the

border of Ω defined by $q=\pm m$. The global minimum represents the equilibrium phase, whereas the remaining local minima represent metastable states. For the D and H values inside the large central diamond-shaped region, two competing metastable states are present. As we cross a spinodal line, the metastable state associated with that spinodal vanishes. The thick dashed lines indicate where the two competing metastable states become degenerate. The thin dotted line for $H\geq 0$ indicates points where the activation barrier heights for the decays $(-)\rightarrow(0)$ and $(0)\rightarrow(+)$ are equal, and analogously for the dotted line for $H\leq 0$. For $H=0$, the activation barrier heights for decay of the (0) metastable state into the degenerate $(+)$ or $(-)$ equilibrium phases are also equal by symmetry. All lines except the exactly obtained spinodal lines have been calculated numerically from Eq. (7) since they involve finding the extrema of $\mathcal{F}^{\mathrm{MF}}$, which has not been done in closed form.

In order to properly characterize the decay of the metastable phases in the long-range Blume-Capel model, we must relax the assumption that the densities m_i and q_i are translationally invariant. We will show that many of the characteristics of the mean-field model remain, such as the equilibrium and metastable configurations and the spinodals, but we also show, in the next section, that the activation barrier heights are significantly reduced, due to nucleating fluctuations of finite longitudinal extent not present in the mean-field approximation. We can express the Hamiltonian of Eq. (4) as

$$\mathcal{H} = -JN\sum_{i=1}^{L}\tfrac{1}{2}(m_{i+1}-m_i)^2 + N\sum_{i=1}^{L}\mathcal{H}^{\mathrm{MF}}(m_i,q_i)\,. \tag{18}$$

The free-energy-density functional is then defined as $\mathcal{F} = (\mathcal{H}-TS)/NL$, where S is the Boltzmann entropy for the $L\times N$ system. The stationarity condition for the free-energy-density functional $\mathcal{F}$ is then given by $2L$ coupled equations:

$$\begin{aligned} -J(m_{i+1}-2m_i+m_{i-1}) + \frac{\partial\mathcal{F}^{\mathrm{MF}}(m_i,q_i)}{\partial m_i} &= 0 \\ \frac{\partial\mathcal{F}^{\mathrm{MF}}(m_i,q_i)}{\partial q_i} &= 0 \end{aligned} \tag{19}$$

for $i=1,\ldots,L$, which can be represented by Eqs. (8) and (9) if we define H_{eff} as a local effective field, $H_{\mathrm{eff}} = J(m_{i+1}+m_{i-1})$, and replace m with m_i elsewhere.

In Refs. [24] and [43] it was shown that a two-state model with long-range interactions in an $L^{d-1}\times\infty$ cylindrical geometry can be mapped to a one-dimensional field theory. We will show that a similar mapping can be applied here. We define functions $m(r)$ and $q(r)$ to be continuous in a dimensionless longitudinal coordinate r, and we force $m(r)=m_i$ and $q(r)=q_i$ at integer values $r=i$. By Taylor's theorem, if $i\leq r\leq i+1$, then $(m_{i+1}-m_i)^2 = (\nabla m(r))^2 + O(\nabla m\nabla^2 m)$. Therefore, if $m(r)$ does not vary too rapidly, then the free-energy density $\mathcal{F}$ for a configuration described by $\{m_i,q_i\}$ is well approximated by the Ginzburg-Landau-Wilson form:

$$\mathcal{F} = \frac{1}{L}\int_0^L dr\,\left[\tfrac{1}{2}J(\nabla m)^2 + \mathcal{F}^{\mathrm{MF}}(m(r),q(r))\right]\,. \tag{20}$$

The density profile $(m(r), q(r))$ of a stationary solution ($\delta\mathcal{F}$=0) is given by the Euler-Lagrange equation:

$$-J\frac{d^2m}{dr^2} + \left.\frac{\partial \mathcal{F}^{\mathrm{MF}}}{\partial m}\right|_{m(r),q(r)} = 0\,, \tag{21}$$

where $(\forall r)$ $(m(r), q(r))$ is restricted to lie within Ω on the ellipse defined by Eq. (9).

In Ref. [24] it was demonstrated that an equation of the form of Eq. (21) has three types of continuous solutions. For each local minimum $(m_{\mathrm{min}}, q_{\mathrm{min}})$ of $\mathcal{F}^{\mathrm{MF}}$, there is a uniform solution $(m(r), q(r))$=$(m_{\mathrm{min}}, q_{\mathrm{min}})$, for which the free-energy density is given by the corresponding mean-field result. In addition, for each local minimum $(m_{\mathrm{ms}}, q_{\mathrm{ms}})$ that is not the (unique) global minimum, there exists a solution that represents the lowest-lying saddle point between $(m_{\mathrm{ms}}, q_{\mathrm{ms}})$ and a second minimum of equal or lower value. If the second minimum is lower, the solution, viewed as a spatial variation in m and q, has the shape of a "droplet" embedded in a sea of the metastable configuration $(m_{\mathrm{ms}}, q_{\mathrm{ms}})$. The configuration (m, q) at the center of the droplet is characterized by the solution to $\mathcal{F}^{\mathrm{MF}}(m, q)$=$\mathcal{F}^{\mathrm{MF}}(m_{\mathrm{ms}}, q_{\mathrm{ms}})$ on the arc of the ellipse defined by Eq. (9) between the two minima. If the second minimum is of equal value, the solution has an "interface" shape, in which the system passes from one minimal configuration to the other. These saddle-point solutions exist if the corresponding metastable minima of $\mathcal{F}^{\mathrm{MF}}$ exist. This means that the spinodals derived earlier in the section, which define the limit of metastability for the mean-field Blume-Capel model, also define the limit of metastability for the long-range model. Other solutions to the Euler-Lagrange equation, which are oscillatory in space, can also exist, but we do not consider them here since their associated free-energy densities are higher than those for the solutions already described.

3 Analytic Continuation of the Free Energy

For the long-range Blume-Capel model with $T < 2J (T_c = 2J$ in the Ising limit $D \to -\infty)$, the free energy F in the limit $N \to \infty$ is not everywhere analytic, but rather exhibits discontinuous gradients along the first-order phase boundaries. However, if we vary the fields D and H continuously through the boundary, an analytic continuation $\tilde{f}$ of the free-energy density across the boundary exists as an analogue of the thermodynamic free-energy density, but with the partition function constrained to configurations that do not allow the system to decay into the equilibrium phase. The analytic continuation is given as the minimum of $\mathcal{F}$ that coincides with the thermodynamic free-energy density at the phase boundary, but increases as the fields depart from the boundary. When the fields reach the spinodal surface, the metastable minimum vanishes, and the analytic continuation becomes complex outside the spinodal. The objective of this section is to calculate the leading behavior of $\tilde{f}$ near the spinodal surface. In Sec. 6 we will compare the finite-range scaling of Im$\tilde{f}$ with

that of the imaginary part of the constrained free-energy density obtained numerically from the constrained-transfer-matrix formalism.

Since the metastable state is translationally invariant, the functional minimization of $\mathcal{F}^{\mathrm{MF}}$ in the space of translationally invariant configurations is sufficient to determine $\tilde{f}$ for the metastable states of the long-range model in the limit $N\to\infty$. Let subscripts to $\mathcal{F}^{\mathrm{MF}}$ denote partial derivatives with respect to the subscripted variables, evaluated at the spinodal. Let $\delta_m = m - m_s$, $\delta_q = q - q_s$, $\delta H = H - H_s$, and $\delta D = D - D_s$ denote variations away from the spinodal. Holding $D{=}D_s$ constant and varying H, we expand the variation of $\mathcal{F}^{\mathrm{MF}}$ from its spinodal value, $\Delta\mathcal{F}^{\mathrm{MF}} \equiv \mathcal{F}^{\mathrm{MF}}(m_s+\delta_m, q_s+\delta_q) - \mathcal{F}^{\mathrm{MF}}(m_s, q_s)$, to third order:

$$\begin{aligned}\Delta\mathcal{F}^{\mathrm{MF}} &= -m_s\delta H - \delta_m\delta H + \tfrac{1}{2}(\delta_m^2\mathcal{F}^{\mathrm{MF}}_{mm} + 2\delta_m\delta_q\mathcal{F}^{\mathrm{MF}}_{mq} + \delta_q^2\mathcal{F}^{\mathrm{MF}}_{qq}) \\ &\quad + \tfrac{1}{6}(\delta_m^3\mathcal{F}^{\mathrm{MF}}_{mmm} + 3\delta_m^2\delta_q\mathcal{F}^{\mathrm{MF}}_{mmq} + 3\delta_m\delta_q^2\mathcal{F}^{\mathrm{MF}}_{mqq} + \delta_q^3\mathcal{F}^{\mathrm{MF}}_{qqq}) + O(\delta^4)\,, \quad (22)\end{aligned}$$

where we have shown only those derivatives that are not identically zero. (Since $\mathcal{F}^{\mathrm{MF}}$ is stationary at the spinodal, $\mathcal{F}^{\mathrm{MF}}_m{=}\mathcal{F}^{\mathrm{MF}}_q{=}0$, and since the fields couple linearly to the order parameters, all field derivatives other than those shown are identically zero.) Since D couples linearly to q, the stationarity condition $\mathcal{F}^{\mathrm{MF}}_q{=}0$ gives an expression for D in terms of m and q that can be expanded to give

$$\delta D = -\delta_m\mathcal{F}^{\mathrm{MF}}_{mq} - \delta_q\mathcal{F}^{\mathrm{MF}}_{qq} - \tfrac{1}{2}(\delta_m^2\mathcal{F}^{\mathrm{MF}}_{mmq} + 2\delta_m\delta_q\mathcal{F}^{\mathrm{MF}}_{mqq} + \delta_q^2\mathcal{F}^{\mathrm{MF}}_{qqq}) + O(\delta^3)\,. \quad (23)$$

Since we only consider variation in H, $\delta D{=}0$, and Eq. (23) can be used to express δ_q in terms of δ_m:

$$\delta_q = -\alpha\delta_m - \frac{1}{2\mathcal{F}^{\mathrm{MF}}_{qq}}(\delta_m^2\mathcal{F}^{\mathrm{MF}}_{mmq} + 2\delta_m\delta_q\mathcal{F}^{\mathrm{MF}}_{mqq} + \delta_q^2\mathcal{F}^{\mathrm{MF}}_{qqq}) + O(\delta^3)\,, \quad (24)$$

where $\alpha \equiv \mathcal{F}^{\mathrm{MF}}_{mm}/\mathcal{F}^{\mathrm{MF}}_{mq} = \mathcal{F}^{\mathrm{MF}}_{mq}/\mathcal{F}^{\mathrm{MF}}_{qq}$, with the second equality following from the condition for inflection at the spinodal, given by Eq. (11). This expansion and those that follow are valid if α is not singular. Analytic calculation of the derivatives using Eq. (7) shows that α is indeed regular. An expansion for δH analogous to Eq. (23) is obtained using the linear coupling of H to m and the stationarity condition $\mathcal{F}^{\mathrm{MF}}_m{=}0$ at the spinodal. We get:

$$\begin{aligned}\delta H &= \delta_m\mathcal{F}^{\mathrm{MF}}_{mm} + \delta_q\mathcal{F}^{\mathrm{MF}}_{mq} + \tfrac{1}{2}(\delta_m^2\mathcal{F}^{\mathrm{MF}}_{mmm} + 2\delta_m\delta_q\mathcal{F}^{\mathrm{MF}}_{mmq} + \delta_q^2\mathcal{F}^{\mathrm{MF}}_{mqq}) + O(\delta^3) \\ &= \tfrac{1}{2}\gamma\delta_m^2 + O(\delta^3)\,, \quad (25)\end{aligned}$$

where $\gamma \equiv \mathcal{F}^{\mathrm{MF}}_{mmm} - 3\alpha\mathcal{F}^{\mathrm{MF}}_{mmq} + 3\alpha^2\mathcal{F}^{\mathrm{MF}}_{mqq} - \alpha^3\mathcal{F}^{\mathrm{MF}}_{qqq}$, and we have used Eq. (24). Substituting the expansions for δ_q and δH into Eq. (22) we obtain

$$\Delta\mathcal{F}^{\mathrm{MF}} = -m_s\delta H - \tfrac{1}{3}\gamma\delta_m^3 + O(\delta^4)\,. \quad (26)$$

By inserting the expression for δ_m in terms of δH from Eq. (25), we obtain

$$\Delta\mathcal{F}^{\mathrm{MF}} = -m_s\delta H - \tfrac{2\sqrt{2}}{3}\gamma^{-1/2}(\delta H)^{3/2} + O(\delta H^2)\,. \quad (27)$$

At this point we note that the only assumptions made in the derivation of Eq. (27) are that the two fields couple linearly to their respective order parameters, and that a free-energy-density functional is well-defined in terms of the temperature, fields, and order-parameters. This result is therefore not particular to our model, but rather more general.

We now apply Eq. (27) to our long-range Blume-Capel model. Inserting $\mathcal{F}^{\rm MF}$ from Eq. (7) and using the condition for inflection at the spinodal, given by Eq. (12), we can express γ analytically in terms of m_s and T:

$$\gamma = \frac{8m_sJ^2}{T}\left(m_s^2 - 1 + \frac{3T}{2J}\right) . \tag{28}$$

Depending on the sign of m_s, $(m_s^2 - 1 + 3T/2J)$, and δH, the value of $\Delta\mathcal{F}^{\rm MF}$ might be real or complex. For the (0)-spinodal surfaces, the equation for the critical magnetization along the lines l_2 and l_3 is $m_c^2 - 1 + 3T/2J = 0$ as discussed below Eq. (17); hence for these surfaces,

$$m_s^2 - 1 + \frac{3T}{2J} < m_c^2 - 1 + \frac{3T}{2J} = 0 . \tag{29}$$

Thus there are two cases. If $m_s\delta H<0$, we are inside the (0)-spinodal, and $\Delta\mathcal{F}^{\rm MF}$ is real, whereas if $m_s\delta H>0$, we are outside the spinodal, and $\Delta\mathcal{F}^{\rm MF}$ is complex. (Referring to Fig. 2, $m_s>0$ for the (0)-spinodal sheet in front, and $m_s<0$ for the (0)-spinodal sheet in back.) For the (+)- and (−)-spinodals we can use Eq. (14) for the explicit form of $m_\pm^2$ to obtain

$$\begin{aligned} m_s^2 - 1 + \frac{3T}{2J} &= -\frac{1}{2} + \frac{T}{J} + \frac{1}{2}\frac{4-\eta\sqrt{1+2T(4-\eta)/\eta J}}{4-\eta} \\ &\geq \frac{T}{J} - \left|\frac{1}{2}\frac{\eta}{4-\eta}\left(1-\sqrt{1+2T\frac{4-\eta}{\eta}J}\right)\right| \\ &\geq \frac{T}{2J} > 0 , \end{aligned} \tag{30}$$

where we have used the inequality $|x^{-1}(1-\sqrt{1+ax})| \leq |a/2|$. Therefore, if $m_s\delta H>0$, we are inside the spinodal, whereas if $m_s\delta H<0$, we are outside. (Referring to Fig. 2, $m_s<0$ for the (−)-spinodal sheet, and $m_s>0$ for the (+)-spinodal sheet.) The results for the analytically continued free-energy density are summarized as follows:

$$\Delta\mathcal{F}^{\rm MF} \approx \begin{cases} -m_s\delta H - \frac{2\sqrt{2}}{3}|\gamma|^{-1/2}|\delta H|^{3/2} & \text{metastable state} \\ -m_s\delta H \pm i\frac{2\sqrt{2}}{3}|\gamma|^{-1/2}|\delta H|^{3/2} & \text{outside spinodal} , \end{cases} \tag{31}$$

where higher-order terms are neglected. Note that this result verifies that every point on the spinodal surfaces calculated in Sec. 2 is a branch point of $\tilde{f}$. From Eq. (31)

we see that outside the spinodal sheets $\mathrm{Im}\tilde{f}$ is proportional to $|H - H_s|^{3/2}$. The form of Eq. (31), with γ appropriately calculated, is true for any mean-field model with two external fields, provided only that the fields couple linearly to their respective order parameters. In the Ising limit ($D \to -\infty$) for this model, Eq. (31) agrees with the analytic continuation for a mean-field Ising ferromagnet [11, 44].

Note that if the fields are between the first-order phase boundary and the spinodal, the analytically continued free energy is real-valued only in the limit of infinite interaction range. However, we are interested in the scaling of the free energy for systems with a long, but finite interaction range. For such systems the continuation is complex, but its imaginary part approaches zero rapidly as $N \to \infty$. The decay of the metastable state happens via the formation of a nucleating droplet of finite extent. The free-energy cost ΔF associated with the formation of this droplet is evaluated as the minimum barrier height for all paths in phase space that connect the metastable state to the stable state. Combining Langer's result, Eq. (1), with the Van't Hoff-Arrhenius law [30], we expect the imaginary part of the analytically continued free-energy density to have a "Boltzmann weight" given by

$$\mathrm{Im}\tilde{f} \propto e^{-\beta \Delta F} . \tag{32}$$

Since the density profile of the nucleating droplet can vary longitudinally, we must relax the assumption of translational invariance to find the free-energy cost of the droplet. Taking the continuum limit used in the previous section, we express δ_m and δ_q as continuous functions of r, and we expand the variation of $\mathcal{F}$ from its spinodal value to third order. Using the form of Eq. (20) for $\mathcal{F}$, we have

$$\begin{aligned} \Delta\mathcal{F} &= \frac{1}{L}\int_0^L dr \left[\tfrac{1}{2}J(\nabla\delta_m)^2 + \Delta\mathcal{F}^{\mathrm{MF}}(m(r), q(r))\right] \\ &= -m_s\delta H + \frac{1}{L}\int_0^L dr \left[\tfrac{1}{2}J(\nabla\delta_m)^2 - \delta_m\delta H + \tfrac{1}{6}\gamma\delta_m^3 + O(\delta^4)\right] , \end{aligned} \tag{33}$$

where we have used Eq. (24) to replace δ_q in Eq. (22) for $\Delta\mathcal{F}^{\mathrm{MF}}$. The Euler-Lagrange equation corresponding to Eq. (21) is thus

$$-J\nabla^2\delta_m - \delta H + \tfrac{1}{2}\gamma\delta_m^2 + O(\delta^3) = 0 . \tag{34}$$

Following Ref. [24], we take the position of the droplet core to be r=0. The critical droplet is local, so the solution to Eq. (34) must be asymptotically uniform in the limit $L \to \infty$, that is $\delta_m(r) \to$ const. as $|r| \to \infty$. We thus have asymptotically

$$\delta_m \to \delta_0 = (2\delta H/\gamma)^{1/2} + O(\delta H), \tag{35}$$

where the sign of δ_m is equal to the sign of γ. If we define $u(r) = \delta_m(r) - \delta_0$, then Eq. (34) becomes

$$-J\nabla^2 u + \gamma\delta_0 u + \tfrac{1}{2}\gamma u^2 + O(\delta^3) = 0 . \tag{36}$$

In the limit $|r|\to\infty$ we may neglect the u^2-term. We thus obtain

$$u(r) \sim \exp(-r/\xi_r) \,, \tag{37}$$

where

$$\xi_r = (J/\sqrt{2})^{1/2}|\gamma\delta H|^{-1/4} + O(\delta H^{1/4}) \tag{38}$$

is the relaxation length of the droplet. The free-energy cost of the critical droplet is given by $\Delta F = NL(\Delta\mathcal{F} - \Delta\mathcal{F}_{\rm ms}^{\rm MF})$, where $\Delta\mathcal{F}_{\rm ms}^{\rm MF}$ is the result in Eq. (31) for the metastable state. Changing variables to u in Eq. (33), we have

$$\begin{aligned} \Delta F &= N\int_0^L dr\left[\tfrac{1}{2}J(\nabla u)^2 + \tfrac{1}{2}\delta_0 u^2 + \tfrac{1}{6}u^3 + O(u^4)\right] \\ &= -\tfrac{1}{12}N\gamma\int_0^L dr[u^3 + O(u^4)] \,, \end{aligned} \tag{39}$$

where we have integrated $(\nabla u)^2$ by parts and used Eqs. (35) and (36). Taking the limit $L\to\infty$, we place the explicit solution to Eq. (36) [14, 15, 16],

$$u(r) = -3\delta_0 \mathrm{sech}^2(r/2\xi_r) \,, \tag{40}$$

into the integral of Eq. (39). Evaluating the integral then gives

$$\begin{aligned} \Delta F &= \tfrac{48\sqrt{2}}{5}N\xi_r|\gamma|^{-1/2}|\delta H|^{3/2}\left[1 + O(\delta H^{1/2})\right] \\ &= \tfrac{48}{5}N(\sqrt{2}J)^{1/2}|\gamma|^{-3/4}|\delta H|^{5/4} + O(\delta H^{7/4}) \,. \end{aligned} \tag{41}$$

In the Ising limit ($D\to-\infty$), this result reduces to the free-energy cost of nucleation for the Q1DI model [24]. The first expression in Eq. (41) illustrates the difference in the behavior of the analytically continued free energy between long-range models [15, 16, 24], for which the length scale of the critical droplet is the field and temperature dependent characteristic length $\xi_r \ll L$, and mean-field models [11, 44], for which the only length scale for fluctuations is the length L of the entire system.

4 Constrained-Transfer-Matrix Formalism

In the first part of this section, the general method of the constrained-transfer-matrix formalism is briefly reviewed. A more extensive discussion is found in Refs. [20, 21, 24, 25]. In the second part the formalism is applied to the long-range Blume-Capel model.

As the transfer-matrix method is usually applied to equilibrium systems, it provides a way to obtain standard thermodynamic state functions, such as the internal-energy density $\mathcal{U}$, the free-energy density f, and correlation functions [45]. Consider a lattice of $L\times N$ sites, with periodic boundary conditions in the L-direction. The lattice is divided into L layers, each containing N sites, and the total

Hamiltonian is decomposed into a sum of layer Hamiltonian operators $\mathcal{H}^{\rm op}$ whose form is independent of the layer index:

$$\mathcal{H} = \sum_{i=1}^{L} \langle X_i | \mathcal{H}^{\rm op} | X_{i+1} \rangle \,, \tag{42}$$

where $\langle X_i|$ and $|X_{i+1}\rangle$ denote the configuration of layers i and $i+1$, respectively. An explicit expression for $\langle X_i|\mathcal{H}^{\rm op}|X_{i+1}\rangle$ in the long-range Blume-Capel case is given in Eq. (52) below. The layer Hamiltonian can be further decomposed into a sum of an interaction part, containing only spin-spin interactions, and a field part, containing only terms proportional to the fields. The transfer matrix $\mathbf{T}$ is defined in terms of its matrix elements in the dual space of configurations of two adjacent layers:

$$\langle X_i \,|\mathbf{T}|\, X_{i+1} \rangle = \exp\left[-\beta \langle X_i | \mathcal{H}^{\rm op} | X_{i+1} \rangle\right] \,. \tag{43}$$

A layer configuration $|X_i\rangle$ can be considered as a direct product of single-spin configurations in that layer: $|X_i\rangle \equiv |s_{1,i}\rangle |s_{2,i}\rangle \cdots |s_{N,i}\rangle$. The transfer matrix for the Blume-Capel model is thus $3^N \times 3^N$. The partition function for the entire $L \times N$ system is given as $\mathcal{Z} = {\rm Tr}(\mathbf{T}^L)$, and the free-energy density for the system is obtained from $\mathcal{Z}$ as $f = -(T/NL) \ln \mathcal{Z}$. In the limit $L \to \infty$, the free-energy density becomes $f = -(T/N) \ln \lambda_0$, where λ_0 is the largest eigenvalue of the transfer matrix. By the Perron-Frobenius theorem, λ_0 is positive and nondegenerate, and the corresponding eigenvector $|0\rangle$ can be chosen to have all positive elements [45, 46].

In the following discussion we restrict ourselves to symmetric transfer matrices $\mathbf{T}$, and we sort the eigenvalues λ_α in order of decreasing magnitude, so that $\lambda_0 > |\lambda_1| \geq \cdots \geq |\lambda_{3^N-1}|$. Constrained transfer matrices $\mathbf{T}_\alpha$ are constructed from the eigenvalues λ_α and the corresponding eigenvectors $|\alpha\rangle$ of the equilibrium transfer matrix $\mathbf{T}$. The idea is to reweight the eigenstates in a simple way so that states near equilibrium are suppressed. The matrix $\mathbf{T}_\alpha$ is taken to commute with $\mathbf{T}$ and can be written as

$$\mathbf{T}_\alpha = \sum_{\beta \geq 0} |\beta\rangle f_\beta(\alpha) \langle \beta| \,, \tag{44}$$

where each $|\beta\rangle$ is an eigenvector of $\mathbf{T}$. As discussed in Refs. [20, 21, 24, 25], constrained joint and marginal probability densities are defined in analogy with the equilibrium ($\alpha = 0$) case:

$$\begin{aligned} P_\alpha(x_i, x_{i+k}) &= \langle \alpha | x_i \rangle \langle x_i | (\lambda_\alpha^{-1} \mathbf{T}_\alpha)^{|k|} | x_{i+k} \rangle \langle x_{i+k} | \alpha \rangle \\ P_\alpha(x_i) &= \langle \alpha | x_i \rangle \langle x_i | \alpha \rangle \,. \end{aligned} \tag{45}$$

It was pointed out in Refs. [9, 18, 19] that the constrained marginal probability densities $P_\alpha(x)$ can be interpreted as actual probability densities of single-layer configurations in a constrained state. In order to ensure that the entire system is characterized by $P_\alpha(x)$, the matrix $\mathbf{T}_\alpha$ must be chosen so that the

constrained joint probability densities $P_\alpha(x,x')$ satisfy the following regularity conditions: (*i*) that $P_\alpha(x)$ can be obtained by summing over the configurations of one layer, $P_\alpha(x)=\sum_{x'} P_\alpha(x,x')$; (*ii*) that $P_\alpha(x,x')$ is well-defined for $k=0$, $P_\alpha(x_i,x_i')=\delta_{x_i,x_i'}P_\alpha(x_i)$; and (*iii*) that $P_\alpha(x,x')$ reflects stochastic independence in the limit $|k|\to\infty$, $\lim_{|k|\to\infty} P_\alpha(x_i,x_{i+k}) = P_\alpha(x_i)\,P_\alpha(x_{i+k})$. For a matrix $\mathbf{T}_\alpha$ chosen to commute with $\mathbf{T}$, these requirements are satisfied if $\mathbf{T}_\alpha$ has the same rank as $\mathbf{T}$, and if its dominant eigenvalue is λ_α. Obviously these conditions do not uniquely determine $\mathbf{T}_\alpha$. For computational convenience we choose a simple form for $\mathbf{T}_\alpha$ that satisfies the above conditions:

$$\mathbf{T}_\alpha = \sum_{\beta=0}^{\alpha} |\beta\rangle \frac{\lambda_\alpha^2}{\lambda_\beta} \langle\beta| + \sum_{\beta=\alpha+1}^{3^N-1} |\beta\rangle \lambda_\beta \langle\beta| \tag{46}$$

if $\lambda_\alpha\neq 0$, and all terms are zero if $\lambda_\alpha=0$. For $\alpha=0$ it is obvious from Eq. (46) that $\mathbf{T}_\alpha$ reduces to the equilibrium transfer matrix.

We are now in a position to define constrained, generalized thermodynamic quantities [20, 21]. The internal-energy density $\mathcal{U}_\alpha$ is given by

$$\mathcal{U}_\alpha = \frac{1}{N} \sum_{X,X'} \langle\alpha|X\rangle \left[\langle X|\lambda_\alpha^{-1}\mathbf{T}_\alpha|X'\rangle \langle X|\mathcal{H}_1^{\mathrm{op}}|X'\rangle\right] \langle X'|\alpha\rangle \,, \tag{47}$$

where $\mathcal{H}_1^{\mathrm{op}}$ is the interaction part of the layer Hamiltonian. In the Blume-Capel model we have two fields, H and D. Consequently we have two field contributions in addition to the interaction part of the Hamiltonian. The order parameter $\mathcal{M}_\alpha$ conjugate to the H-field is given by

$$\mathcal{M}_\alpha = \frac{1}{N} \sum_{X} \langle\alpha|X\rangle \langle X|M^{\mathrm{op}}|X\rangle \langle X|\alpha\rangle \,, \tag{48}$$

where M^{op} is the magnetization operator acting on the layer configuration $|X\rangle$. Similarly, the order parameter $\mathcal{Q}_\alpha$ conjugate to the D-field is given by

$$\mathcal{Q}_\alpha = \frac{1}{N} \sum_{X} \langle\alpha|X\rangle \langle X|Q^{\mathrm{op}}|X\rangle \langle X|\alpha\rangle \,, \tag{49}$$

where Q^{op} counts the number of nonzero spins in a layer with configuration $|X\rangle$. The constrained entropy density $\mathcal{S}_\alpha$ is defined in analogy with that of a stationary ergodic Markov information source [47] and is given by

$$\mathcal{S}_\alpha = -\frac{1}{N} \sum_{X,X'} \langle\alpha|X\rangle \left[\langle X|\lambda_\alpha^{-1}\mathbf{T}_\alpha|X'\rangle \mathrm{Ln}\langle X|\lambda_\alpha^{-1}\mathbf{T}_\alpha|X'\rangle\right] \langle X'|\alpha\rangle \,, \tag{50}$$

where Ln is the principal branch of the complex logarithm. This constrained entropy density may be complex, since $\mathbf{T}_\alpha$ is not a positive matrix in general. To see this,

note that for $|\alpha\rangle$ ($\alpha \neq 0$) to be orthogonal to $|0\rangle$, the elements of $|\alpha\rangle$ must be of mixed sign. Since λ_α is the largest eigenvalue of $\mathbf{T}_\alpha$, the largest contribution to $\mathbf{T}_\alpha$ is the projection $|\alpha\rangle\lambda_\alpha\langle\alpha|$, which must contain negative elements Therefore, the argument to the principal value of the logarithm (Ln) may be negative. The branch cut is taken along the negative real axis, so that the domain of $\mathrm{Ln}(z)$ is $|z|>0$, $-\pi<\arg(z)\leq\pi$. In analogy with equilibrium thermodynamics the free-energy density associated with the eigenstate $|\alpha\rangle$ is defined by

$$f_\alpha = \mathcal{U}_\alpha - H\mathcal{M}_\alpha + D\mathcal{Q}_\alpha - TS_\alpha \,. \tag{51}$$

We will apply the formalism described above to the long-range Blume-Capel model Hamiltonian of Eq. (4). From the definition, Eq. (3), it follows that $M_i = \langle X_i|M^{op}|X_i\rangle$ and $Q_i = \langle X_i|Q^{op}|X_i\rangle$. The layer Hamiltonian matrix element $\langle X_i|\mathcal{H}^{op}|X_{i+1}\rangle$ is written in the symmetrized form

$$\langle X_i|\mathcal{H}^{op}|X_{i+1}\rangle = -\frac{J}{N}M_iM_{i+1} + \frac{D}{2}(Q_i + Q_{i+1}) - \frac{H}{2}(M_i + M_{i+1}) \,, \tag{52}$$

so that we obtain a symmetric transfer matrix from Eq. (43). As can be seen from Eq. (52), the layer Hamiltonian is invariant under all permutations of the individual spins, since it only depends on the total magnetizations, M_i and M_{i+1}, and the total numbers of nonzero spins, Q_i and Q_{i+1}. This implies that the transfer matrix can be contracted to a reduced basis set consisting of states $|M_iQ_i\rangle$, as described in detail in App. 8. The dimension of the contracted transfer matrix is easily seen to be

$$\dim = \sum_{Q=0}^{N}(Q+1) = \tfrac{1}{2}(N+1)(N+2) \,, \tag{53}$$

and the elements of the contracted transfer matrix are given by

$$\begin{aligned}\langle MQ|\mathbf{T}|M'Q'\rangle \;&=\; \sqrt{g(M,Q)g(M',Q')} \\ &\quad\times \exp\left(-\beta\left[-\frac{J}{N}MM' + \frac{D}{2}(Q+Q') - \frac{H}{2}(M+M')\right]\right) \,,\end{aligned} \tag{54}$$

where $g(M,Q)$ is the multiplicity factor given in Eq. (6). In App. 8 it is shown that Eqs. (47), (48), and (49) for $\mathcal{U}_\alpha$, $\mathcal{M}_\alpha$, and $\mathcal{Q}_\alpha$ remain valid with the following substitutions: $|X\rangle\rightarrow|MQ\rangle$ and $|X'\rangle\rightarrow|M'Q'\rangle$. Similarly, sums over layer configurations X and X' are contracted to sums over (M,Q) and (M',Q'). The only equation that is modified is the expression for the entropy per site [20]:

$$\begin{aligned}S_\alpha \;&=\; -\frac{1}{N}\sum_{MQ}\sum_{M'Q'}\langle\alpha|MQ\rangle \\ &\quad\times\left[\langle MQ|\lambda_\alpha^{-1}\mathbf{T}_\alpha|M'Q'\rangle \mathrm{Ln}\left(\frac{\langle MQ|\lambda_\alpha^{-1}\mathbf{T}_\alpha|M'Q'\rangle}{\sqrt{g(M,Q)g(M',Q')}}\right)\right]\langle M'Q'|\alpha\rangle \,.\end{aligned} \tag{55}$$

In addition to the fact that the transfer matrix **T** is invariant under the spin permutations, which led to the above contraction, other more complex symmetries may be present. This is the case for the long-range Blume-Capel model since, as we show in App. 8, the rank of the matrix is $(2N+1)$, which is much smaller than the dimension of the contracted matrix. This means that most of the eigenvalues are zero, and that the matrix can be reduced further by projecting out the null space. This further reduction is important, since in order to define the CTM it suffices to diagonalize the reduced matrix. In the numerical computation the reduction of the matrix size from $(N+1)(N+2)/2$ to $(2N+1)$ is obviously a great advantage, because much larger system sizes can be studied. In App. 8 a general method for the decomposition of our transfer matrix is discussed.

5 Numerical Transfer-Matrix Results

In this section we discuss the numerical results obtained by applying the CTM formalism. Equation (54) is used to set up an $(N+1)(N+2)/2$ square symmetric transfer matrix **T**. As described in detail in App. 8, this matrix is block diagonalized by a unitary transformation $\mathbf{STS}^{\mathrm{t}}$ that preserves its symmetries. The null space is then projected out, leaving a $(2N+1)\times(2N+1)$ symmetric matrix which is diagonalized using routines `tred2` and `tqli` from Press, *et al.*, [48]. The bulk of the work was performed in 64-bit precision on an HP9000/735 workstation. In certain cases sufficient accuracy could only be obtained using 128-bit precision on a Cray Y-MP/432 supercomputer. The numerical data presented here required approximately 700 CPU-hours on the workstation and 20 CPU-hours on the Cray.

The constrained transfer matrices $\mathbf{T}_\alpha$ $(\alpha=0,\ldots,2N)$ are constructed from the eigenvalues λ_α and eigenvectors $|\alpha\rangle$ using the definition given by Eq. (46). We back-transform $\mathbf{T}_\alpha$ from the eigenspace of the reduced transfer matrix into layer-configuration space $\{|MQ\rangle\}$ by the inverse transformation $\mathbf{S}^{\mathrm{t}}\mathbf{T}_\alpha\mathbf{S}$. Using this form for $\mathbf{T}_\alpha$ we calculated the constrained free-energy densities f_α from Eqs. (47)–(51). The attainable system sizes are limited both by numerical underflow at low temperatures and high fields and by the CPU time required, which increases as $O(N^3)$. We varied the system size from $N=6$ to $N=24$.

Figure 4 shows the eigenvalue spectrum of the equilibrium transfer matrix **T** as a function of H for $N=24$ with $D/J=1.1$ and $T/J=0.25$, well below the mean-field tricritical point. The eigenvalues are displayed as $-(T/JN)\ln|\lambda_\alpha|$ $(\alpha=0,\ldots,2N)$, so that the lowest branch is the equilibrium free-energy density. The reduced transfer matrix gives a total of 49 branches. These branches are symmetric with respect to $H=0$, and oscillate as functions of H, exhibiting avoided crossings at several points. A closer examination of these avoided crossings in the Ising limit revealed that the gaps go to zero exponentially with N [23] up to approximately the spinodal field. Thus the lines denoted as (0), (−), and (+) (see below) actually consist of several branches. It

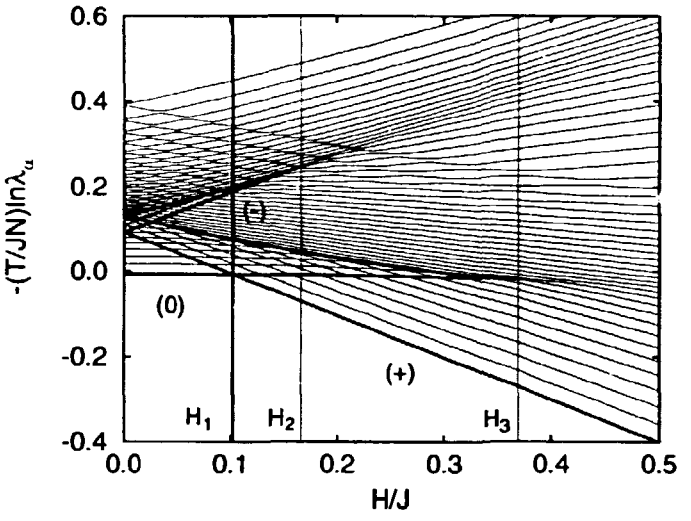

Figure 4: Eigenvalue spectrum for N=24, D/J=1.1, and T/J=0.25 shown *vs.* H/J for $0 \leq H/J \leq 0.5$. The spectrum is symmetric upon reflection about H=0 and interchange of (+) and (−). The thick vertical line indicates the mean-field first-order transition between the (0) and the (+) state at $H_1/J \approx 0.10$, whereas the thin vertical lines mark the (−)-spinodal at $H_2/J \approx 0.17$ and the (0)-spinodal at $H_3/J \approx 0.37$. Also included are bold curves representing the stationary points of the mean-field free-energy-density functional. The virtually straight lines correspond to the stable and metastable states (0), (+), and (−), and the upward-concave curves represent the uniform unstable stationary points. See the text for a detailed description.

was shown by McCraw and Schulman [9] that it is possible to analytically continue the eigenvalues around these crossings.

By drawing a line segment in Fig. 3 at D/J=1.1 from H/J=0 to H/J=0.5 representing the H-scan, we can calculate from the mean-field approximation the intersection with both the spinodal and equilibrium lines. The values obtained in this fashion are $H_1/J \approx 0.10$ for the first-order equilibrium transition between the (0) state and the (+) state, $H_2/J \approx 0.17$ for the (−)-spinodal and $H_3/J \approx 0.37$ for the (0)-spinodal. These H-fields are shown in Fig. 4 as vertical lines. The different branches can be identified by their slopes due to the identity [23]

$$\frac{T}{JN}\frac{\partial \ln|\lambda_\alpha|}{\partial H} = \mathcal{M}_\alpha \,. \tag{56}$$

Since the (0) state has roughly zero magnetization, the slope of the corresponding branch, by Eq. (56), is nearly zero. Similarly, the (+) and the (−) states have roughly magnetization $m \approx \pm 1$, so the slopes of their corresponding branches are near −1 and +1, respectively. In Fig. 4 the mean-field solutions for the three local minima in the free-energy functional are shown by bold curves. The (0) state appears as the horizontal line and extends from $H=-H_3$ to $H=H_3$, the (−) state

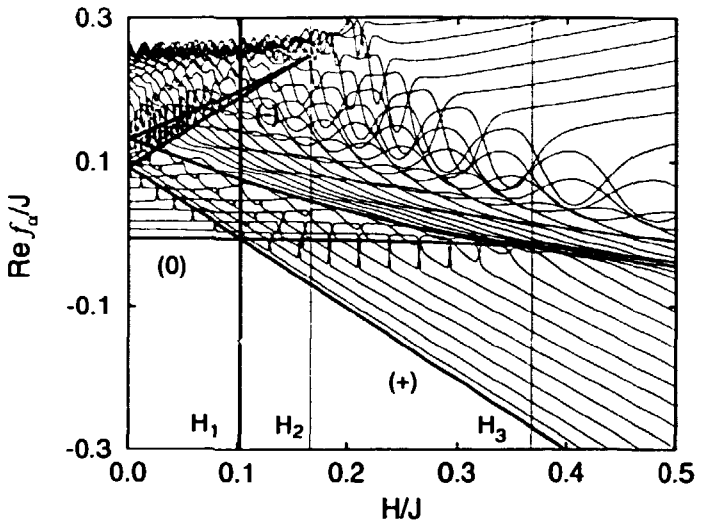

Figure 5: The real parts of the constrained free-energy densities $\mathrm{Re}f_\alpha/J$ shown *vs.* H/J. The parameters are the same as in Fig. 4, and the vertical lines and bold curves have the same meanings. For clarity only 35 of the 49 branches are shown. Note that the vertical scale is different from Fig. 4. See the text for a detailed description.

appears as a diagonal line and extends from $H/J=-\infty$ to $H=H_2$, and the (+) state appears as a diagonal line and extends from $H=-H_2$ to $H/J=\infty$. These lines are in such close agreement with the transfer-matrix branches that the branches are completely obscured by them. In addition, the two unstable mean-field solutions are also indicated by bold curves, easily identified by their upward curvature. The two unstable states terminate at the (−)-spinodal ($H=H_2$) and at the (0)-spinodal ($H=H_3$). At the termination points the unstable solutions merge with the metastable states.

The transfer-matrix spectrum in Fig. 4 may be interpreted as follows. For $-H_1\leq H\leq H_1$, (0) is the lowest-lying branch, and thus represents the stable state, while (+) and (−), which lie above, are metastable. For $H_1\leq H\leq H_2$ the (0) state has become metastable, while (+) is the stable state, and (−) remains metastable. At $H=H_2$, the gaps between nearly degenerate eigenvalues vanish far less rapidly with N than for $H<H_2$, making the gaps visible in the figure. This corresponds to the crossing of the (−)-spinodal, and hence the disappearance of the metastable (−) state. For $H_2\leq H\leq H_3$ the (+) state remains stable, while (0) remains metastable until the (0)-spinodal is crossed at $H=H_3$. For $H\geq H_3$ the (+) state is stable, and no metastable states exist. The transfer-matrix eigenvalues of Fig. 4 thus agree closely with the mean-field picture of metastability discussed in Sec. 2.

The real parts of the constrained free-energy densities, $\mathrm{Re}f_\alpha$, are shown in Fig. 5. The parameters are the same as in Fig. 4. Out of a total of 49 branches only the

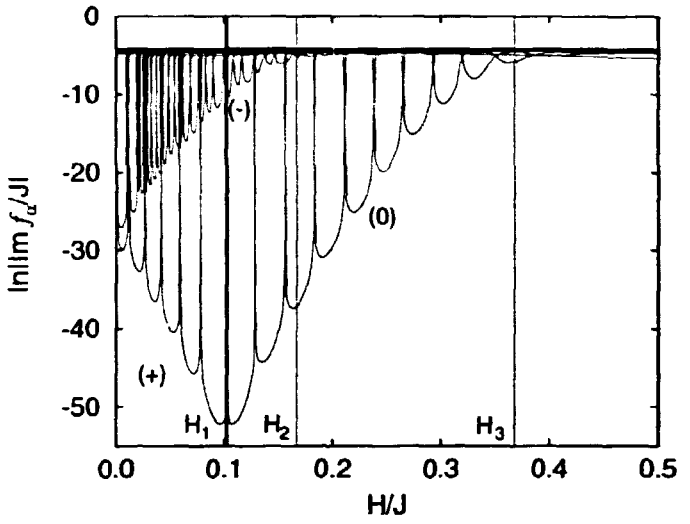

Figure 6: The imaginary parts of the constrained free-energy densities $|\mathrm{Im}f_\alpha/J|$ shown on a logarithmic scale *vs.* H/J. The parameters are the same as in Fig. 4, and the vertical lines have the same meanings. The envelopes of the lobe structures correspond to different metastable states as indicated. See the text for a detailed description.

35 that correspond to the largest eigenvalues are shown. The remaining branches, which contribute only to the band of unstable states with high free-energy densities and do not extend beyond the range of the branches shown, were removed for clarity. The vertical lines at $H=H_1$, H_2, and H_3 have the same meanings as in Fig. 4. The field-dependence of the quantities shown in Figs. 4 and 5 resemble each other closely, and in particular the stable and metastable branches are nearly left unaltered by the reweighting of the eigenvalues. However, the spectrum of the constrained free-energy densities is somewhat compressed compared to the eigenvalue spectrum and contains multilevel crossings. The bold curves in the figure show the five extrema in the mean-field free-energy-density functional corresponding to the (0), (+), and (−) states and the two unstable states, as discussed above. The branches of $\mathrm{Re}f_\alpha$ representing the stable and metastable branches are again completely obscured by the bold curves, and are thus in excellent agreement with the equilibrium and analytically continued metastable free-energy densities.

The imaginary parts of all the constrained free-energy densities $|\mathrm{Im}f_\alpha|$ are shown on a logarithmic scale versus H in Fig. 6. The parameters and the vertical lines are the same as in Fig. 4. The most striking features are the extremely small values and the lobe structure of the branches that correspond to the metastable states shown in Figs. 4 and 5. Each lobe corresponds to a different value of α, and the crossings of lobes correspond to the avoided crossings in the eigenvalue spectrum. By comparison with the real parts of the constrained free-energy densities, different

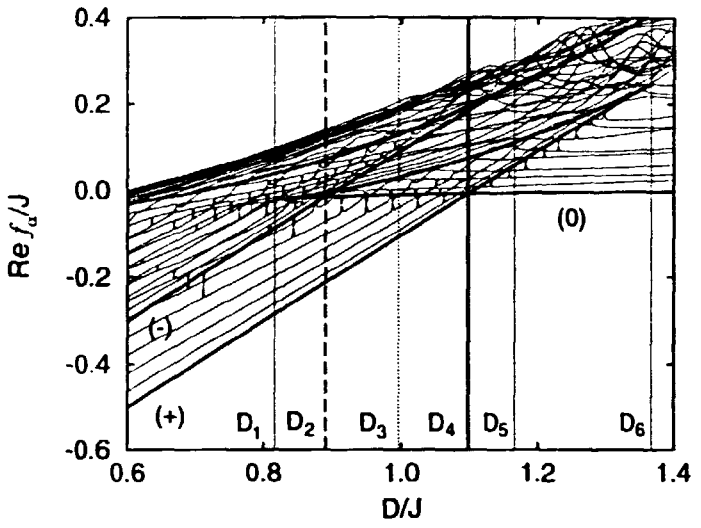

Figure 7: The real parts of the constrained free-energy densities $\mathrm{Re}f_\alpha/J$ for N=18, H/J=0.1, and T/J=0.25, shown as functions of D/J for $0.6 \leq D/J \leq 1.4$. The vertical lines indicate the (0)-spinodal at $D_1/J \approx 0.82$, the exchange of metastable states at $D_2/J \approx 0.90$, the point of equal barrier heights at $D_3/J \approx 0.99$, the equilibrium transition at $D_4/J \approx 1.10$, the $(-)$-spinodal at $D_5/J \approx 1.17$, and the $(+)$-spinodal at $D_6/J \approx 1.37$. The bold curves have the same meaning as in Figs. 4 and 5. See the text for a detailed description.

"branches" of the lobe structure can be identified. The set of lobes that decrease in value with increasing H for $0 \leq H \leq H_1$ corresponds to the metastable $(+)$ state, whereas the set of lobes that increase in value with increasing H for $H_1 \leq H \leq H_3$ corresponds to the metastable (0) state. Finally, the set of lobes that start at H=0 and terminate at the $(-)$-spinodal ($H=H_2$) correspond to the metastable $(-)$ state. Since the transfer-matrix eigenvalue spectrum is symmetric about H=0, the set of lobes corresponding to the $(+)$ metastable state continues to $H=-H_2$, and the set of lobes corresponding to the $(-)$ metastable state starts at $H=-H_1$. The envelopes of these sets of lobes exhibit qualitative behavior that is strikingly similar to that predicted for the analytically continued free-energy densities in that they are exponentially suppressed with increasing N for $|H|$ less than its appropriate spinodal value. In Sec. 6 we will show that this agreement is also quantitative.

The results presented above show the transfer-matrix data as functions of the H-field. In Figs. 7 and 8, the real and imaginary parts of the constrained free-energy densities are shown as functions of the D-field for $0.6 \leq D/J \leq 1.4$ for N=18 and H/J=0.1 at T/J=0.25, giving rise to a total of 37 branches. In analogy with the H-scan we draw a line segment in Fig. 3 representing the D-scan, thereby obtaining values of D corresponding to the following mean-field transitions: $D_1/J \approx 0.82$ for the (0)-spinodal, $D_2/J \approx 0.90$ for the exchange of metastable states, $D_3/J \approx 0.99$ for the

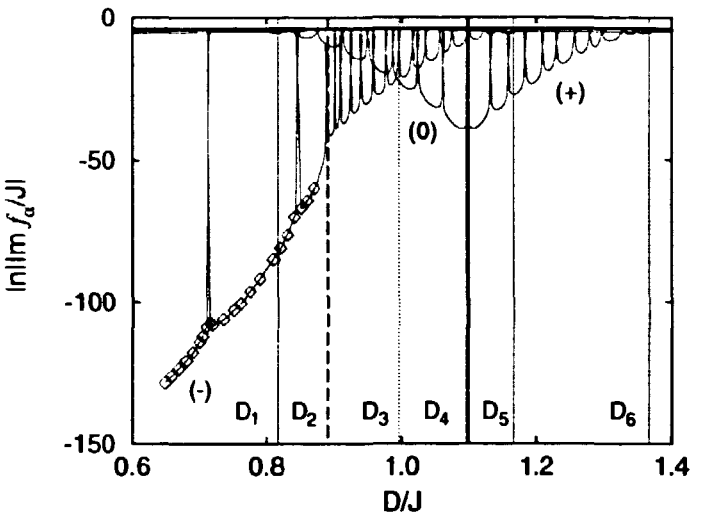

Figure 8: The imaginary parts of the free-energy densities $|\mathrm{Im}f_\alpha/J|$ shown on a logarithmic scale *vs.* D/J. The parameters are the same as in Fig. 7, and the vertical lines have the same meaning. The envelopes of the lobe structures correspond to different metastable states. Diamonds are data points obtained using extended numerical precision (128 bit). See the text for a detailed description.

barrier heights being equal, $D_4/J\approx 1.10$ for the equilibrium transition, $D_5/J\approx 1.17$ for the $(-)$-spinodal, and $D_6/J\approx 1.37$ for the $(+)$-spinodal. These values are indicated as vertical lines. In Fig. 7 we show $\mathrm{Re}f_\alpha/J$ together with bold curves indicating the mean-field results for the stable, metastable and unstable states. The states can again be identified from the slopes of their branches due to the identity

$$-\frac{T}{JN}\frac{\partial \ln|\lambda_\alpha|}{\partial D} = Q_\alpha \,. \tag{57}$$

Thus both the $(+)$ and the $(-)$ branches have slopes near unity, while the (0) state has a slope near zero. For $D\leq D_4$, the $(+)$ state is stable, while for $D\geq D_4$, it remains metastable until the $(+)$-spinodal at $D=D_6$. The bold line nearly parallel to the $(+)$ branch is the $(-)$ branch, which terminates at the $(-)$-spinodal at $D=D_5$. The horizontal bold line is the (0) state, which is metastable for $D_1\leq D\leq D_4$ and stable for $D>D_4$. An exchange of $(-)$ and (0) as the lowest-lying metastable state occurs at $D=D_2$, as seen by the crossing of the two corresponding bold lines.

The imaginary parts of the constrained free-energy densities $|\mathrm{Im}f_\alpha|$ are shown on a logarithmic scale versus D in Fig. 8. The data shown extend over 55 decades. The solid lines for $\ln|\mathrm{Im}f_\alpha/J|\geq -60$ were calculated with 64-bit precision on a HP9000/735 workstation. Extended precision (128-bit) was used for the remaining parts. These data points, shown as diamonds, were calculated on a Cray Y-MP/432 supercomputer. The lobe structure is identified as follows. The lobes that increase in value with

increasing D for $D_4 \leq D \leq D_6$ correspond to the (+) metastable state, whereas those that decrease in value for $D_1 \leq D \leq D_4$ correspond to the (0) metastable state. The remaining lobes for $D \leq D_5$ correspond to the (−) metastable state. Again, the qualitative behavior is very similar to the analytically continued free-energy density. Note also that the lobe structures corresponding to the (−) and (0) metastable states intersect at $D \approx D_3$, which is approximately equidistant in H from the (−)- and (0)-spinodals, as can be seen in Fig. 3. By Eq. (41), the barrier heights $\Delta F_{(-)\to(0)}$ and $\Delta F_{(0)\to(+)}$ are therefore equal to leading order in the expansion about the spinodals, just as their mean-field counterparts $\Delta \mathcal{F}^{\mathrm{MF}}$, even though the dependence on δH for the mean-field barriers are quite different. This result suggests that $|\mathrm{Im} f_\alpha|$ for the metastable state is related to the free-energy barrier height involved in the transition. Further evidence is given by the sudden change in behavior for the (−) metastable branch at $D = D_2$. This change can be explained by the fact that the shape of the critical droplet undergoes a drastic change as the relative stabilities of the two metastable states are exchanged. For $D_2 < D < D_4$, the critical droplet is one through which the (−) metastable state decays into the (0) metastable state before it has a chance to decay finally to the (+) stable state. However, for $D_1 < D < D_2$, the (0) metastable state becomes too costly for a system in the (−) metastable state to decay into it. Instead, the critical droplet is one in which the core magnetization is close to that in the (+) equilibrium phase, and the magnetization $m(r)$ passes directly through zero on its way to the value corresponding to the metastable (−) state as $|r| \to \infty$, without exhibiting a significant plateau corresponding to the (0) metastable state. This droplet is somewhat larger than the one corresponding to an initial decay into the metastable (0) state, and hence it is more costly to form. We will discuss the implications of this result in Sec. 8.

Based on the work of Langer [3, 5], we then conjecture that $|\mathrm{Im} f_\alpha|$ is directly related to the decay rates of the metastable states. In Sec. 6 we will make this connection more quantitative by showing that the scaling behavior of $|\mathrm{Im} f_\alpha|$ agrees with the scaling behavior of the analytically continued free-energy density, considered in Sec. 3.

6 Finite-Range Scaling of the Constrained Free Energy

In this section we apply finite-range scaling to the transfer-matrix results of Sec. 5, and we compare these scaling results to the scaling relations for the analytically continued free energy found in Sec. 3. The results in this section were calculated with $D/J = 1.1$ and $T/J = 0.25$, corresponding to the H-scans shown in Figs. 5 and 6. We are interested in obtaining values from branches representing a "pure metastable" phase $|\alpha\rangle$, so for each N we select values of H for which $\lambda_\alpha = (\lambda_{\alpha-1}\lambda_{\alpha+1})^{1/2}$, thus ensuring a "safe" distance from the near-degeneracies in the transfer-matrix spectrum. These

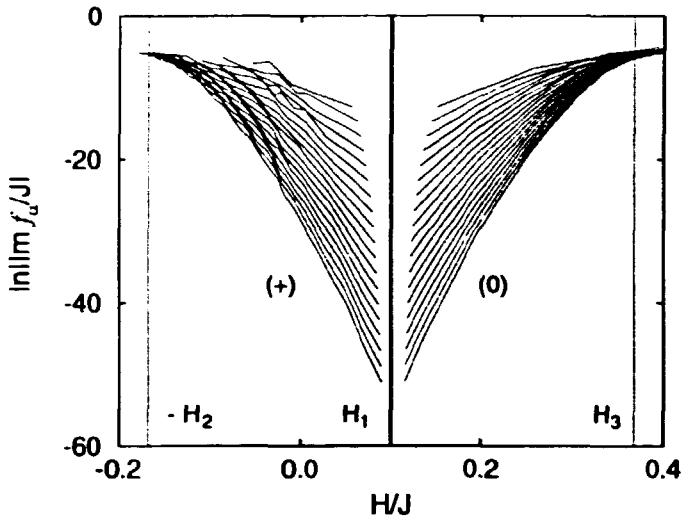

Figure 9: Piecewise-linear envelopes for the lobes of $\ln|\mathrm{Im}f_{(+)}/J|$ (left) and $\ln|\mathrm{Im}f_{(0)}/J|$ (right) for a system at D/J=1.1, T/J=0.25, and with N in the range $6 \leq N \leq 24$. The transition lines mark the (+)-spinodal at $H=-H_2$, the first-order transition at $H=H_1$, and the (0)-spinodal at $H=H_3$. See the text for a detailed description.

points are used to construct envelopes over the lobes of $|\mathrm{Im}f_\alpha|$ shown in Fig. 6. Two sets of such envelopes are shown in Fig. 9, one (left) for the (+) metastable state, and one (right) for the (0) metastable state, for values of N ranging from N=6 to N=24. As N increases, these values drop exponentially to zero between the first-order transition at H_1 and the spinodals at $-H_2$ and H_3, whereas near the spinodals there appears to be a crossover to a slower scaling. This crossover can be seen from the curvature of $|\mathrm{Im}f_{\alpha,N}|$. As N increases, a singularity in the curvature develops, pushing closer to the spinodal. This singularity was also observed for the Q1DI model [24]. In the present study it was found that some of the branches, particularly for the (+) and (−) metastable states in field regions where they were not the lowest-lying metastable state, showed substantial mixing between nearly degenerate eigenvectors. In these regions the branches did not always extend in such a way as to form envelopes without inflections, even with the above eigenvalue criterion satisfied. An example of this behavior in the (−) metastable state is shown in Fig. 6 for $0<H<H_2$. The (+) metastable state shows the same behavior for $-H_2<H<0$, which causes the roughness of the envelopes shown in Fig. 9 for this region.

To obtain the scaling behavior for fields inside the spinodal, we first assume a form for $|\mathrm{Im}f_\alpha|$, based on the results of Eqs. (32) and (41), as

$$\ln|\mathrm{Im}f_{\alpha,N}(D,H,T)| \sim -\beta N^\sigma \Delta(D,H,T)\,, \tag{58}$$

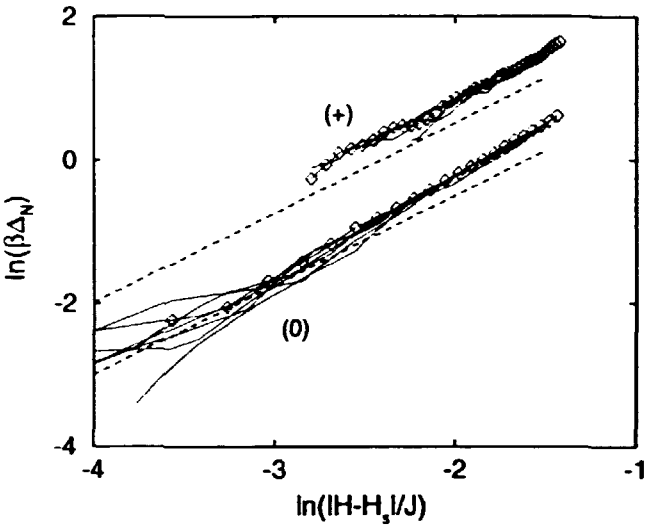

Figure 10: Finite-N estimates for $\beta\Delta(D,H,T)$ in Eq. (58) for the (0) and (+) metastable states, shown on a log-log scale *vs.* $|H-H_s|/J$ for $12\leq N\leq 24$. The diamonds show the estimates for the largest size, N=24. The two dashed lines indicate the corresponding exact ϕ^3 field-theoretical values for $\beta\Delta F$ from Eq. (41). For clarity, both the analytical and numerical results for the (+) state are shifted up by a distance of unity on this logarithmic scale. See the text for a detailed description.

where the exponent σ and the function $\Delta(D,H,T)$ are undetermined. By Eq. (32), we expect $N\Delta(D,H,T)$ to be the barrier height ΔF, as given by Eq. (41). Since $\Delta(D,H,T)$ is expected to be independent of N, we should find σ=1. For a given field H, we interpolate values of $\ln|\mathrm{Im}f_{\alpha,N}|$ from the envelope points using a piecewise linear form. A finite-range estimate for σ was calculated using methods described in Refs. [24, 43],

$$\sigma \approx (\ln 2)^{-1} \ln\left(\frac{\ln|\mathrm{Im}f_{\alpha,24}| - \ln|\mathrm{Im}f_{\alpha,12}|}{\ln|\mathrm{Im}f_{\alpha,12}| - \ln|\mathrm{Im}f_{\alpha,6}|}\right) , \tag{59}$$

giving $\sigma\approx$1.1. Finite-range estimates $\beta\Delta_N$ for $\beta\Delta(D,H,T)=\beta\Delta F/N$ were then calculated for $12\leq N\leq 24$, assuming σ=1:

$$\beta\Delta_N = -\tfrac{2}{N}(\ln|\mathrm{Im}f_{\alpha,N}| - \ln|\mathrm{Im}f_{\alpha,N/2}|) . \tag{60}$$

Fig. 10 shows the estimates $\beta\Delta_N(D,H,T)$ at D/J=1.1 and T/J=0.25, as calculated by Eq. (60), for the (0) and (+) metastable states respectively, plotted on a log-log scale as functions of $|H-H_s|$. The data for the largest system, N=24, are shown as diamonds. These results are compared with the free-energy cost of nucleation obtained from Eq. (41). As can be seen from the figure, the agreement between the extrapolated CTM estimates and the exact results is quite good, considering that the field corrections to the ϕ^3 field theory are expected to be substantial, as was demonstrated in Ref. [24] for the Q1DI model.

7 Monte Carlo Results

The Monte Carlo method is a standard method for studying lattice-gas Hamiltonians, such as the long-range Blume-Capel model. We used the Metropolis algorithm [49, 50, 51] with non-conserved order parameter, where at each step in the Markov process individual spins were proposed to be flipped at random. The system considered had L=200 layers, each containing N=7 spins, and periodic boundary conditions were imposed in the L-direction. All simulations were performed at T/J=0.25, and with a total of 2000 Monte Carlo steps per layer (MCSL). The values of N, D, and H were chosen in order to make nucleation reasonably probable in the time allotted.

In Fig. 11(a)-(d) particular realizations of the decay of four metastable states into their respective equilibrium states are shown. Three of their corresponding phase points are shown in Fig. 3 as solid dots. In case (c), the position is not shown in Fig. 3 since the parameters fall outside the displayed region. Horizontally, the spatial direction extends over the L layers, while the vertical axis is the time axis, in units of 10 MCSL. The bottom row corresponds to t=0 MCSL, while the top row corresponds to t=2000 MCSL. The gray-scale in the plots relates linearly to the average magnetization within the layer. Black corresponds to m=+1, gray to m=0, and white to m=−1. In Fig. 11(a), D/J=1.15 and H/J=−0.1. The system starts in the metastable (+) state. After approximately 1000 MCSL, a critical droplet of the (0) state forms. The droplet then grows linearly in time by roughly linear motion of the domain walls, until it spans the system. Note the periodic boundary conditions. In Fig. 11(b), D/J=0.983 and H/J=−0.249. The system starts in the metastable (+) state. After approximately 200 MCSL, a critical droplet forms, and the state decays into the metastable (0) state. The system remains in the metastable (0) state until a critical droplet of the (−) state causes the system to decay into the (−) equilibrium state. In Fig. 11(c), D/J=0.8 and H/J=−0.42. The free-energy-density functional has two minima, corresponding to a stable (−) state, and a metastable (+) state. In the MC simulation, the system again starts in the metastable (+) state, and we see qualitatively the same behavior, except that the decay goes directly from (+) to (−) since the metastable (0) state does not exist. Note the formation of two independent droplets, which coalesce after they have nucleated. Finally, in Fig. 11(d), D/J=0.95 and H/J=0.0 the system is started in the (0) metastable state. Critical droplets of both the (+) and (−) state cause the system to decay. The purely D-field-driven domain growth at this phase point, in contrast to the H-field-driven growth shown in (a)-(c), appears much more diffuse on the time scale considered in the calculations. After 1000 MCSL the system reaches a configuration where only the (+) and the (−) state are present, reminiscent of late-stage spinodal decomposition.

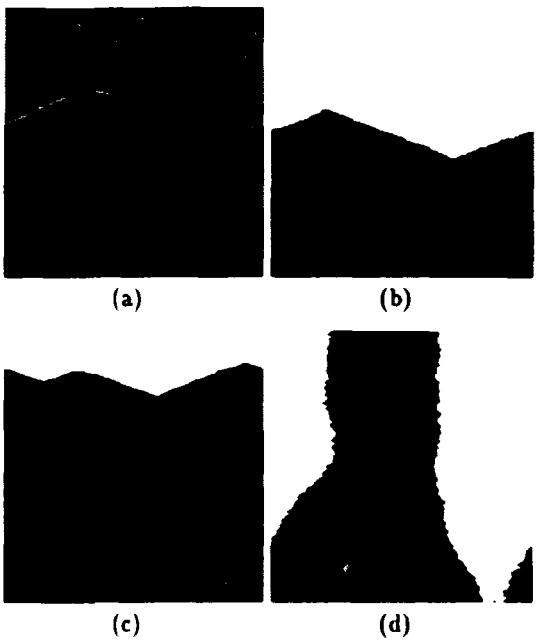

Figure 11: Dynamical behavior of metastable states in the long-range Blume-Capel model. Simulations with L=200, N=7, are performed at T/J=0.25, using a total of t=2000 Monte Carlo steps per layer. The spatial direction is given horizontally, and the time axis vertically. The gray-scale is chosen so that m=+1 is black, m=0 gray, and m=−1 white. The parameters are: (a) D/J=1.15, H/J=−0.1; (b) D/J=0.983, H/J=−0.249; (c) D/J=0.8, H/J=−0.42; and (d) D/J=0.95, H/J=0.

8 Conclusion

In this paper we have applied analytic continuation and a recently developed constrained-transfer-matrix (CTM) formalism to study the stationary properties of metastability in a system with competing metastable states. In addition we have studied the decay of metastable states by Monte Carlo simulation. Langer [3, 4] related the imaginary part of the analytic continuation of the free energy into the region of metastability, $\mathrm{Im}\tilde{F}$, to the decay rate of the metastable states as given by Eq. (1). In a recent study of an Ising model with weak, long-range interactions [24], excellent quantitative agreement was found between the imaginary part of the constrained free-energy density $\mathrm{Im}f_a$ and the decay-rate density of the metastable state as measured from the activation barrier. However, as discussed in the introduction, for systems with several metastable states, Gaveau and Schulman [17] have argued that $\mathrm{Im}\tilde{F}$ is not necessarily a valid measure of the decay-rate density. Motivated by this, the purpose of the present work has been to establish to

what extent the imaginary part of the free-energy density from the CTM formalism can be interpreted as a decay rate in more complicated systems, containing several metastable states.

We have studied a variant of the Blume-Capel model with weak, long-range interactions. One reason for doing so is that for a certain range of fields this model exhibits two competing metastable phases, for which questions can be raised about the interpretation of the analytically continued free energy. Also, the model is simple enough to allow extensive symmetry reduction of the transfer matrix, as shown in Apps. 8 and 8, so that relatively large system sizes could be considered. We have obtained an exact analytic expression for the finite-temperature spinodal and have used this to calculate the various critical lines in the phase diagram in a very simple manner. In the region of the spinodal we have mapped the Hamiltonian to a ϕ^3 field theory to obtain an expression for the free-energy cost of nucleation. We were thus able to calculate the leading term in an expansion around the spinodal of the "Boltzmann weight" that appears in the analytic continuation of the free energy across the first-order phase transition.

We have outlined the CTM formalism, by which a complex constrained free-energy density can be constructed by reweighting the eigenvalues from the transfer matrix of the equilibrium system. The results for the real part of the metastable constrained free-energy density $\mathrm{Re}f_\alpha$ are in excellent agreement with those of the mean-field free-energy density. The associated imaginary part $|\mathrm{Im}f_\alpha|$ is extremely small, showing exponential dependence on the interaction range inside the classical spinodal. In the region of competing metastability it was found that $\mathrm{Im}f_\alpha$ for a metastable state is closely related to the activation barrier involved in the transition, which according to the Van't Hoff-Arrhenius formula of chemical reaction theory, is related to the decay rate. More quantitative evidence was given in Sec. 6, where we applied finite-range scaling to $|\mathrm{Im}f_\alpha|$. There we found very good agreement between the finite-range scaling of $|\mathrm{Im}f_\alpha|$ and the height of the activation barrier obtained by exact analytic continuation.

Our numerical results have demonstrated that the CTM method provides for any pure metastable phase a value for $|\mathrm{Im}f_\alpha|$ that agrees with the Arrhenius law for the decay rate of that particular metastable phase. In the case where two metastable phases are present, the CTM method gives a distinct value of $|\mathrm{Im}f_\alpha|$ for each phase, which can easily be continued through points where these phases are degenerate. The usual procedure of analytic continuation of the free energy, on the other hand, has no mechanism for distinguishing coexistent metastable phases, and thus gives an imaginary part related only to the lowest activation barrier which separates *any one* of the coexistent phases from the equilibrium phase. An example of this type of result was given in Ref. [17] as a "counterexample" to Eq. (1). We, however, interpret that result as being in agreement with Eq. (1) by noting that the configuration space to which the partition function is constrained, and from which the analytically

continued free-energy density measures the escape rate, includes *both* of the degenerate metastable phases, rather than a single pure metastable phase.

In Sec. 7 we studied dynamically the decays of competing metastable states by Monte Carlo simulation. The results confirm that the decay of a particular metastable state might happen either directly or via a succession of separate steps, depending on the availability and relative stability of a second metastable state intermediate between the initial one and the equilibrium phase.

The CTM method has proven to be a highly successful tool in the characterization of metastable phases. It is a nonperturbative method that treats all possible fluctuations in a single calculation. The fluctuations that are important to nucleation are automatically identified, in contrast to the analytical calculations, where the relevant fluctuations must be introduced by hand. This method might therefore be used to study metastability in disordered systems, such as spin glasses, which are known to posses a large number of metastable states so that the critical fluctuations are difficult to characterize. However, the computational requirements of applying the CTM method to such a problem would be enormous.

Acknowledgments

We would like to thank M. Grant and C. C. A. Günther for useful discussions. T. Fiig was supported by the Danish Research Academy. The research was supported in part by Florida State University through the Supercomputer Computations Research Institute (Department of Energy Contract No. DE-FC05-85ER25000), the Center for Materials Research and Technology, and through Cray Y-MP supercomputer time. This work was also supported by National Science Foundation Grant No. DMR-9013107.

Appendix A. Contraction of the Transfer Matrix

This appendix provides a mapping of the transfer matrix from layer-configuration space onto a reduced space. Denote the layer-configuration vector space by $\mathcal{X}$. Since the configuration vectors $|X\rangle \in \mathcal{X}$ can be expressed as direct products of single-spin configurations $|X_i\rangle = |s_{1,i}\rangle |s_{2,i}\rangle \cdots |s_{N,i}\rangle$, $\dim(\mathcal{X}) = 3^N$ for the long-range Blume-Capel model, and the set $\{|X\rangle\}$ constitutes a 3^N-dimensional orthonormal basis for $\mathcal{X}$. The transfer matrix $\mathbf{T}$ is an operator $\mathbf{T} : \mathcal{X} \to \mathcal{X}$. Assume that we have a symmetry group G_U and operators $\mathbf{U} : \mathcal{X} \to \mathcal{X}$ that represent elements of G_U and also commute with $\mathbf{T}$. Symmetry transformation operators must be unitary, so $\mathbf{U}$ must be a cyclic transformation with finite period. This means that the configuration space $\mathcal{X}$ can be divided into equivalence classes, each invariant under G_U. We denote the equivalence classes by C_k, $(k = 1, \ldots, K)$, and we relabel the configuration vectors as $|X_{k,j}\rangle$, where the index k refers to class C_k. Thus $|X_{k,j}\rangle \in C_k$, and the index $j = 1, \ldots, g_k$ runs through all g_k configurations in the class.

Let $\mathbf{O}$ be an arbitrary operator that is invariant under G_U (for the more general case, in which $\mathbf{O}$ has a definite symmetry under G_U, see Ref. [52]). We then have the following fundamental identity:

$$\sum_{i=0}^{3^N-1} \mathbf{O}|X_i\rangle = \sum_{k=1}^{K} \sum_{j=1}^{g_k} \mathbf{O}|X_{k,j}\rangle \,. \tag{A1}$$

A reduced vector space $\mathcal{V}$ is spanned by the orthonormal basis $\{|V_k\rangle\}_{k=1}^{K}$, where

$$|V_k\rangle = \frac{1}{\sqrt{g_k}} \sum_{j=1}^{g_k} |X_{k,j}\rangle. \tag{A2}$$

Thus $\dim(\mathcal{V}) = K$.

If the layer Hamiltonian for a system is invariant under G_U, then the transfer matrix $\mathbf{T}$ is also invariant under G_U. Written as an operator, $\mathbf{T}$ is thus easily transformed into the reduced basis by Eqs. (A1) and (A2):

$$\begin{aligned} \mathbf{T} &= \sum_{k,k'} \sum_{X \in C_k} \sum_{X' \in C'_k} |X\rangle e^{-\beta \langle X|\mathcal{H}^{\mathrm{rp}}|X'\rangle} \langle X'| \\ &= \sum_{k,k'} |V_k\rangle \sqrt{g_k g_{k'}}\, e^{-\beta \langle V_k|\mathcal{H}^{\mathrm{rp}}|V_{k'}\rangle} \langle V_{k'}| \,. \end{aligned} \tag{A3}$$

If we consider the Blume-Capel case, the reduced basis set is $|R_k\rangle \equiv |M_k Q_k\rangle$, $k = 1, \ldots, (N+1)(N+2)/2$, and the multiplicity factor $g_k = g(M_k, Q_k)$ is given by Eq. (6). By substituting appropriately, Eq. (54) is recovered.

Now consider the transformation of Eqs. (47)–(50). Let $|\nu\rangle \in \mathcal{V}$ be an eigenvector in the reduced space, and let $|\alpha\rangle \in \mathcal{X}$ be the corresponding eigenvector in configuration space. It follows from Eq. (A2) that

$$\langle X_{k,j}|\alpha\rangle = \frac{\langle V_k|\nu\rangle}{\sqrt{g_k}} \quad (\forall j) \,. \tag{A4}$$

Expressing $\mathcal{M}_\alpha$ in the reduced basis is now simple:

$$\begin{aligned}\mathcal{M}_\alpha &= \frac{1}{N}\sum_{k=1}^{K}\sum_{j=1}^{g_k}\langle\alpha|X_{k,j}\rangle\langle X_{k,j}|M^{\mathrm{op}}|X_{k,j}\rangle\langle X_{k,j}|\alpha\rangle \\ &= \frac{1}{N}\sum_{k=1}^{K}\langle\nu|V_k\rangle M_k\langle V_k|\nu\rangle\ , \end{aligned} \tag{A5}$$

where Eqs. (A1), (A2), and (A4) are used, and the multiplicity factors introduced by Eq. (A4) are canceled in the sum. The transformation of Eqs. (47)–(50) are all obtained in the same manner.

Appendix B. Decomposition of the transfer matrix

In this appendix the transfer matrix **T** is decomposed by applying a unitary transformation **S** so that $\mathbf{STS}^{\dagger}$ is block diagonal, which allows the separation of all the zero eigenvalues of **T**. The dimension of the original transfer matrix from App. 8 is $\dim(\mathbf{T}) = (N+1)(N+2)/2$, while the reduced transfer matrix has the dimension of $\mathrm{rank}(\mathbf{T}) = 2N+1$.

The transfer matrix can be written as **T=DAD**, where **D** is a diagonal matrix that contains interactions within a layer, and **A** contains interactions between layers [53]. In the Blume-Capel case the matrix elements of **A** are given by

$$\langle MQ|\mathbf{A}|M'Q'\rangle = \exp[\beta J M M'/N]\,, \tag{B1}$$

and the matrix elements of **D** are given by

$$\langle MQ|\mathbf{D}|M'Q'\rangle = \sqrt{g(M,Q)}\exp[-\beta(DQ-HM)/2]\delta_{M,M'}\delta_{Q,Q'}\,. \tag{B2}$$

The matrix **A** is independent of Q and Q', which means that the rank of **A** is just the number of distinct values of the magnetization, since **D** is of full rank; $\mathrm{rank}(\mathbf{T}) = \mathrm{rank}(\mathbf{A}) = 2N+1$. We organize the basis vectors $|MQ\rangle$ in groups according to the magnetization M, $(M{=}-N, -N+1, \ldots, N)$. As an example, the basis vectors for $N{=}2$ are organized in the following way: $\{|-2\,2\rangle, |-1\,1\rangle, |0\,0\rangle, |0\,2\rangle, |1\,1\rangle, |2\,2\rangle\}$. It can be shown in general for the long-range Blume-Capel model, that the number of basis vectors $n(M)$ with magnetization M is $n(M) = \lfloor 1+(N-|M|)/2 \rfloor$, where $\lfloor\cdots\rfloor$ denotes the integer value.

We start by constructing a matrix **B** that block diagonalizes **A**. Let **B** be a block diagonal matrix, where the $n(M){\times}n(M)$ square block corresponding to magnetization M is denoted $\mathbf{B}_M$, and define an $n(M){\times}n(M)$ square matrix $\mathbf{J}_M$ with all its elements equal to unity. We define $\mathbf{B}_M$ as a unitary matrix that diagonalizes $\mathbf{J}_M$. This will be satisfied if we choose the column vectors of $\mathbf{B}_M$ to be an orthonormal basis of eigenvectors for $\mathbf{J}_M$. However, $\mathbf{B}_M$ is not uniquely defined in this fashion, since $\mathrm{rank}(\mathbf{J}_M){=}1$. To make a specific choice for $\mathbf{B}_M$, we select the eigenvector corresponding to the single nonzero eigenvalue of $\mathbf{J}_M$ as the last column.

We define a matrix **C** by $\mathbf{C}{\equiv}\mathbf{BAB}^{\dagger}$. Due to the particular choice for all $\mathbf{B}_M$, it can be shown with a little effort that the **C** matrix has a special matrix form, which

we will call a C-form:

$$\mathbf{C} = \quad . \tag{B3}$$

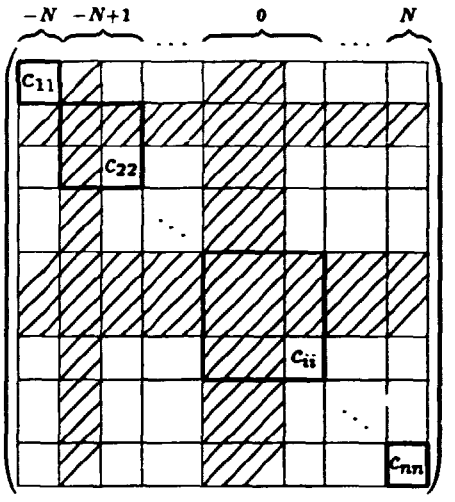

As indicated by the curly brackets in Eq. (B3) the basis vectors are grouped together according to magnetization $M=-N,-N+1,\ldots,N$. All elements within the hashed regions are zero, and the only nonzero elements occupy the last row and column within each magnetization group. From Eq. (B3) it is clear that there exists a permutation matrix $\mathbf{P}$ such that $\mathbf{PCP}^t$ reduces to a block matrix of size $(2N+1)\times(2N+1)$, and all elements outside this block are zero. For each diagonal block $\mathbf{C}_M$ (outlined by thick lines in Eq. (B3)), with $\dim(\mathbf{C}_M)=n(M)$, there is only one nonzero element, which is located at the bottom row diagonal position.

The unitary transformation matrix $\mathbf{S}$ that block diagonalizes $\mathbf{T}$ can now be determined based on the properties of the C-form. The transformation of $\mathbf{T}$ can be expanded as

$$\mathbf{STS}^t = \left(\mathbf{SDB}^t\right)\left(\mathbf{BAB}^t\right)\left(\mathbf{SDB}^t\right)^t . \tag{B4}$$

Hence from Eq. (B4) it follows that the transformed transfer matrix $\mathbf{STS}^t$ will have the C-form if the matrix product between $\mathbf{SDB}^t$ and $\mathbf{C}$ preserves the C-form. It is sufficient to restrict the unitary transformation $\mathbf{S}$ so that it can be decomposed into a block diagonal matrix. The blocks are denoted $\mathbf{S}_M$, $(M=-N,-N+1,\ldots,N)$.

Therefore $\mathbf{SDB}^t$ also decomposes into a block diagonal matrix, and it suffices to show that for all M, $\mathbf{S}_M(\mathbf{D}_M\mathbf{B}_M^t)\mathbf{C}_M$ has the same form as $\mathbf{C}_M$. This is equivalent to requiring that all rows of $\mathbf{S}_M$, except for the last row, are orthogonal to the last column in the matrix product $\mathbf{D}_M\mathbf{B}_M^t$. Since all columns in $\mathbf{D}_M\mathbf{B}_M^t$ are linearly independent, $\mathbf{S}_M$ can be constructed by using a Gram-Schmidt orthogonalization process on the column vectors in $\mathbf{D}_M\mathbf{B}_M^t$. Since $\mathbf{S}$ is unitary, the transformed transfer matrix $\mathbf{STS}^t$ is symmetric and can be reduced by the permutation matrix $\mathbf{P}$ into a $(2N+1)\times(2N+1)$ reduced transfer matrix. This concludes the proof of the decomposition.

References

[1] J. D. Gunton, M. San Miguel, and P. S. Sahni, in *Phase Transitions and Critical Phenomena, Vol. 8*, edited by C. Domb and J. L. Lebowitz (Academic, London, 1983).

[2] K. Binder, Rep. Prog. Phys. **50**, 783 (1987).

[3] J. S. Langer, Ann. Phys. **41**, 108 (1967).

[4] J. S. Langer, Phys. Rev. Lett. **21**, 973 (1968).

[5] J. S. Langer, Ann. Phys. **54**, 258 (1969).

[6] K. Binder and E. Stoll, Phys. Rev. Lett. **31**, 47 (1973).

[7] K. Binder, Phys. Rev. B **8**, 3423 (1973).

[8] K. Binder and H. Müller-Krumbhaar, Phys. Rev. B **9**, 2328 (1974).

[9] R. J. McCraw and L. S. Schulman, J. Stat. Phys. **18**, 293 (1978).

[10] R. J. McCraw, Phys. Lett. **75A**, 379 (1980).

[11] C. M. Newman and L. S. Schulman, J. Stat. Phys. **23**, 131 (1980).

[12] G. Roepstorff and L. S. Schulman, J. Stat. Phys. **34**, 35 (1984).

[13] M. Büttiker and R. Landauer, Phys. Rev. Lett. **43**, 1453 (1979).

[14] M. Büttiker and R. Landauer, Phys. Rev. A **23**, 1397 (1981).

[15] W. Klein and C. Unger, Phys. Rev. B **28**, 445 (1983).

[16] C. Unger and W. Klein, Phys. Rev. B **29**, 2698 (1984).

[17] B. Gaveau and L. S. Schulman, Lett. Math. Phys. **18**, 201 (1989).

[18] V. Privman and L. S. Schulman, J. Phys. A **15**, L231 (1982).

[19] V. Privman and L. S. Schulman, J. Stat. Phys. **31**, 205 (1982).

[20] P. A. Rikvold, Prog. Theor. Phys. Suppl. **99**, 95 (1989).

[21] P. A. Rikvold, Physica Scripta **T38**, 36 (1991).

[22] P. A. Rikvold, B. M. Gorman, and M. A. Novotny, AIP Conf. Proc. **256**, 549 (1992).

[23] M. A. Novotny, W. Klein, and P. A. Rikvold, Phys. Rev. B **33**, 7729 (1986).

[24] B. M. Gorman, P. A. Rikvold, and M. A. Novotny, preprint FSU-SCRI-93-153, submitted to Phys. Rev. E.

[25] C. C. A. Günther, P. A. Rikvold, and M. A. Novotny, Phys. Rev. Lett. **71**, 3898 (1993).

[26] C. C. A. Günther, P. A. Rikvold, and M. A. Novotny, (unpublished).

[27] P. A. Rikvold, H. Tomita, S. Miyashita, and S. W. Sides, (unpublished).

[28] M. E. Fisher, Physics **3**, 255 (1967).

[29] O. Penrose, Heriot-Watt University preprint (1993).

[30] P. Hänggi, P. Talkner, and M. Borkovec, Rev. Mod. Phys. **62**, 251 (1990).

[31] M. Blume, Phys. Rev. **141**, 517 (1966).

[32] H. W. Capel, Physica **32**, 966 (1966).

[33] M. Blume, V. J. Emery, and R. B. Griffiths, Phys. Rev. A **4**, 1071 (1971).

[34] P. A. Rikvold, Electrochim. Acta **36**, 1689 (1991), and refs. cited therein.

[35] A. N. Berker and M. Wortis, Phys. Rev. B **14**, 4946 (1976).

[36] J. D. Kimel, P. A. Rikvold, and Y.-L. Wang, Phys. Rev. B **45**, 7237 (1992).

[37] D. P. Landau, Phys. Rev. B **33**, 7700 (1986).

[38] R. J. Speedy and C. A. Angell, J. Chem. Phys. **65**, 851 (1976).

[39] A. J. Leggett, Rev. Mod. Phys. **47**, 331 (1975).

[40] J. R. Schrieffer, *Theory of Superconductivity* (Addison-Wesley, New York, 1983).

[41] K. Binder, Phys. Rev. A **29**, 341 (1984).

[42] R. B. Griffiths, Phys. Rev. Lett. **13**, 715 (1970).

[43] P. A. Rikvold, B. M. Gorman, and M. A. Novotny, Phys. Rev. E **47**, 1474 (1993).

[44] W. Paul, D. W. Heermann, and K. Binder, J. Phys. A **22**, 3325 (1989).

[45] C. Domb, Adv. Phys. **9**, 149 (1960).

[46] M. Marcus and H. Minc, *A Survey of Matrix Theory and Matrix Inequalities* (Dover, New York, 1964).

[47] R. E. Blahut, *Principles and Practice of Information Theory* (Addison-Wesley, Reading, 1987), pp. 61–64.

[48] W. H. Press, S. A. Teukolsky, W. T. Vetterling, and B. P. Flannery, *Numerical Recipes in C* (Cambridge University Press, Cambridge, 1992).

[49] D. W. Heermann and A. N. Burkitt, *Parallel Algorithms in Computational Science* (Springer, Berlin, 1991).

[50] K. Binder, in *Monte Carlo Methods in Statistical Physics*, edited by K. Binder (Springer, Berlin, 1979).

[51] K. Binder and D. W. Heermann, *Monte Carlo Simulation in Statistical Physics* (Springer, Berlin, 1988).

[52] P. A. Rikvold, K. Kaski, J. D. Gunton, and M. C. Yalabik, Phys. Rev. B **29**, 6285 (1934).

[53] M. A. Novotny, J. Math. Phys. **20**, 1146 (1979).

Paper V

Diffusive Description of Lattice Gas Models

Journal of Statistical Physics, Vol. 71, Nos. 3/4, 1993

Diffusive Description of Lattice Gas Models

Thomas Fiig[1] and Henrik Jeldtoft Jensen[2,3]

Received July 9, 1992; final November 19, 1992

We have investigated a lattice gas model consisting of repulsive particles following deterministic dynamics. Two versions of the model are studied. In one case we consider a *finite open system* in which particles can leave and enter the lattice over the edge. In the other case we use periodic boundary conditions. In both cases the density fluctuations exhibit a $1/f$ power spectrum. The individual particles behave asymptotically like ordinary random walkers. The collective behavior of these particles shows that due to the deterministic dynamics the particles behave as if they are correlated in time. We have numerically investigated the power spectrum of the density fluctuations, the lifetime distribution, and the spatial correlation function. We discuss the appropriate Langevin-like diffusion equation which can reproduce our numerical findings. Our conclusion is that the deterministic lattice gases are described by a diffusion equation without *any* bulk noise. The open lattice gas exhibits a crossover behavior as the probability for introducing particles at the edge of the system becomes small. The power spectrum changes from a $1/f$ to a $1/f^2$ spectrum. The diffusive description, proven to be valid for a moderate boundary drive, fails altogether when the drive goes to zero.

KEY WORDS: Diffusion equation; power spectra; lattice gas; exact solutions; correlation functions; lifetime distribution; single particle properties; collective properties; dynamical crossover.

1. INTRODUCTION

One of the open questions in statistical physics is how to derive effective diffusive Langevin-like equations on the basis of the microscopic interactions in a many-body system. This taks has only been achieved in very special cases, such as in simple one-dimensional models.[1]

[1] Physics Department, Risø National Laboratory, DK-4000 Roskilde, Denmark.
[2] The Niels Bohr Institute, DK-2100 Copenhagen, Denmark.
[3] Present address: Department of Mathematics, Imperial College, London SW7 2BZ, United Kingdom.

0022-4715/93/0500-0653$07.00/0 © 1993 Plenum Publishing Corporation

The coarse-grained hydrodynamic equations, in which all fluctuations are integrated out, can be established by considering the symmetries and conservations of the system, and assuming the existence of an appropriate regularity of the problem so that gradient expansions are possible.[2] This leads to partial differential equations such as the ordinary diffusion equation, say, of the form

$$\partial_t n = \gamma \nabla^2 n + F[n, \nabla n] \tag{1}$$

where $F[n, \nabla n]$ denotes some general function which takes care of all the higher-order terms in the expansion in n and ∇n. The fundamental problem arises when one wants to account for fluctuations. This is most often done by adding some kind of noise, consistent with the symmetries and conservations of the system, to the right-hand side of the diffusion equation

$$\partial_t n = \gamma \nabla^2 n + F[n, \nabla n] + \rho \tag{2}$$

Lacking anything better, one normally assumes the fluctuating source ρ to be a delta-correlated (in time as well as in space) Gaussian process.[3,4] Though power law distributed noise has recently been considered,[5] the important point is that the assumed form of the noise term determines the fluctuations of the system described by (2). This makes it particularly unsatisfactory that we do not know how to determine the form of the fluctuating source term from the microscopics of the considered many-body system.

Our aim in the present paper is to put this problem into perspective by presenting results for a very simple lattice gas model.[6] Consider a lattice gas consisting of hard-core nearest-neighbor repulsive particles. Particles are allowed to enter or leave the system at the edge. The behavior of the individual particles can, for instance, be characterized by the distribution of the time $D(t)$ they spend on the lattice from the time they enter from an edge until they leave. In addition, one can determine the dispersion of the particle position with time: $R^2(t) = \langle [\mathbf{r}(t) - \mathbf{r}(t=0)]^2 \rangle$. The collective behavior of the particle system is *partly* characterized by the fluctuations in the total number of particles on the system $N(t)$. The striking point is that the long-time behavior of this model [which is captured in $N(t)$] depends on the kind of microdynamics the particles follow in each time step. Studies of two-dimensional lattice gases show that the low-frequency behavior of the power spectrum $S(f)$ of $N(t)$ depends on whether the updating algorithm is stochastic or deterministic. In both cases the power spectrum displays power-law behavior

$$S(f) \propto 1/f^{\beta} \tag{3}$$

For moderate boundary drive, the deterministic lattice gas model has $\beta = 1$ (see ref. 6 and below). A similar lattice gas with hard-core repulsion drive by stochastic Monte Carlo dynamics was studied by Andersen *et al.*,[7] who found $\beta = 3/2$ in one, two, and three dimensions.

The behavior of the single-particle characteristics $D(t)$ and $R^2(t)$, however, is not sensitive to the difference between stochastic and deterministic updating. In both cases one finds scaling behavior

$$D(t) \propto 1/t^{\alpha}, \qquad R^2(t) \propto t \tag{4}$$

with $\alpha = 3/2$, which suggests that the individual particles asymptotically experience ordinary random walks.[7,4] Moreover, as the drive at the boundary becomes small, the deterministic model exhibits a crossover to $\beta = 2$. The single-particle quantities D_s and $R^2(t)$ have the same scaling behavior independent of the strength of the boundary drive.

The exponents $\alpha = \beta = 3/2$ are characteristic of noninteracting random walkers independent of dimension[7,20] and can be reproduced by a diffusion equation like (2) with a conserving bulk noise term.[14,20] The exponents $\alpha = 3/2$ and $\beta = 1$ can be reproduced, independent of dimension, by a diffusion equation like (1) driven by a white noise boundary condition without *any* bulk noise, (see refs. 12 and 14 and below). This scaling behavior is *independent* of possible nonlinear terms in the diffusion equation.[14] We do not know of any consistent diffusive description which allows us to describe the region of low boundary drive with $\alpha = 3/2$ and $\beta = 2$.

It is worthwhile to point out that any deviation from the scaling relation $\alpha + \beta = 3$ indicates that important correlations exist between the individual particles.[9] With this in mind we note that the particles in the stochastically driven model behave as if there were no correlations between the particles. Thus, the stochastic element present in each update is able to destroy the interparticle correlations produced by the interaction. This is not the case when the model is driven deterministically. Although the particles perform erratic individual motion, as seen from the random walker form of $D(t)$ and $R^2(t)$, they continue to be correlated even after many collisions. This difference is the reason why the Langevin description in terms of (2) has to assume two different kinds of fluctuating source terms for the two types of updating algorithms. We found this result difficult to anticipate.

Below we concentrate on details of the deterministic lattice gas. In

[4] The exponent α was mistakenly determined to be equal to 2 in ref. 6. The reason for this mistake and the correct determination are described in Section 4.3 of the present paper.

Section 2 we introduce the model. Section 3 contains a detailed analytic solution of the linear diffusion equation, solved in a finite region and driven with a white noise boundary condition. We calculate the density fluctuations, the spatial correlation function, the power spectrum, and the lifetime distribution. We present our simulation results in Section 4: the measured diffusion constant for tracer diffusion as well as for collective diffusion, the power spectrum, lifetime distribution, correlation functions, and the structure factor. In order to investigate the crossover in the behavior as the drive at the edge becomes small, we devote Section 4.6 to the study of crossover behavior as a function of boundary drive. In Section 5 we describe a completely deterministic periodic model which also exhibits $1/f$ fluctuations in the particle density.

2. THE MODEL

The lattice gas model is constructed to simulate particles which follow Stokesian dynamics. That is, the equation of motion has the form $\eta \mathbf{v} = \mathbf{F}$, where η is the friction coefficient, $\mathbf{v}$ the velocity, and $\mathbf{F}$ the total force acting on the particle.

Consider now a two-dimensional square lattice of $N \times N$ sites. Each site can be empty or occupied. Particles on *nearest neighbor* sites repel each other with a central force of unit strength. The dynamics is deterministic and defined in the following way. For each particle we sum up all the forces acting upon the particle in the normal vectorial fashion. If the resulting force is nonzero, we move the particle one lattice site in the direction according to the resulting force (diagonal moves are accepted). In case of competition where two particles which are acted upon by a force of equal strength want to move into the same site, neither particle moves. This will be termed the *blocking mechanism*. Finally, if two particles want to move to the same site but are acted upon by forces of unequal strength, the particle with the largest force wins. The whole lattice is simultaneously updated. The updating rules are illustrated in Fig. 1 in the case of an 8×8 lattice.

The boundary drive acts as a particle reservoir which tends to set up an external pressure by occupying the outer boundary by fixed particles (the cross-hatched particles in Fig. 1), which tends to push particles on neighbor sites into the lattice.

In each iteration, the particles at the boundary sites (i.e., the particles which are nearest neighbor to the cross-hatched particles) are annihilated, and new particles are introduced at all the boundary sites with a probability p per site.

Figure 2 shows a series of snapshots of our lattice gas model, which

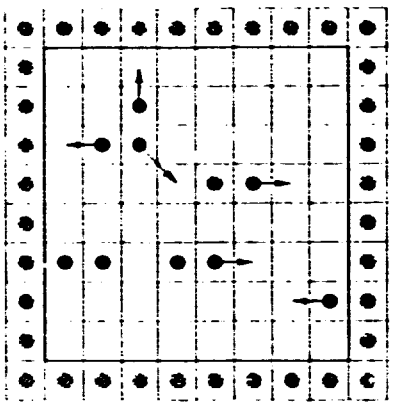

Fig. 1. Updating rules for the deterministic lattice gas model. The arrows on the particles indicate where the particles move to in the next iteration. The particles without any arrow do not move. The case where two or more particles want to enter the same site needs special consideration. First, for competition between two particles which are acted upon by a force of equal strength, no particle moves. This is shown for the four particles occupying the third row from the bottom. Second, if two particles want to move to the same site but are acted upon by forces of unequal strength, the particle with the largest force wins, as shown for the particle with the diagonal arrow.

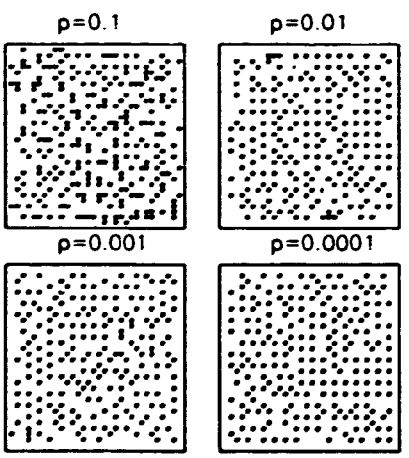

Fig. 2. Series of snapshots for a fixed lattice site of 32×32 for different values of the boundary drive p. As p is reduced, the external pressure ceases, thereby allowing the continued growth of ordered domains.

illustrates the particle configuration for a 32 x 32 lattice for different values of p. All snapshots are taken after the lattice gas has equilibrated. For $p = 10^{-1}$, we see the particles occupying the lattice more or less uniformly, with no observable pattern. Several of the particles are seen to be nearest neighbors, and are thus likely to move in the next iteration. Moving on to $p = 10^{-2}$, one immediately sees a difference in the configuration. Now a much smaller fraction of the particles are nearest neighbors, giving rise to the formation of domains of ordered particles sitting in a cubic lattice. It can readily be checked that the cubic pattern has a degeneracy of four. Thus, the dynamics for small p can be thought of as an interplay among domains of different types, the competition between the external drive which tends to frustrate the formation of the ordered structure and the energy-driven development of this pattern. For $p = 10^{-3}$ and finally $p = 10^{-4}$, this development continues, creating larger and larger ordered domains. In the limit of vanishing p it is expected that the lattice ends up in one monodomain extending through the lattice.

One might wonder why the nearest neighbor interaction used does not lead to a checkerboard pattern of density 1/2 at low p. The checkerboard pattern will, like the observed cubic pattern, minimize the interaction energy. However, the checkerboard pattern is unstable to perturbations. A particle displaced one site in the checkerboard pattern will produce a perturbation which propagates through the whole pattern, whereas a similar perturbation of the cubic pattern only propagates one-dimensionally.

3. DIFFUSIVE DESCRIPTION

The lattice gas described above consists of repulsive particles moving around on the lattice. We will now attempt to describe the lattice gas from a macroscopic point of view by introducing a continuous model. The application of such a model to the discrete lattice gas model is only valid at a coarse-grained level, where the microscopic motion of the particles has been averaged out. The simplest possible description one can think of is the linear diffusion equation. In order to determine to what degree the diffusion equations offers an adequate description, we introduce a coarse-grained density $n(\mathbf{r}, t)$, which denotes the number density of particles, in a volume element around $\mathbf{r}$ at time t. We will concentrate on three properties, the power spectrum $S(f)$ of the total number of particles on the lattice, the spatial correlation function $C(\mathbf{r}, \mathbf{r}')$, and the lifetime distribution $D(t)$. In order to calculate these quantities only the fluctuations in $n(\mathbf{r}, t)$ around its average value $\langle n(\mathbf{r}, t) \rangle$ enter into the calculation. Thus the absolute value of $\langle n(\mathbf{r}, t) \rangle$ is irrelevant and for convenience we will take this as zero.

The appropriate boundary condition on $n(\mathbf{r}, t)$ should be taken such as to mimic the boundary d ·ve on the lattice gas model. In the lattice gas model, the particle density at the boundary varies in a stochastic manner, which is characterized by the lack of long-time correlations. Thus, it is natural to apply a whi·. noise boundary condition on $n(\mathbf{r}, t)$.

The diffusion equation should be solved in a bounded region Ω, where $\Omega = [0, L] \times [0, L]$. The side length $L = Na_0$ is measured in units of the lattice spacing a_0. Hence

$$\frac{\partial n(\mathbf{r}, t)}{\partial t} = \gamma \nabla^2 n(\mathbf{r}, t) + \rho(\mathbf{r}, t) \qquad (\mathbf{r} \in \Omega,\ t > 0) \tag{5}$$

$$n(\mathbf{r}, t) = \eta(\mathbf{r}, t) \qquad (\mathbf{r} \in S,\ t > 0) \tag{6}$$

where S denotes t·· surface of Ω. The Dirichlet condition consists of fixing $n(\mathbf{r}, t)$ to take the v·lue $\eta(\mathbf{r}, t)$, which is a white noise boundary term.[5]

The solution to (5) and (6) can be expressed in terms of the appropriate Green's function $G(\mathbf{r}, t | \mathbf{r}_0, t_0)$. The Green's function is the propagator to a pulse at $\mathbf{r}_0 \in \Omega$ at time t_0. The causality condition forces $G(\mathbf{r}, t | \mathbf{r}_0, t_0) = 0$ when $t < t_0$.

The Green's function is a solution to the problem involving an impulsive point source

$$\frac{\partial G(\mathbf{r}, t | \mathbf{r}_0, t_0)}{\partial t} - \gamma \nabla^2 G(\mathbf{r}, t | \mathbf{r}_0, t_0) = \delta(\mathbf{r} - \mathbf{r}_0)\, \delta(t - t_0) \qquad (\mathbf{r} \in \Omega,\ t > 0) \tag{7}$$

where the Green's function should be chosen to satisfy the homogeneous boundary condition $G(\mathbf{r}, t | \mathbf{r}_0, t_0) = 0$ when $\mathbf{r}_0 \in S_0$ or $\mathbf{r} \in S$.

The Green's function is now used to construct the solution for the particle density $n(\mathbf{r}, t)$ (see ref. 16, Chapter 7). Hence, in general,

$$\begin{aligned} n(\mathbf{r}, t) = {} & \int_0^t \int_{\Omega_0} G(\mathbf{r}, t | \mathbf{r}_0, t_0)\, \rho(\mathbf{r}_0, t_0)\, d\Omega_0\, dt_0 \\ & + \int_{\Omega} G(\mathbf{r}, t | \mathbf{r}_0, 0)\, n(\mathbf{r}_0, 0)\, d\Omega_0 \\ & + \gamma \int_0^t \int_{S_0} [G(\mathbf{r}, t | \mathbf{r}_0, t_0)\, \nabla_0 n(\mathbf{r}_0, t_0) \\ & - n(\mathbf{r}_0, t_0)\, \nabla_0 G(\mathbf{r}, t | \mathbf{r}_0, t_0)]\, dS_0\, dt_0 \end{aligned} \tag{8}$$

[5] Diffusion driven by a boundary noise was considered by Liu[10] in connection with $1/f$ noise in metals. See also the review by Duta and Horn.[11]

The first term in (8) represents the response of a volume noise term, which we will *disregard* because we are only concerned with the deterministic lattice gas model. The second term represents the effect of having an initial condition on $n(\mathbf{r}, t)$. This term can, however, be ignored, because we are only interested in ensemble properties, which we assume to be independent of the initial condition. Finally, using the homogeneous condition of the Green's function, we obtain that the first part in the third term vanishes. Hence,

$$n(\mathbf{r}, t) = -\gamma \int_0^t \int_{S_0} n(\mathbf{r}_0, t_0) \nabla_0 G(\mathbf{r}, t | \mathbf{r}_0, t_0)\, dS_0\, dt_0 \tag{9}$$

The solution to (7) may be obtained by the method of eigenfunction expansion, whereby we expand the Green's function on the eigenfunctions to the Laplacian ∇^2 on the domain Ω subject to zero homogeneous Dirichlet condition,

$$\nabla^2 u(\mathbf{r}) = \lambda u(\mathbf{r}) \tag{10}$$

The eigenfunctions and eigenvalues are obtained by the method of separation of variables.[18] Hence,

$$u_{mn} = \frac{2}{L} \sin \frac{m\pi x}{L} \sin \frac{n\pi y}{L}, \qquad \lambda_{mn} = -\left[\left(\frac{m\pi}{L}\right)^2 + \left(\frac{n\pi}{L}\right)^2\right] \tag{11}$$

where the indices m, n take the values $(m, n = 1, \ldots, \infty)$. The Green's function can now be obtained by expanding $G(\mathbf{r}, t | \mathbf{r}_0, t_0)$ on the eigenfunctions (11), and the Green's function can now be written

$$G(\mathbf{r}, t | \mathbf{r}_0, t_0) = \sum_{m=1}^{\infty} \sum_{n=1}^{\infty} u_{mn}(\mathbf{r})\, u_{mn}(\mathbf{r}_0) \exp[\gamma \lambda_{mn}(t - t_0)]\, \Theta(t - t_0) \tag{12}$$

where $\Theta(t)$ is the Heaviside step function, included to force $G = 0$ when $t < t_0$. The Green's function (12) is now to be substituted into (9) to get the formula for $n(\mathbf{r}, t)$. The noise term $\eta(\mathbf{r}, t)$ is separated into four parts, $\eta^{(i)}(\mathbf{r}, t)$, where $i = 1, \ldots, 4$ corresponds to the four boundaries of Ω.

After evaluating the gradient of the Green's function and simplifying the expression, we obtain

$$\begin{aligned} n(\mathbf{r}, t) = -\frac{2\gamma}{L} \sum_{m=1}^{\infty} \sum_{n=1}^{\infty} u_{mn}(\mathbf{r}) \int_0^t dt_0 \exp[\gamma \lambda_{mn}(t - t_0)]\, \Theta(t - t_0) \\ \times \left\{ \int_0^L dx_0 \sin\left(\frac{m\pi x_0}{L}\right)\left(\frac{n\pi}{L}\right) [\eta^{(3)}(\mathbf{r}_0, t_0) \cos(n\pi) - \eta^{(1)}(\mathbf{r}_0, t_0)] \right. \\ \left. \times \int_0^L dy_0 \sin\left(\frac{n\pi y_0}{L}\right)\left(\frac{m\pi}{L}\right) [\eta^{(2)}(\mathbf{r}_0, t_0) \cos(m\pi) - \eta^{(4)}(\mathbf{r}_0, t_0)] \right\} \end{aligned} \tag{13}$$

Now we are in a position to calculate the power spectrum and other quantities. It is important to recognize that (13) is generally valid for any boundary drive $\eta(\mathbf{r}, t)$, though here we restrict this to include only white noise. This assumption can easily be stated in terms of the correlation function between the individual noise terms. We will assume that the noise terms are uncorrelated in space and time, in correspondence with the boundary conditions for the deterministic lattice gas model, with zero average:

$$\begin{aligned} \langle \eta^{(i)}(\mathbf{r}, t)\, \eta^{(j)}(\mathbf{r}', t') \rangle &= A\delta_{ij}\delta(\mathbf{r}-\mathbf{r}')\,\delta(t-t') \\ \langle \eta^{(i)}(\mathbf{r}, t) \rangle &= 0 \end{aligned} \tag{14}$$

where $\langle \cdots \rangle$ denotes an ensemble average. The ensemble average is performed by considering a huge number of independent realizations of the white noise term $\eta^{(i)}(\mathbf{r}, t)$. The ensemble average is as usually converted to a time and space average. Thus, for any function $f(\mathbf{r}, t)$, the average $\langle f(\mathbf{r}, t) \rangle$ is calculated from

$$\langle f(\mathbf{r}, t) \rangle = \frac{1}{L^2} \int_\Omega d\Omega \lim_{T\to\infty} \frac{1}{T} \int_0^T dt\, f(\mathbf{r}, t) \tag{15}$$

The functional form of $\eta^{(i)}(\mathbf{r}, t)$ is not given *a priori*, but is chosen to match our needs. The actual form of $\eta^{(i)}(\mathbf{r}, t)$ we choose is

$$\begin{aligned} \eta^{(i)}(\mathbf{r}, t) &= \sum_{n=1}^{N} \eta_n^{(i)}(\mathbf{r}, t) \\ \eta_n^{(i)}(\mathbf{r}, t) &= \delta(\mathbf{r}-\mathbf{r}_n^{(i)})\, \Delta t \sum_{k=0}^{\infty} \delta(t - t_{k,n}^{(i)}) - p\delta(\mathbf{r}-\mathbf{r}_n^{(i)}) \end{aligned} \tag{16}$$

where Δt is our time unit. The expression (16) is very appealing physically, and we will explain it in the following. Consider a specific lattice site along the border i, $\mathbf{r}_n^{(i)}$, where the index n picks one of the N possible choices. The noise term acting on this site is termed $\eta_n^{(i)}(\mathbf{r}, t)$. The time sequence $\{t_{k,n}^{(i)}\}$ $(k = 0, \ldots, \infty)$ is selected in such a way that on average p elements from the series fall in each time interval of duration Δt. If we neglect the term $p\delta(\mathbf{r}-\mathbf{r}_n^{(i)})$ in $\eta_n^{(i)}(\mathbf{r}, t)$, this corresponds to a particle entering the lattice site $\mathbf{r}_n^{(i)}$ exactly when $t = t_{k,n}^{(i)}$. [The term containing p could be neglected in the whole analysis, but is included here such that the average value $\langle \eta_n^{(i)}(\mathbf{r}, t) \rangle$ is zero.] This choice is a matter of convenience, and is valid because we only consider the fluctuations in $n(\mathbf{r}, t)$. The form of the noise term $\eta^{(i)}(\mathbf{r}, t)$ is just a sum over the individual noise terms $\eta_n^{(i)}(\mathbf{r}, t)$ acting on the lattice sites.

The amplitude factor A in (14) controls the number of particles which enter the lattice over the rim and is calculated by substituting (16) into (14), using the definition of the average given by (15). By applying Campell's theorem,[19] we obtain

$$A = \frac{Np\,\Delta t}{L^2} \tag{17}$$

3.1. Power Spectrum

The power spectrum $S(f)$ of the total number of particles is evaluated from Fourier transformation of the integrated particle density given by

$$N(\omega) = \int_{-\infty}^{\infty} dt \exp(i\omega t) \int_{\Omega} d\Omega\, n(\mathbf{r}, t) \tag{18}$$

By substituting (13) into (18), we obtain

$$\begin{aligned} N(\omega) = 16\pi\gamma \sum_{m_1=1}^{\infty}{}' \sum_{n_1=1}^{\infty}{}' \frac{1}{\lambda\gamma_{m_1 n_1} + i\omega} \int_{-\infty}^{\infty} dt_0 \exp(i\omega t_0) \\ \times \left\{ \int_0^L dx_0 \sin\left(\frac{m_1 \pi x_0}{L}\right)\left(\frac{1}{m_1 L}\right) [\eta^{(1)}(\mathbf{r}_0, t_0) + \eta^{(3)}(\mathbf{r}_0, t_0)] \right. \\ \left. \times \int_0^L dy_0 \sin\left(\frac{n_1 \pi y_0}{L}\right)\left(\frac{1}{n_1 L}\right) [\eta^{(2)}(\mathbf{r}_0, t_0) + \eta^{(4)}(\mathbf{r}_0, t_0)] \right\} \end{aligned} \tag{19}$$

where the summation symbol $\sum'$ denotes that the sum indices in (19) are restricted to odd values. Further, we have changed the upper limit in the t_0 integral from t to ∞, which is allowed because of the Heaviside function in (13). The power spectrum $S(\omega)$ is obtained from

$$S(\omega)\,\delta(\omega - \omega') = \langle N(\omega)\, N^*(\omega') \rangle \tag{20}$$

The delta function in the definition (20) represents the dc component of $N(t)$. The ensemble average is handled by (14), whereby we obtain

$$\begin{aligned} \langle N(\omega)\, N^*(\omega') \rangle = \frac{512\pi^3\gamma^2 A}{La_0} \sum_{m_1=1}^{\infty}{}' \sum_{m_2=1}^{\infty}{}' \sum_{n_1=1}^{\infty}{}' \sum_{n_2=1}^{\infty}{}' \frac{\delta(\omega - \omega')}{(\lambda_{m_1 n_1}\gamma + i\omega)(\lambda_{m_2 n_2}\gamma - i\omega')} \\ \times \left[\left(\frac{1}{n_1}\right)^2 \delta_{n_1, n_2} + \left(\frac{1}{m_1}\right)^2 \delta_{m_1, m_2} \right] \end{aligned} \tag{21}$$

It should be recognized in (21) that the summation indices m_2 in the first part and n_2 in the second part collapse because of the orthogonality relation of the eigenfunctions.

The occurrence of the prefactor $1/a_0$ in (21) results because the integral over $\eta^{(1)}(\mathbf{r}_0, t_0)$ is a line integral, while the boundary noise is a particle density. This is treated by averaging $\eta^{(1)}(\mathbf{r}_0, t_0)$ over one lattice unit a_0.

The next step is to introduce the eigenvalues (11) back into (21). After some algebra we get

$$S(\omega)=\frac{512AL^3}{\pi a_0}\left[\sum_{m_1=1}^{\infty}{}'\left(\frac{1}{m_1^2}\right)\left(\sum_{n_1=1}^{\infty}{}'\frac{1}{n_1^2+m_1^2-i\omega L^2/\pi^2\gamma}\right)\right.$$
$$\times\left(\sum_{n_2=1}^{\infty}{}'\frac{1}{n_2^2+m_1^2+i\omega L^2/\pi^2\gamma}\right)+\sum_{n_1=1}^{\infty}{}'\left(\frac{1}{n_1^2}\right)\left(\sum_{m_1=1}^{\infty}{}'\frac{1}{m_1^2+n_1^2-i\omega L^2/\pi^2\gamma}\right)$$
$$\left.\times\left(\sum_{m_2=1}^{\infty}{}'\frac{1}{m_2^2+n_1^2+i\omega L^2/\pi^2\gamma}\right)\right] \tag{22}$$

The summation can now be evaluated using the identity[17]

$$\sum_{n=1}^{\infty}{}'\frac{1}{n^2-z}=\frac{\pi}{4\sqrt{z}}\tan\left(\frac{\pi\sqrt{z}}{2}\right), \qquad z\in\mathbb{C} \tag{23}$$

As can be seen from (22), the summation (23) occurs together with a summation of the complex conjugate. Putting everything together, we obtain

$$S(\omega)=\frac{64AL^3\pi}{a_0}\sum_{m=1}^{\infty}{}'\frac{1}{m^2}\frac{1}{(m^4+\omega^2L^4/\pi^4\gamma^2)^{1/2}}$$
$$\times\tan\left[\frac{\pi}{2}\left(-m^2+\frac{i\omega L^2}{\pi^2\gamma}\right)^{1/2}\right]\tan\left[\frac{\pi}{2}\left(-m^2-\frac{i\omega L^2}{\pi^2\gamma}\right)^{1/2}\right] \tag{24}$$

To continue with the calculation, we introduce the notation

$$u_m=\mathrm{Re}\left(-m^2+\frac{i\omega L^2}{\pi^2\gamma}\right)^{1/2}$$
$$v_m=\mathrm{Im}\left(-m^2+\frac{i\omega L^2}{\pi^2\gamma}\right)^{1/2} \tag{25}$$

where Re and Im are the real and the imaginary parts, respectively. It should be recognized that u_m and v_m are both positive. By introducing (25) into (24), we obtain

$$S(\omega)=\frac{64AL^3\pi}{a_0}\sum_{m=1}^{\infty}{}'\frac{1}{m^2}\frac{1}{(m^4+\omega^2L^4/\pi^4\gamma^2)^{1/2}}\frac{\cosh(\pi v_m)-\cos(\pi u_m)}{\cosh(\pi v_m)+\cos(\pi u_m)} \tag{26}$$

The minimal value of ε_m occurs for $\omega = 0$, which makes $\varepsilon_m = m$. Thus, $\cosh(\pi\varepsilon_m) \geq \cosh(\pi m) \gg 1$; this means that, to a good approximation, we can disregard the term $\cos(\pi u_m)$ in both the numerator and the denominator:

$$S(\omega) \simeq \frac{64\pi A L^3}{a_0} \sum_{m=1}^{\infty} \frac{1}{m^2} \frac{1}{(m^4 + \omega^2 L^4/\pi^4 \gamma^2)^{1/2}} \tag{27}$$

It now turns out that only the first term $m = 1$ in (27) contributes significantly to the sum, because of the rapidly decreasing term $1/m^2$.

Substituting the formula for A in (27), we can write the final result for the power spectrum as

$$S(\omega) \simeq \frac{64\pi L^2 p\, \Delta t}{a_0^2} \frac{1}{(1 + \omega^2 L^4/\pi^4 \gamma^2)^{1/2}} \tag{28}$$

which compared to (26) is accurate to within 15%. We define a characteristic frequency ω_c from (28) that will be especially important in our subsequent discussion of our computer simulations:

$$\omega_c = \gamma \left(\frac{\pi}{L}\right)^2 \tag{29}$$

From (28) it follows that for $\omega \ll \omega_c$, $S(\omega)$ is almost constant, which gives rise to white noise, while for $\omega \gg \omega_c$, we obtain $S(\omega) \propto 1/\omega$. Notice that $S(\omega = 0)$ scales with the volume of the system. This is to be expected on the following grounds. The average of the total number of particles on the lattice scales with the volume of the system; thus, $\langle N(t) \rangle \propto L^2$. Hence the fluctuation in $N(t)$ is of the order of $\Delta N(t) \sim \langle N(t) \rangle^{1/2} \propto L$. The power spectrum is expressible as the cosine transform of $\langle \Delta N(t)^2 \rangle$ (the Wiener–Khintchine theorem[21]) and is seen to scale with L^2.

It has been pointed out that $1/f$ noise would result from the driven diffusion equation[12,14]; however, this case was for a semi-infinite system, which does not have the crossover to white noise at low frequencies. For our purpose, this finite-size effect is of particular importance because the crossover frequency is readily determined from our computer experiments, and the finite-size dependence can be checked.

3.2. Correlation Functions

We now turn to the discussion of the spatial correlation functions. The correlation between the particle numbers at position $n(r, t)$ and at position

$n(\mathbf{r}', t')$ is usually described in terms of the equal-time correlation function $C(\mathbf{r}, \mathbf{r}')$ defined by

$$C(\mathbf{r}, \mathbf{r}') = \langle [n(\mathbf{r}, t) - \langle n(\mathbf{r}, t) \rangle][n(\mathbf{r}', t) - \langle n(\mathbf{r}', t) \rangle] \rangle \tag{30}$$

where $\langle \cdots \rangle$, as before, denote an ensemble average. The calculation of the correlation function is done in the same fashion as the evaluation of the power spectrum. The formula (30) can be simplified by noting that the particle density is constructed in such a way that $\langle n(\mathbf{r}, t) \rangle = 0$. Hence,

$$C(\mathbf{r}, \mathbf{r}') = \frac{2\gamma p\, \Delta t}{L^2 a_0^2} \sum_{m_1=1}^{\infty} \sum_{m_2=1}^{\infty} \sum_{n_1=1}^{\infty} \sum_{n_2=1}^{\infty} \frac{1}{m_1^2 + n_1^2 + m_2^2 + n_2^2} u_{m_1 n_1}(\mathbf{r})\, u_{m_2 n_2}(\mathbf{r}') \times \{[1 + (-1)^{m_1 + m_2}] n_1 n_2 \delta_{m_1 m_2} + [1 + (-1)^{m_1 + m_2}] m_1 m_2 \delta_{n_1 n_2}\} \tag{31}$$

In expression (31) it is necessary to introduce an ultraviolet cutoff corresponding to the smallest wavelength on our lattice, i.e., one lattice constant. This means that all sum indices takes values from 1 to N.

Figure 3 is a plot of (31) for a system size of $N = 33$. We have fixed $\mathbf{r} = (L/2, L/2)$ to the center of the lattice, while $\mathbf{r}' = (x, L/2)$ sweeps the lattice horizontally. We see oscillations with a wavelength of one lattice unit; this comes from the fact that the sum has been truncated, leaving maximum intensity on the Fourier component, corresponding to the wavelength of one lattice unit.

At a larger scale we see variation, showing that the correlation function is larger when $\mathbf{r}'$ approaches the border. To understand this behavior, notice that $\langle n(\mathbf{r}', t) \rangle = 0$, which follows from (13), while $\langle n(\mathbf{r}', t)^2 \rangle$

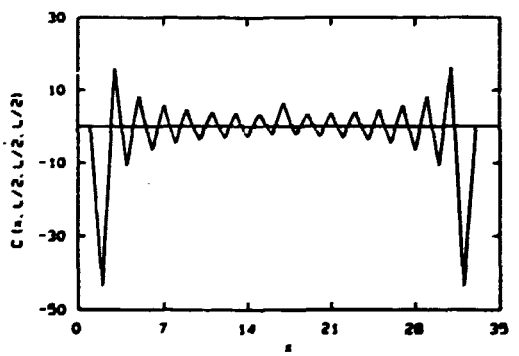

Fig. 3. Spatial correlation function $C(\mathbf{r}, \mathbf{r}')$ for $N = 33$, where $\mathbf{r}$ is fixed to the center of the lattice and $\mathbf{r}'$ sweeps the lattice horizontally.

depends on r', decreasing toward the center of the lattice. From this it follows that the fluctuation in the correlation function is damped toward the center of the lattice. At the center itself we see a small peak. In Section 4 we present computer simulations showing a quite different behavior.

3.3. Lifetime Distribution

The lifetime distribution characterizes the survival times of the particles on the lattice. It is defined as the ensemble average of the time each individual particle spends on the lattice. This is in general impossible to treat from a macroscopic point of view, because the path and lifetime of a particle are highly correlated with those of the other particles. In this section, we calculate the lifetime distribution from our diffusive description of the lattice gas model.

The lifetime distribution can only be calculated in a probabilistic manner, that is, we treat the particles as if they were noninteracting random walkers.

We consider a delta spike in (x_0, y_0) at time $t_0 = 0$ in the particle density and follow how the total particle probability leaks out of the domain Ω. The lifetime distribution is calculated from

$$D(t) = -\frac{\partial}{\partial t}\int_{\Omega} d\Omega\, n(\mathbf{r}, t) \tag{32}$$

The expression (32) can be simplified by introducing the diffusion equation (5) for the partial derivative. Hence,

$$D(t) = -\gamma \int_{\Omega} d\Omega\, \nabla^2 n(\mathbf{r}, t) = -\gamma \int_{S} d\mathbf{S} \cdot \nabla n(\mathbf{r}, t) \tag{33}$$

The particle density $n(\mathbf{r}, t)$ to be substituted into (33) is the Green's function given by (12), where $t_0 = 0$, whereby we obtain

$$D(t) = \frac{-16\gamma}{L^2} \sum_{m=1}^{\infty}{}' \sum_{n=1}^{\infty}{}' \sin\left(\frac{m\pi x_0}{L}\right) \sin\left(\frac{n\pi y_0}{L}\right) \times \left(\frac{n}{m} + \frac{m}{n}\right) \exp(\gamma \lambda_{mn} t)\, \Theta(t) \tag{34}$$

In our lattice gas model, particles enter over the rim, and the lifetime distribution is a simple average over all initial particle positions. To do this in Eq. (34) needs some care, because, by definition, the Green's function takes zero value on the surface $S = \partial\Omega$. This means that $D(t)$ would be

identically zero if we follow this path. To obtain a reasonable answer, we need to introduce the particle close to the surface from the bulk. The obvious choice is to choose this distance as one lattice unit a_0. The calculation, however, poses no difficulty. Hence,

$$D(t) = \frac{64 a_0}{L^3} \sum_{m=1}^{\infty}{}' \sum_{n=1}^{\infty}{}' \left(\frac{n}{m} + \frac{m}{n}\right)^2 \exp(7\lambda_{mn} t)\, \Theta(t) \tag{35}$$

In the following we are only concerned with the asymptotic expansion of (35). Thus it is sufficient to obtain an approximate solution.

To proceed, the double sum for the lifetime distribution can be changed to a product of single sums. Define

$$S_\alpha(a) = \sum_{n=1}^{\infty}{}' n^\alpha \exp(-an^2) \tag{36}$$

We will define a crossover time t_c, which is simply given by $t_c = 1/\omega_c$, where ω_c is the crossover frequency obtained from finite-size scaling of the power spectrum (29). Hence the lifetime distribution (35) can be written as

$$D(t) \propto S_{-2}(t/t_c)\, S_2(t/t_c) + S_0(t/t_c)^2 \tag{37}$$

The single sum (36) can be approximated by applying the Euler–Maclaurin formula.[22] Thus

$$S_\alpha(t/t_c) = \frac{1}{2}\int_1^\infty x^\alpha \exp\left(-\frac{t}{t_c}x^2\right) dx + \frac{1}{2}\exp\left(-\frac{t}{t_c}\right) + R_\alpha \tag{38}$$

We have retained the leading correction, which is just the function $x^\alpha \exp(-ax^2)$ evaluated at the boundary values of the integral, but we will disregard higher-order corrections R_α. The integrals are all expressible in terms of the error function [ref. 23, formula (3.461.5)]. Putting everything together, we find

$$D(t) \propto \exp(-2t/t_c)(t/t_c)^{-3/2} \tag{39}$$

From (39) we see that there exists a region where the lifetime distribution follows an algebraic scaling law with exponent 1.5, independent of lattice size. This is due to the fact that the error function is slowly varying compared to the algebraic term. For times t larger than some characteristic value t_c, the distribution falls off exponentially. This crossover comes from the finite size of the system and t_c is shown to scale with the volume of the lattice.

4. RESULTS OF COMPUTER SIMULATION

In this section we describe the results of computer simulations of the deterministic lattice gas model introduced in Section 2. In the mathematical formulation of the model used in the computer simulations we introduce a discrete variable $\tau(\mathbf{r}, t)$, which is analogous to the particle density $n(\mathbf{r}, t)$ used in the diffusive description. Let $\tau(\mathbf{r}, t) = 0$ if the lattice site $\mathbf{r} = (i, j)$ at time t is empty; otherwise we set $\tau(\mathbf{r}, t) = 1$. The individual particle path through the lattice will be denoted $\mathbf{r}(t)$. Thus the particle enters at the boundary at position $\mathbf{r}(t = 0)$. The particle then diffuses around and at a later moment t' is annihilated. The time t' is termed the *lifetime* of the particle.

4.1. Diffusion Constant

In the description of the continuous model of the lattice gas, there enter two parameters: the amplitude of the white noise A, which was discussed in Section 3, and the diffusion constant γ. The lattice gas model has, however, only one free parameter, p. Thus we expect that γ is some function of p.

We have calculated the *tracer* diffusion coefficient D by measuring the ensemble average of the mean square displacement $R^2(t)$ of the particles,

$$R^2(t) = \langle [\mathbf{r}(t) - \mathbf{r}(t = 0)]^2 \rangle \tag{40}$$

which was shown to scale linearly with t. The linear behavior was found for all values of p and we obtained $D(p) \propto p$. This result suggests that the individual particles in the lattice gas move as ordinary random walkers; only the tracer diffusion constant is affected by changing p.

It is important to distinguish between *tracer* diffusion and *collective* diffusion. The diffusion constant entering the diffusion equation is the *collective* diffusion constant γ. It is defined as the proportionality constant between an infinitesimal density gradient applied to the system and the response in the particle current.

In our computer simulations, an estimate for γ has been obtained by considering the lattice gas model with periodic boundary conditions in the y direction and introducing a density gradient by applying different p at the two remaining boundaries. This effectively reduces the dimensionality of the system to one dimension. For $p = 10^{-1}$ at the left-hand side and $p = 0$ at the right-hand side, the lattice gas entered a steady state where the density across the system was found to drop linearly. By measuring the average particle current through the system per time step J and the density gradient ∇n, we can determine γ by $\gamma = J/(N \nabla n)$, where N is the linear extent of the

lattice. The diffusion constant γ showed a considerable size dependence. For our largest system $N = 128$ we obtained $\gamma = 1.9$.

Reducing the boundary drive to $p \leq 10^{-2}$ on the left-hand side, we obtained a constant density throughout the bulk, but with a density drop in the vicinity of the rightmost border. This result supports diffusive behavior for moderate boundary drives $p \sim 10^{-1}$, while it predicts that in the limit of small p the diffusive description is not valid. This result will be supported further in the succeeding sections, but for now it suffices to draw the parallel back to Fig. 2, which made it clear that the lattice gas showed qualitatively different behavior when p was reduced from $p = 10^{-1}$ to $p = 10^{-2}$.

4.2. Power Spectrum

We have obtained the power spectrum by Fourier transformation of the time signal for the total number of particles on the lattice. In order to obtain sufficient statistics, it is necessary to perform an ensemble average containing several independent runs. Thus $S(f)$ is obtained by

$$S(f) = \left\langle \left| \sum_{t=1}^{T} \left(\sum_{\mathbf{r}} n(\mathbf{r}, t) \right) \exp(i2\pi f t) \right|^2 \right\rangle \tag{41}$$

The angular brackets denote averaging over many different time series.

Figure 4 shows the power spectrum for the lattice gas for different lattice sizes where the boundary drive is fixed to $p = 10^{-1}$. The power spectrum satisfies an algebraic scaling law $S(f) \propto 1/f^{\beta}$, where the exponent $\beta = 1$. For the lattice of size 128×128, the scaling region extends for over three orders of magnitude. The deviation from $\beta = 1$ is caused by our finite system size as well as a finite time resolution. At high frequencies, the deviation is due to aliasing.[13] The low-frequency crossover to white noise is caused by the finite system size; as the system size increases, the crossover frequency is reduced. [In Section 3.1 we calculated the power spectrum (28) from the linear diffusion equation. The result showed that the power spectrum should scale as $S(f) \propto 1/f$ for f larger than the frequency f_c, which is in accordance with the computer simulations.]

From (29) we see that f_c should scale inversely with the volume of the lattice. The crossover frequency f_c can be obtained from the numerical simulations in Fig. 4 by locating the characteristic frequency where the power spectrum exhibits a crossover from $1/f$ noise to white noise, as indicated by the small arrows on Fig. 4. Good agreement with the scaling relation is observed.

The diffusion constant γ which enters the diffusive description can be calculated by substituting numerical values for system size N and crossover

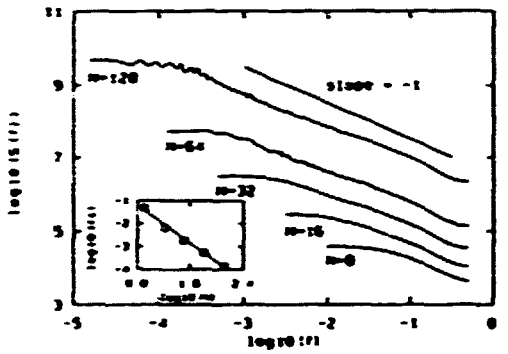

Fig. 4. The power spectrum $S(f)$ for the deterministic lattice gas model for different lattice sizes. It is seen to satisfy algebraic scaling with exponent $\beta = 1$. From the inset it follows that the crossover frequency f_c scales inversely with the volume of the system. The boundary drive is fixed to $p = 10^{-1}$ in all simulations.

frequency f_c into (29). The fact that f_c satisfies the above-mentioned scaling relation implies that γ is independent of system size. Direct evaluation yields $\gamma = 1.4$.

In Section 4.1 the value of the diffusion constant was estimated independently to be $\gamma = 1.9$. However, the use of periodic boundary conditions will, in general, cause an enhanced particle current because we have eliminated the noise from the horizontal borders, which makes it easier for the particles to follow the stream. If the diffusive description is to be taken seriously, we should expect the difference between the two values to disappear in the thermodynamic limit.

The value of the exponent β depends on the strength of the boundary drive. In Fig. 5 the lattice size is fixed to 16×16, while p is varied. As can be seen from the figure, the power spectrum scales as $S(f) \propto 1/f^{\beta}$ at frequencies which are large compared to f_c. However, the exponent exhibits a crossover from $\beta = 1$ for $p > p_c$ to $\beta = 2$ as the boundary drive is reduced from $p = 10^{-1}$ to $p = 10^{-4}$.

This result cannot be explained from the diffusion equation, where we obtained an exponent $\beta = 1$ independent of the free parameters γ and A. Thus, when p is reduced below $p = 10^{-2}$, the diffusion equation does not offer an adequate description of the lattice gas. This conclusion supports the previous observation that the collective diffusion constant was ill defined at small p values.

The dependence of the crossover frequency f_c on p can be obtained from Fig. 5. The crossover frequency is determined as before and we have indicated f_c with small arrows; we get $f_c \propto p$, which is to be expected on

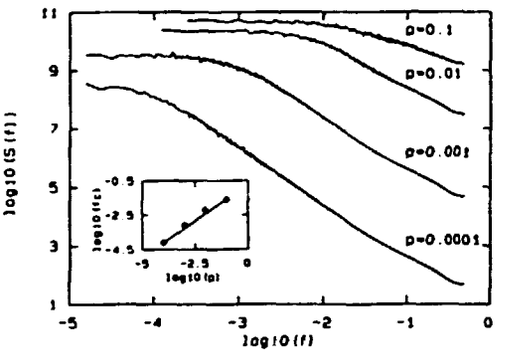

Fig. 5. Power spectrum $S(f)$ for the deterministic lattice gas model. The boundary drive is varied between $p = 10^{-1}$ and $p = 10^{-4}$. Note that the critical exponent exhibits a crossover from $\beta = 1$ to $\beta = 2$ as the boundary drive vanishes. In all simulations we have used a 16×16 lattice.

the following simple-minded argument. We consider a situation where we reduce the boundary drive from p_1 to p_2. Thus the number of particles which are introduced into the lattice is reduced by this ratio p_2/p_1. If we now assume that the qualitative behavior of the lattice gas is unaffected, this reduction can be thought of as redefining our time unit by the reciprocal of this ratio. From this the frequency dependence of p follows. It is interesting that f_c continues to be proportional to p with the same proportionality constant through the region where β changes from 1 to 2.

4.3. Lifetime Distribution

To investigate why the exponents change so dramatically with p, we have calculated the lifetime distribution of the particles. The lifetime distribution is obtained by labeling the particles and following them through each iteration. We record the number of iterations each particle survives in a subsystem of the lattice and calculate the histogram. Thus, if the particle trajectory is given by $\mathbf{r}(t)$, where $\mathbf{r}(t=0) \in \partial\Omega_{sub}$, we set $t = 0$ when the particle enters over the boundary of the subsystem; the lifetime of the particle is defined as $t' = \max\{t \mid \mathbf{r}(t) \in \Omega_{sub}\}$. In the numerical simulation, there is no need to average over independent runs, because the system itself is self-averaging, in the sense that new particles are continuously supplied at the boundary, which are incorporated in the statistics.

It is important to use a subsystem, because the activity at the boundary is much higher than in the bulk, due to the white-noise boundary condition. This will overestimate $D(t)$ for small values of t and lead to a

too high value for the α exponent.[6] It should be recognized that the use of subsystems is a computational trick to mask out the initial transient behavior and that the correct α exponent would show up for large system sizes. In all simulations the subsystem chosen is $\Omega_{sub} = [L/4, 3L/4] \times [L/4, 3L/4]$.

Figure 6 shows the lifetime distribution $D(t)$ for different subsystem sizes when the boundary drive is fixed to $p = 10^{-1}$. We observe that $D(t)$ follows a power law $D(t) \propto 1/t^{\alpha}$ when t is smaller than some crossover time constant t_c, which is indicated by small arrows.

For t larger than t_c we see an exponential decay. The exponent α approaches a constant value $\alpha = 1.5$ independent of the lattice size, and shows some transient behavior for the small systems. [In Section 3.3 we calculated the lifetime distribution (39) from the linear diffusion equation. The result showed that the lifetime distribution should scale as $D(t) \propto 1/t^{3/2}$ for t less than t_c, while $D(t)$ should decay exponentially for t larger than t_c, which is in accordance with the computer simulations.]

In Section 3.3 we defined $t_c = 1/\omega_c$. Thus the crossover time t_c is expected to scale with the volume of the lattice. From the inset of Fig. 6, we see that this is indeed the case.

In the following we examine the consequences of reducing the boundary p on the lifetime distribution.

[6] This effect leads, unfortunately, to an overestimate of the α exponent. See refs. 6 and 24. The power spectrum of the number of particles within the subsystem has the same scaling exponent as for the number of particles on the whole system.

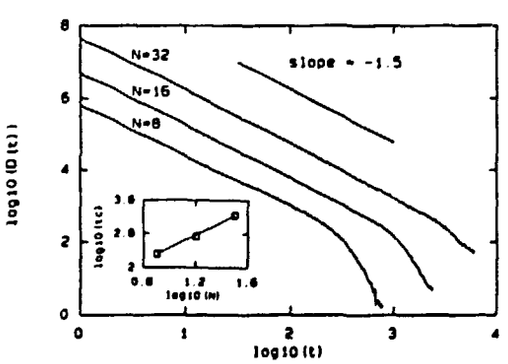

Fig. 6. The lifetime distribution $D(t)$ for different subsystem sizes, with a fixed boundary drive of $p = 10^{-1}$. The lifetime distribution scales as a power law with exponent $\alpha = 1.5$ for $t < t_c$, while for $t > t_c$ we observe an exponential decay. The inset shows the size dependence on the crossover time t_c.

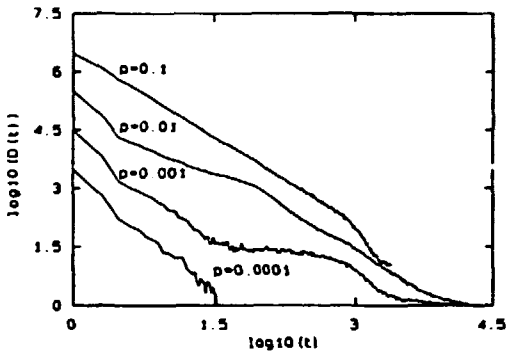

Fig. 7. The lifetime distribution $D(t)$ for a 16×16 subsystem shown for different values of p.

Figure 7 shows the lifetime distribution for a subsystem of size 16×16 for various values of p. For $p = 10^{-1}$ we observe that the lifetime distribution scales according to a power law $D(t) \propto 1/t^{\alpha}$ with exponent $\alpha = 1.5$. This suggests that the particles diffuse through the lattice asymptotically as independent random walkers.

For p in the range $p \in [10^{-2}, 10^{-3}]$ the scaling behavior vanishes and $D(t)$ develops a peak contribution at short lifetimes and a bump at intermediate lifetimes. When p is reduced further to below $p = 10^{-4}$, the lifetime distribution again displays power law behavior, however with an exponent which is slightly higher that before. By increasing the system size, the qualitative behavior for $p \in [10^{-2}, 10^{-3}]$ does not cnange, while the α exponent for $p = 10^{-4}$ retains its original value $\alpha = 1.5$. The results for $p \in [10^{-2}, 10^{-3}]$ is probably due to finite-size effects and we believe that $\alpha = 1.5$ should hold independently of p.

4.4. Correlation Functions

The equal-time pair correlation function is defined analogously to (30), only the particle density $n(\mathbf{r}, t)$ is substituted by $z(\mathbf{r}, t)$. Hence,

$$C(\mathbf{r}, \mathbf{r}') = \langle [z(\mathbf{r}, t) - \langle z(\mathbf{r}, t) \rangle][z(\mathbf{r}', t) - \langle z(\mathbf{r}', t) \rangle] \rangle \qquad (42)$$

The computer simulation poses no complications, except that good statistics is needed. We only consider the case where $\mathbf{r}$ is fixed to the center of the lattice, while $\mathbf{r}'$ is allowed to move horizontally through the lattice. We have simulated the correlation function for the lattice gas for a lattice of size 33×33 for three different boundary drives, $p = 10^{-1}$, $p = 10^{-2}$, and $p = 10^{-3}$. In the case of the correlation function it is important to use an

odd number of lattice sites in the system. This comes from the fact that the boundary conditions on a finite lattice must be such that the four ordered structures of cubic symmetry can exist as a monodomain on the lattice.

The results are shown in Fig. 8. The correlation function is seen to be symmetrical around the center of the lattice, which reflects that our system has inversion symmetry. From our central peak, the function oscillates from even to odd lattice sites with a decreasing amplitude. This behavior is expected on the following grounds. Assume that the site at the center is occupied, $z(L/2, L/2) = 1$. Thus, the particle is part of a particular domain of cubic symmetry. The characteristic size of the domain is called the correlation length ξ. As we let r′ scan horizontally through the lattice, the correlation function will reflect the cubic symmetry of the ordered domain. In a simple theory we would expect the correlation function to exhibit an Ornstein–Zernike type of behavior,[25] where the amplitude of the correlation function is exponentially damped as $\exp(-|\mathbf{r}-\mathbf{r}'|/\xi)$.

The oscillatory behavior is, however, different for the three boundary drives. For $p = 10^{-1}$ the oscillation is damped after approximately $\xi = 2$ lattice sites, while for $p = 10^{-2}$ the correlation function continues to oscillate all the way from the center of the lattice to the border: this corresponds to a long-range order of particles sitting in a regular grid, in accordance with our discussion in Section 2. This feature is even more pronounced for $p = 10^{-3}$, where the amplitude is larger.

The general behavior of the correlation function for different values of the driving field p thus resembles the situation one would expect for a thermodynamic system, where the driving field is substituted by the temperature. The divergence of the correlation length as $p \to 0$ could be

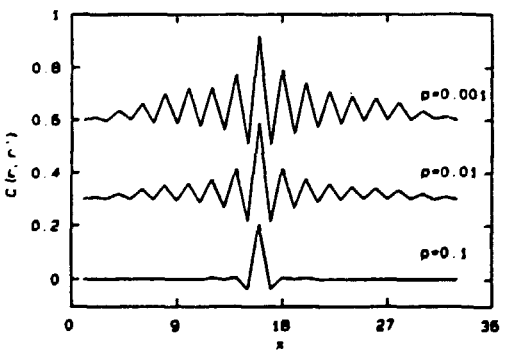

Fig. 8. Spatial correlation function $C(\mathbf{r}, \mathbf{r}')$ for the deterministic lattice gas model. The boundary drive is varied between $p = 10^{-1}$ and $p = 10^{-3}$. In all simulations we have used a 33×33 lattice. The correlation functions for $p = 10^{-2}$ and $p = 10^{-3}$ are displaced vertically by 0.3 and 0.6, respectively.

interpreted as a phase transition. We will return to this point in the next section.

In Section 3.2 we calculated $C(\mathbf{r}, \mathbf{r}')$ from the diffusion equation. Returning to Fig. 3, we see pronounced oscillations, with a wavelength of one lattice constant. The origin of these is, however, completely different, as explained. The similarity between the two correlation functions is, apart from the central peak, merely accidental and we are led to the conclusion that we cannot pursue the diffusive description to account for the fine details in the lattice gas model.

4.5. Structure Factor

We have seen in Section 4.4 that the diffusive description of the lattice gas is invalidated for $p < p_c$, where we have estimated p_c to be in the range $p_c \in [10^{-2}, 10^{-1}]$. If the crossover in the critical β exponent is associated with a kind of phase transition at $p = p_c$, this should be detected in the structure factor.

The structure factor $S(\mathbf{q})$ is defined as the Fourier transform of the density–density correlation function $C(\mathbf{r}, \mathbf{r}')$,

$$S(\mathbf{q}) = \frac{1}{N^2} \sum_{\mathbf{r}} \sum_{\mathbf{r}'} \exp[-i2\pi\mathbf{q}\cdot(\mathbf{r}-\mathbf{r}')]\, C(\mathbf{r}, \mathbf{r}') \tag{43}$$

The structure factor $S(\mathbf{q})$ can in principle be evaluated for all $\mathbf{q}$ vectors, but if the finite system Ω is extended to infinity by means of periodic boundary conditions, it can easily be shown that only the q-vectors $\mathbf{q} = (h/L, k/L)$, where $(h = 0,..., N)$ and $(k = 0,..., N)$, give a nonzero contribution to the structure factor.

In the computer simulations it is more convenient to formulate the structure factor in a slightly different way. Following ref. 25, we obtain

$$S(\mathbf{q}) = \frac{1}{N^2} \left\langle \left| \sum_{\mathbf{r}} \exp(-i2\pi\mathbf{q}\cdot\mathbf{r})\, z(\mathbf{r}, t) \right|^2 \right\rangle \tag{44}$$

The formation of domains of cubic symmetry should show up as a peak in $S(\mathbf{q})$ for $\mathbf{q} = (1/2, 0)$. Thus, it is sufficient to calculate $S(\mathbf{q})$ for a scan along the q_x axis. The results are shown on Fig. 9 for a 33×33 system with $p = 10^{-1}$, $p = 10^{-2}$, and $p = 10^{-3}$. This corresponds to the parameters used in Fig. 3. The solid curves through the data points represent a least square fit to a Lorenz function. From the fit we obtain the full-width half-maximum w of the peaks. The correlation length ξ can be estimated from w by $\xi = 1/w$.

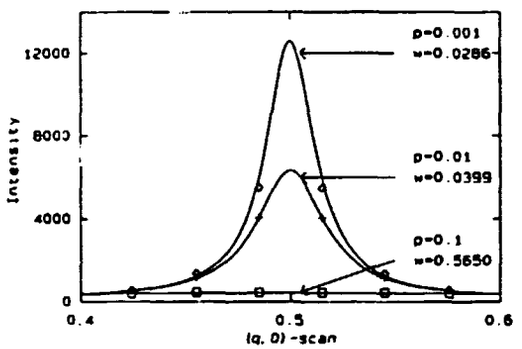

Fig. 9. Structure factor for a 33 × 33 lattice for different values of p. The structure factor $S(\mathbf{q})$ shows a diffuse peak around $\mathbf{q} = (1/2, 0)$. The width of the peak decreases with p, indicating that as $p \to 0$, larger and larger domains form.

From the results we see that there is a dramatic increase in the correlation length, from $p = 10^{-1}$ ($\xi \sim 2$) to $p = 10^{-2}$ ($\xi \sim 25$). For $p \leqslant 10^{-3}$ the correlation length exceeds the system size.

For a thermodynamic system undergoing a second-order phase transition, the correlation length diverges as $T \to T_c$. Thus, for a finite system we expect the correlation length $\xi(T)$ to obtain its maximum value for $T = T_c$. From Fig. 9, we see that the correlation length continues to increase as p is reduced below p_c, which indicates that the phase transition occurs at $p = 0$ and not at $p = p_c$.

This implies that the crossover is not induced by a phase transition, as we know from the standard theory of critical phenomena, but rather by the dynamics, as will be explained in the next section.

4.6. Crossover

The change in the fluctuation spectrum from a $1/f$ spectrum to a $1/f^2$ spectrum occurs as the density $n = n(p)$ on the system becomes so small that system loses its dynamical connectedness across the lattice. The density as a function of the introduction probability p can easily be estimated. In steady state, the in- and outflux of particles over the edge are equal. The probability for a particle to enter the lattice is, to leading order, $p(1-n)$. First, the particle should enter an edge site, which happens with probability p. In order for the particle to be able to move from the edge site into the lattice, the neighbor site has to be empty; this occurs with probability $1-n$. The probability for a particle to leave the system is, to leading order, equal to $n(1-p)n$. The particle has to sit in a site next to the edge site; this give

us one factor n; furthermore, the particle has to have a nearest neighbor in the direction onto the lattice, which is there with probability n, and finally the nearest neighbor site on the edge should be vacant, which gives another factor $1-p$.

The solution $n(p)$ to the equality $p(1-n)=n^2(1-p)$ is plotted in Fig. 10, together with the measured density. One observes that the density converges to a value of about 1/4 as p becomes smaller than about 10^{-1}. At this density, no particle needs to have any nearest neighbor, and hence the particle system cannot lower its density further by its own repulsive interaction. The particle system is not able to support density waves across the system for these low densities.

In order to quantify this crossover in the dynamical connectedness, we have measured the distribution of damage clusters of the system as a function of p. The damage clusters are defined as follows. The system is first taken into the stationary state. Next two parallel runs are made from initial configurations which only differ by the location of one single particle which has been placed in one of the edge sites. The system is simulated a number of time steps equal to the linear size N of the lattice. This number of time steps will suffice for allowing a perturbation to transverse the system if a dynamical connection exists across the lattice. By comparing the two runs, we are able to identify the number s of lattice sites which have been influenced by the extra particle. These sites define a damage cluster of size s. During these N time steps, no particles are allowed to leave or enter the system over the edge.

By repeating this procedure, we can measure the size distribution $D(s)$ of the damage clusters. Figure 11 shows a semilogarithmic plot of the dis-

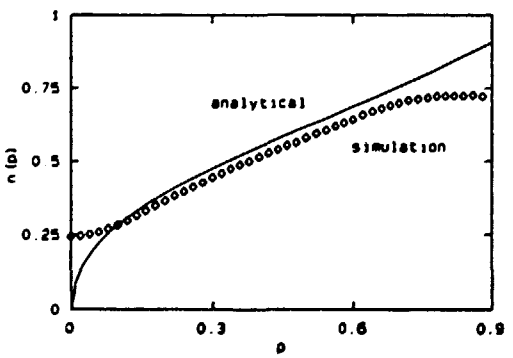

Fig. 10. The density $\langle n(p)\rangle$ as a function of the boundary drive p from computer simulation and analytical calculations.

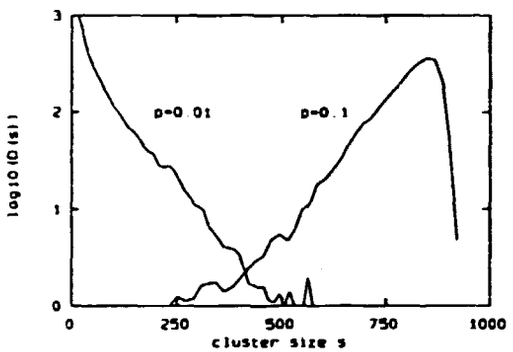

Fig. 11. The size distribution $D(s)$ of damage clusters shown on a semilogarithmic plot for the boundary drive $p = 10^{-1}$ and $p = 10^{-2}$. The system size is 32×32. The main contribution to the distribution is shifted toward lower cluster sizes as p is reduced, signaling a crossover in dynamical connectivity.

tribution for two different values of p. The first distribution is measured with $p = 10^{-2}$, which is in the low-drive region in the sense that the average density is about 1/4 and that the power spectrum exponent β is about to crossover from the value 1 to the value 2. The distribution exhibits approximately an exponential behavior. The other distribution is measured with $p = 10^{-1}$. This distribution is very broad with support at cluster sizes all the way up to the total system size. For this p value, $\beta = 1$ and $n(p)$ is slightly larger than 1/4.

We have studied the size dependence of the average cluster size per time step $\bar{s} = \langle s \rangle / N$. The motivation for considering this quantity is as follows. If the whole system happens to be ordered in the cubic pattern discussed at the end of Section 2, a damage cluster is always of size N. Hence $\bar{s} = 1$. As soon as the system becomes connected, the number of sites in a damage cluster $s(t)$ after t time steps may grow exponentially like $s(t) \sim a^t$ with a equal to the average number of nearest neighbors, i.e., $1 < a < 4$. Our simulations show that in the small-p region, $\bar{s}$ stays finite at a value of order one as the system size is increased. For p larger than 10^{-1}, $\bar{s}$ grows with the system size. The nature of this crossover is the subject of current investigations.

5. THE PERIODIC LATTICE GAS MODEL

The periodic lattice gas model is defined in analogy with the previous lattice gas model, with the exception that the open boundary is substituted by periodic boundary conditions. In this manner we obtain a pure model,

without a surface, and with translational symmetry, both vertically and horizontally. The total number of particles is conserved, and it should be noticed that when $\langle z(\mathbf{r}, t)\rangle \leqslant 0.5$, there is a possibility that the activity stops, because no particle repels any other. However, this is not likely to happen, and was only observed for $\langle z(\mathbf{r}, t)\rangle < z_c$, where $z_c \approx 0.3$. The situation $\langle z(\mathbf{r}, t)\rangle < z_c$ is trivial in the sense that the density is so low that no density fluctuations can be supported, due to the lack of dynamical connectivity in the system.

The power spectrum $S(f)$ is calculated as the Fourier transform of the total number of particles inside a subsystem, while the lifetime distribution is calculated as before. The size of the subsystem is chosen to be $\Omega_{sub} = [L/4, 3L/4] \times [L/4, 3L/4]$. The results for the power spectrum are shown in Fig. 12, while the corresponding results for the lifetime distribution are shown in Fig. 13. In the simulations we used a fixed particle density $\langle z(\mathbf{r}, t)\rangle = 0.3$, which corresponds to the density for the boundary-driven system at $p = 10^{-1}$, as can be seen from Fig. 10.

It follows that both $S(f)$ and $D(t)$ for the periodic lattice gas model display power law scaling with exponents corresponding to the case $p > p_c$ for the boundary-driven model. Further, the exponents proved to be independent of the particle density $[\langle z(\mathbf{r}, t)\rangle > z_c]$.

The correlation function $C(\mathbf{r}, \mathbf{r}')$ has been calculated for $\langle z(\mathbf{r}, t)\rangle > z_c$. The results are compatible with those for $p > p_c$.

The observation of $1/f$ fluctuations in the particle number of a subvolume in the completely deterministic periodic lattice gas raises some questions about the applicability of our analytic description. If we assume that the observed power spectrum also in this case is a consequence of boundary-driven diffusion, we need to conclude that the surrounding

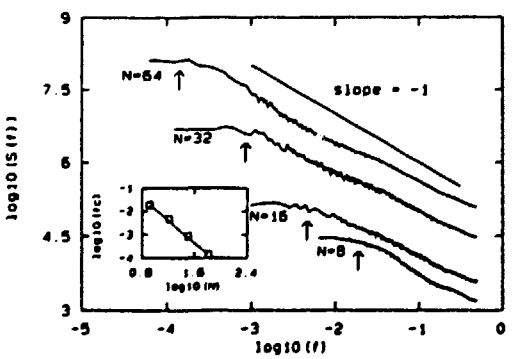

Fig. 12. Power spectrum $S(f)$ for the periodic lattice gas model for different subsystem sizes. The density of particles is fixed to $\langle z(\mathbf{r})\rangle = 0.3$.

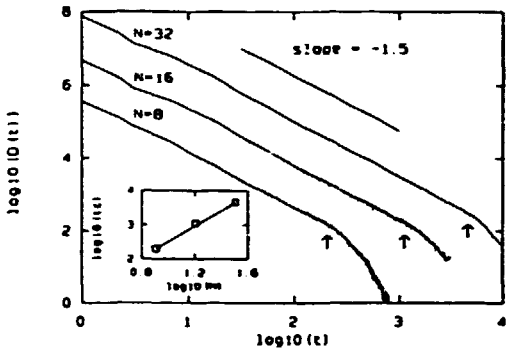

Fig. 13. The lifetime distribution $D(t)$ for the periodic lattice gas model for different subsystem sizes.

system effectively produces a white noise drive of the $z(\mathbf{r}, t)$ at the boundary of the subsystem. [This is certainly consistent with the numerically observed spectrum of the boundary values of $z(\mathbf{r}, t)$, but the power spectrum of the local quantity $z(\mathbf{r}, t)$ for some fixed $\mathbf{r}$ always numerically appears to be white.] However, since the boundary is arbitrarily chosen, a white noise boundary condition for the subsystem seems to be equivalent to a white noise bulk term in the diffusion equation. This lead to an inconsistency, since we know that a white noise bulk term produces a $1/f^{3/2}$ spectrum. We have not yet been able to argue in a convincing way for the form of noise terms to be included in the Langevin equation describing periodic lattice gas.

We should also like to mention that we expect that the fluctuation spectrum of a gas of interacting particles which are allowed to move continuously in space will exhibit $1/f^{3/2}$ as soon as the particle trajectories become chaotic. The restriction to a discrete lattice hinders the lattice gas particles from developing truly chaotic trajectories, although, as indicated by the lifetime distribution, the particles do behave at long times as random walkers. This point is currently under investigation by the use of molecular dynamics simulations of particles moving in the continuous plane.

6. CONCLUSION

We have presented a detailed analysis of $1/f$ fluctuations in a lattice gas in which particles move according to deterministic rules. Two realizations of the model have been studied: a completely deterministic periodic model and an open system with a stochastic drive at the boundary. In both

models we observe a $1/f$ power spectrum for the density fluctuations within a subvolume.

The simulation results were compared to analytic results derived from a macroscopic Langevin description in terms of a simple diffusion equation subject to a white noise boundary condition. It is important to emphasis that this description does not include any fluctuating bulk source term.

The $1/f$ spectrum found in the case of deterministic dynamics is in contrast to results for lattice gases driven by Monte Carlo dynamics. The density fluctuation spectrum for such models has previously been found to exhibit a power spectrum which scales as $1/f^{3/2}$.[7] Such fluctuations can be described by the use of a diffusion equation in which a conserving bulk noise term is included.[14, 20]

Although the deterministic and the stochastic lattice gases have different density fluctuations, the individual particles do, in both cases asymptotically, perform ordinary random walks. The difference between the two models consist in different correlations among the particles. In the deterministic model, the particles remain correlated, whereas in the stochastic case, correlations are lost with time. This shows up in the following way. Strictly independent particles will fulfill the scaling relation $\alpha + \beta = 3$, where the lifetime scales as $D(t) \sim 1/t^{\alpha}$ and the power spectrum scales as $S(f) \sim 1/f^{\beta}$.[9] This scaling relation is found to be fulfilled for the stochastic lattice gas, whereas the deterministic gas has $\alpha = 3/2$ and $\beta = 1$.

It is interesting to investigate in more detail the connection between the microscopic dynamics and the form of the fluctuating source term to be included in an effective Langevin diffusive description. We have found that deterministic dynamics on a lattice is to be described without a fluctuating bulk source term. Does this result change as the trajectories of the particles are allowed to be more complex? We would expect that interacting particles moving in a continuum will produce density fluctuations which need a bulk noise term in the effective Langevin equation as soon as the particle trajectories become chaotic. This issue is currently under investigation.

ACKNOWLEDGMENTS

H. J. J. is supported by the Danish Natural Science Research Council. T. F. is supported by the Danish Research Academy.

REFERENCES

1. J. L. Lebowitz. *Physica* 140A:232 (1986), and references therein.
2. D. Forster, *Hydrodynamic Fluctuations, Broken Symmetry, and Correlation Functions* (Benjamin, New York, 1975).

3. T. Hwa and Kadar, *Phys. Rev. Lett.* 62:1813 (1989).
4. G. Grinstein, D.-H. Lee, and S. Sachdev, *Phys. Rev. Lett.* 64:1927 (1990).
5. Y.-C. Zhang, *Physica A* 170:1 (1990).
6. H. J. Jensen, *Phys. Rev. Lett.* 64:3103 (1990).
7. J. V. Andersen, H. J. Jensen, and O. G. Mouritsen, *Phys. Rev. B* 44:439 (1991).
8. P. Bak, C. Thang, and K. Wiesenfeld, *Phys. Rev. Lett.* 59:381 (1987).
9. H. J. Jensen, K. Christensen, and H. C. Fogedby, *Phys. Rev. B* 40:7425 (1989).
10. S. H. Liu, *Phys. Rev. B* 16:4218 (1977).
11. P. Duta and P. M. Horn, *Rev. Mod. Phys.* 53:497 (1981).
12. H. J. Jensen, *Physica Scripta* 43:593 (1991).
13. R. N. Bracewell, *The Fourier Transform and Its Applications* (McGraw-Hill, New York, 1986).
14. G. Grinstein, T. Hwa, and H. J. Jensen, *Phys. Rev. A* 45:R559 (1992).
15. L. Jacobs and C. Rebbi, *J. Comp. Phys.* 41:203 (1981).
16. P. M. Morse and H. Feshbach, *Methods of Theoretical Physics* (McGraw-Hill, New York, 1953).
17. G. D. Mahan, *Many-Particle Physics* (Plenum Press, New York, 1990).
18. P. Duchateau and D. W. Zachmann, *Partial Differential Equations* (McGraw-Hill, New York, 1986).
19. S. O. Rice, in *Selected Papers on Noise and Stochastic Processes*, N. Wax, ed. (Dover, New York, 1954).
20. H. C. Fogedby *et al.*, *Mod. Phys. Lett. B* 5:1837 (1991).
21. D. K. C. MacDonald, *Noise and Fluctuations: An Introduction* (Wiley, New York, 1962).
22. M. Abramowitz and I. A. Stegun, *Handbook of Mathematical Functions* (Dover, New York, 1972).
23. I. S. Gradshteyn and I. M. Ryzhik, *Table of Integrals, Series, and Products* (Academic Press, New York, 1980).
24. H. J. Jensen, *Mod. Phys. Lett.* 5:625 (1991).
25. H. E. Stanley, *Introduction to Phase Transitions and Critical Phenomena* (Oxford University Press, Oxford, 1971).

Bibliographic Data Sheet **Riso-R-734(EN)**

Title and author(s)

Ordering Phenomena and Non-equilibrium properties of Lattice Gas Models

Thomas Fig

ISBN	ISSN
87-550-1959-5	0106-2840

Dept. or group	Date
Physics Department	March 1994

Groups own reg. number(s)	Project/contract No.

Pages	Tables	Illustrations	References
214	1	74	115

Abstract (Max. 2000 char.)

This report falls within the general field of ordering processes and non-equilibrium properties of lattice gas models.

The theory of diffuse scattering of lattice gas models originating from a random distribution of clusters is considered. We obtain relations between the diffuse part of the structure factor $S_{diff}(q)$, the correlation function $C(r)$, and the size distribution of clusters $\mathcal{D}(n)$. For a number of distributions we calculate $S_{diff}(q)$ exactly in one dimension, and discuss the possibility for a Lorentzian and a Lorentzian square lineshape to arise.

We discuss the two- and three-dimensional oxygen ordering processes in the high T_c superconductor $YBa_2Cu_3O_{6+x}$ based on a simple anisotropic lattice gas model. We calculate the structural phase diagram by Monte Carlo simulation and compared the results with experimental data. The structure factor of the oxygen ordering properties has been calculated in both two and three dimensions by Monte Carlo simulation. We report on results obtained from large scale computations on the Connection Machine, which are in excellent agreement with recent neutron diffraction data. In addition we consider the effect of the diffusive motion of metal-ion dopants on the oxygen ordering properties on $YBa_2Cu_3O_{6+x}$.

The stationary properties of metastability in long-range interaction models are studied by application of a constrained transfer matrix (CTM) formalism. The model considered, which exhibits several metastable states, is an extension of the Blume Capel model to include weak long-range interactions. We show, that the decay rate of the metastable states is closely related to the imaginary part of the equilibrium free-energy density obtained from the CTM formalism.

We discuss a class of lattice gas model for dissipative transport in the framework of a Langevin description, which is capable of producing power law spectra for the density fluctuations. We compare with numerical results obtained from simulations of a lattice gas model consisting of repulsive particles obeying deterministic dynamics, driven by a white noise boundary condition.

Descriptors INIS/EDB

Available on request from:
Risø Library, Risø National Laboratory (Risø Bibliotek, Forskningscenter Risø)
P.O. Box 49, DK-4000 Roskilde, Denmark
Phone (+45) 46 77 46 77, ext. 4004/4005 · Telex 43 116 · Telefax (+45) 46 75 56 27

RISØ

OBJECTIVE

The objective of Risø National Laboratory is to further technological development in three main areas: energy, environment and materials.

USERS

Risø's scientific results are widely applied in industry, agriculture and public services. Risø contributes its share of new knowledge to the global research community.

RESEARCH PROFILE

Risø emphasises long-term and strategic research providing a solid scientific foundation for the technological development of society.

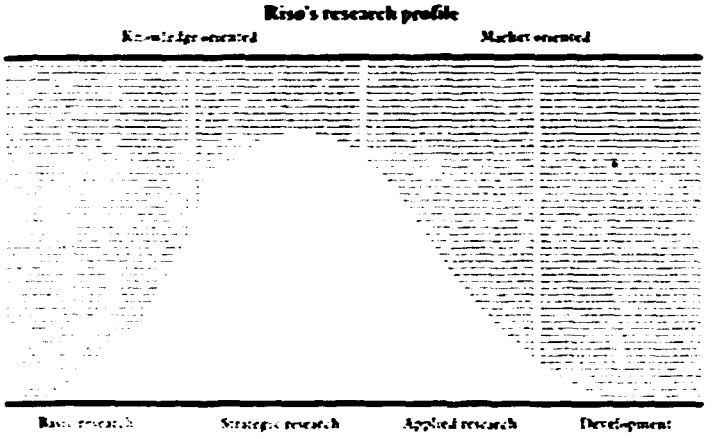

PRIORITY AREAS

- **Combustion and gasification**
- **Wind energy**
- **Energy materials**
- **Energy and environmental planning**
- **Assessment of environmental loads**
- **Reduction of environmental loads**
- **Safety and reliability of technical systems**
- **Nuclear safety**
- **Atomic structure and properties of materials**
- **Advanced materials and materials technologies**
- **Optics and fluid dynamics**

Risø-R-734(EN)
ISBN 87-550-1959-5
ISSN 0106-2840

Available on request from:
Risø Library
Risø National Laboratory
P.O. Box 49, DK-4000 Roskilde, Denmark
Phone +45 46 77 46 77, ext. 4004/4005
Telex 43116, Telefax 46 75 56 27